

**Simulation and Modeling of
Whistler Mode Wave Growth
Through Cyclotron Resonance
with Energetic Electrons
in the Magnetosphere**

A Dissertation

Submitted to the Department of Electrical Engineering
and the Committee on Graduate Studies
of Stanford University
in Partial Fulfillment of the Requirements
for the Degree of
Doctor of Philosophy

By
Curtis Ray Carlson

June 1987

Copyright © 1987
 by
 Curtis Ray Carlson

© Copyright 1987

by

Curtis Ray Carlson

I certify that I have read this thesis and that in my opinion it is fully adequate, in scope and quality, as a dissertation for the degree of Doctor of Philosophy.

(Principal Advisor)

I certify that I have read this thesis and that in my opinion it is fully adequate, in scope and quality, as a dissertation for the degree of Doctor of Philosophy.

I certify that I have read this thesis and that in my opinion it is fully adequate, in scope and quality, as a dissertation for the degree of Doctor of Philosophy.

Approved for the University Committee
on Graduate Studies:

Dean of Graduate Studies

the first of these is the fact that the
the second is the fact that the
the third is the fact that the

the fourth is the fact that the

the fifth is the fact that the
the sixth is the fact that the
the seventh is the fact that the

the eighth is the fact that the
the ninth is the fact that the
the tenth is the fact that the

the eleventh is the fact that the
the twelfth is the fact that the

the thirteenth is the fact that the
the fourteenth is the fact that the

Abstract

This dissertation presents new models and simulations of wave growth experienced by electromagnetic waves propagating through the magnetosphere in the whistler mode. For these waves, which have frequencies below the electron gyro and plasma frequencies, the magnetospheric plasma acts like a natural amplifier often amplifying the waves by ~ 30 dB. The mechanism for growth is cyclotron resonance between the circularly polarized waves and the gyrating energetic electrons which make up the Van Allen radiation belts. The main emphasis is to simulate single frequency wave pulses, in the 2-6 kHz range, that have been injected into the magnetosphere, near $L \simeq 4$, by the Stanford transmitting facility at Siple Station, Antarctica. However, the results of this thesis can also be applied to naturally occurring signals, signals from other transmitters, non CW signals, and signals in other parts of the magnetosphere which are not probed by the Siple Station transmitter.

Simulations using a new transient model reproduce, for the first time, exponential wave growth (25-250 dB/s) and saturation (20-35 dB) coincident with a linearly increasing frequency versus time (up to 60 Hz/s). No other simulation or modeling efforts have simultaneously predicted these experimentally observed features, particularly the linear frequency increase. The transient model includes the geomagnetic inhomogeneity and electrons ranging in all three dimensions of velocity space. The methods for calculating the phased bunched currents, stimulated radiation, and radiation propagation are also unique and are based upon test particle electron trajectories calculated by integrating nonlinear equations of motion generalized to allow the evolution of the frequency and wave number at each point in space.

The results show the importance of the transient aspects in the wave growth process. The wave growth established as the wave propagates toward the equator, is given a spatially advancing wave phase structure by the geomagnetic inhomogeneity. Through the feedback of this radiation upon other electrons, the conditions are set up which result in the linearly increasing output frequency with time. The transient simulations also show that features like growth rate and total growth are simply related to the various parameters, such as applied wave intensity, energetic electron flux, and energetic electron distribution.

Acknowledgments

This research was supervised by Professors R. A. Helliwell and U. S. Inan. I am sincerely grateful for their constant support and guidance. I want to express a special thanks to my principal advisor, professor R. A. Helliwell, for his constant encouragement, sincere interest in this work, and for the countless hours of discussion which profoundly influenced this research and my personal development.

I want to express my appreciation to Drs. D. L. Carpenter and T. F. Bell for their valuable suggestions and comments, and to Ev Paschal for supplying the data analyses. I also want to thank my third reader, Professor J. W. Goodman, for reviewing this manuscript.

Thanks are due to many other members of the VLF group and the Space, Telecommunications, and Radioscience Laboratory of Stanford for their help, instruction, and friendship.

I want to express my gratitude to my parents and my brother who have supported and encouraged my education. As time goes on, I appreciate more and more the sacrifices they have made.

Most of all I want to thank my wife Molly, who has shared the stress and reward of my doctoral studies. Molly was always there when I needed her and, as a genuine expression of love, selflessly toiled with me to prepare this document for which I am grateful.

This research was supported by the National Aeronautics and Space Administration under contract NGL-05-020-008 and by the Division of Polar Programs of the National Science Foundation under contracts DPP-83-17092 and DPP-83-18508. Acknowledgement is made to the National Center for Atmospheric Research, which is sponsored by the National Science Foundation, for the computing time used in this research.

Table of Contents

<u>Chapter</u>	<u>Page</u>
1. Introduction	1
1.1. The Earths' Magnetosphere	1
1.2. Experimental results	4
1.3. Whistler-mode wave-particle interactions	7
1.4. Outline of this report	11
1.5. Contributions of this work	13
2. Physics of gyroresonant wave-particle interactions	15
2.1. Model of the inner magnetosphere	15
2.2. Whistler-mode wave propagation	17
2.3. Dynamics of trapped radiation belt particles	19
2.4. Energetic electron distribution function	26
2.5. Test particle trajectories and phased bunched currents	29
2.6. Numerical methods and algorithms	47
3. Quasi-steady state models and simulations	53
3.1. Steady state simulations with negligible feedback	53
3.2. Self consistent steady state simulation	72
3.3. The two port model	75
4. Transient model and simulations	87
4.1. The transient model	87
4.2. Transient simulations	94
4.3. Comparison with experiment	114
5. Summary and recommendations	117
5.1. Summary	117
5.2. Recommendations for future work	119
Appendix A. Noise generation	127
Appendix B. Equations of motion	129
Appendix C. Program Documentation	131
References	151

List of Tables

<u>Figure</u>		<u>Page</u>
2.1.	Reference model parameters	30
2.2.	Maximum perturbed velocity values	36
4.1.	Transient simulation parameters	95
4.2.	Growth rates and saturation levels	108

List of Figures

<u>Figure</u>	<u>Page</u>
1.1. The earths' magnetosphere	2
1.2. Interaction region locations	4
1.3. Evolution of a riser triggering pulse	6
1.4. Frequency evolution of the riser triggering pulse	7
1.5. Wave structure and electron motion	8
2.1. Dipole field geometry	16
2.2. Off-equatorial to equatorial field strength ratio	19
2.3. Vector relations for electron velocity	20
2.4. Wave-particle angular relationships	23
2.5. Relative phase shift	26
2.6. Anisotropic pitch angle distribution	28
2.7. Electron trajectories with $v_{\parallel eq} = v_{Req}$	32
2.8. Current from the equatorially resonant electrons	34
2.9. Phase mixing	35
2.10. Electron trajectories with $v_{\parallel eq} = 1.02v_{Req}$	39
2.11. Current from the offequatorially resonant electrons	40
2.12. Electron trajectories with trapped behavior	41
2.13. Phase space plots of trapping zones	43
2.14. Interaction length and location versus $v_{\parallel eq}$	44
2.15. Equatorially and offequatorially resonant currents	46
2.16. Spatial discretization method	48
2.17. Error associated with the predictor corrector algorithm	50
2.18. Mesh schemes for sampling the energetic distribution	52
3.1. Homogeneous $\mathbf{B}_s(\alpha_{eq}, v_{\parallel eq}); f(v, \alpha) = 1$	56
3.2. Homogeneous $\mathbf{B}_s(\alpha_{eq}, v_{\parallel eq}); f(v, \alpha) = v^{-6}$	57
3.3. Homogeneous $\mathbf{B}_s(v_{\parallel eq})$ and $\mathbf{B}_s(\alpha_{eq})$	58
3.4. Homogeneous $\mathbf{B}_s(z)$	60
3.5. Inhomogeneous $\mathbf{B}_s(\alpha_{eq}, v_{\parallel eq})$	61
3.6. Inhomogeneous $\mathbf{B}_s(v_{\parallel eq})$	63
3.7. Inhomogeneous $\mathbf{B}_s(\alpha_{eq})$	65
3.8. Inhomogeneous $\mathbf{J}(z)$	66
3.9. Inhomogeneous $\mathbf{B}_s(z)$	67

3.10.	v_{\parallel} edge effects in $\mathbf{J}(z)$ and $\mathbf{B}_s(z)$	69
3.11.	$\mathbf{B}_s(v_{\parallel})$ and $\mathbf{B}_t(v_{\parallel})$ accompanying the previous figure	70
3.12.	Self consistent steady state	74
3.13.	Distribution for the self consistent steady state	75
3.14.	Two-port feedback model	77
3.15.	Gain curves for $v_{\parallel} = v_{Req}$	79
3.16.	Beamformer for two-port calculations	80
3.17.	Gain versus beamwidth	81
3.18.	Gain versus beamcenter	82
3.19.	Gain curve using the beamformer	84
3.20.	Stable growth using two-port model	85
3.21.	Unstable growth using two-port model	85
4.1.	Distributed feedback model	88
4.2.	The transient model	89
4.3.	Electron injection scheme	93
4.4.	Pulse propagation in space and time	96
4.5.	Wave growth (dB) versus z and t	97
4.6.	Wave growth (pT) versus z and t	98
4.7.	Phase bunched current versus z and t	99
4.8.	Output field	100
4.9.	Output growth rate and frequency	102
4.10.	Output field parametric in df/dt	103
4.11.	Output field parametric in τ	104
4.12.	Self excited output field parametric in df/dt	105
4.13.	Evolution of a pulse with termination triggering	106
4.14.	Output field parametric in applied field	109
4.15.	Output field parametric in electron flux	110
4.16.	Output field parametric in pitch angle anisotropy	111
4.17.	Output field parametric in $h(v_{\parallel})g(\alpha)$	113
4.18.	Comparison of simulations with data	115
5.1.	Evolution of a pulse with sidebands	122

Chapter 1. Introduction

This research concerns the cyclotron resonant interactions between whistler-mode electromagnetic waves and energetic electrons in the earth's magnetosphere. Through this interaction, energy is exchanged between the resonant electrons and the whistler-mode waves resulting in wave growth or damping. This chapter includes a brief description of the magnetosphere, wave-particle interactions, previous work in this field, and a review of specific contributions presented in this thesis.

1.1. The Earth's Magnetosphere

The earth's magnetosphere is a region of space contained within an outer boundary, or magnetopause, that separates the interplanetary and geomagnetic fields. The supersonic solar wind impinging upon the earth's dipole-like magnetic field gives the magnetosphere its large scale structure shown in Figure 1.1. In the sunward direction the magnetosphere is compressed by the solar wind and extends out to about 10 earth radii. In the anti-sunward direction the geomagnetic field is pulled out into a tail extending several hundred earth radii. The inner boundary of the magnetosphere is taken to be approximately 100 km above the earth's surface [Lyons and Williams, 1984].

This thesis deals with a type of wave-particle interaction found throughout the magnetosphere. The inner magnetosphere is defined by the geomagnetic field lines with $L < 6$ (i.e. field lines which extend out less than 6 earth radii at the geomagnetic equator). These field lines can be approximated by a distortion free dipole field.

The inner magnetosphere is a magnetoplasma composed of thermal electrons and positive ions that can be divided into two constituents, a cold background plasma and a hot energetic plasma. The cold plasma consists of particles with energies less than 1 eV and is believed to originate from the ionosphere, a layer of the earth's atmosphere ionized by solar radiation and extending from 60 km to ~ 1000 km altitude. The cold plasma is believed to flow up the magnetic field lines from the upper layer, or F-region, of the ionosphere. Cold plasma densities measured at the magnetic equator gradually decrease with increasing distance from the earth until a sharp decrease in plasma density occurs at the plasmapause [Carpenter, 1963]. The region within the

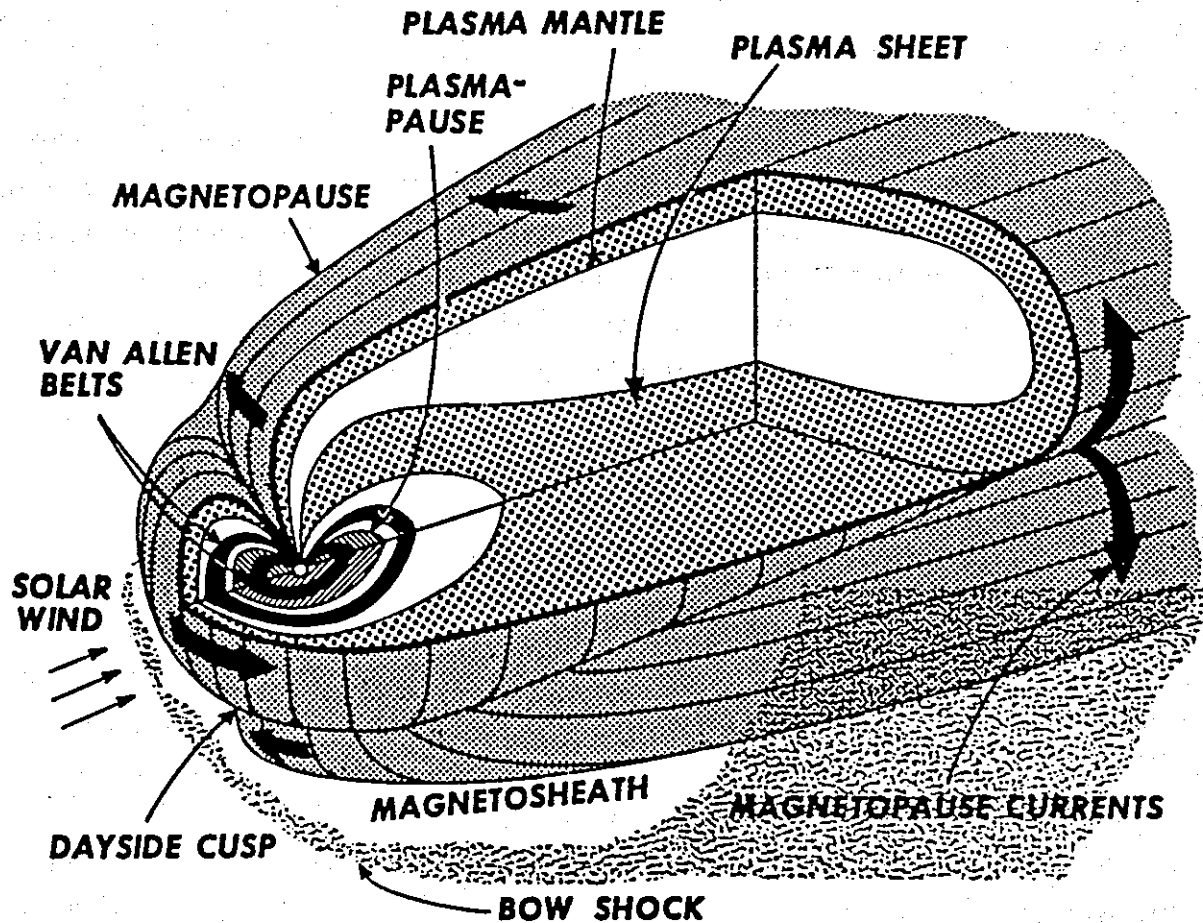


Figure 1.1. A 3-dimensional cutaway view of the earth's magnetosphere (from *Park* [1978]). This figure shows how the geomagnetic field is blown into a comet-like shape by the solar wind.

plasmopause is called the plasmasphere. The plasmapause is field aligned and begins at about $L=4-5$ during quiet geomagnetic conditions [*Park and Carpenter*, 1978].

The hot energetic plasma consists of magnetically trapped particles with energies ranging from ~ 100 eV to hundreds of MeV. These charged particles gyrate about the magnetic field lines, bounce back and forth between magnetically conjugate mirror points and drift across field lines [*Schultz and Lanzerotti*, 1974]. These particles make up the Van Allen radiation belts.

A variety of plasma waves propagate in the magnetosphere [*Anderson*, 1983; *Melrose*, 1986; *Shawhan*, 1979a,b]. The wave mode of importance in this study is the whistler-mode which can propagate at frequencies below the electron gyro and plasma frequencies. When propagating through a smooth background plasma, whistler-mode

waves are nonducted with elliptical polarization and propagate at an angle to the geomagnetic field. Whistler-mode waves can also be guided by gradients in the cold plasma, such as the plasmapause [Inan and Bell, 1977], or ducted by field aligned enhancements or depletions in the cold plasma at frequencies below or above the one-half electron gyrofrequency, respectively [Smith *et al.*, 1960; Smith, 1960, 1961; Scarabucci and Smith, 1971; Walker, 1976; Strangeways, 1980, 1981a,b]. A combination called hybrid mode propagation can exist where ducted whistler-mode waves propagate down the field lines, reflect off of the topside ionosphere, and continue propagating in a nonducted mode [Bell *et al.*, 1983; Smith *et al.*, 1985; Rastani *et al.*, 1985]. Guided or ducted waves have wave-normals roughly aligned with the geomagnetic field. A whistler-mode wave whose wave-normal is aligned with the geomagnetic field is said to be longitudinally propagating and is a circularly polarized wave. In any case, the sense of rotation is the same as the gyrating electrons.

The whistler-mode gets its name from the whistling sound of dispersed electromagnetic impulses generated by lightning, called whistlers, first described by Preece in 1894 [Al'pert, 1980]. Whistlers have been observed between 100 Hz and 1 MHz [Shawhan, 1979]. The first explanation of whistlers hypothesized the existence of the plasmasphere [Storey, 1953] and a more detailed analysis of whistler dispersion led to the discovery of the 'nose' whistler [Helliwell *et al.*, 1956] which in turn led to the discovery of the plasmapause [Carpenter, 1963]. The magnetosphere has also turned out to be a natural laboratory for the study of wave-particle interactions. A tool which successfully exploits magnetospheric whistler-mode signals is the Stanford University VLF transmitter at Siple Station, Antarctica ($L \simeq 4$) [Helliwell and Katsufakis, 1974, 1978]. The Siple transmitter and the geomagnetically conjugate receiving station at Roberval, Quebec (now at Lake Mistissini, Quebec), are used to investigate a broad range of topics including VLF antennas, magnetospheric electric fields, duct locations, electron number densities, occurrence properties of ducted signals, wave-induced electron precipitation, wave growth and saturation, wave growth threshold, triggered emissions, suppression, VLF induced quiet bands, entrainment, side-band generation, spectral broadening, earth-ionosphere waveguide propagation, power line harmonic radiation, and magnetospheric hiss [Bell and Inan, 1981; Bell *et al.*, 1985, 1983, 1981, 1980; Carlson, 1983; Carlson *et al.*, 1985; Carpenter, 1980; Carpenter and Bao, 1983; Carpenter and Miller, 1983, 1976; Carpenter *et al.*, 1985; Helliwell, 1983a,b, 1979, 1975, 1974; Helliwell and Katsufakis, 1978, 1974; Helliwell *et al.*, 1986a,b, 1980, 1975; Inan and Helliwell, 1982; Inan *et al.*, 1977; Kimura *et*

al., 1983, 1981; *Kintner et al.*, 1983; *Park*, 1981; *Park and Chang*, 1978; *Paschal and Helliwell*, 1984; *Raghuram et al.*, 1977a,b; *Rastani et al.*, 1985; *Sonwalkar and Inan*, 1986; *Sonwalkar et al.*, 1984; *Stiles*, 1974; *Stiles and Helliwell*, 1977, 1975; *Tkalcevic*, 1983].

1.2. Experimental results

The main focus of this thesis is the interaction between ducted VLF whistler-mode waves and the radiation belt electrons. More specifically, the growth of single frequency ducted wave pulses is studied, although evidence and analyses imply that results from single frequency studies can be applied to variable frequency signals [*Helliwell*, 1970; *Carlson et al.*, 1985] and even to broadband 'noise-like' signals [*Helliwell et al.*, 1986]. The sketch in Figure 1.2 shows the predicted interaction region for ducted, constant frequency signals centered at the geomagnetic equator.

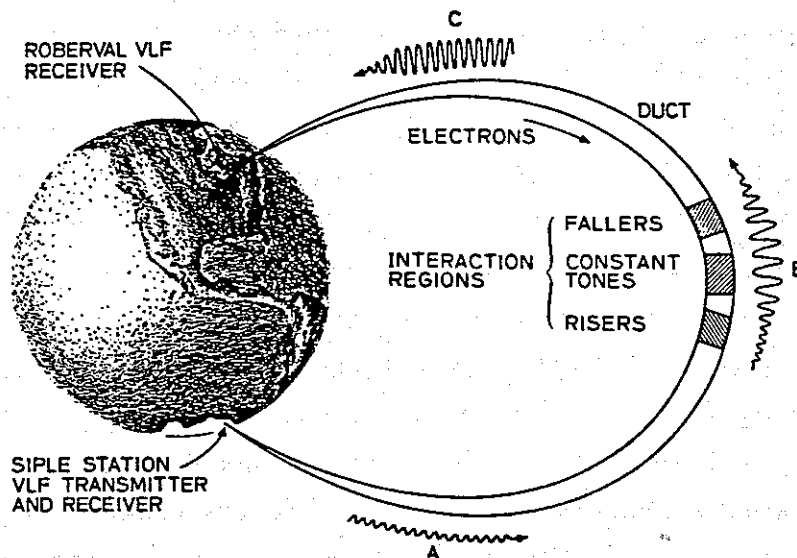


Figure 1.2. Sketch of ducted VLF propagation from Siple Station, Antarctica, and Roberval, Quebec (from *Helliwell* [1986]). As suggested by *Helliwell* [1967] the interaction region is located around the equator for constant frequency signals, and upstream or downstream of the equator for falling or rising frequency signals, respectively.

Two characteristic measures of wave growth are the growth rate and the saturation level. The growth itself can be somewhat irregular but in many cases is

exponential, with growth rates between 25 dB/s and 250 dB/s, reaching saturation after 20-35 dB of total growth [Stiles and Helliwell, 1977]. Satellite measurements of the unamplified signal strength have been limited and none has yet been made *in situ* of a ducted signal. Satellite based field strength measurements of nonducted Siple signals place the input field strength between 0.01 pT and 0.3 pT [Inan *et al.*, 1977; Rastani *et al.*, 1985]. The actual field strength necessary for wave growth within a duct is of interest since there is a power threshold below which wave growth is not possible [Helliwell *et al.*, 1980]. Two possible explanations for this growth threshold have been given. One explanation is based on the signal to noise ratio in the magnetosphere. The other explanation requires that the wave intensity exceed the threshold above which electrons can become trapped in the potential well of the wave. Many wave growth theories, as will be discussed, are based on this trapping threshold. However, the model developed and applied in this thesis does not require trapping for wave growth to occur.

Simulations or models of whistler-mode wave growth should reproduce both the amplitude and phase evolution of a received signal. While the spectral characteristics of these signals have been analyzed for many years, most studies have examined only signal amplitudes as functions of frequency and time and have not considered the signal phases. Recent work has begun to include phase analysis [Paschal and Helliwell, 1984; Dowden *et al.*, 1978; Rietveld *et al.*, 1978; Rietveld, 1980]. Phase measurements of signals from the Siple VLF transmitter [Paschal and Helliwell, 1984] show that pulses with temporal growth have a relative phase advance with time and thus a positive frequency offset from the transmitted signal, often starting at the very beginning of the pulse.

One of the pulses analyzed by Paschal and Helliwell [1984] is reproduced in Figure 1.3 and includes the traditional spectrogram and amplitude versus time displays along with the phase versus time display. This pulse, received at Roberval, Quebec, was transmitted from Siple Station, Antarctica. Besides the exponential wave growth (36 dB/s) up to a peak or saturated level, Figure 1.3 also shows the initial frequency offset (1.1 Hz), advance in phase during wave growth, a jump in the phase advance rate indicating the release of the triggered emission, and the constant frequency advance versus time of the rising emission. This phase advance rate is plotted in Figure 1.4 and indicates that prior to triggering, the phase advance versus time was nearly parabolic since the frequency increase rate is nearly linear at ~ 9 Hz/s. Measurements made of a few more pulses, like the pulse shown in Figure 1.3, suggest

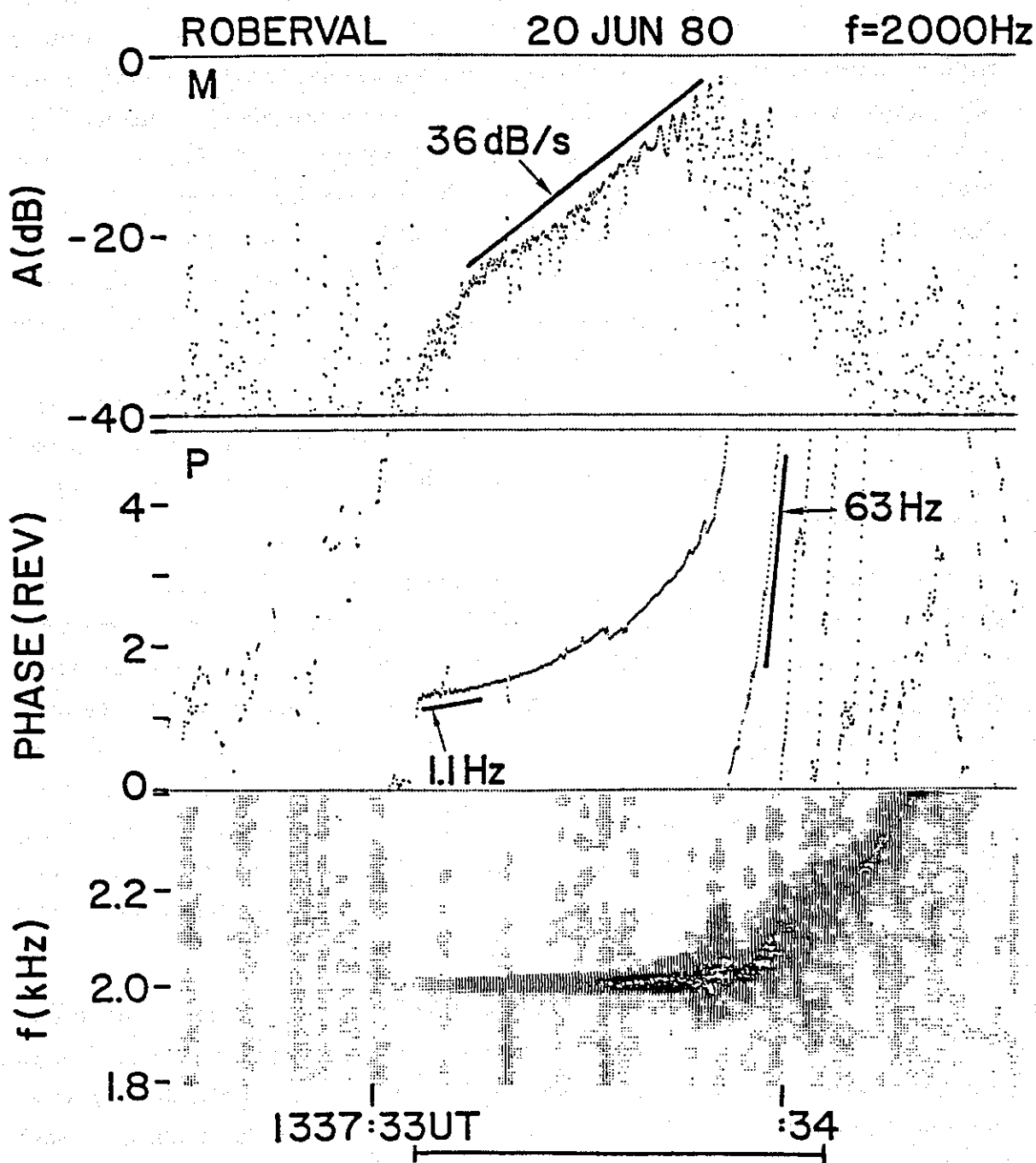


Figure 1.3. Displays of a 1 second, 2 kHz Siple pulse received at Roberval (from Paschal and Helliwell, 1984). The spectrogram (top panel) shows a triggered rising emission. The magnitude plot (middle panel) indicates a 36 dB/s growth rate up to a saturated level after ~ 20 dB of total growth. The phase relative to the transmitted phase (bottom panel) shows an initial frequency offset of 1.1 Hz from the transmitted signal. The phase advance with time, prior to triggering, is nearly parabolic indicating a linear increase in frequency with time.

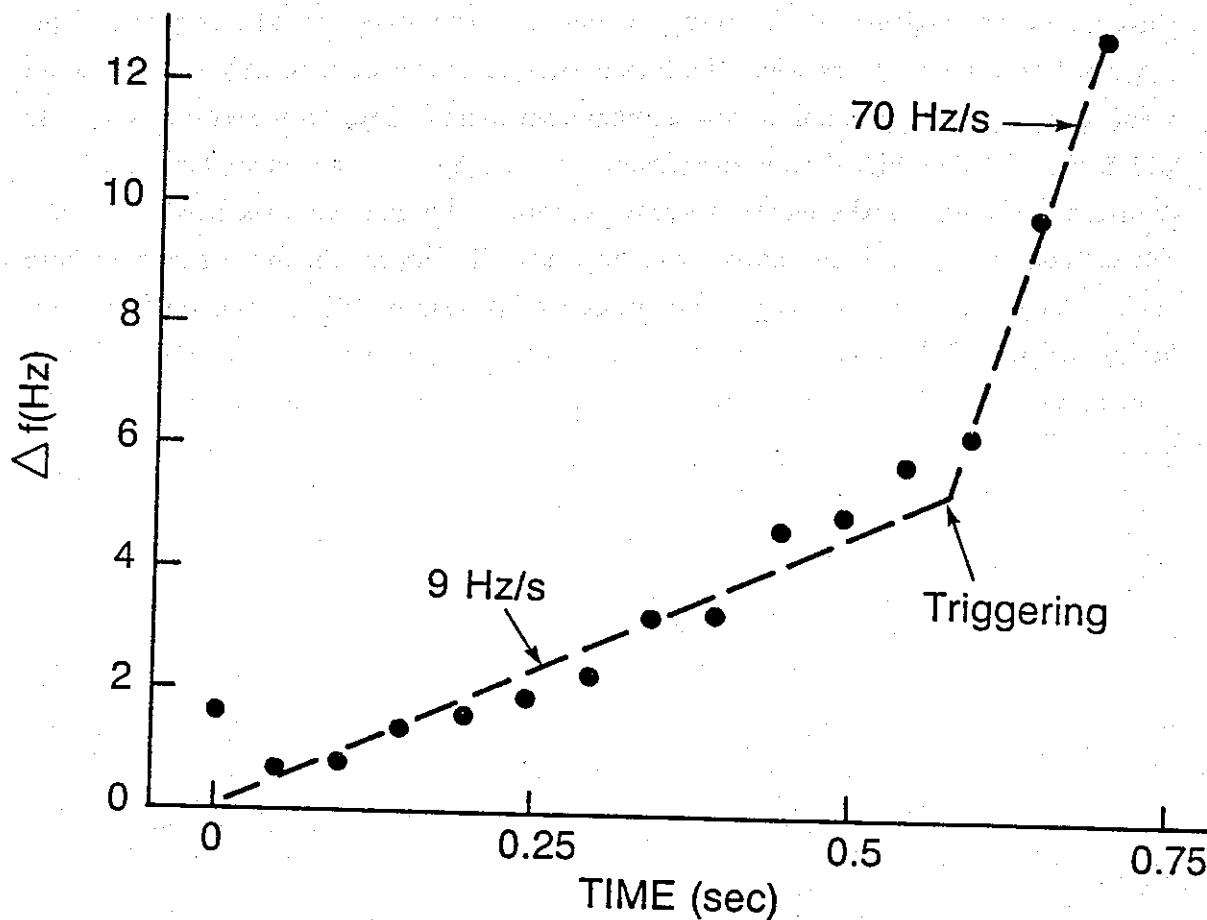


Figure 1.4. Frequency versus time for the pulse in Figure 1.3 calculated by simply measuring the slope of the phase curve. Prior to triggering, the frequency increases nearly linearly with time at ~ 9 Hz/s.

that the higher the growth rate the higher the rate of frequency increase which range up to 60 Hz/s.

The simulation efforts in this thesis concentrate on reproducing the features described above and shown in Figure 1.3, namely:

- I. Exponential wave growth.
- II. Saturation.
- III. Parabolic phase advance in time.

1.3. Whistler-mode wave-particle interactions

Wave-particle interactions are a significant and integral part of the global dynamics of magnetospheric particles [Gendrin, 1975]. Wave-particle interactions can occur

through either longitudinal (Landau) resonance or cyclotron (gyro) resonance. Longitudinal resonance occurs when the phase velocity of the wave matches the electron velocity component parallel to the geomagnetic field. Cyclotron resonance occurs when the Doppler-shifted wave frequency, as seen by a counterstreaming electron, approximately equals the electron gyrofrequency. This can be visualized using the sketches of a wave field and an electron trajectory in Figure 1.5. Since the wave field is right-hand circularly polarized, the angular relationship between the electrons' velocity vector and the wave field vectors can become stationary over an extended time period, thus allowing a cumulative energy exchange between the electrons and the wave.

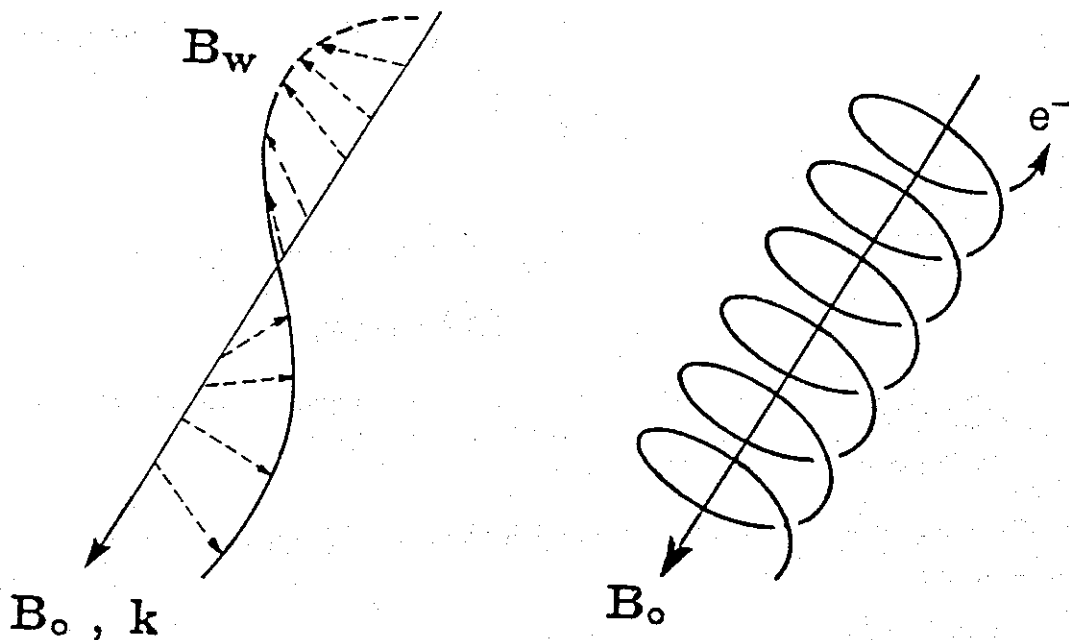


Figure 1.5. Snapshot of the right-hand circularly polarized wave field and the trajectory of a gyrating electron.

The importance of cyclotron resonance as a mechanism for whistler-mode wave growth was first suggested by *Brice* [1963] and *Dungey* [1963] and has been the basis for most theoretical treatments and simulations which followed. A good review of the early ideas is given by *Helliwell* [1965] and a review of the attempts to understand coherent effects in whistler-mode wave-particle interactions prior to 1979 is given by *Matsumoto* [1979]. *Helliwell* [1967] proposed a phenomenological theory for the

growth and triggering of coherent whistler-mode waves which utilized both nonlinear currents and the inhomogeneity. *Helliwell's* theory included a nonlinear saturation mechanism and linked the frequency evolution to the inhomogeneity of the geomagnetic field. Figure 1.2 summarizes the role of the inhomogeneity in *Helliwell's* theory indicating that coherent VLF waves propagating along the geomagnetic field will interact significantly with the energetic electrons around the geomagnetic equator if the signal is constant frequency. However, if the coherent wave frequency is increasing or decreasing with time, then the interaction region will be located downstream or upstream of the geomagnetic equator, respectively. This phenomenological model has been generalized and successfully applied [*Carlson et al.*, 1985; *Dowden*, 1971a,b; *Dysthe*, 1971; *Helliwell*, 1970; *Helliwell et al.*, 1986a,b; *Winglee*, 1985] and remains a useful tool for interpreting experimental results.

Most other studies of the gyroresonance interaction were performed within the framework of a linear or quasilinear approach (for reviews see *Gendrin* [1975], *Liemohn* [1974], or *Matsumoto* [1979]) with the most notable being the work by *Kennel and Petschek* [1966]. However, there is a general agreement that the emission triggering process involves both the nonlinearity and the inhomogeneity [*Matsumoto*, 1979]. Several theoretical works and models have specifically included the geomagnetic inhomogeneity [*Bell*, 1984, 1986; *Bell and Inan*, 1981; *Carlson et al.*, 1985; *Das and Kulkarni*, 1975; *Dowden*, 1971a,b; *Dowden et al.*, 1978; *Dysthe*, 1971; *Helliwell*, 1967, 1970, 1986a,b; *Helliwell and Inan*, 1982; *Karpman et al.*, 1974a,b, 1975; *Matthews et al.*, 1984; *Matsumoto and Omura*, 1981; *Molvig et al.*, 1986; *Murdoch*, 1983; *Neubert et al.*, 1987; *Nunn*, 1971, 1974, 1984; *Omura*, 1985; *Rathmann et al.*, 1978; *Roux and Pellat*, 1978; *Sudan and Ott*, 1971; *Vomvoridis and Denavit*, 1979; *Vomvoridis et al.*, 1982; *Winglee*, 1985].

Some of these theoretical works have assumed *a priori* that only the electrons trapped in the wave potential well contribute to the wave growth [*Das and Kulkarni*, 1975; *Dowden et al.*, 1978; *Molvig et al.*, 1986; *Nunn*, 1971, 1974, 1984; *Roux and Pellat*, 1978; *Sudan and Ott*, 1971]. However, these models all fail to provide a saturation mechanism and require an applied wave intensity above or near the maximum measured levels. The trapping assumption has not been validated by studies which have examined both trapped and untrapped electrons [*Bell and Inan*, 1981; *Matsumoto and Omura*, 1981, 1983; *Omura and Matsumoto*, 1982]. One appeal of trapped electron models is the easy identification of trapped electrons via the trapping condition. Trapped electrons also obey constants of the motion which can be

utilized to develop simple analytic expressions. Some of these models have produced emission forms claimed to be reproductions of the actual phenomena [Das and Kulkarni, 1975; Nunn, 1974; Molvig *et al.*, 1986; Roux and Pellat, 1978]. However, these forms are not consistent with recent data analyses and with the present knowledge of triggered emission morphology. For example, some models generate pretermination fallers which have not been seen in the data. A theory by Vomvoridis *et al.* [1982] looked at growth rates from trapped and untrapped electrons. Numerical implementation showed a threshold for growth which implied that the trapped electrons were responsible for the growth. However, this growth was significant only in the upstream region and also did not lead to saturation. Other simulations have shown that in this same upstream region, trapped electrons can actually damp the wave [Omura and Matsumoto, 1982].

One theory, a feedback model developed by Helliwell and Crystal [1973] predicted saturation and exponential growth but did not account for the observed phase advance. A later model [Helliwell and Inan, 1982] was also able to predict the advancing phase by including the inhomogeneity. This model is explored further in chapter 3.

Karpman *et al.* [1974a,b,c] developed a nonlinear theory in an inhomogeneous plasma which included trapped and untrapped electrons and was based upon generalized theorems of phase conservation. Their work predicts a frequency shift proportional to the product of the linear growth rate, trapping period, and a term related to the inhomogeneity. The nonlinear evolution of the wave packet is also related to these quantities. In applying their theory, Karpman *et al.* [1974b,c] predict a modulational instability with a period near the propagation delay through the magnetosphere similar to observations [Bell and Helliwell, 1971; Likhter *et al.*, 1971; Park, 1981]. Another interesting approach was taken by Murdoch [1983] in which analytic expressions were developed by assuming weakly nonlinear interactions. However, Murdoch predicted that growth rates and frequency shifts would be proportional to the square of the electric field strength, which is not supported by the observations.

Because of the assumptions that have been required in order to apply modern mathematical tools to the problems of plasma physics, a fully general theory for whistler-mode wave growth and emission triggering has not been developed. As an alternative some researchers have turned to computer simulation. Some whistler-mode simulation efforts include, in some form, the geomagnetic inhomogeneity [Matthews *et al.*, 1984; Matsumoto and Omura, 1983; Omura, 1985; Omura and Matsumoto, 1982; Rathmann *et al.*, 1978; Vomvoridis, 1978; Vomvoridis and Denavit, 1980]. Like the

analytical theories, these simulations have not been able to adequately reproduce the experimental results.

All of the simulations of wave growth performed in an inhomogeneous magnetic field employed the long time scale (LTS) simulation model developed by *Rathmann et al.* [1978]. The results from *Rathmann et al.* gave 56 dB of wave growth at ~ 3200 dB/s and -34 Hz offset for an applied wave of 0.05 pT. Wave damping at a rate of -1460 dB/s was obtained for an applied wave of 800 pT. These numbers were generated by denormalizing their results for typical Siple field line conditions. These findings, while not in agreement with the experimental results, are consistent with the growth rates and frequency shifts predicted by the dispersion relationship for their monoenergetic beam of electrons. *Vomvoridis'* [1978] work is essentially the same as that of *Rathmann et al.* [1978]. *Vomvoridis and Denavit* [1980] used the LTS method and constant static magnetic field gradients in order to determine growth rates from trapped and untrapped electrons. This work [*Vomvoridis and Denavit*, 1979, 1980] is in agreement with, and laid the ground work for, the more rigorous and realistic treatment done by *Vomvoridis et al.* [1982]. *Omura and Matsumoto* [1982] and *Omura* [1985] also used the LTS method, with a slight modification to improve stability, to investigate the roles of the trapped and the untrapped electrons. They found that trapped or untrapped electrons grew or damped the wave, respectively, on the downstream side of the equator and vice versa on the upstream side of the equator. The trapped electrons were created artificially by injecting them at their resonance points instead of by looking at electrons which would be trapped naturally. Other simulation efforts [*Matthews et al.*, 1984; *Matsumoto and Omura*, 1983] have described the evolution of the energetic electron distribution in the presence of a coherent wave but have not included wave growth.

1.4. Outline of this thesis

The main goal of this thesis is to develop a working model which can be used to simulate whistler-mode wave growth and thus lead to a better understanding of the wave growth process. The strategy focuses on calculating the currents and radiation from test particle trajectories. The models are similar to those used by *Helliwell and Inan* [1982] and *Helliwell and Crystal* [1973] except that the models used here are more realistic and comprehensive. Besides considering the nonlinear currents in an inhomogeneous geomagnetic field, a full range of energetic electron velocities are included. The results confirm that the problem is difficult and that much more

work is needed before a more robust model will be available. However, the results are encouraging and, for the first time, a transient test particle simulation has reproduced the three main experimental features listed in the last section. The outline of the organization of this thesis follows.

Chapter 2 describes the basic physics for cyclotron resonant wave-particle interactions. A model of the inner magnetosphere is developed and electron motion and wave propagation using this model are established. Electron trajectories and the nonlinear currents are examined for a range of electron velocities and wave intensities. The methods for obtaining the resonant currents and the stimulated radiation from the electron trajectories are given. Several useful tools and concepts are studied as well as some general numerical methods.

Chapter 3 examines the steady state response of the energetic electron distribution to applied waves for cases of negligible and significant growth. A model for finding self consistent steady state solutions is given. Wave growth and frequency shifts are modeled using a two-port feedback model. Again a large distribution of energetic electrons is considered as well as a range of applied wave intensities.

Chapter 4 develops a transient model which can investigate the details of wave growth as the leading edge of the wave propagates through the region. A method is developed for selecting the center parallel velocity of the electrons to be introduced into the wave, which can maximize the average growth rate. Results are given for a variety of wave intensities, electron fluxes, and distribution functions.

Chapter 5, the last chapter, includes a summary of the results as well as suggestions for future work.

Appendix A derives the method used for including bandlimited Gaussian noise in the transient simulation program.

Appendix B derives an alternative form of the equations of motion which does not require the calculation of trigonometric functions.

Appendix C includes the documentation and source code listing for the transient simulation program.

1.5. Contributions of this work

- 1) Used steady state wave field concepts to examine phased bunched currents and stimulated radiation versus v_{\parallel} and α . The results show that the inhomogeneity and the v^{-n} falloff in the number density combine to make the $\sim 45^\circ$ pitch angle, near equatorially resonant electrons, the largest contributors to the stimulated radiation. However, integrating over v_{\parallel} and α result in a large degree of cancellation. Uncancelled currents near the high v_{\parallel} edge of the integrated v_{\parallel} range contribute to large 'edge effect' currents. Control of these edge effects require a weighting function in v_{\parallel} .
- 2) Steady state concepts are also employed to develop models for determining self consistent steady state fields with significant growth, and also a two-port model for simulating temporal wave growth. Both of these models include integrations over all velocity space dimensions. However, the inability of the two-port model to describe certain transient phenomena and also the undesirable sensitivity of the two-port model to the injected electron distribution, are evidence of the need for a transient model.
- 3) Developed a transient model which can simulate the full space-time evolution of a wave pulse, including frequency and wave number shifts, as the pulse crosses the equatorial region. Application of the transient model has, for the first time, reproduced the experimentally observed exponential wave growth, total growth, linear frequency increase, and even the period of amplitude and frequency oscillations. No other simulation or modeling efforts have simultaneously predicted these experimentally observed features, particularly the linear frequency increase. The electrons included in the transient simulations are governed by a selection function. A maximum likelihood test estimates the parameters of this selection function in such a way that the average growth rate is maximized. In doing so, the test predicts, for the first time, that when an applied wave is present, the measured wave frequency at the output of the interaction region should advance with time. This test also identifies the important electrons and the important role of the geomagnetic inhomogeneity, both of which are consistent with *Helliwell's* [1967] theory.

Chapter 2. Physics of gyroresonant wave-particle interactions

To study wave-particle interactions, complete mathematical descriptions of the medium and particle motion are needed. In the following, a model of the inner magnetosphere is developed upon which group velocity, phase velocity, wave number, gyrofrequency, plasma frequency, and other parameters are based. These parameters are used to integrate the equations of motion, yielding electron trajectories, transverse currents, and stimulated whistler-mode radiation. The numerical techniques employed are also discussed.

2.1. Model of the inner magnetosphere

Within the inner magnetosphere, the geomagnetic field closely resembles a dipole field. The equation describing a dipole field line is

$$r = R_{eq} \cos^2 \lambda \quad (2.1)$$

where r is the distance of the field line from the earth's center, R_{eq} is the value of r at the geomagnetic equator, and λ is the geomagnetic latitude measured north from the geomagnetic equator. A convenient field line descriptor for the dipole approximation is the McIlwain L shell parameter defined by

$$L = \frac{R_{eq}}{R_0} \quad (2.2)$$

where R_0 is the earth's radius. The dipole field approximation holds for $L \leq 6$ and is employed here since this is the region of interest in this thesis. Figure 2.1 graphically defines the dipole relations and the direction of wave propagation and resonant particle motion.

The electron gyrofrequency f_H and static magnetic field strength B_0 along a dipole field line are given by

$$f_H(\lambda) = \frac{eB_0}{2\pi m} = 8.736 \times 10^5 \frac{\sqrt{1 + 3\sin^2 \lambda}}{L^3 \cos^6 \lambda} \quad (2.3)$$

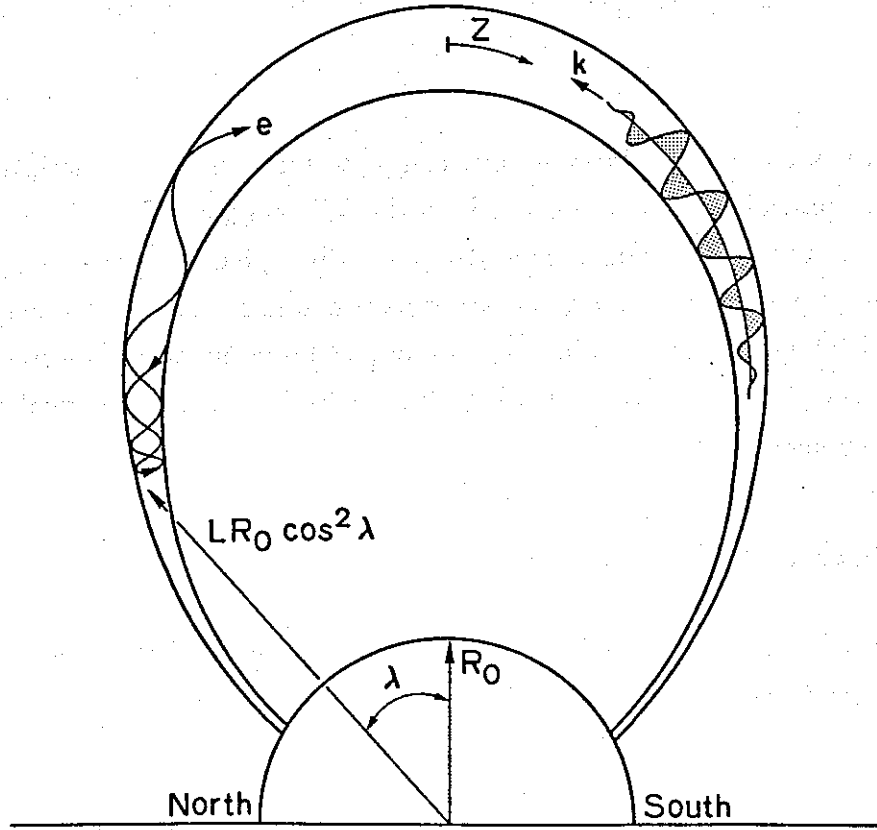


Figure 2.1. Sketch of the wave and particle geometry along an $L = 4$ field line. The relationships between the wave, resonant electrons, and the dipole field depicted in this figure are the same as those assumed throughout this thesis. The wave is propagating northward in the direction of the geomagnetic field and advancing geomagnetic latitude λ . The counter streaming resonant electrons move southward in the direction of advancing field line position z .

where e and m are the electron charge and mass respectively. The field line position z is related to geomagnetic latitude λ by

$$z = -\frac{R_{eq}}{\sqrt{12}} \left[\ln \left(\sqrt{1 + 3\sin^2 \lambda} + \sqrt{3\sin^2 \lambda} \right) + \sqrt{(1 + 3\sin^2 \lambda)(3\sin^2 \lambda)} \right] \quad (2.4)$$

where a circular approximation valid near the equator is

$$z \simeq -111 L \lambda_{deg} \text{ (km)}. \quad (2.5)$$

The minus sign in equations (2.4) and (2.5) comes from λ and z being measured in opposite directions from the geomagnetic equator. For waves originating in the north

(Figure 2.1) λ and z would be measured in the same direction, changing the sign of equations (2.4) and (2.5). Small deviations from a dipole model can be important in terms of wave-particle interactions and should be kept in mind. The earth's ring current distorts the magnetic field by a potentially significant amount [Gail, 1987] but the details are beyond the scope of this thesis.

The wave propagation relations depend on the cold plasma density. Within the plasmopause, the cold plasma density is nearly in diffusive equilibrium. Outside the plasmopause a collisionless model gives a better approximation (*e.g.* an R^{-4} model). In terms of wave-particle interactions, the spatial variation of the gyrofrequency is much more significant than the spatial variation of the cold plasma density. For this reason, the details of cold plasma models are not discussed here. The cold plasma model used throughout is the diffusive equilibrium model DE-1 [Angerami and Thomas, 1964; Park, 1972]. A very convenient way to represent the plasma density dependence in the propagation relations is through the plasma frequency given by

$$f_P(z) = \frac{1}{2\pi} \sqrt{\frac{n(z)e^2}{m\epsilon_0}}. \quad (2.6)$$

2.2. Whistler-mode wave propagation

Whistler-mode waves propagate throughout the magnetosphere in both ducted and nonducted modes. A qualitative discussion of whistler-mode wave propagation is given in the introduction. The remainder of this thesis considers only ducted, longitudinal, whistler-mode, plane wave propagation. For these waves, the magnetospheric medium is believed to vary sufficiently slowly so that the WKB approximation [Budden, 1961] can be used. The equations for wave propagation derived and used in this thesis assume the WKB approximation. Even in later sections, when the wave frequency becomes a function of space and time, the wave is assumed to propagate as a single frequency wave.

Longitudinal propagation is characterized by the wave number vector \mathbf{k} being parallel to the geomagnetic field \mathbf{B}_0 . For this case the whistler-mode refractive index is given by

$$\mu(z) = \sqrt{1 + \frac{f_P(z)^2}{f(f_H(z) - f)}} \simeq \sqrt{\frac{f_P(z)^2}{f(f_H(z) - f)}} \quad (2.7)$$

where z is the position along B_0 and f is the wave frequency. The approximation is well justified within the inner magnetosphere, and especially within the plasmasphere where typically $f_P \gg f_H$. Using (2.7), the following expressions for wave number, phase velocity, and group velocity are derived:

$$\begin{aligned} k &= \frac{2\pi f \mu}{c} \\ &= \frac{2\pi f_P}{c} \sqrt{\frac{f}{f_H - f}}, \end{aligned} \quad (2.8)$$

$$\begin{aligned} v_p &= \frac{2\pi f}{k} \\ &= c \frac{\sqrt{f(f_H - f)}}{f_P}, \end{aligned} \quad (2.9)$$

$$\begin{aligned} v_g &= 2\pi \frac{df}{dk} \\ &= 2v_p(1 - f/f_H). \end{aligned} \quad (2.10)$$

The (z) has been dropped for convenience in the above expressions and in many of the following expressions.

Because the refractive index is a function of z , the wave field components are also functions of z . However, the wave intensity also varies due to the guiding effects of the geomagnetic field. Assume that the wave energy is confined to the duct and is uniformly distributed across a cross-section of the duct. For a dipole field, the cross-sectional area of a field aligned duct is inversely proportional to the dipole field intensity. Given this model, the wave intensity associated with a wave group, in the absence of wave growth or damping, is related to the equatorial wave intensity of the same group by [Inan *et al.*, 1982]

$$B_w = B_{w\text{eq}} \sqrt{\frac{k f_H}{k_{\text{eq}} f_{H\text{eq}}}} = B_{w\text{eq}} D \quad (2.11)$$

where the 'eq' subscripts denote equatorial values. A plot of $D = B_w/B_{w\text{eq}}$ for typical parameters (see Table 2.1) is given in Figure 2.2. For other L values within the inner magnetosphere and for frequencies within the range $0.2 < f/f_{H\text{eq}} < 0.5$, plots of D are similar and deviate by only 10% at high latitudes with respect to the curve in Figure 2.2. The effect of f_P upon D is also negligible since the gradient of f_P is much

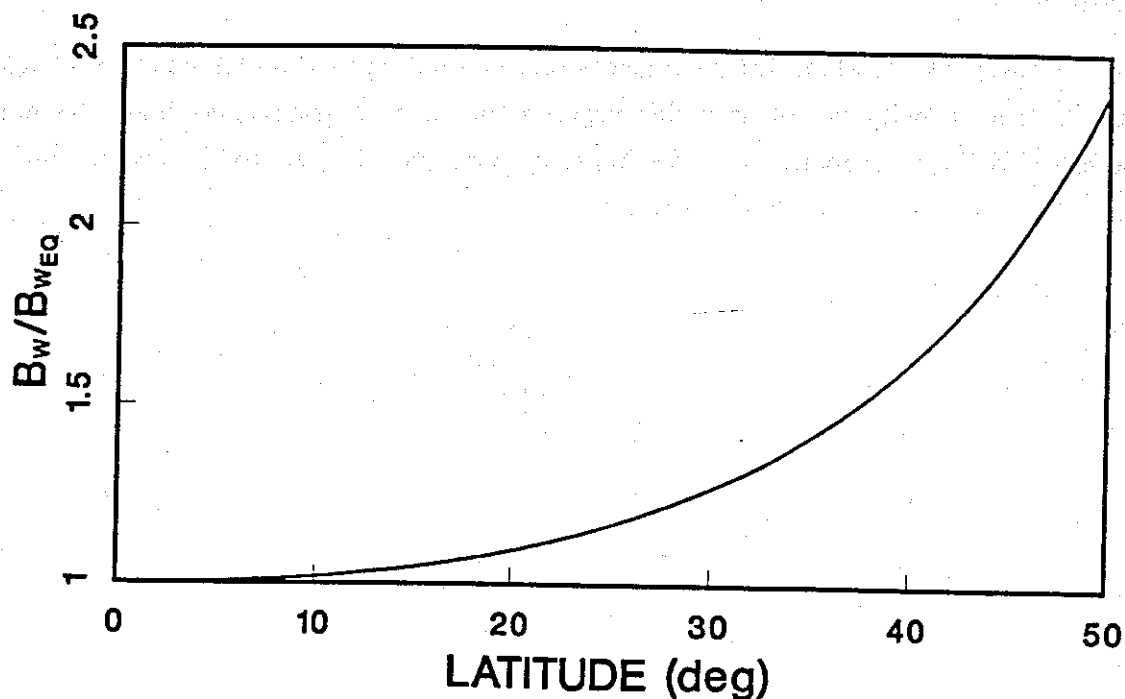


Figure 2.2. Plot of the ratio of the wave magnetic field strength to the equatorial field strength for a constant applied field. This figure is based on the assumption that the wave energy is uniformly spread over the duct flux tube so that, for the power flow within the duct to remain constant, the field strength must vary with position. The parameters used are the same as those in Table 2.1.

less than the gradient of f_H along the field line. Figure 2.2 does show that near the equator, the wave intensity is not a significant function of position.

2.3. Dynamics of trapped radiation belt particles

While the cold plasma determines the wave refractive index, the hot plasma characteristics control the energy exchange during wave-particle interactions. The magnetically trapped particles which make up the hot plasma, gyrate about the geomagnetic field while bouncing between conjugate mirror points. In addition, the curvature, radial gradient, and longitudinal gradient of the dipole field and the presence of static electric fields cause the electrons to drift. In other words, the center of gyration does not lie on a single field line. Compared to the size of the wave-particle interaction region, these drifts are believed to be insignificant and are neglected. Thus, the electron motion can be described by simple gyro motion centered on a single field line. For more details of charged particle motion see *Hess [1968]*, *Roederer [1970]*, and

Artsimovich and Lukyanov [1980].

A framework useful for describing electron motion is defined in Figure 2.3 in which the electron velocity vector \mathbf{v} is decomposed into a cylindrical coordinate system having velocity components perpendicular, \mathbf{v}_\perp , and parallel, \mathbf{v}_\parallel , to the geomagnetic field \mathbf{B}_0 , and a cyclotron phase angle θ .

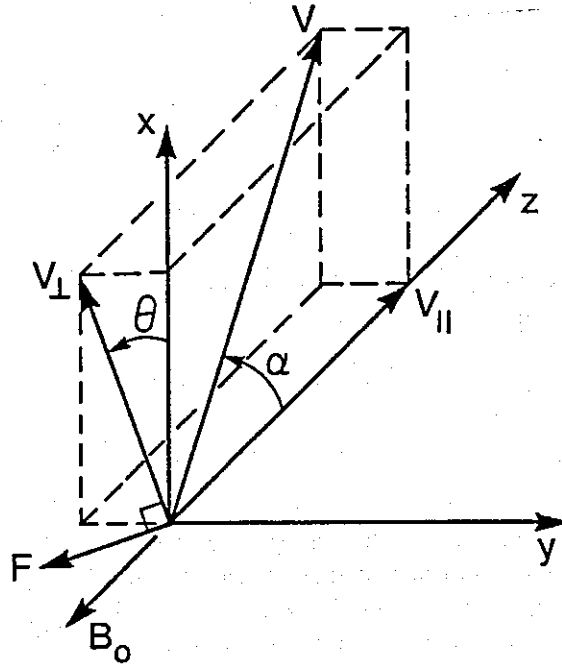


Figure 2.3. Sketch showing the relationship of the electrons' velocity to the geomagnetic field. Defined are the electrons' velocity v , pitch angle α , parallel velocity v_\parallel , perpendicular velocity v_\perp , and gyrophase θ .

The radius of circular gyration for an electron is

$$R_H = \frac{v_\perp}{2\pi f_H}. \quad (2.12)$$

The total electron velocity remains constant since the static electric field is neglected and the magnetic field can not do work on the electron. The fact that the magnetic field does no work on the electron means that the amount of flux linked by the orbit of an electron must remain constant and the following relation emerges as an 'adiabatic invariant',

$$\frac{\sin^2 \alpha}{f_H} = \text{constant}. \quad (2.13)$$

Taking the derivatives with respect to time of velocity, equation (2.13), gyrophase, and position yields the following set of differential equations of motion:

$$\frac{dv}{dt} = 0, \quad (2.14a)$$

$$\frac{d\alpha}{dt} = \frac{v_{\perp}}{2f_H} \frac{\partial f_H}{\partial z}, \quad (2.14b)$$

$$\frac{d\theta}{dt} = 2\pi f_H, \quad (2.14c)$$

$$\frac{dz}{dt} = v_{\parallel}. \quad (2.14d)$$

These equations, when integrated with respect to time, can be used to trace out the trajectory of an adiabatic electron. In order to describe wave-particle interactions, the Lorentz forces due to the wave fields must be added to these adiabatic equations of motion [Dysthe, 1971; Inan, 1977].

This thesis is concerned only with cyclotron resonant wave-particle interactions, a restriction which is incorporated into the derived equations. The whistler-mode wave propagating in the same direction as the geomagnetic field is right-hand circularly polarized while counterstreaming electrons trace out left-handed helices. Cyclotron resonance occurs when the Doppler-shifted wave frequency seen by an electron nearly matches the electrons' gyrofrequency. Thus the resonant electron sees a slowly varying or stationary wave field. Assuming longitudinal propagation the cyclotron resonance condition is

$$v_{\parallel} \simeq v_R = \frac{2\pi}{k} \left(\frac{f_H}{\gamma} - f \right) \quad (2.15)$$

where γ is the relativistic constant and, as this equation implies, significant resonance occurs for v_{\parallel} 's close to the resonance velocity v_R . For the cases considered here, $\gamma \simeq 1$ since the energies of resonant electrons are typically ≤ 50 keV. To derive an approximate expression for change in resonant frequency Δf_R in terms of a percentage change in parallel velocity $\% \Delta v_{\parallel}$ consider

$$\begin{aligned} \% \Delta v_{\parallel} &\simeq 100 \Delta f_R \left(\frac{1}{v_R} \frac{\partial v_R}{\partial f} \right) \\ &= -50 \Delta f_R \frac{f_H + 2f}{f(f_H - f)}. \end{aligned} \quad (2.16)$$

To a good approximation over the range $f_H/5 < f < f_H/2$, the resonant frequency

shift per percentage change in v_{\parallel} is

$$\frac{\Delta f_R}{\% \Delta v_{\parallel}} \simeq \frac{f_H}{400} \simeq 37 \text{ (Hz/\%)} \quad (2.17)$$

which was derived by setting $f = f_H/2$.

As long as the field seen by the electron is approximately constant, a significant interaction can occur. The interaction model developed by *Helliwell* [1967] recognized that the length of the wave-particle interaction region maximizes at the equator for constant frequency signals. To visualize this, assume adiabatic electron motion and let the cyclotron phase ϕ be the angle between the waves' magnetic field and the electrons' perpendicular velocity. When $d\phi/dt = 0$, the wave and the electron are in first order resonance (2.15). The effective length of resonance (*i.e.* the length of the region over which ϕ varies by π [*Helliwell*, 1970]) maximizes when $d^2\phi/dt^2 = 0$, a condition known as 'second order resonance'. For a given electron, the point where $d^2\phi/dt^2 = 0$ depends on the local change in wave frequency with time, $\partial f/\partial t$. In other words, second order resonance occurs if the variation of the electron parallel velocity v_{\parallel} along the electron orbit is matched by the variation of v_R . For constant frequency signals, second order resonance occurs with electrons resonant at the magnetic equator. Electrons with $v_{\parallel \text{eq}} > v_{R \text{eq}}$ experience first order resonance on either side of the magnetic equator while, for electrons with $v_{\parallel \text{eq}} < v_{R \text{eq}}$, (2.15) is not satisfied anywhere. A more general description of second order resonance is given by *Helliwell*, [1970] or *Carlson et al.*, [1985]. The fact that coherent radiation does indeed maximize for electrons resonant near the equator is demonstrated later.

Figure 2.4 defines the angular relationships, at any point in space, to be used throughout the text. All angles are positive in the direction of wave rotation. \mathbf{B}_{ref} and \mathbf{E}_{ref} represent the field components of a reference wave structure governed only by cold plasma propagation. Throughout this thesis \mathbf{B}_{ref} is the same as the externally applied field which has propagated into the interaction region. The total wave field, \mathbf{B}_w and \mathbf{E}_w , makes an angle ψ with the reference field. The angle ψ will vary with position and time because of wave-particle interactions. Each electrons' cyclotron phase ϕ is measured from $-\mathbf{B}_w$. The net cyclotron phase of a group of electrons $\Sigma \mathbf{v}_{\perp}$ and their associated current \mathbf{J} and stimulated radiation \mathbf{B}_s are measured from $-\mathbf{B}_w$, \mathbf{B}_w , and \mathbf{B}_{ref} respectively (these quantities are developed in section 2.5). The component of \mathbf{B}_s parallel or antiparallel to \mathbf{B}_w will grow or damp the wave, respectively. The component of \mathbf{B}_s perpendicular to \mathbf{B}_w will rotate or 'twist' wave

field making $\psi \neq 0$. Of course, for the spatial phase structure of the total wave field to deviate or become 'twisted' relative to the applied single frequency wave, the observed frequency at a point of 'twisting' must deviate, at some time, from the applied frequency. However, a steady state twisted field could exist where the observed frequency everywhere is the same as the applied frequency. The resonance condition (2.15) is only valid for a wave which has not been modified by wave-particle interactions. The nonrelativistic cyclotron resonance condition including this spatial twisting through the $d\psi/dt$ term is

$$\frac{d\phi}{dt} = k(v_R - v_{\parallel}) - \frac{d\psi}{dt} \simeq 0. \quad (2.18)$$

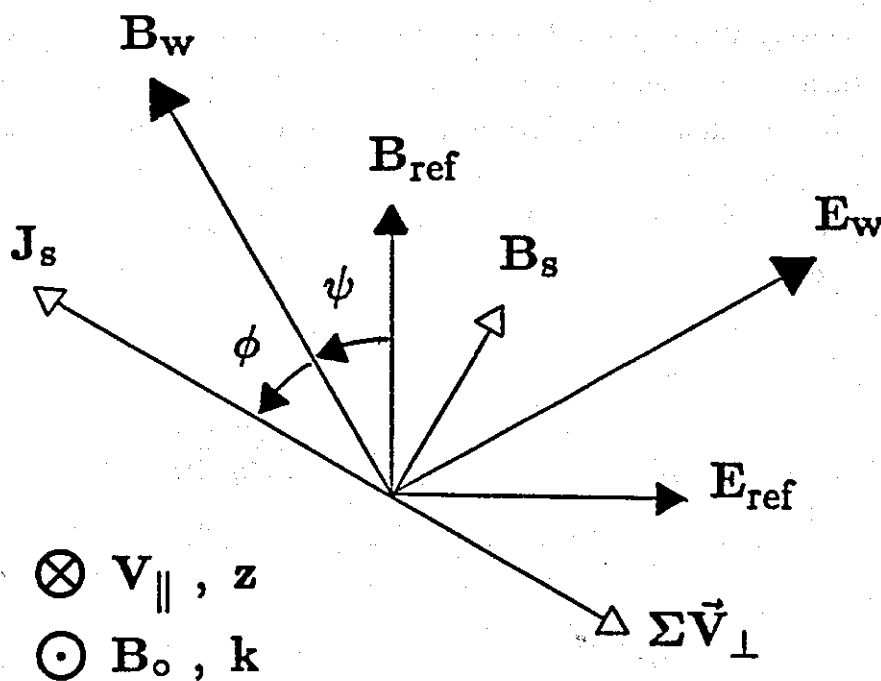


Figure 2.4. Sketch defining the angular relationships, at any point in space, between the wave, electrons, and currents. B_{ref} and E_{ref} represent a reference wave structure governed only by cold plasma propagation. B_w and E_w are the total wave field vectors. Each electrons' cyclotron phase ϕ is measured from $-B_w$. The net cyclotron phase of a group of electrons $\Sigma \mathbf{v}_{\perp}$, and their associated current \mathbf{J} , and stimulated radiation B_s , are measured from $-B_w$, B_w , and B_{ref} respectively.

The twisting, growth, or damping of the wave field is a direct of Lorentz wave forces altering the particle distribution resulting in a net particle current and hence

radiation. The Lorentz force on an electron by a wave is given by

$$\mathbf{F} = -e[\mathbf{E}_w + \mathbf{v} \times \mathbf{B}_w] . \quad (2.19)$$

Breaking this down into forces parallel and perpendicular to the geomagnetic field gives

$$\mathbf{F}_{\parallel} = -e[\mathbf{v}_{\perp} \times \mathbf{B}_w] , \quad (2.20a)$$

$$\mathbf{F}_{\perp} = -e[\mathbf{E}_w + \mathbf{v}_{\parallel} \times \mathbf{B}_w] . \quad (2.20b)$$

These forces accelerate the electrons in the parallel and perpendicular directions and also alter the electrons' gyrofrequency. Transforming the velocity equation (2.14a) and pitch angle equation (2.14b) into parallel and perpendicular velocity equations and then adding the Lorentz acceleration terms, gives two of four equations of motion. Since the magnitude of the Lorentz forces depend directly on the cyclotron phase rather than the gyrophase, it is convenient to express the third equation of motion as the rate of change of cyclotron phase instead of gyrophase. Thus, adding the centripetal acceleration terms to equation (2.18) gives the third equation of motion. Taking advantage of the fact that for a plane wave $|\mathbf{E}_w| = v_p |\mathbf{B}_w|$, the equations of motion are

$$\frac{dv_{\parallel}}{dt} = \frac{eB_w}{m} v_{\perp} \sin \phi - \frac{v_{\perp}^2}{2f_H} \frac{\partial f_H}{\partial z} , \quad (2.21a)$$

$$\frac{dv_{\perp}}{dt} = -\frac{eB_w}{m} (v_{\parallel} + v_p) \sin \phi + \frac{v_{\perp} v_{\parallel}}{2f_H} \frac{\partial f_H}{\partial z} , \quad (2.21b)$$

$$\frac{d\phi}{dt} = k(v_R - v_{\parallel}) - \frac{eB_w}{m} (v_{\parallel} + v_p) \frac{\cos \phi}{v_{\perp}} - \frac{d\psi}{dt} , \quad (2.21c)$$

$$\frac{dz}{dt} = v_{\parallel} . \quad (2.21d)$$

The $\sin \phi$ term in (2.21b) and the centripetal acceleration term in (2.21c) arise from \mathbf{F}_{\perp} not being parallel to \mathbf{v}_{\perp} . These equations are derived assuming a steady state wave structure. However, they are also valid for a time dependent wave structure so long as the wave frequency and wave number change slowly. In such a case, time and position dependent offsets $\Delta\omega$, Δk , and Δv_p arise relative to the reference or unperturbed quantities of ω , k , and v_p . The unperturbed resonance condition including these offsets is

$$\frac{d\phi}{dt} = \omega_h - \omega - kv_{\parallel} - \Delta\omega - \Delta kv_{\parallel} . \quad (2.22)$$

But this is exactly equation (2.18) since

$$\frac{d\psi}{dt} = \frac{\partial\psi}{\partial t} + \frac{\partial\psi}{\partial z} \frac{dz}{dt} = \Delta\omega - \Delta kv_{\parallel}. \quad (2.23)$$

The phase velocity offset is neglected since it only appears as a small correction to F_{\perp} in equations (2.21b) and (2.21c) or equivalently,

$$v_{\parallel} + v_p + \Delta v_p \simeq v_{\parallel} + v_p. \quad (2.24)$$

The previous discussion neglects the effect of Δv_p upon wave propagation since it is assumed that all wave energy propagates at the reference phase and group velocities. However, given two wave packets at slightly different frequencies, an observer moving at the phase velocity of one wave packet experiences a rotating wave field. To derive a general expression for this phase rotation, start with the following WKB description of the wave phase

$$\xi(\omega, z, t) = \int_0^t \omega dt - \int_0^z k dz. \quad (2.25)$$

Converting this into the frame of the phase velocity of a reference wave gives

$$\begin{aligned} \xi_{ref}(\omega, z) &= \xi(\omega, z, t) \Big|_{\frac{dz}{dt} = v_p(\omega_{ref}, z)} \\ &= \int_0^z \left(\frac{\omega}{v_p} - k \right) dz. \end{aligned} \quad (2.26)$$

Taking the derivative of equation (2.26) with respect ω gives the relative phase delay which, when multiplied by the frequency separation, approximately gives the amount of accumulated phase rotation of the second wave that the observer would record as a function of position and frequency separation,

$$\Delta f \frac{d\xi_{ref}}{d\omega} = \Delta f \int_0^z \left(\frac{1}{v_p} - \frac{1}{v_g} \right) dz \quad (\text{cycles}). \quad (2.27)$$

Figure 2.5 gives a plot of the relative phase delay $d\xi_{ref}/d\omega$, as a function of the normalized frequency and parametric in N_{eq} for waves which have propagated across the interaction region (taken to be from 250 to -250 km at $L = 4$). The relative phase delay is converted into a phase shift with units of degrees/Hertz in order to

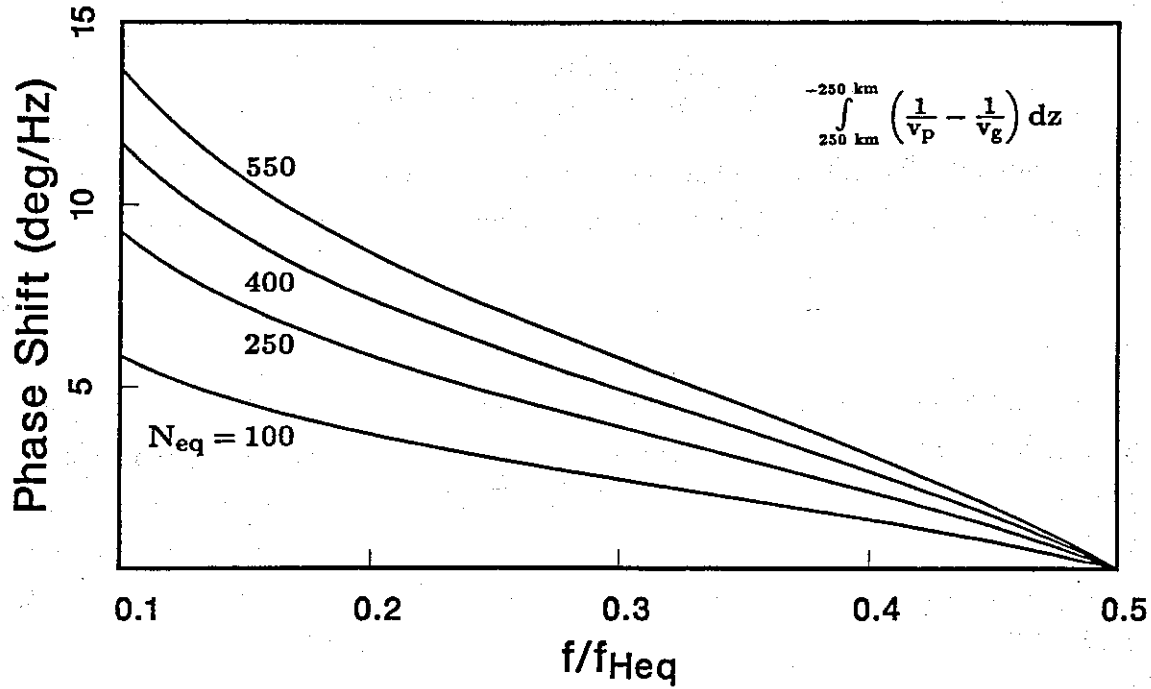


Figure 2.5. The relative phase shift for two waves, 1 Hz apart, after propagating from -250 to 250 km. This is the total shift in phase of the higher frequency wave, relative to the lower frequency wave, as measured by an observer moving at the phase velocity of the lower frequency wave. This phase shift is plotted versus normalized wave frequency and parametric in equatorial electron density N_{eq} .

make it easier to apply. For example, if $f/f_{Heq} = 0.375$, $N_{eq} = 400$ el/cm³, and the frequency separation is 10 Hz, the observed relative phase shift would be $\sim 33^\circ$. Thus, to minimize the error associated with propagating all energy at frequency independent group and phase velocities, the applied frequency should be either near the equatorial half gyrofrequency, where $v_p = v_g$, or the simulations should be limited to cases of small frequency deviation. While the calculations in this chapter and in the first section of the next chapter are carried out using $f/f_{Heq} = 0.375$, in all subsequent sections, where feedback and frequency shifts are considered, $f/f_{Heq} = 0.5$.

2.4. Energetic electron distribution function

The magnitude of currents and stimulated fields calculated from electron trajectories depend upon the number of energetic electrons involved in the interaction and on the distribution of these electrons in velocity and configuration space. Although there are several ways to represent this information [Roederer, 1970], the velocity

space distribution function $f(v, \alpha)$ is well suited for wave-particle interaction studies.

The velocity space distribution function $f(v, \alpha)$ has dimensions of $\#/(m^6 \cdot s^3 \cdot \text{ster})$ so that the number density of electrons is determined by integrating over velocity space. The velocity space volume element, given in terms of velocity, pitch angle, and gyrophase, is $v^2 \sin \alpha dv d\alpha d\theta$. Since the distribution function is assumed to be uniform in gyrophase, integration over θ yields 2π . Thus, the number density of electrons at any point in space is

$$N(z) = 2\pi \int_{\alpha} \int_v f(v, \alpha) v^2 \sin \alpha dv d\alpha \quad (\#/m^3). \quad (2.28)$$

Choosing the limits of integration in (2.28) gives the number density within the selected region of velocity space.

It is convenient to work only with the equatorial distribution function $f(v, \alpha_{eq})$ rather than having to know $f(v, \alpha)$ at every point along the field line. An adiabatic transformation of (2.28) only involves $\sin \alpha d\alpha$ and gives

$$N(z) = \frac{\pi f_H}{\sqrt{f_{Heq}}} \int_{\alpha_{eq}} \int_v f(v, \alpha_{eq}) \frac{v^2 \sin(2\alpha_{eq})}{\sqrt{f_{Heq} - f_H \sin^2 \alpha_{eq}}} dv d\alpha_{eq}. \quad (2.29)$$

The model for $f(v, \alpha_{eq})$ used in this thesis is [Inan, 1977]

$$f(v, \alpha_{eq}) = A v^{-n} g(\alpha_{eq}) \quad (2.30)$$

where A and n are constants and $g(\alpha_{eq})$ represents the pitch angle dependence. When $g(\alpha_{eq}) = 1$ the distribution function depends only upon velocity and is said to be isotropic in pitch angle. Anisotropic and nearly isotropic pitch angle distributions have been observed in the magnetosphere [Lyons and Williams, 1975]. An example of an anisotropic pitch angle distribution is given in Figure 2.6 which corresponds to one measured by Anderson [1976]. Figure 2.6 was generated using

$$g(\alpha) = a \sin^x \alpha + (1 - a) \sin^y \alpha \quad (2.31)$$

with $a = 0.2$, $x = 0.2$, and $y = 12$ [Inan, 1977].

The lack of electrons below 6° in Figure 2.6 corresponds to those electrons whose mirror points are within the atmosphere and thus suffer collisions. As a result, these

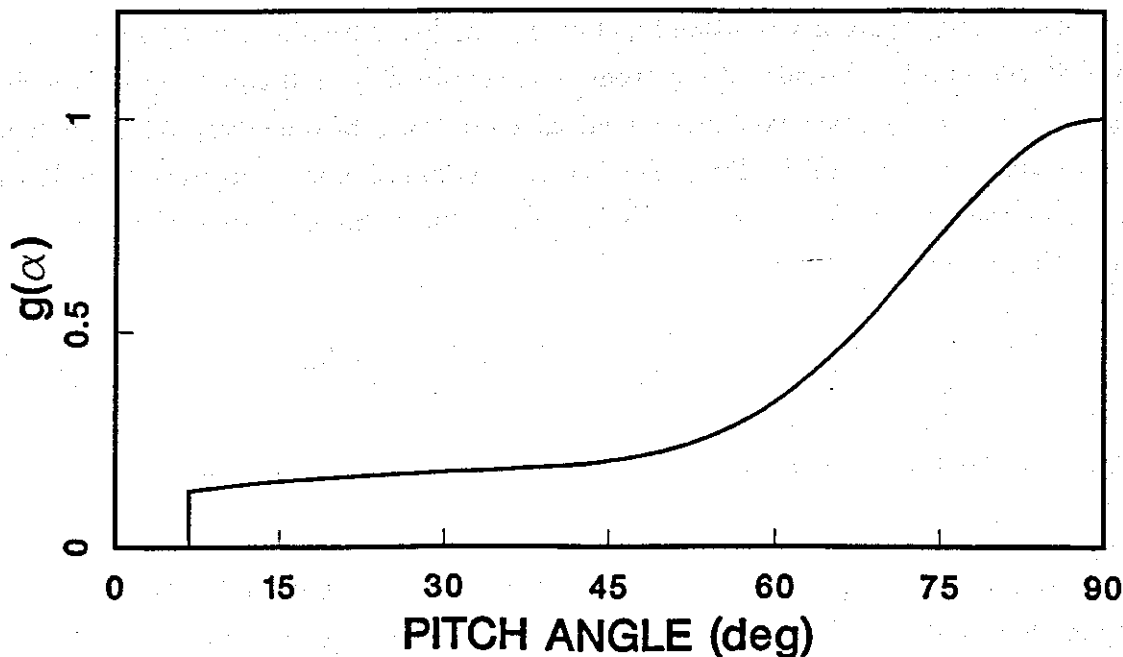


Figure 2.6. Example of an equatorial pitch angle dependence $g(\alpha)$, which results in a highly anisotropic distribution function of the form $f(v, \alpha) = v^{-n}g(\alpha)$. Except at low pitch angles, where the lack of electrons corresponds to the loss cone, $g(\alpha) = 0.2\sin^{0.2}\alpha + 0.8\sin^{1.2}\alpha$.

electrons lose their energy to the atmosphere and do not mirror back into the magnetosphere. An altitude of 100 km is generally taken as the altitude above which electrons mirror and below which electrons do not mirror. The equatorial pitch angle corresponding to a mirror point of 100 km altitude defines the equatorial 'loss cone' pitch angle α_{lc} . The existence of a loss cone makes the distribution function anisotropic even if $g(\alpha) = 1$ everywhere above the loss cone.

Measurements show that the distribution tends to roll off with energy. OGO 3 satellite measurements of the differential energy spectrum (discussed below) at $L \simeq 5.5$ [Schield and Frank, 1970] fit a $v^{-3\pm 0.5}$ ($E^{-1.5}$) power law for electrons with energies thought to significantly contribute to cyclotron wave growth. This $v^{-3\pm 0.5}$ differential energy spectrum converts to a $v^{-5\pm 0.5}$ distribution function [e.g., Chang, 1983] or $n \simeq 5$. This value of n is consistent with a value of n produced by a model of the lower cutoff of ground based magnetospheric whistler-mode signals [Carlson et al., 1985]. The same lower cutoff model also produced, at a different time, $n \simeq 12$ suggesting that n can have a wide range of values and can be time varying.

Observed distributions are conventionally described using the differential energy spectrum which has units $\#/\text{m}^2 \cdot \text{s} \cdot \text{ster} \cdot \text{keV}$. The constant A is related to the differential energy spectrum Φ_{E_0} of electrons at a given energy E_0 (keV) and with $\alpha = 90^\circ$ by

$$A = \Phi_{E_0} \left(\frac{m^2}{mc^2} \right) \left(\frac{\gamma_0^5}{\gamma_0^2 - 1} \right) E_0^{n/2} \quad (2.32)$$

where mc^2 is the rest energy of the electron and $\gamma_0 = (1 - v^2/c^2)^{-1/2}$ is the relativistic constant associated with E_0 [Chang, 1983; Chang and Inan, 1983].

2.5. Test particle trajectories and phased bunched currents

In order to compute electron trajectories, the equations of motion must be integrated. The numerical methods and algorithms for integrating the equations of motion and determining currents and fields are developed in the next section. Following are some examples of the calculation of electron trajectories for cyclotron resonant electrons using the medium and wave parameters given in Table 2.1. This first example includes 12 electrons, initially distributed uniformly in cyclotron phase, entering the wave field 2000 km upstream of the equator, and with unperturbed equatorial values for pitch angles and parallel velocities of 45° and v_R respectively. The plots in Figure 2.7 show the evolution of v_{\parallel} , v_{\perp} , α , v , and ϕ for each electron in the presence of a 1 pT monochromatic wave. In Figure 2.7, and in many of the figures to follow, the velocities are converted to percentages of $v_{R\text{eq}}$. Each plot in Figure 2.7 includes the adiabatic curves for the electron whose v_{\perp} is antiparallel to \mathbf{B}_w at the equator. The adiabatic trajectory is calculated using the same equations and algorithms, with B_w set equal to zero. Also included in Figure 2.7a is the plot of the resonance velocity v_R . These curves provide a simple way of seeing how the electrons are affected by the wave.

The plots in Figure 2.7 show that, for these electrons, the most significant interactions occur in a region centered near the equator. The velocity plot (Figure 2.7d) shows that, on the average, the electrons generally lost energy in the interaction. Correspondingly, there are changes in pitch angle and gyrophase. During and after the interaction, the gyrophase distribution (Figure 2.7e) becomes nonuniform. This process has been called phase bunching and represents a transverse right-hand polarized current [Helliwell and Crystal, 1973]. The changes in velocity, and hence energy, are due exclusively to the wave electric field while the changes in α and ϕ are due

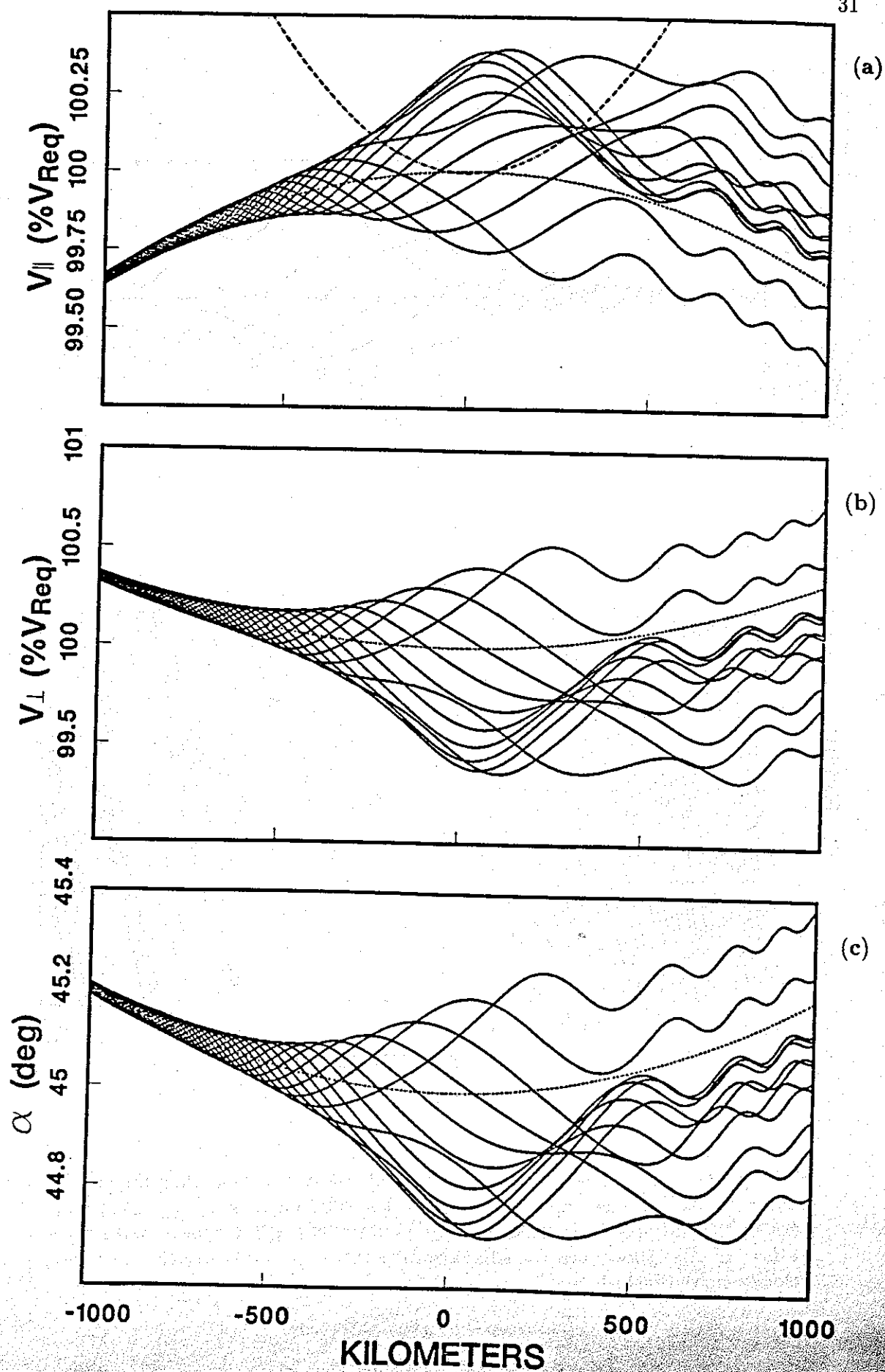
Table 2.1. Parameters for the reference model

Inputs:

L	4	
R_0	6371.2	km
R_1	7371.2	km
N_{eq}	400	el/cm ³
Φ_{E_0}	10^{12}	#/m ² ·s·ster·keV
E_0	1	keV
T_e	1600	°K
H^+, He^+, O^+	90, 8, 2	%
f	3/8	f_H
B_{ineq}	1	pT
$v_{\parallel \text{eq}}$	$v_{R\text{eq}}$	m/s
α_{eq}	45	degrees
$\Delta v_{\parallel \text{eq}}$	$.0001 v_{R\text{eq}}$	m/s
$\Delta \alpha_{\text{eq}}$	10	degrees
N_ϕ	12	electrons
N_M, N_μ	800, 4	steps
$z_{\text{up}}, -z_{\text{down}}$	-2000	km
z_{fe}	400	km

Outputs:

λ_0, λ_1	60, 57.5	degrees
α_{lc}	6.7	degrees
$B_{0\text{eq}}$	488	nT
$f_{H\text{eq}}$	13.7	kHz
$f_{P\text{eq}}$	180	kHz
$\Delta \lambda$.01	degrees
k_{eq}	2.92	rad/km
$2\pi/k_{\text{eq}}$	2160	m
$v_{p\text{eq}}$	11000	km/s
$v_{g\text{eq}}$	13800	km/s
$v_{R\text{eq}}$	18400	km/s
$E_{R\text{eq}}$.964	keV
λ_m	23.1	degrees



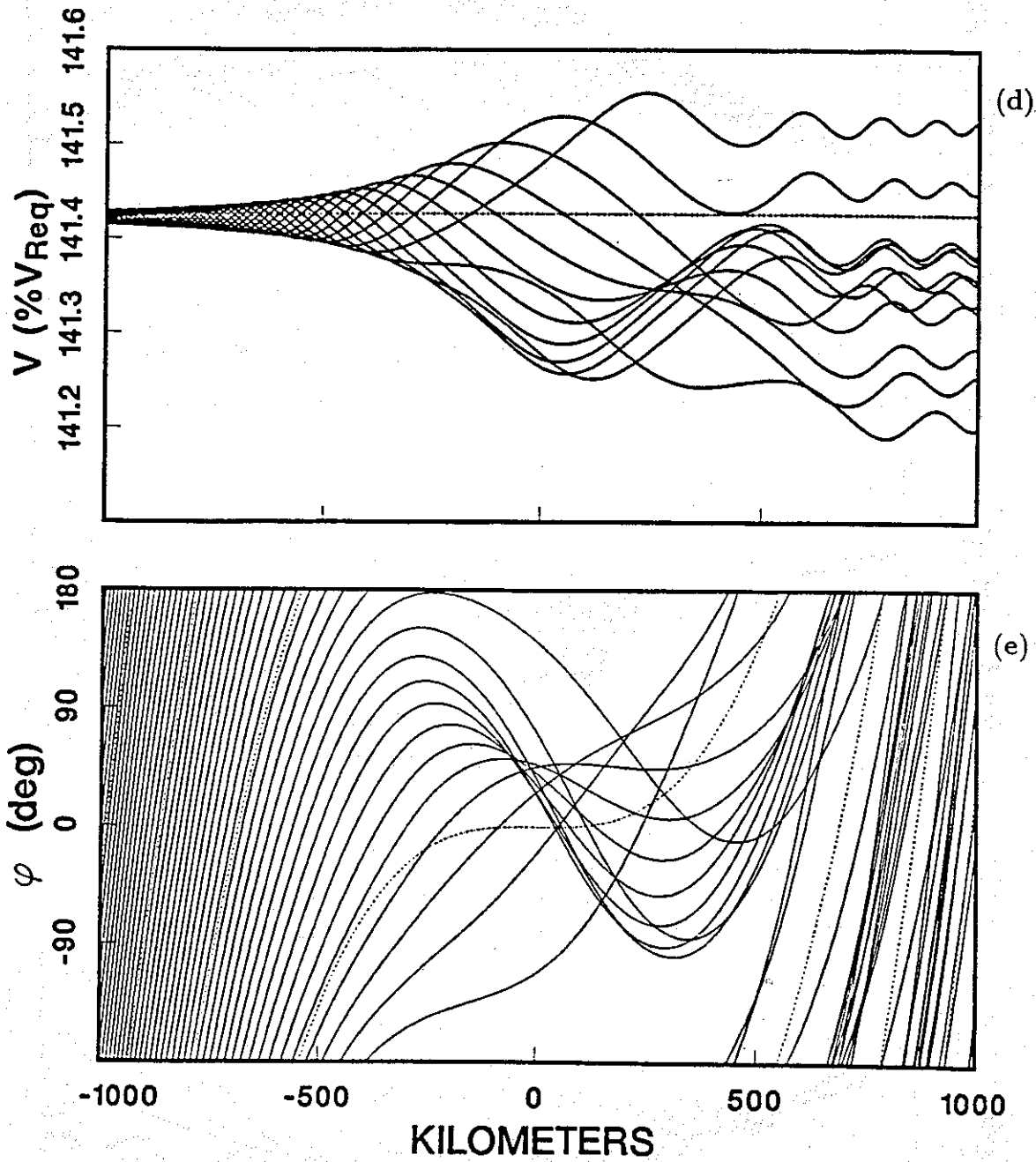


Figure 2.7. Plots showing the trajectories of twelve electrons using the parameters in Table 2.1. These plots (solid) show the evolution of v_{\parallel} , v_{\perp} , α , v , and ϕ for each equatorially resonant electron in the presence of a $1pT$ monochromatic wave at $L = 4$. Also shown are the adiabatic trajectories (dotted) and the resonance velocity curve (dashed curve in v_{\parallel} plot).

to both \mathbf{B}_w and \mathbf{E}_w [Inan, 1977]. For this reason, \mathbf{B}_w and \mathbf{E}_w work together to set up conditions for wave growth and damping. The $\mathbf{v} \times \mathbf{B}$ force tries to pull all of the electrons into a position such that the \mathbf{v}_\perp 's are antiparallel to \mathbf{B}_w . Since \mathbf{B}_w can not do any work on the electrons, this is accomplished by exchanging parallel and perpendicular electron kinetic energies. This amounts to translating the electron helices in space with respect to their adiabatic helices so that their cyclotron phases tend to become bunched rather than uniformly distributed. \mathbf{E}_w can do work on the electrons and, with the electrons nonuniformly distributed in cyclotron phase due to \mathbf{B}_w , the net exchange of energy between the wave and the electrons can be significant. At lower pitch angles, the $\mathbf{v}_\perp \times \mathbf{B}_w$ force is reduced. Thus, as is shown in the next chapter, the bunching effect of \mathbf{B}_w on small pitch angles becomes negligible and the stimulated currents, although small, are mainly due to \mathbf{E}_w acceleration.

With the electron trajectories in mind, quantitative descriptions of phase bunched currents and stimulated radiation can be developed. This is most easily done when the system is in steady state. By steady state it is meant that an observer at any point in space would see a constant wave amplitude and frequency for all time.

Any set of electrons that encounter the wave at the same time, will cross some downstream point at different times. This means that electrons must be continually introduced into the wave to determine the electron distribution at some point in space and time. However, for a steady state system, all electrons with identical initial conditions follow identical trajectories. In this case, the curves in Figure 2.7 are equivalent to a snapshot of 12 continuous streams of electrons [Helliwell and Crystal, 1973; Helliwell and Inan, 1982]. Making a steady state approximation therefore permits a rather simple and straightforward method of deriving stimulated current and radiation directly from the curves in Figure 2.7.

For an unperturbed energetic electron distribution $f(v, \alpha)$, the 12 test electrons represent $2\pi f(v, \alpha) v^2 \sin \alpha dv d\alpha$ electrons per unit volume. The current associated with the phase bunched electrons can be represented by a sheet current calculated by summing over all perpendicular velocities within a slab of thickness Δz . The current per unit slab thickness is thus given by [Helliwell and Inan, 1982]

$$\mathbf{J}(z) = -e \int_{\phi} \int_{\alpha} \int_v \mathbf{v}_\perp(z) f(v, \alpha) v^2 \sin \alpha dv d\alpha d\phi \quad (\text{A/m}^2). \quad (2.33)$$

Each current sheet launches a wave in both directions. All such current sheets act like an end-fire antenna array in that there is only substantial addition of coherent

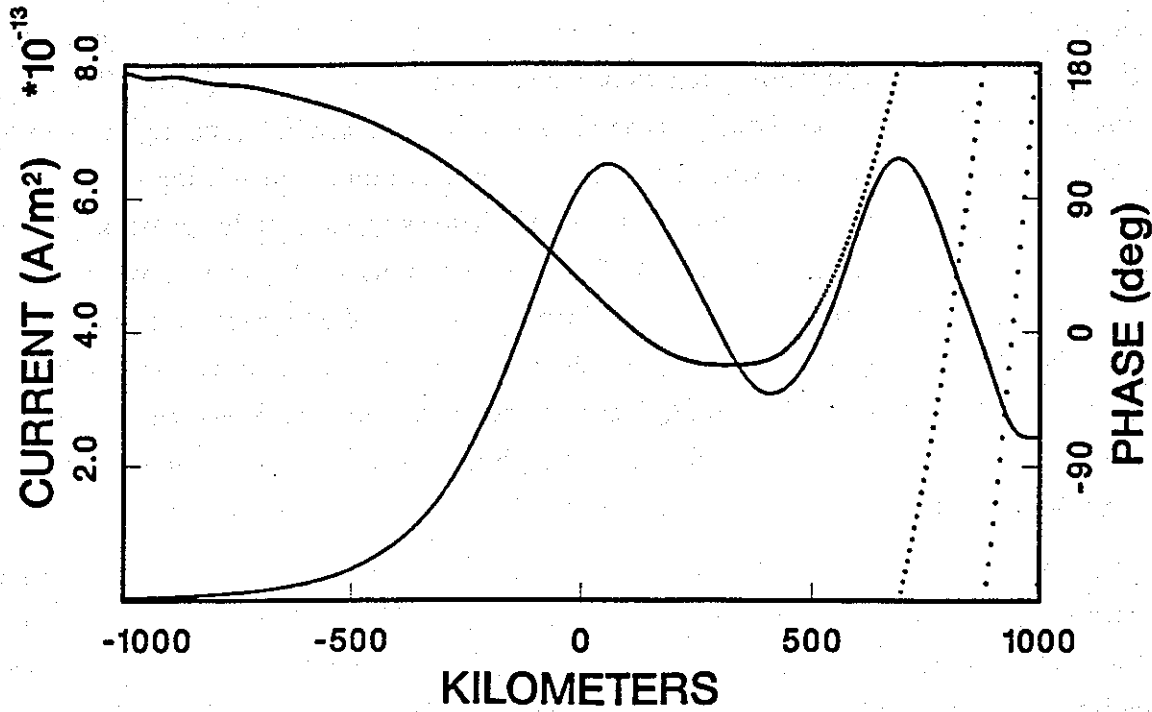


Figure 2.8. Magnitude (solid) and phase (dotted) of the current associated with the electron trajectories in Figure 2.7.

radiation in the wave direction (opposite to v_{\parallel}) [Brice, 1963; Helliwell and Crystal, 1973]. At any point in space, the stimulated radiation associated with the current sheet can be determined from Maxwell's equations. The total radiation at a given point in space would be the sum of the applied wave, the stimulated radiation associated with the local current sheet, and the radiation that has propagated to this point in space from other current sheets. The field radiated from a current sheet of unit thickness is

$$\Delta B_s(z) = \frac{\mu_0}{2} [\mathbf{J}(z) \times \mathbf{n}] \quad (2.34)$$

where \mathbf{n} is the unit vector in the \mathbf{k} direction. When steady state is assumed, the stimulated radiation from each current sheet remains constant so that the total radiation at a point z is

$$\mathbf{B}_w(z) = D(z) \left\{ \int_{+\infty}^z \frac{\Delta B_s(z)}{D(z)} dz + \mathbf{B}_{ineq} \right\} \quad (2.35)$$

where \mathbf{B}_{in} is a constant applied input field (e.g. a key-down ground based VLF transmitter).

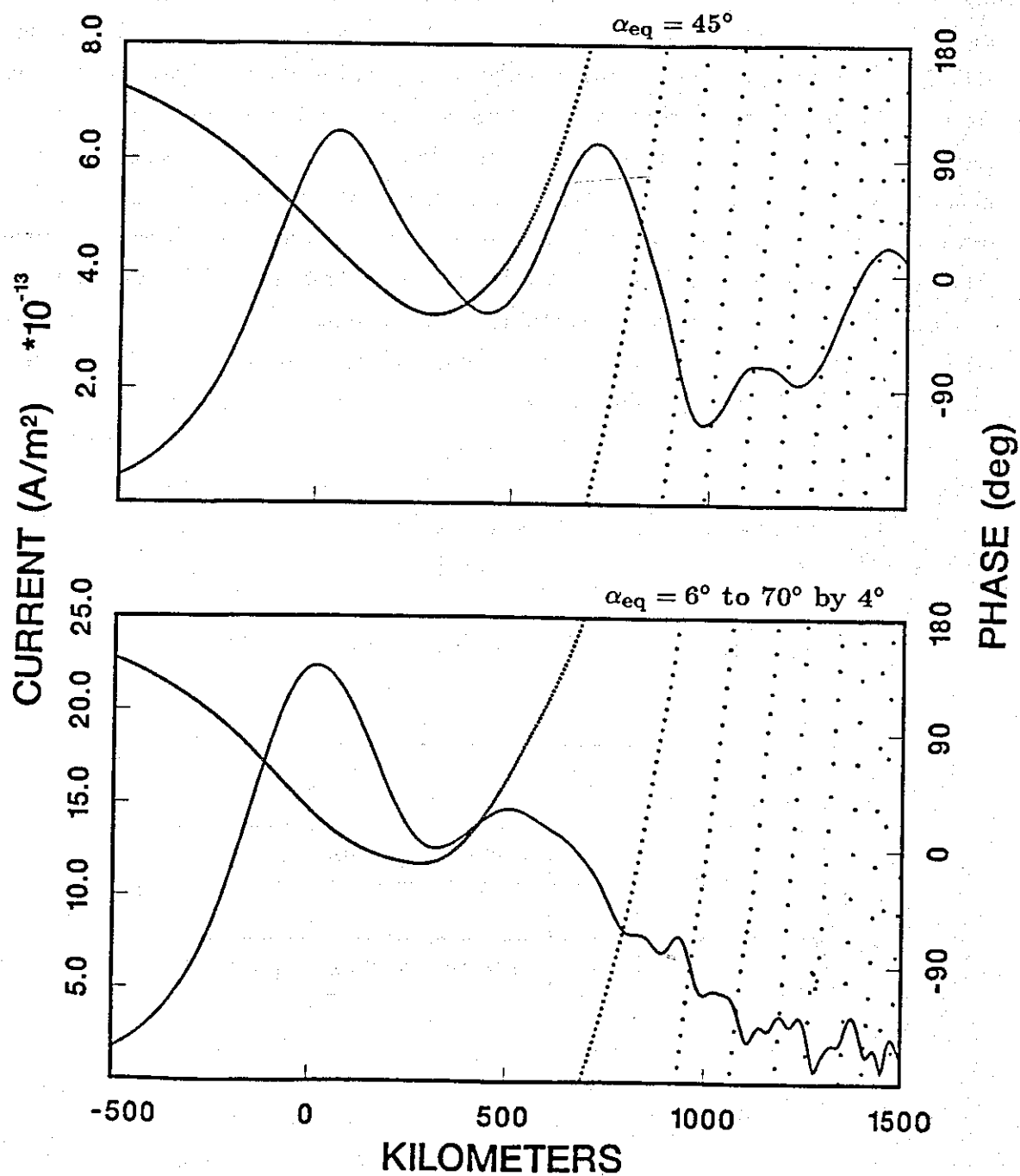


Figure 2.9. Plots showing the effects of phase mixing. The top panel shows the current from the same electrons in Figure 2.8. In the bottom panel however, 17 sets of 12 electrons were injected into the wave covering the range of pitch angles from 6° to 70° in 4° steps. Because kv_{\parallel} is different for each pitch angle, integration over pitch angle tends to cancel the current in the downstream region.

The calculated current corresponding to the electrons of Figure 2.7 is shown in Figure 2.8 with the current magnitude and phase being given by the solid and dotted lines respectively. The current magnitude at $z = -1000$ km is quite small even though the electrons, injected into the wave at $z = -2000$ km, have been in the wave field for 1000 km. The current begins to grow rapidly at $z \simeq -400$ km which, from Figure 2.7e, corresponds to the unperturbed cyclotron phase curve coming within $\sim 90^\circ$ of exact resonance. The magnitude of the current first peaks when the electrons have become phased bunched about $-\mathbf{B}_w$ (see Figure 2.7). A second current peak occurs further down the field line as a result of the electrons having different velocities and hence different $d\phi/dt$'s after their interaction with the wave. This rebunching will continue on down the field line for these electrons. The stimulated radiation components associated with this rebunched current will not add coherently because the current phase is rotating so rapidly. Furthermore, when integrating over more than just a single pitch angle or parallel velocity, the downstream currents associated with each component of the energetic electron distribution tend to cancel each other. This effect is called phase mixing and is demonstrated in the lower panel of Figure 2.9 in which a 6° to 70° pitch angle range has been included.

Table 2.2. Cyclotron phase of maximum perturbed values.

Phase	$\frac{dv_{\parallel}}{dt}$	$\frac{dv_{\perp}}{dt}$	$\left \frac{d\phi}{dt}\right $	v_{\parallel}	v_{\perp}	J
180°				$v_{\parallel} < v_R$	$v_{\parallel} > v_R$	\times
90°	\times					
0°			\times	$v_{\parallel} > v_R$	$v_{\parallel} < v_R$	$v_{\parallel} < v_R, \alpha$ small
-90°		\times				

The current phase in Figure 2.8 has distinctly different behavior in the upstream, equatorial, and downstream regions. Upstream of the interaction region the current phase is just below 180° or nearly antiparallel to \mathbf{B}_w . This is in the direction opposite to the current phase which results from phase bunching of electrons about $-\mathbf{B}_w$. However, these upstream off-resonant electrons are only slightly perturbed by the

wave which causes the electrons to execute nearly sinusoidal oscillations about their adiabatic trajectories. The phasing of these oscillations is easily revealed by inspection of the equations of motion (2.21) and is illustrated in Table 2.2. Indicated in Table 2.2 are the cyclotron phase angles at which the various parameters are a maximum. The minimum values are not indicated in Table 2.2 since they would occur 180° out of phase with the maximum values. The phase angles of maximum dv_{\parallel}/dt and dv_{\perp}/dt follow directly from the $\sin \phi$ and $-\sin \phi$ terms in equations (2.21a) and (2.21b) respectively. The cyclotron phase angle at which v_{\parallel} or v_{\perp} maximizes, depends on the sense of cyclotron phase rotation. If $v_{\parallel} < v_R$ then the cyclotron phase advances with time and vice versa for $v_{\parallel} > v_R$. The dependence of maximum values upon the relationship of v_{\parallel} to v_R is so indicated in Table 2.2. The maximum rate of cyclotron phase rotation $|d\phi/dt|$ occurs at $\phi = 0^\circ$ and is determined by $(v_R - v_{\parallel})$ in equation (2.21c). From this perturbation analysis, the electrons should be slightly concentrated about the cyclotron phase corresponding to a minimum in $|d\phi/dt|$ which is at $\phi = 180^\circ$. Thus, the current phase should be 180° from \mathbf{B}_w which is the upstream current phase in Figure 2.8. This analysis is based on the assumption that the perturbations in v_{\parallel} and hence $|d\phi/dt|$ are relatively more significant than the perturbations in v_{\perp} . However, at low pitch angles, the perturbations on v_{\parallel} can become small since v_{\perp} is small. In this case, the cyclotron phase distribution remains fairly uniform and the current phase corresponds to the cyclotron phase of maximum v_{\perp} . The cyclotron phase of maximum v_{\perp} depends on the sense of cyclotron phase rotation, resulting in an off-resonant current phase at 180° or 0° for $v_{\parallel} > v_R$ or $v_{\parallel} < v_R$ respectively. The static field inhomogeneity terms in equations (2.21a) and (2.21b) and the wave field term in equation (2.21c) are neglected in this analysis, possibly accounting for the current phase angles not being exactly 0° or 180° .

In the equatorial region, the length of time that the wave forces act on the particles per cyclotron period has increased enough to significantly deviate the electrons from their adiabatic trajectories. These wave forces tend to bunch the electron cyclotron phases about $-\mathbf{B}_w$. Thus, the current phase shifts from $\sim 180^\circ$ toward 0° . The current phase actually goes below 0° because of electron momentum. The large, nonresonant current in the downstream region is dominated by the inhomogeneity causing the current phase to rotate at about the adiabatic cyclotron phase rotation rate.

The trajectories plotted in Figure 2.7 represent only a small class of cyclotron resonant electrons. Electron trajectories, currents, and stimulated fields depend upon

many parameters including v , B_w , L , N_{eq} , and f . The following trajectory calculations demonstrate the role of electron velocity and applied field intensity. Trajectories are calculated for two cases. In both cases, the parameters of Table 2.1 are used except that the electron parallel velocity is increased by 2%. In the second case the applied wave intensity is increased by a factor of 10.

Figure 2.10 shows plots of $v_{||}$, v , and ϕ versus position for the first case. The intersections of the adiabatic $v_{||}$ curve and the v_R curve in Figure 2.10a show that, by increasing $v_{||}$ by 2%, there are now first order resonant interactions at -1000 km and 1000 km. Figure 2.10b shows that there is significant energy exchange between the wave and individual electrons within each interaction region. However, as opposed to the equatorial resonance case where the net energy exchange was mostly from the electrons to the wave, the net energy exchange in Figure 2.10b appears to be only weakly from the wave to the electrons. Figure 2.10c shows the cyclotron phase behavior in which the phase bunching following the first resonance is clearly pronounced while there does not appear to be strong phase bunching following the second resonance. This lack of phase bunching is due to the electrons encountering their second resonance at various points in space and with a nonuniform cyclotron phase distribution, all a result of their earlier upstream resonance. This effect is also evident in Figure 2.11 which shows an asymmetry in the current profiles associated with each resonance. Including a full range of pitch angles and a range of parallel velocities tends to improve the symmetry in the current peaks and can reduce the current between resonances through phase mixing. As a result, the phase bunching and current resulting from the second resonance behaves more like that of a uniform 'fresh' distribution of electrons injected at the equator.

Increasing the wave intensity causes some electrons to oscillate about the resonance velocity curve as shown in Figure 2.12a. This is called phase trapping and occurs when the $\mathbf{v}_{\perp} \times \mathbf{B}_w$ is so strong that the electrons oscillate about $-\mathbf{B}_w$, as shown in Figure 2.12c. The manner in which energy is exchanged between the trapped electrons and the wave is, from Figure 2.12b, quite opposite to that of the untrapped electrons. The trapped electrons, on the average, take energy from the wave along the upstream side of the equator and give the energy back on the downstream side. Untrapped electrons, on the other hand, give energy to the wave within their first resonance and, in general, take energy from the wave within their second resonance. This effect was investigated in wave growth simulations [Omura and Matsumoto, 1982] where it was found that trapped electrons damped the wave on the upstream side

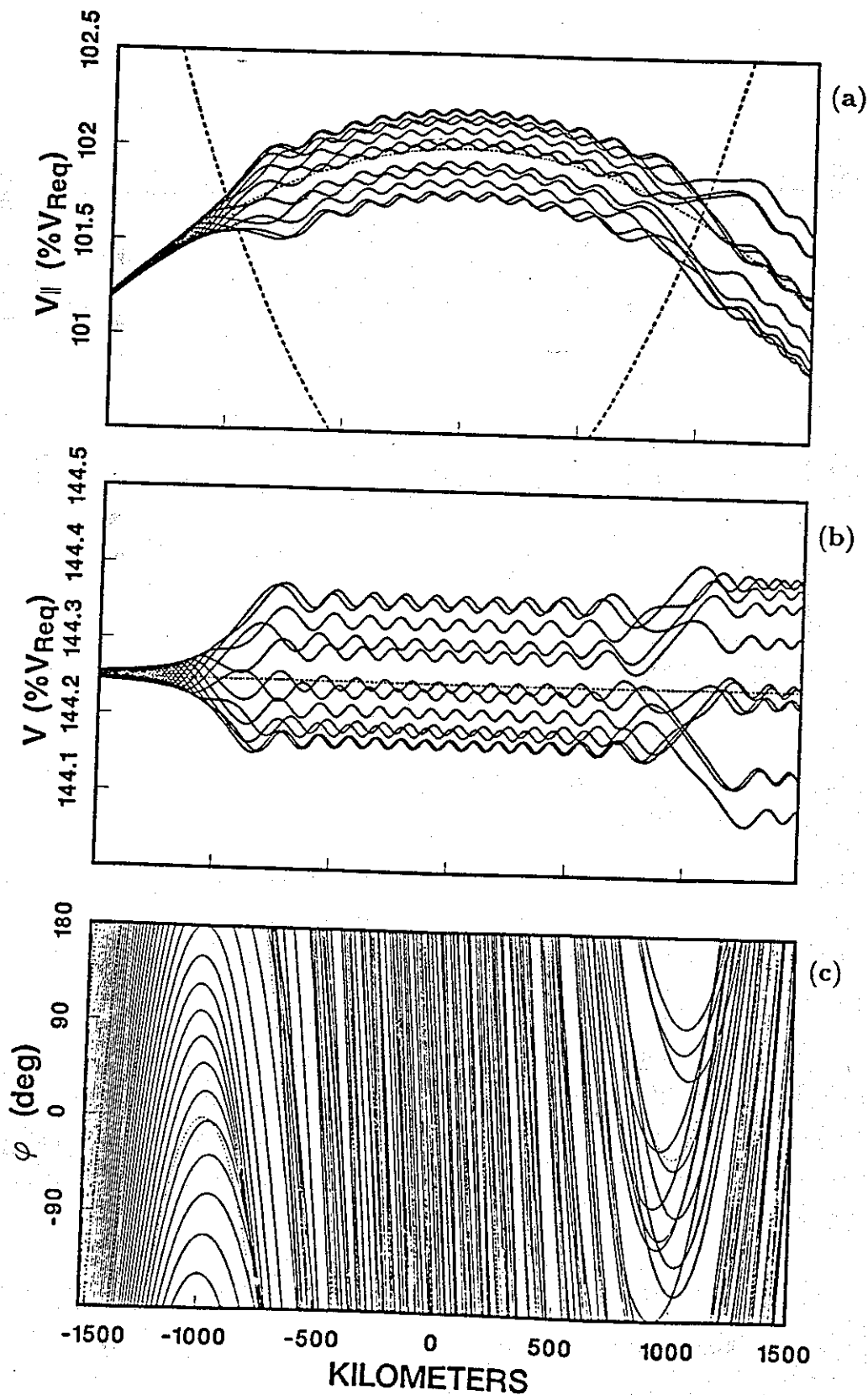


Figure 2.10. Plots (solid) of $v_{||}$, v , and ϕ versus position for electrons interacting with a 1 pT wave at $L = 4$. Also shown are the adiabatic trajectories (dotted) and the resonance velocity curve (dashed). The adiabatic equatorial $v_{||}$ is 2% above v_{Req} resulting in two resonances at about ± 1000 km.

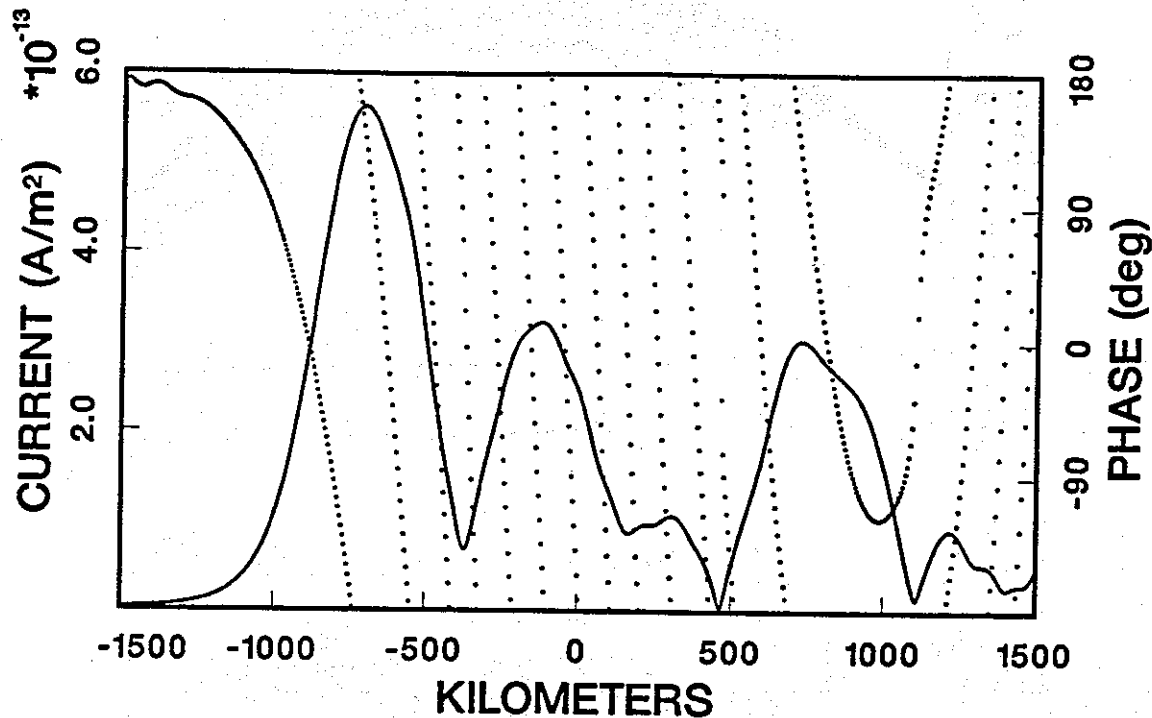


Figure 2.11. Magnitude (solid) and phase (dotted) of the current associated with the electron trajectories in Figure 2.10.

and amplified the wave on the downstream side. The opposite was found to be true for untrapped electrons. This effect is examined further in the next chapter where growth and damping is shown to depend upon various parameters including B_w , v , and α .

The physics of trapping has been extensively studied (see *Matsumoto*, [1979] for a review). Trapped electron behavior can be related to a simple pendulum by making B_w the analogue of gravity and the electron, in the wave frame, the analogue of a pendulum. Taking the second derivative of (2.21c) and neglecting B_w dependent terms gives

$$\frac{d^2\phi}{dt^2} = k \left(\frac{dv_R}{dt} - \frac{dv_{\parallel}}{dt} \right) + \frac{dk}{dt} (v_R - v_{\parallel}) - \frac{d^2\psi}{dt^2} \quad (2.36)$$

which, when taking $v_{\parallel} \simeq v_R$, reduces to

$$\frac{d^2\phi}{dt^2} = k \left(\frac{dv_R}{dt} - \frac{dv_{\parallel}}{dt} \right) - \frac{d^2\psi}{dt^2} \quad (2.37)$$

Substituting in (2.21a), calculating dv_R/dt for $df/dt = 0$, and making the approxi-

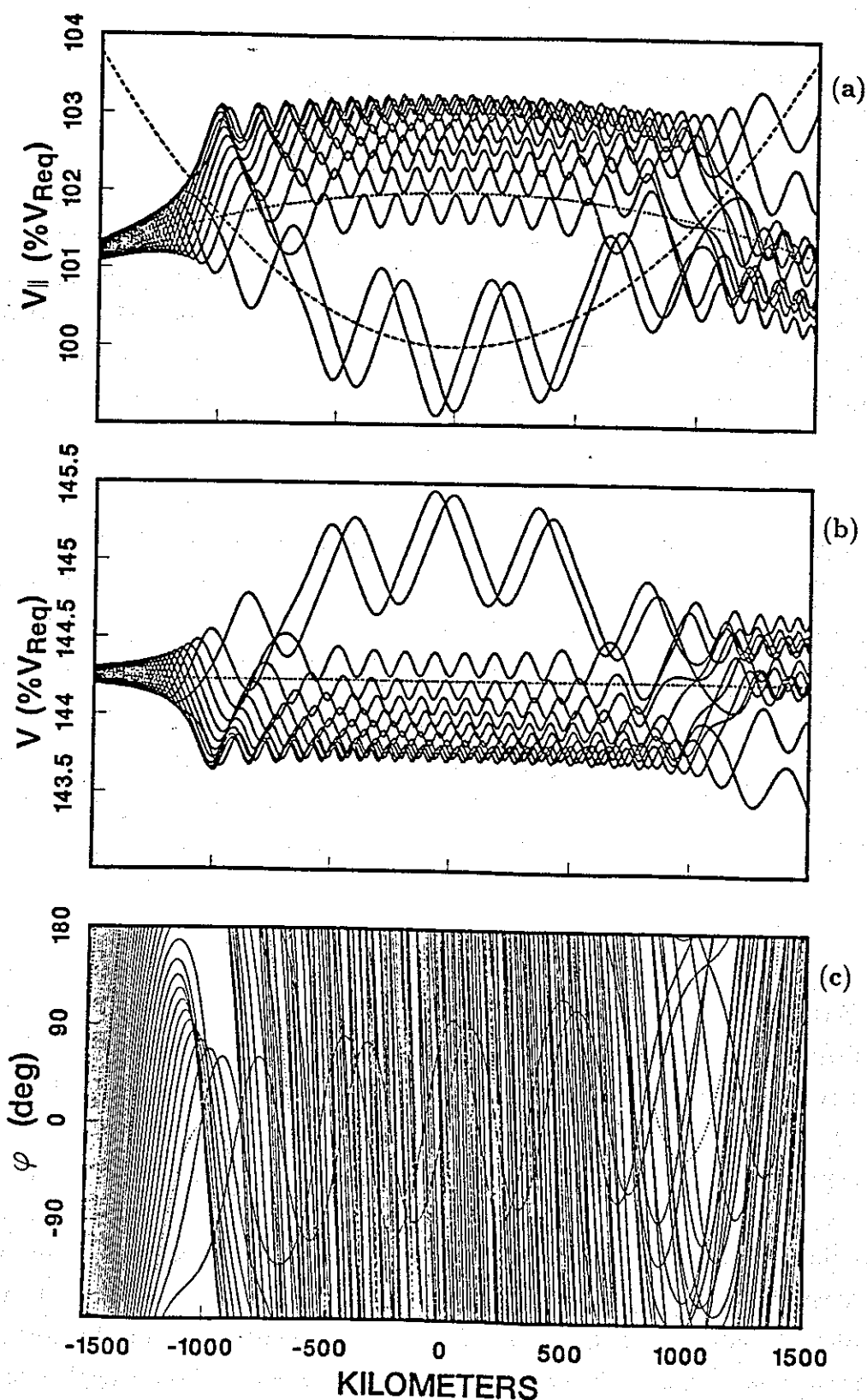


Figure 2.12. Plots (solid) of $v_{||}$, v , and ϕ versus position for a case with a 10 pT wave intensity but otherwise identical to that of Figure 2.10. These plots show the behavior of two trapped electrons. Also shown are the adiabatic trajectories (dotted) and the resonance velocity curve (dashed).

mation that $df_P/dt \simeq 0$, yields the pendulum equation

$$\frac{d^2\phi}{dt^2} + \frac{eB_w}{m}kv_{\perp}\sin\phi = \left[3\pi v_{\parallel} + \frac{kv_{\perp}^2}{2f_H}\right]\frac{\partial f_H}{\partial z} - \frac{d^2\psi}{dt^2}. \quad (2.38)$$

The right side of equation (2.38) is the forcing function which depends upon both the static field inhomogeneity and wave field twisting. In this sense, spatial twisting of the wave field is just an additional inhomogeneity and, in general, a first order term. The second term on the left is the restoring force function which includes the $\mathbf{v}_{\perp} \times \mathbf{B}_w$ force. The amplitude of the restoring force term is often written as

$$\omega_t^2 = \frac{eB_w}{m}kv_{\perp} \quad (2.39)$$

where ω_t is called the trapping frequency which, as is shown later, is closely related to whether an electron is trapped or not and, for trapped electrons, determines the frequency at which the trapped electron oscillates about $-\mathbf{B}_w$. However, the generalized pendulum equation can have periodic, quasiperiodic, and chaotic solutions [Jensen, 1987; Per Bak, 1986; Lichtenberg and Lieberman, 1983].

Electrons can become trapped if the trapping frequency is large enough to overcome the inhomogeneity. Thus, a useful quantity for describing the wave-particle interaction is the ratio of the inhomogeneity terms to the restoring force term

$$R = \frac{1}{\omega_t^2} \left(\left[3\pi v_{\parallel} + \frac{kv_{\perp}^2}{2f_H} \right] \frac{\partial f_H}{\partial z} - \frac{d^2\psi}{dt^2} \right) \quad (2.40)$$

where R is known as the inhomogeneity ratio [Nunn, 1971]. Since no trapping can occur if $|R| > 1$, the spatial region where $|R| < 1$ is called the 'trapping zone'. In the case where there is no wave field twisting, R is negative on the upstream side, zero at the equator, and positive on the downstream side as governed by $\partial f_H / \partial t$. Similarly, $|R|$ increases with increasing distance from the equator. Thus, in this symmetric case, the trapping zone is largest at the equator and vanishes at some latitude depending on the wave intensity, wave number, and electron perpendicular velocity. A sketch of the trapping regions, in the v_{\parallel} - ϕ plane, and the associated particle trajectories at various points along a field line, are given in Figure 2.13. As demonstrated in Figure 2.13, a nonzero value of R causes the center cyclotron phase angle of the trapping zone to become shifted, with the direction of shift being related to the sign of R .

The existence of a trapping zone does not necessarily imply trapped electrons. In Figure 2.12 only two electrons were trapped while more than two adiabatic trajectories

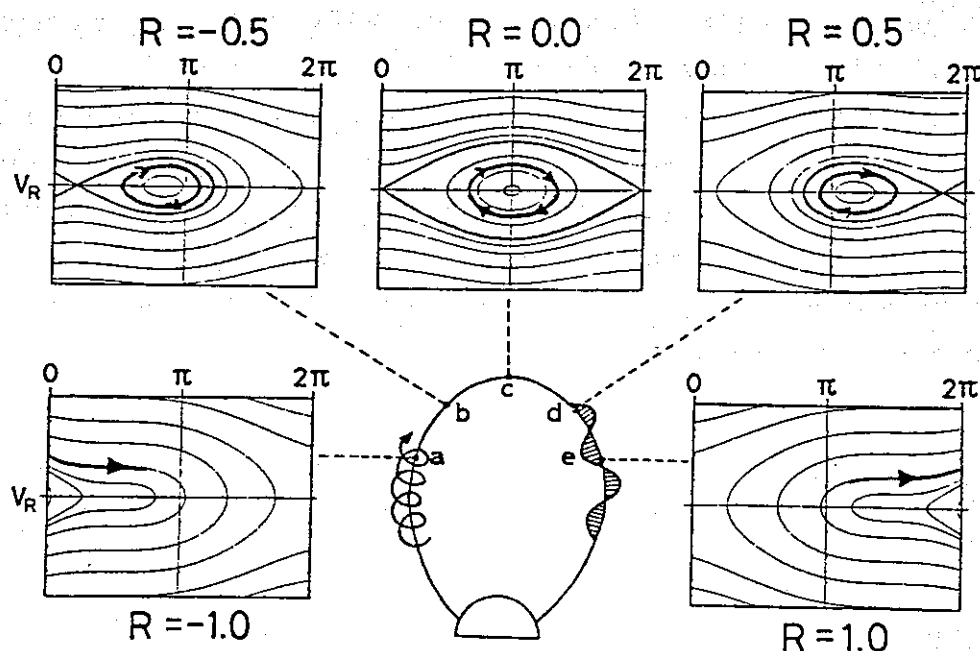


Figure 2.13. Sketch of the trapping regions, in the $v_{\parallel}-\phi$ phase space plane, and the associated particle trajectories at various points along a field line (from Matsumoto, [1986]). Non-zero values of R cause the center cyclotron phase angle of the trapping zone to become shifted with the direction of shift being related to the sign of R .

passed through the trapping zone. What is happening, in this case, is that the electron trajectories flow around the trapping zone and only those electrons whose momentum carries them into the trapping zone, as the trapping region changes shape with position, are actually trapped. If electrons encounter an abrupt wave front right at their resonance point, then all of these electrons would be trapped. Thus, in order for electrons to become trapped or detrapped, the trapping region has to change shape relative to the electrons. Two sources of this change are the static field inhomogeneity and variations in the applied wave intensity. Even if an electron becomes trapped, it may become detrapped in a time less than a trapping period, giving it a trajectory similar to that of an untrapped electron. Thus, an increased wave intensity would not necessarily trap more electrons.

When electron trapping is not significant, a measure of the interaction region is the adiabatic interaction length L_p [Helliwell, 1970]. L_p is the maximum length over which the unperturbed phase curve for an electron is within $\pi/2$ of $-\mathbf{B}_w$. This defines

a region which is approximately the same as the region within which the average energy of the electron changes as a result of the wave-particle interaction [Inan *et al.*, 1978]. Figure 2.14 is a plot of L_p and resonance location versus $v_{\parallel \text{eq}}$. L_p approaches 0 at both the high and low v_{\parallel} ends of Figure 2.14. For a parabolic approximation to the earth's magnetic field, L_p falls off as the square root of the resonance location for the high v_{\parallel} end. The peak in L_p actually occurs for $v_{\parallel \text{eq}} > v_{R \text{eq}}$ because the conjugate interaction regions defined by L_p , overlap for $v_{\parallel \text{eq}}$ less than about 0.2% of $v_{R \text{eq}}$. L_p discontinuously drops by a factor of two where the interaction regions no longer overlap. How conjugate interaction regions actually interact is investigated further in the next chapter.

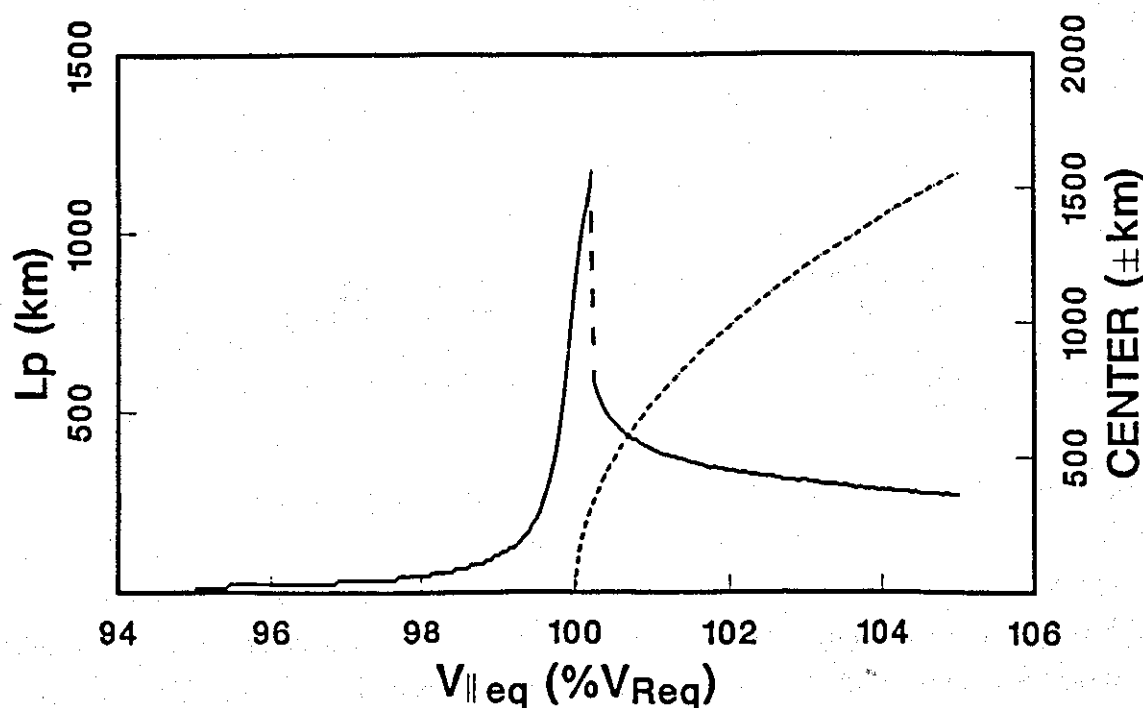


Figure 2.14. Plot of L_p (solid) and resonance location, or 'center', (dashed) versus $v_{\parallel \text{eq}}$. L_p is defined here as the maximum length over which the unperturbed phase curve for an electron is within $\pi/2$ of $-\mathbf{B}_w$. L_p corresponds to the region over which significant energy exchange occurs between the wave and the electrons.

The characteristic 'resonance time' for an electron to traverse the interaction region is defined as

$$T_r = \frac{L_p}{v_{\parallel}} \quad (2.41)$$

A convenient measure of the amount of phase bunching is the ratio of the resonance time to the time required to bunch the electrons [Helliwell and Inan, 1982]. The bunching time T_b is defined as

$$T_b = \frac{\pi}{2\omega_t} \quad (2.42)$$

which is a quarter of the trapping period [Helliwell, 1967]. In general, a subpopulation of electrons becomes maximally bunched within the interaction region if $T_b < T_r$. The usefulness of this bunching time to resonance time ratio is demonstrated in the following analysis of equatorial versus offequatorial resonant currents.

Besides looking at the general aspects of equatorial and offequatorial resonant trajectories and currents, it is also important to study the relative significance of the two interaction regions. Comparison of the peak currents in Figure 2.8 and Figure 2.11 show that the current peak following equatorial resonance in Figure 2.8 is about the same as the peak current following the upstream resonance in Figure 2.11. However, since the latter current peak occurs outside of its interaction region, phase mixing makes it less significant as demonstrated in Figure 2.9. Thus, a proper comparison of equatorial and offequatorial currents should include all of the electrons resonant at these points. Figure 2.15 achieves this by looking at the current from all the electrons (*i.e.* a full range of pitch angles) which have resonant velocities of v_{Req} and $1.03v_{Req}$. The currents associated with two wave intensities, 0.1 and 5.0 pT, are shown in Figure 2.15. These currents have been normalized by the maximum possible current that would result if all electrons were exactly in phase (see discussion in the next chapter). In general, the normalized current from maximally phase bunched electrons would be ~ 0.7 [Helliwell and Crystal, 1973]. However, since there are two separate interaction regions in Figure 2.15, 0.35 would be the maximum possible neglecting constructive addition from the two sets of electrons. The results shown in Figure 2.15 can be explained in terms of phase mixing and T_b/T_r . T_b/T_r is a minimum at the equator since, from Figure 2.14, the interaction length gets shorter with distance from the equator. T_b/T_r also gets smaller as the wave intensity increases. In the 0.1 pT case, $T_b \simeq T_r$ for 45° pitch angle, equatorially resonant electrons but $T_b > T_r$ for most of the offequatorially resonant electrons. Consequently, there is significant phase mixing associated with both interaction regions resulting in peaks below 0.35. In the 5.0 pT case $T_b < T_r$ for most electrons and the equatorial current peak is approaching its maximum of 0.35. Also the ratio of the offequatorial current peak to the equatorial current peak has increased from ~ 0.04 to ~ 0.5 . Increasing B_{in} further will eventually result in both current peaks being ~ 0.35 . So while the

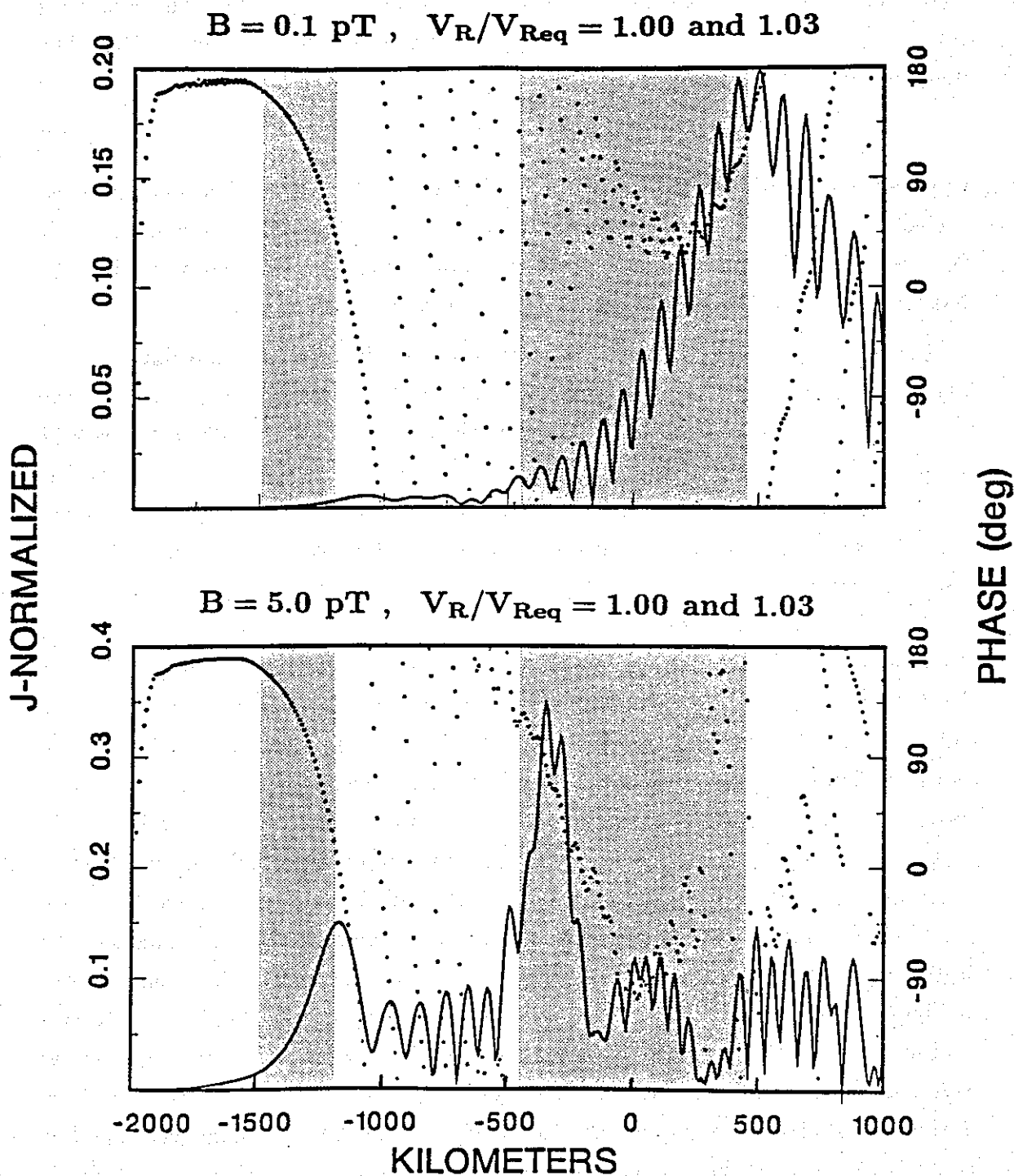


Figure 2.15. Comparison of equatorial and off-equatorial currents at two different wave intensities, 0.1 and 5.0 pT. Included are all electrons resonant at the equator and ~ 1300 km off the equator where $v_R = 1.03v_{Req}$. The shaded strips indicate the interaction regions from Figure 2.14. Compared to simple theory, the ratio of the off-equatorial to equatorial resonant current peak in the 0.1 pT case is smaller due to phase mixing and, in the 5.0 pT case, larger due to rapid bunching.

inhomogeneity and phase mixing act to confine the phased bunched current to the equatorial region, high wave fields act to spread the interaction out. This lengthening could result in a loss of coherence, promote sideband activity, and possibly provide a saturation mechanism. In the weak wave limit, as $T_b \gg T_r$, the current within the interaction region increases parabolically with position $J(z) \propto z^2$ [Helliwell and Inan, 1982; Helliwell and Crystal, 1973], for electrons having the same unperturbed α and v_{\parallel} . This might suggest a minimum of 0.1 in the ratio of the offequatorial to equatorial current for the electron and medium parameters of Figure 2.15. However, the 0.1 pT case exhibits a ratio of ~ 0.04 . The reason for this difference is the increased efficiency of phase mixing for the offequatorially resonant electrons due to $\partial f_H / \partial z \neq 0$.

There is evidence that electrons with $v_R > 1.03v_{Req}$ do not significantly contribute to the wave growth. Experiments have shown that wave particle interactions involving two single frequency signals, tend to be independent of each other if their frequency separation Δf is greater than ~ 100 Hz [Helliwell, 1983; Helliwell et al., 1986a,b].

2.6. Numerical methods and algorithms

In this section, the basic numerical approach to calculating electron trajectories is examined. Other algorithms specific to the steady state or transient models are described later.

As discussed earlier, there are three general components of the physical system being considered, the energetic electrons, the whistler-mode radiation, and the ambient medium. Necessary information regarding each of these constituents needs to be tracked so that currents and fields can be calculated at any point in space and, for transient cases, at any point in time. The models used throughout are one-dimensional since all quantities are assumed uniform in the infinite plane transverse to the earth's magnetic field. The discretization of the one spatial dimension, along a field line, is demonstrated in Figure 2.16. A limited region is first selected by specifying upstream and downstream limits, z_{up} and z_{down} , respectively. The corresponding latitudes are determined using equation (2.4) and a root finding technique [Dowell and Jarratt, 1972]. As shown in Figure 2.16, the limited region is then divided into some number of steps N_M , with equal latitudinal spacing $\Delta\lambda$; these are called macro steps. At each macro step, all the medium and propagation parameters are calculated and stored in arrays using the equations and models described at the beginning of this chapter. For the purposes of integrating the equations of motion, each macro

step is further divided into some integer number of micro steps N_μ . The medium and propagation parameters at each micro step are interpolated from the stored values at neighboring macro steps. Thus, the number of macro steps must be sufficient so that the error associated with the interpolation of medium and propagation parameters is not significant. During a single execution of any of the computer programs used in this thesis, the macro step size remains constant for each electron trajectory calculation. However, the number of micro steps per macro step depends on the initial velocity and pitch angle of each electron and also on the maximum wave intensity. Thus the number of micro steps per macro step can change several times during any single computer code execution.

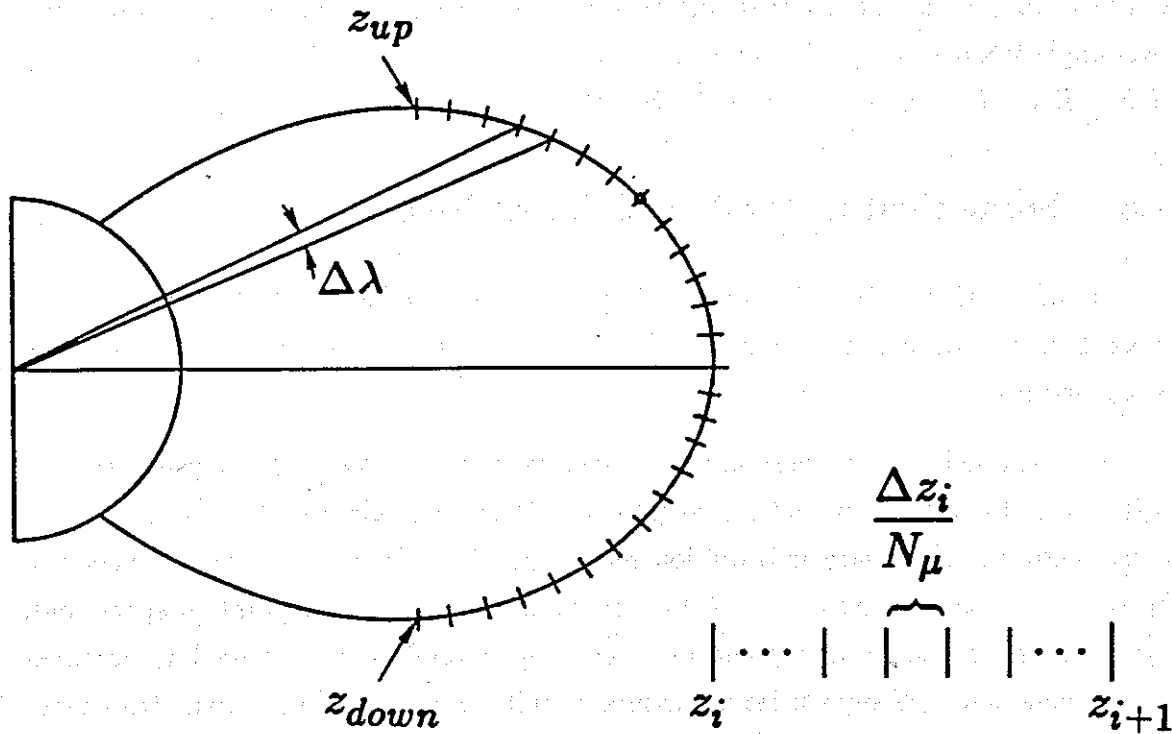


Figure 2.16. Demonstration of the spatial discretization scheme. A limited region of a field line is divided into macro steps. The lower right schematic shows the subdividing of a macro step into micro steps, defining the spatial step size for the integration of the equations of motion.

The method used to integrate the equations of motion (2.21) is a fourth-order predictor-corrector method developed by *Ralston* [1978]. This method, chosen by *Inan* [1977], was designed to have both reasonably small error and numerical stability.

As a test of the accuracy of the predictor-corrector method, adiabatic trajectories are calculated by integrating the equations of motion and also by direct calculation of the adiabatic invariants. The difference between the two solutions represents the numerical error of the predictor-corrector algorithm. The resulting error in v , α , and ϕ are plotted in Figure 2.17 for the parameters of Table 2.1.

The numerical error in α and ϕ associated with the predictor-corrector method is approximately proportional to the macro step size. The pitch angle error is not significant. The accumulated cyclotron phase error within the interaction region (± 500 km) is $\sim 4^\circ$, however, a simple integration of the $d\phi/dt$ error was employed to generate the phase error curve so the actual cyclotron phase error is possibly less than shown. In any case, steady state simulations of wave growth, conducted for various micro and macro step sizes, indicated that even coarser step sizes could be used. The error associated with the velocity is very small and remains approximately constant at a value which was accumulated during the first few macro steps. The nature of the velocity error is such that it does not vary in a simple way with macro or micro step size spacing.

Although the trajectory errors are small, the macro and micro step sizes must be chosen with care. The macro step spacing is mostly determined by the desired output information since program output is only stored at macro step points. Caution must still be exercised since undersampling physically significant fluctuations in the trajectories or currents can result in nonphysical currents or radiation, respectively. In the previous trajectory calculations, the macro step spacing needed to be sufficiently small so that variations in v_{\parallel} , v_{\perp} , and ϕ can be smoothly followed. For cases where currents and radiation are the desired outputs, the macro step spacing can be increased since integration over the electron distribution function tends to cancel out fast variations in the individual electron trajectories.

Another aspect of electron trajectory calculation is the injection of electrons into the wave field. The problem arises because, in the steady state, electrons continuously encounter the wave field and, in the transient case, electrons enter at the smoothly varying wave front. However, when doing simulations, it is desirable to inject the electrons as close as possible to the interaction region in order to minimize CPU time consumption. When injecting electrons into the full output wave field, a 'step response' results which is not desirable.

For the trajectory or simulation calculations, the electrons are introduced in a two step fashion. For the first four micro steps, up to and including the second macro

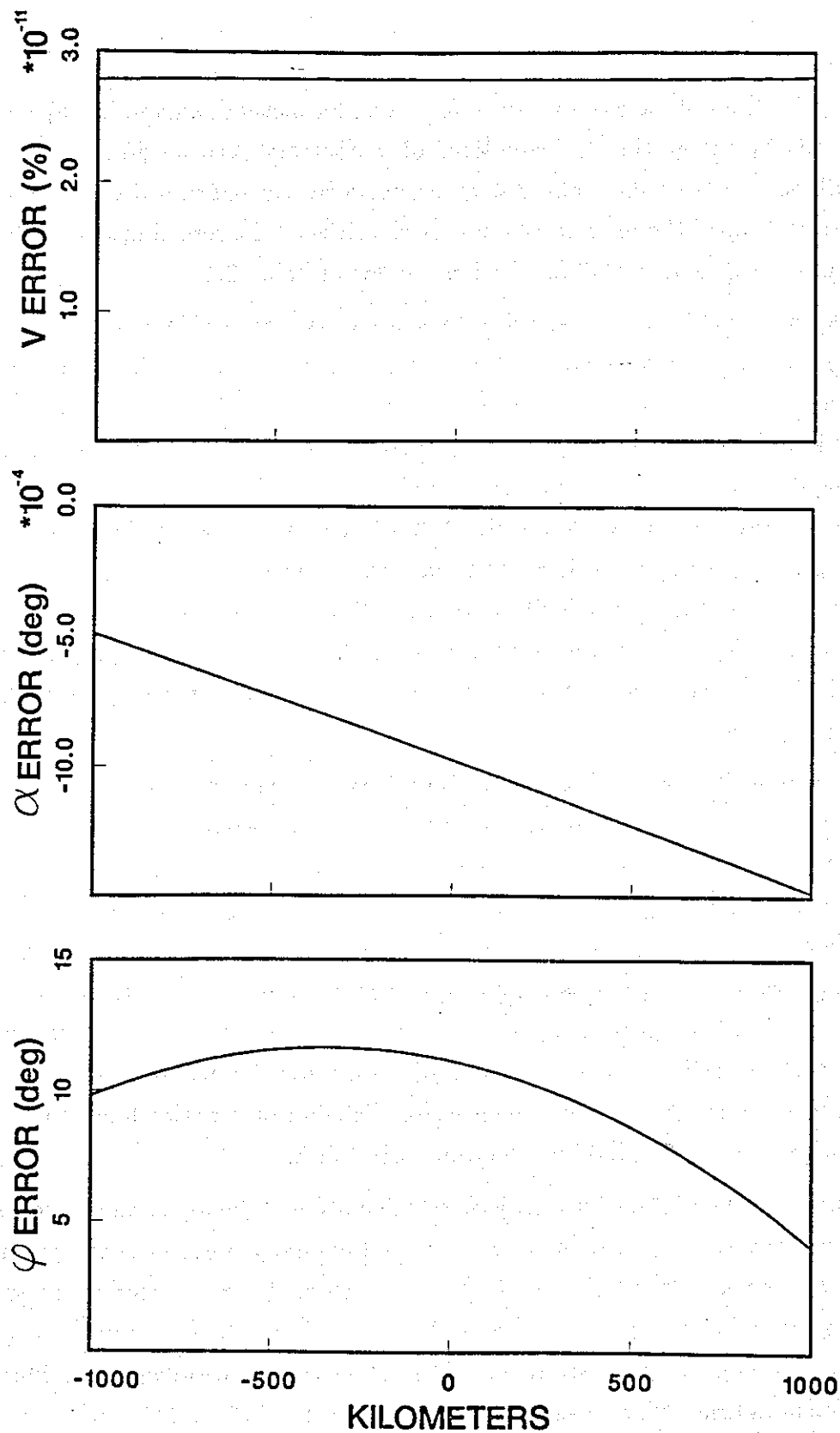


Figure 2.17. Error in v , α , and ϕ associated with the integration of the equations of motion using the predictor-corrector algorithm and zero wave field. The errors are calculated by comparing the integrated equations of motion to adiabatic electron trajectories.

step, the wave field is turned off and the electron trajectories are determined using the adiabatic invariants. This gives the electron parameters at four points as are required for the application of the predictor-corrector routine. The predictor-corrector routine is then used to integrate the equations of motion for the successive points with a non-zero wave field. To minimize the step response (except at the leading edge in some of the transient cases) the following function multiplies the wave field

$$\sin^2\left(\frac{\pi(z - z_2)}{2z_{fe}}\right) \quad \text{for} \quad z_2 < z < z_2 + z_{fe} \quad (2.43)$$

where z_2 is the position at the second macro step. Thus, the front end is sinusoidally tapered for a distance of z_{fe} km. Without this front end taper, the current plots shown previously would look different. Most noticeable would be a substantial buildup in the current magnitude prior to resonance, with a rotating rather than the constant 180° current phase. For wave growth simulations using a single initial v_{\parallel} and α , $z_{fe} \geq 100$ km is necessary. Integration over the electron distribution function also tends to eliminate the 'noisy' step response, in which case a shorter taper or even no taper can be used. This step response is the same effect *Winglee* [1985] tagged as a 'new' type of phase bunching. However, *Winglee* did not investigate the 'smooth' injection or the cancellation of this step response when integrating over v_{\parallel} and α .

The last major aspect of the simulations is the sampling of the energetic distribution function. The basic types of sampled distribution functions are demonstrated in Figure 2.18 which shows the location of test particles in the v_{\perp} - v_{\parallel} plane of velocity space. Each dot in Figure 2.18 represents N_{ϕ} test electrons uniformly distributed in gyrophase. Each test electron is taken to represent all electrons within the Δv_{\parallel} , $\Delta\alpha$, $\Delta\phi$ volume of velocity space surrounding the test particle. Typical values for the spacing of the test particles are given in Table 2.1. When including more than a single parallel velocity, the distribution function is often tapered at the v_{\parallel} edges in order to reduce 'edge' effects. This does not need to be done for the α edges since the current magnitudes already go to zero at these edges. More is said on this in the next chapter when simulations using the sampling schemes shown in Figure 2.18 are performed.

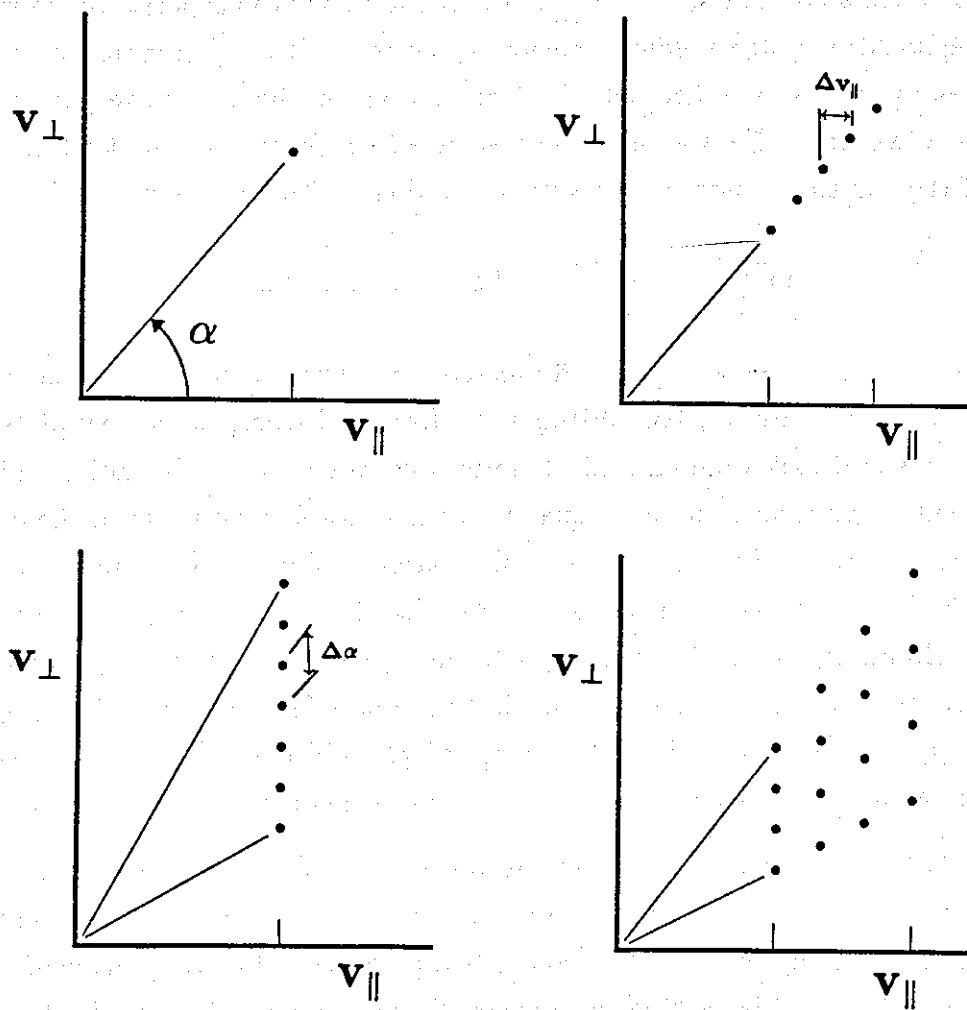


Figure 2.18. Examples of four meshes used to sample the energetic electron distribution function in the $v_{\perp} - v_{\parallel}$ plane. Each dot represents N_{ϕ} test electrons uniformly distributed in cyclotron phase. Each test electron represents all electrons in its vicinity.

Chapter 3. Quasi-steady state models and simulations

This chapter employs steady state concepts to investigate wave growth. In steady state, a stationary receiver placed anywhere, would receive a constant amplitude, constant frequency wave field for all time, a condition that is seldom observed. In the last chapter the equations were developed which describe the electron current sheet and steady state radiation. In the first part of this chapter; the energetic electron flux is assumed to be so small that the stimulated radiation does not significantly perturb the applied signal. These cases study the total stimulated radiation and the stimulated radiation versus v_{\parallel} and α . The calculations are performed for both homogeneous and inhomogeneous magnetic fields with various applied wave intensities.

In the second part of this chapter, simulations with significant wave growth are performed using quasi-steady state models. The first of these applies an iteration technique for finding self consistent steady state fields. The second of these employs a two-port feedback technique to simulate temporal wave growth. Both of these are labeled quasi-steady state models because the wave field is assumed to be in steady state while electron trajectories, currents, and stimulated radiation are being calculated. However, in both cases, the stimulated radiation updates the total wave field, creating the 'steady state' field for the next set of trajectory calculations.

3.1. Steady state simulations with negligible feedback

The stimulated radiation resulting from wave-particle interactions contributes to the total wave field, as is outlined in the last chapter. This section explores the characteristics of this radiation and its dependencies. In order to make this study tractable, the feedback of the stimulated radiation upon subsequent electrons is taken to be negligible. This is equivalent to assuming a very small energetic electron flux since the stimulated radiation and associated sheet current magnitude are proportional to this flux. Superposition can then be used since summing the stimulated radiation from the individual velocity space cells gives the stimulated radiation from the entire electron distribution. However, superposition does not hold when studying transient wave growth since feedback makes a given electron trajectory dependent on all the previous electron trajectories. The dependence of B_s upon B_{in} , $f(v, \alpha)$, v_{\parallel} , α , and

the interaction region inhomogeneity is the main result of this section.

Plotting B_s at the output, or upstream, end of the region versus α_{eq} and $v_{||eq}$ is useful since the dependence upon α and $v_{||}$ are given directly and also because the distribution function just becomes a weighting function for the magnitude surface. An analytic description of this surface follows directly from the equations in the previous chapter. Specifically, start with the discrete form of the current equation

$$\mathbf{J}(\alpha_{eq}, v_{||eq}, z) = \frac{\pi q}{\sqrt{f_{Heq}}} f(v, \alpha_{eq}) v^2 \sin(2\alpha_{eq}) \Delta\alpha_{eq} \Delta v \frac{f_H(z) \sum_i \mathbf{v}_{\perp i}(\alpha_{eq}, v_{||eq}, z)}{\sqrt{f_{Heq} - f_H(z) \sin^2 \alpha_{eq}}} \quad (\text{A/m}^2), \quad (3.1)$$

and then integrate to get the stimulated radiation

$$\mathbf{B}_s(\alpha_{eq}, v_{||eq}, z) = D(z) \frac{\mu_0}{2} \int_{z_{down}}^z \frac{[\mathbf{J}(\alpha_{eq}, v_{||eq}, z) \times \mathbf{n}]}{D(z)} dz \quad (\text{T}), \quad (3.2)$$

where $D(z)$ is the ducting factor derived in the last chapter. In practice, of course, the integration over z is approximated by a discrete summation. The total current or field at each point in space is then calculated by summing over all discrete values of α and $v_{||}$ as follows

$$\mathbf{J}(z) = \sum_i \sum_j \mathbf{J}(\alpha_{eq_i}, v_{||eq_j}, z), \quad (3.3)$$

$$\mathbf{B}_s(z) = \sum_i \sum_j \mathbf{B}_s(\alpha_{eq_i}, v_{||eq_j}, z), \quad (3.4)$$

$$\mathbf{B}_w(z) = \mathbf{B}_s(z) + D(z) \mathbf{B}_{in}. \quad (3.5)$$

It is also instructive to plot $\mathbf{B}_{sout}(\alpha_{eq})$ versus $v_{||eq}$ and $\mathbf{B}_{sout}(v_{||eq})$ versus α_{eq} , given by

$$\mathbf{B}_{sout}(\alpha_{eq}) = \sum_i \mathbf{B}_s(\alpha_{eq_i}, v_{||eq_i}, z_{up}), \quad (3.6)$$

and

$$\mathbf{B}_{sout}(v_{||eq}) = \sum_i \mathbf{B}_s(\alpha_{eq_i}, v_{||eq_i}, z_{up}). \quad (3.7)$$

Throughout the rest of this thesis, \mathbf{B}_{sout} is written as \mathbf{B}_s and is distinctly different than $\mathbf{B}_s(z)$. Also, in any of the following plots of radiation, when position is not

an abscissa, the quantity plotted is the radiation at the output of the region \mathbf{B}_{sout} , where $z = z_{up}$.

Feedback has been assumed to be negligible, equivalent to assuming a very small flux of energetic electrons. Since the absolute magnitude of the flux is not important as long as the flux is small, all magnitude plots in this section are normalized. Magnitude surface plots of $\mathbf{B}_s(\alpha_{eq}, v_{||eq})$ are normalized so that the peak value is unity. Plots of $\mathbf{B}_s(v_{||eq})$ and $\mathbf{B}_s(\alpha_{eq})$ are normalized by B_s so that relative contributions are easily determined. $\mathbf{J}(z)$ plots are normalized by

$$J_N(z) = \frac{\pi q f_H(z) \Delta \alpha_{eq} \Delta v}{\sqrt{f_{Heq}}} \sum_i \sum_j f(v_{i,j}, \alpha_{eq_i}) v_{i,j}^2 \sin(2\alpha_{eq_i}) \frac{\sum_k v_{\perp k}(\alpha_{eq_i}, v_{||eq_j}, z)}{\sqrt{f_{Heq} - f_H(z) \sin^2 \alpha_{eq_i}}} \quad (\text{A/m}^2) \quad (3.8)$$

which is essentially equations (3.1) and (3.3) except that a magnitude sum instead of a vector sum over v_{\perp} is performed. Thus, if at some point in space, all v_{\perp} 's were aligned then the normalized current would be unity. With this normalization, the current magnitude gives a measure of the completeness of phase bunching. $\mathbf{B}_s(z)$ is normalized by

$$B_N = \int_{z_{down}}^{z_{up}} \left| \frac{d\mathbf{B}_s(z)}{dz} \right| dz \quad (3.9)$$

making \mathbf{B}_{sout} also a measure of the coherence of the radiation over the considered region.

Homogeneous region

For tutorial purposes, let's first examine the stimulated radiation from wave-particle interactions in a 2000 km long homogeneous region with an applied field of 1.0 pT and an $f(v, \alpha) = 1$ distribution. A plot of $\mathbf{B}_s(\alpha_{eq}, v_{||eq})$ is shown in Figure 3.1. Each grid point represents the stimulated radiation propagating out of the region from 12 electrons uniformly distributed in gyrophase and injected into the region with the indicated $v_{||}$ and α . Besides a 400 km front end taper applied to B_{in} , a 250 km taper is applied to the downstream current before integrating which helps to reduce the noise associated with abruptly turning off the current at the downstream boundary. The magnitude surface in Figure 3.1 shows that B_s is greatest for high α resonant electrons. The phase surface in Figure 3.1 is consistent with resonant

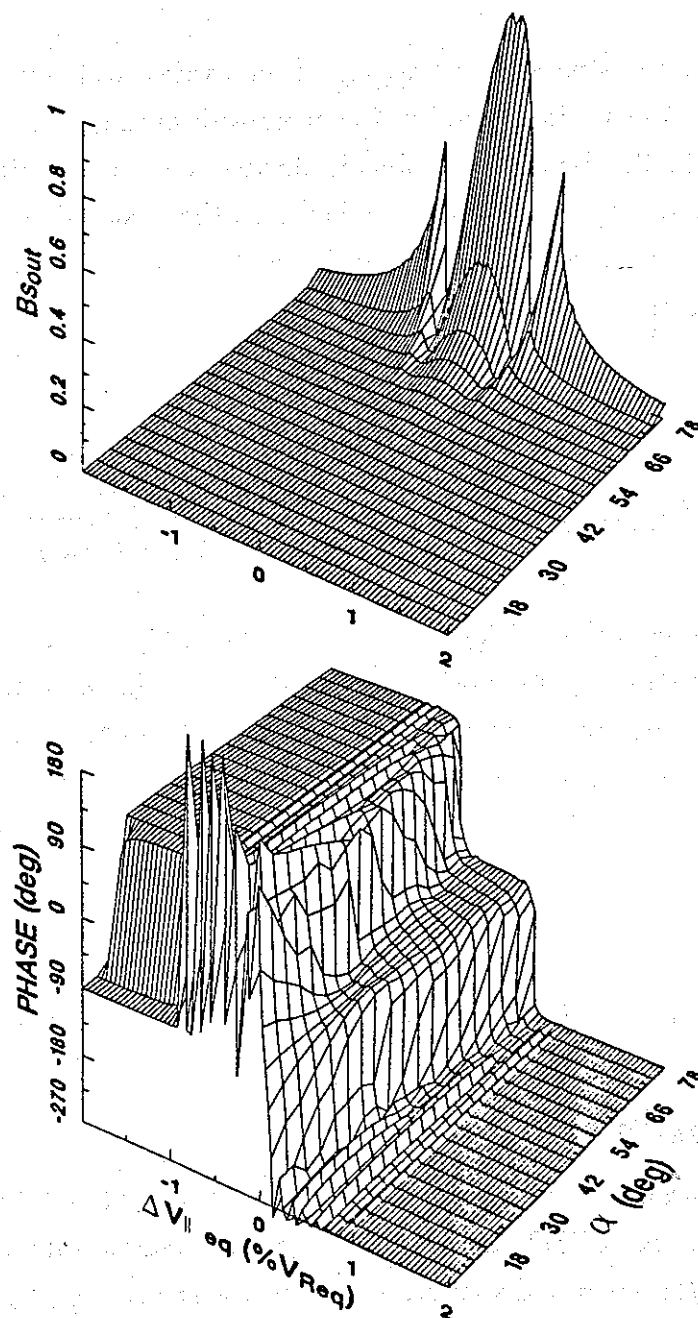


Figure 3.1. Magnitude and phase surfaces of $B_s(\alpha_{eq}, v_{||eq})$ for a 2000 km long homogeneous region with $B_{in} = 1$ pT, $f(v, \alpha) = 1$. The magnitude surface shows that the peak radiation comes from high pitch angle, resonant electrons. The phase surface shows that the peak radiation is lagging the applied wave by 90° .

electrons having their average current aligned with the applied magnetic field. The offresonant currents are antiparallel to the applied field except for low pitch angle electrons with v_{\parallel} 's below resonance, which have currents aligned with the wave field. This offresonant current behavior is explained in the last chapter and summarized in Table 2.2. The -90° ledge in the phase plot in Figure 3.1 shows that a significant number of offresonant electrons are displaying resonant or trapped behavior.

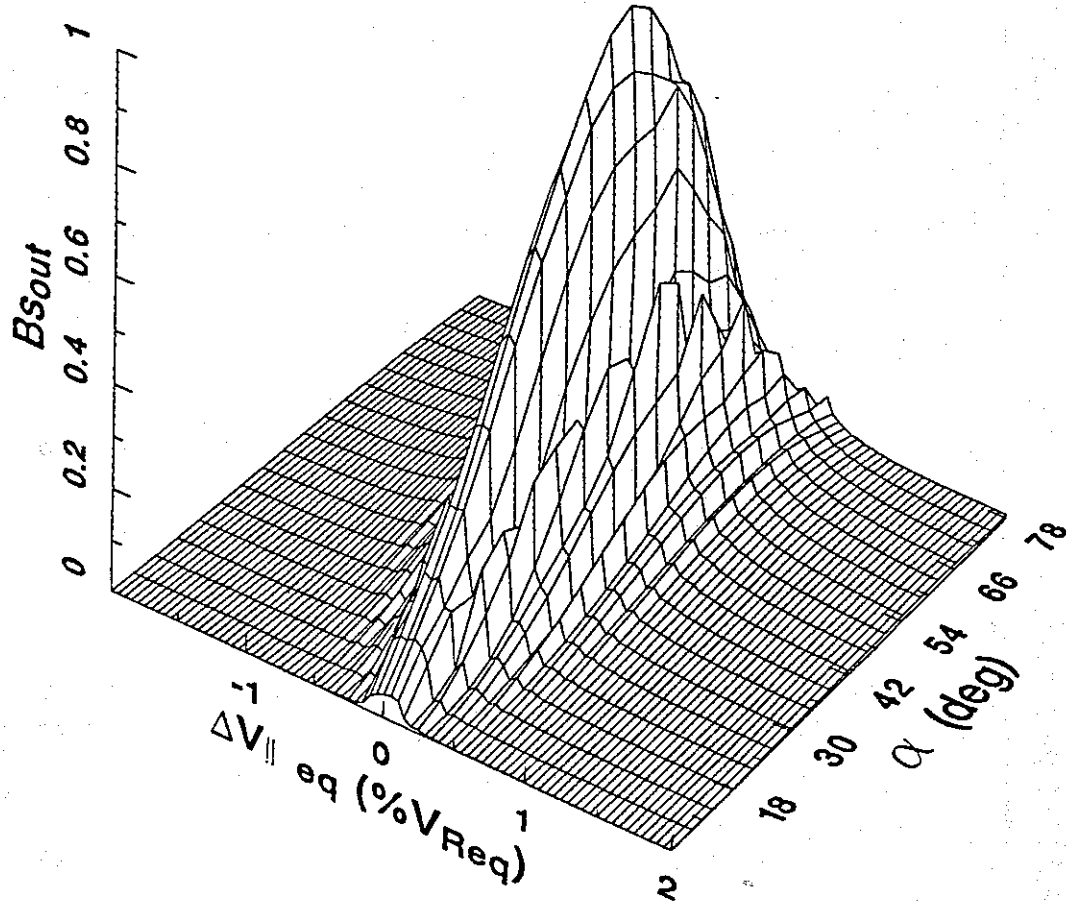


Figure 3.2. Magnitude surface of $B_s(\alpha_{eq}, v_{\parallel eq})$ for the same conditions and 2000 km long homogeneous region as in Figure 3.1 except that $f(v, \alpha) = v^{-6}$. With the addition of a falloff in number density with increasing energy, the peak radiation is now coming from the $\sim 45^\circ$ α 's.

The $B_s(\alpha_{eq}, v_{\parallel eq})$ magnitude surface is tutorial since a unity distribution function is used. Figure 3.2 is the $B_s(\alpha_{eq}, v_{\parallel eq})$ magnitude surface using a distribution function of the form v^{-6} . This figure shows that resonant electrons are the major contributors

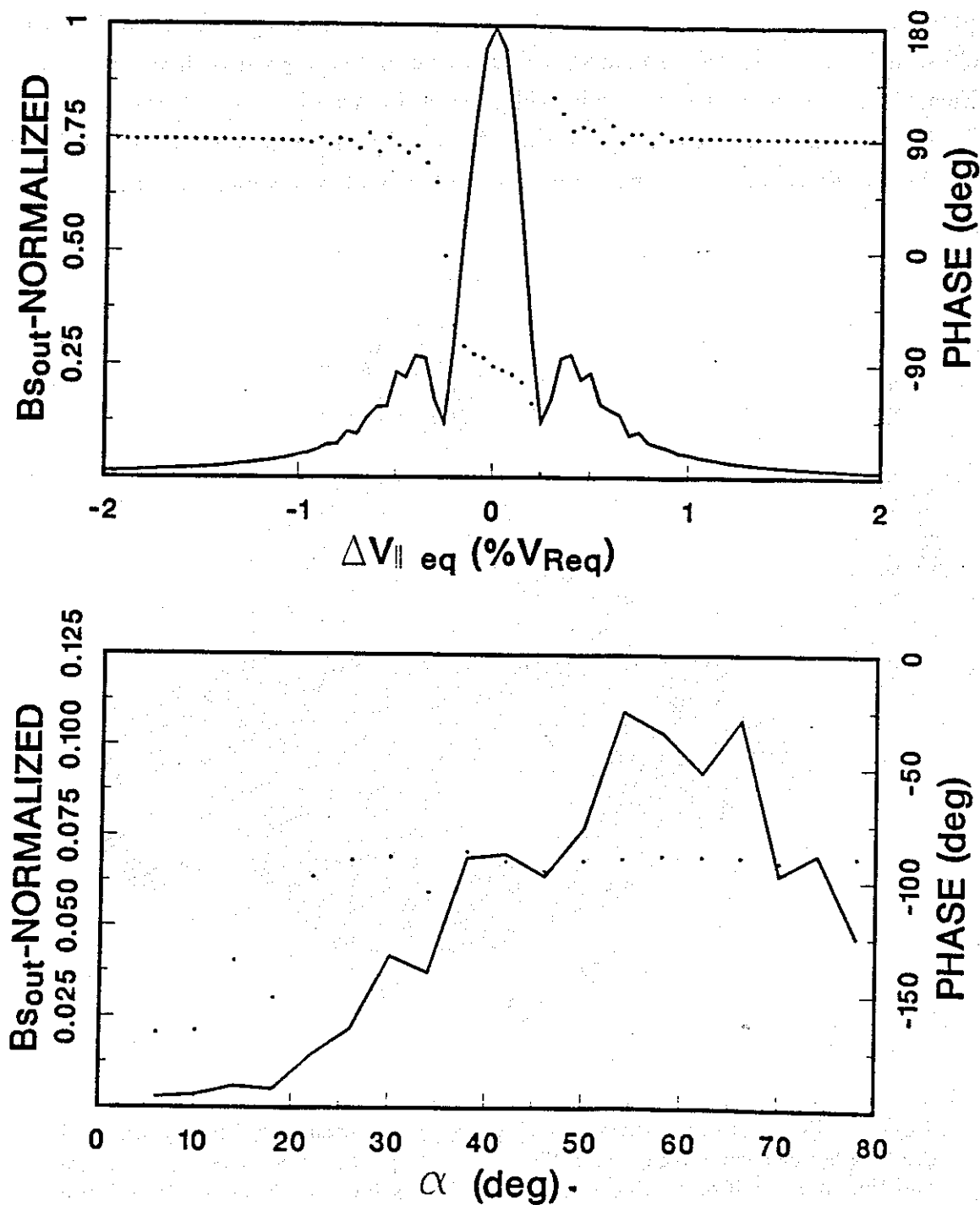


Figure 3.3. $B_s(v_{\parallel eq})$ (top panel) and $B_s(\alpha_{eq})$ (bottom panel) for the same case as in Figure 3.2. $B_s(v_{\parallel eq})$ and $B_s(\alpha_{eq})$ are generated by integrating over α_{eq} and $v_{\parallel eq}$ respectively. The magnitude (solid) and phase (dotted) are given in both plots. To first order, these curves look like simple cross sections of the surfaces in Figure 3.1 and Figure 3.2.

to B_s even with the power law falloff in the distribution of electrons with electron energy. However, the pitch angle at the peak in B_s has now dropped to $\simeq 45^\circ$ with the range of significant α 's greatly increasing.

Figure 3.3 gives plots of $B_s(\alpha_{eq})$ and $B_s(v_{\parallel eq})$ after integration over v_{\parallel} and α respectively. The $B_s(\alpha_{eq})$ plot in Figure 3.3 indicates that the maximum contribution is coming from the 55° to 60° pitch angle electrons with a $\sim -90^\circ$ phase characteristic of radiation from resonant or trapped electrons. The phase of the radiation from the low pitch angle electrons is further retarded into the attenuating range of -90° to -180° suggesting acceleration by E_w . The reason the low pitch angle phase for $B_s(\alpha_{eq})$ is not predicted by simple examination of Figure 3.2 is because of the large degree of cancellation which results from the integration over v_{\parallel} . In contrast, the -90° radiation from the higher pitch angle electrons is easily predicted by the coincidence of a $B_s(\alpha_{eq}, v_{\parallel eq})$ magnitude peak and a -90° 'ledge' for nearly resonant v_{\parallel} 's. The $B_s(v_{\parallel eq})$ plot in Figure 3.3 looks very much like a simple cross section of the surfaces in Figure 3.2 and shows the connection between the sidelobe structure in $B_s(v_{\parallel eq})$ and the transition from resonant to perturbed radiation. The $B_s(v_{\parallel eq})$ curve also reveals the nearly exponential falloff of B_s away from resonance.

While the previous figures dealt with the stimulated radiation at the output, Figure 3.4 plots the total stimulated radiation versus position. The magnitude of $B_s(z)$ changes almost linearly with position and the phase is nearly constant at -90° indicating that the magnitude and phase of the current versus position are nearly constant.

The region length (2000 km for these homogeneous results) is also the interaction length when the region is homogeneous and does influence the characteristics of the results. In general, increasing the length of the homogeneous region tends to narrow the range of v_{\parallel} over which there is significant B_s . Also, the -90° 'ledge' in the phase surface around v_R tends to become more flat and broad indicating that integrating over a longer interaction region tends to reduce the incoherent contributions relative to the coherent contributions.

Inhomogeneous region

The geomagnetic field inhomogeneity causes the resonance velocity to be a function of position, with the minimum resonance velocity occurring at the geomagnetic equator. Consequently, an adiabatic electron satisfies the resonance condition never, once, or twice depending on whether its $v_{\parallel eq}$ is less than, equal to, or greater than

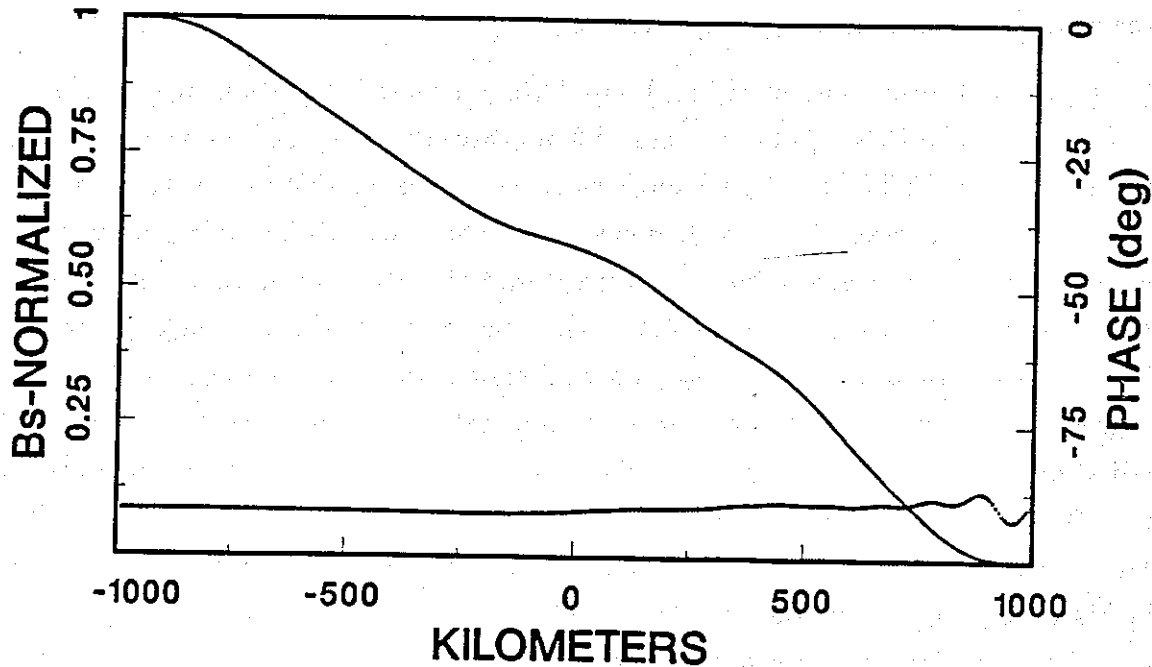


Figure 3.4. $B_s(z)$ for the same case as in Figure 3.2. The magnitude (solid) changes almost linearly with position and phase (dotted) is nearly constant about -90° indicating that the magnitude and phase of the current versus position varies about constant values.

v_{Req} , respectively. It is a general result that for $v_{\parallel eq}$'s less than v_{Req} , the radiation characteristics are the same for both homogeneous and inhomogeneous regions and follow from a perturbation analysis. However, the inhomogeneity causes the radiation characteristics to become more complicated for $v_{\parallel eq}$'s greater than v_{Req} because of the conjugate interaction regions for these electrons.

For this steady state inhomogeneous analysis, the applied wave intensities are set to 10.0, 1.0, and 0.1 pT in order to compare results from weak, intermediate, and strong wave fields. Comparison of the $B_s(\alpha_{eq}, v_{\parallel eq})$ surfaces given in Figure 3.5 show several noteworthy differences. The symmetry about v_{Req} , present in the homogeneous case, is missing because of the conjugate interaction regions for the high v_{\parallel} electrons. The slow falloff of the magnitude with v_{\parallel} for the 0.1 pT case in Figure 3.5 for the high v_{\parallel} 's results from strong conjugate coupling. For weak wave intensities, the first interaction initiates a slow phase bunching process which leads to a large phase bunched current upon entry into the second conjugate interaction region. The v_{\parallel} and α dependent quantities, like interaction length and conjugate interaction re-

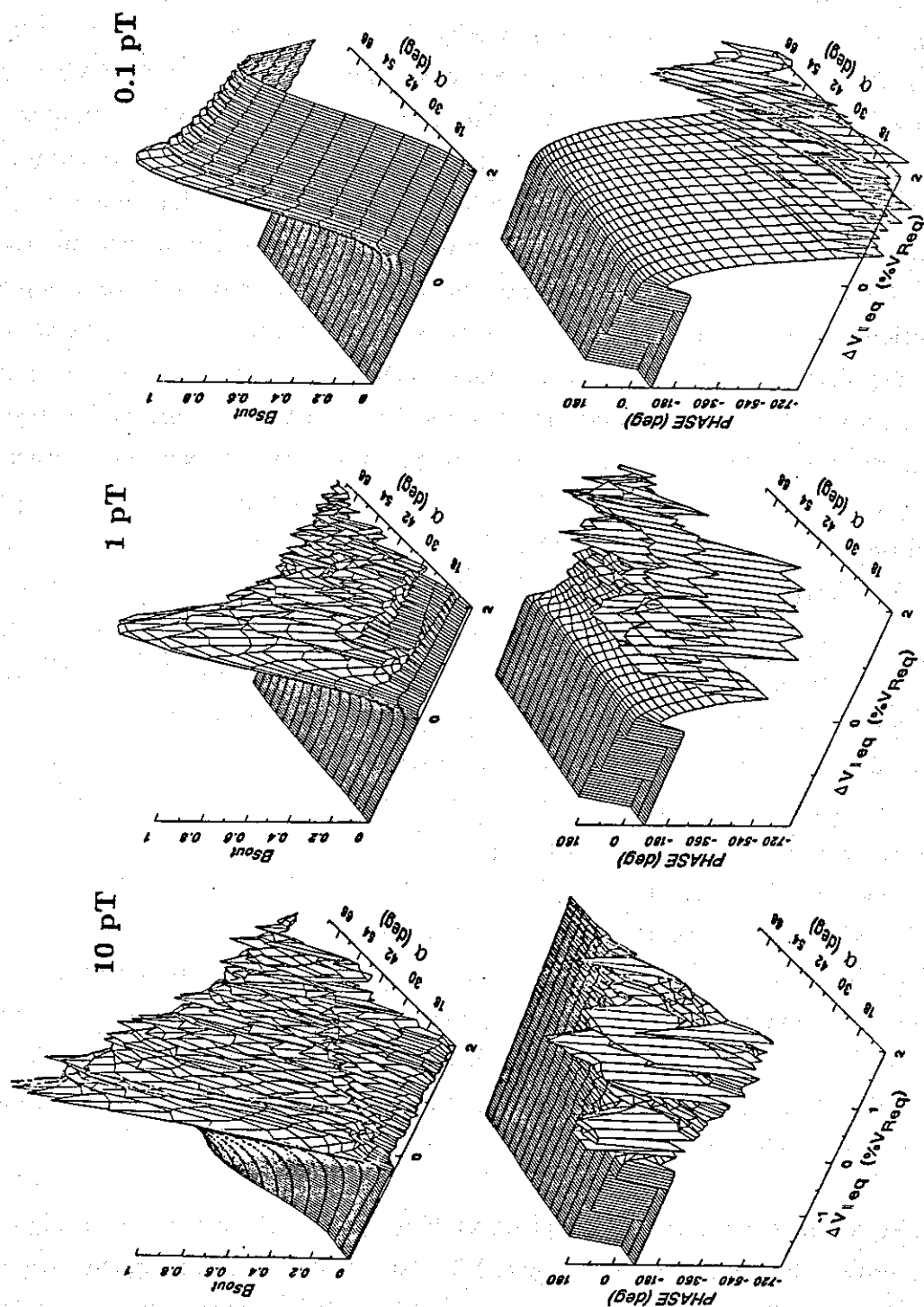


Figure 3.5. Magnitude and phase surfaces of $B_s(\alpha_{eq}, v_{leq})$ for a 3400 km equatorially centered inhomogeneous region with B_{in} 's of 10.0, 1.0, and 0.1 pT in the left to right pannels, respectively. $f = 3/8 f_{Heq}$, $f(v, \alpha) = v^{-6}$.

gion separation, evidently tend to balance each other to give this slow falloff. Another B_{in} dependent feature worth noting is the significance of the low $v_{||}$ radiation relative to the radiation from equatorially resonant electrons in the 10.0 pT case when compared to the 1.0 and 0.1 pT cases. This results from increased phase bunching within a cyclotron period for these nonresonant, low $v_{||}$ electrons. The phase surfaces for low $v_{||}$'s are similar to the homogeneous case but are much different for high $v_{||}$'s which also show a definite B_{in} dependence. The phase fluctuations are due to the distribution of phases for the phased bunched currents prior to entry into the conjugate interaction region. The greater number of phase cycles is also due to conjugate interaction coupling. For electrons with $v_{||}$'s just above v_{Req} the phase bunched currents are given a small amount of phase retardation between the two interaction regions. The further apart the interactions, the more the phase retardation. In practice, an algorithm is employed to try to make a continuous phase surface out of the phase information between -180° and 180° . This algorithm breaks down however, when either the distribution sampling becomes too sparse, a true discontinuity exists in the phase surface at a point of zero radiation in the $v_{||}$ - α plane, or the 'unrolling' of the phase is halted by an arbitrary lower limit set here at $\sim -720^\circ$. This algorithm break down is marked by the transition of a smooth phase surface to a fluctuating surface. The most obvious B_{in} dependent feature in the phase surfaces is the transition from a retarding phase versus $v_{||}$ to a constant phase versus $v_{||}$ as B_{in} or α is increased. The source of the retarding phase versus $v_{||}$ has just been discussed, but the constant phase versus $v_{||}$ at high α 's in the 10.0 pT case results from complete bunching within a time shorter than a resonance time (*i.e.* $T_b < T_r$). In other words, the phase bunching and debunching process can be repeated several times within the interaction region and can even occur within a cyclotron period in a region outside an interaction region. The current phase of these bunching peaks tends to be scattered about 180° . Thus, paradoxically, the radiation behaves like the perturbed radiation from the low $v_{||}$ electrons.

Integration over α removes the pitch angle dimension of the surfaces in Figure 3.5 and gives the plots of $B_s(v_{||eq})$ in Figure 3.6. Except for phase mixing, the magnitude curves in Figure 3.6 look like cross sections of Figure 3.5 at intermediate pitch angles. The effects of phase mixing are evident in the high $v_{||}$ portions of the 1.0 and 0.1 pT magnitude curves in Figure 3.6, showing a relative reduction when compared to a cross sections of the Figure 3.5 magnitude surfaces. Specifically, the slow rolloff of $B_s(\alpha_{eq}, v_{||eq})$ with high $v_{||}$ for the 0.1 pT case in Figure 3.5c has been phase mixed

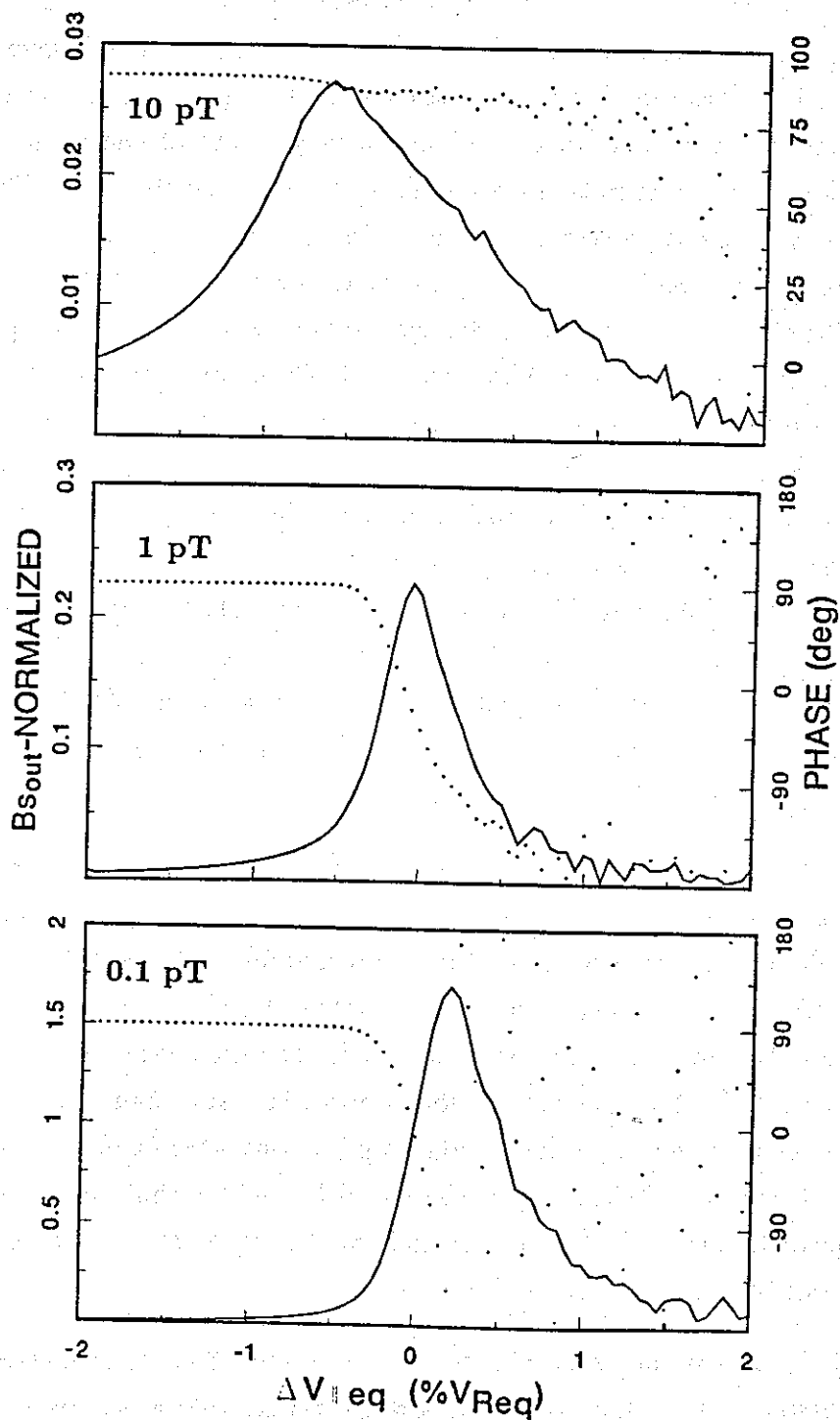


Figure 3.6. Magnitude (solid) and phase (dotted) of $B_s(v_{\parallel eq})$ for the same cases in Figure 3.5. These figures show the effect of the applied wave intensity which was 10.0, 1.0, and 0.1 pT in the top, middle, and bottom panels respectively.

away in Figure 3.6. B_{in} dependent effects visible in Figure 3.6 include a shift in v_{\parallel} of the $B_s(v_{\parallel eq})$ magnitude peak and the change in the relative significance of low v_{\parallel} radiation compared to radiation from equatorially resonant electrons. The shift of the $B_s(v_{\parallel eq})$ magnitude peak to lower v_{\parallel} 's with increasing applied wave intensity is related to the decrease in T_b with increased B_{in} . If a group of electrons become maximally bunched coincident with a minimum in the rate of change of cyclotron phase, then the current integration over z tends to be relatively large. This occurs for low B_{in} 's within the downstream conjugate interaction region, and for moderate B_{in} 's within the equatorial interaction region. However, for large B_{in} 's, the cyclotron phase within the interaction region, as defined by the adiabatic cyclotron phase, can rotate through several cycles and the bunching and debunching process repeated more than once. Thus, for large applied fields, there tends to be significant cancellation of the currents when integrated over z . Consequently, increased radiation from nonresonant electrons, combined with this 'erosion' of the radiation from resonant electrons, results in a peak in the radiation from nonresonant electrons. A feature of the phase curves which isn't apparent in Figure 3.5 is the nearly 180° phase for the high v_{\parallel} radiation in Figure 3.6. Again this suggests E_w acceleration of the electrons. Closer examination shows that most of the radiation from a single sheet of electrons cancels upon integration over z , with the 'residual' being in the attenuation direction. This is the case for both upstream and downstream interaction regions.

$B_s(\alpha_{eq})$ curves in Figure 3.7 also look, to first order, like simple cross sections near v_{Req} of the $B_s(\alpha_{eq}, v_{\parallel eq})$ surfaces in Figure 3.5, with the major contributions coming from the 45° to 65° electrons. The amplitude fluctuations versus α_{eq} for the 1.0 and 0.1 pT cases increased as a result of integration over v_{\parallel} . The phases for the low α 's are the same in these cases as it is for the homogeneous case shown in Figure 3.3. The phase is poorly defined for intermediate and high α 's in the 0.1 pT case because of conjugate interaction region coupling, but is well defined in the 1.0 pT case. While the phase of $B_s(\alpha_{eq})$ is consistent with the idea that electrons resonant near the equator dominate in the integration over v_{\parallel} , 'edge effects' associated with the high v_{\parallel} limit of the distribution play an important role.

$J(z)$ and $B_s(z)$ are shown in Figure 3.8 and Figure 3.9. It is interesting that Figure 3.6 and Figure 3.7 indicate that the v_{\parallel} and α ranges were adequate and included the sources of significant radiation. However, Figure 3.8 and Figure 3.9 both indicate that the upper $v_{\parallel eq}$ limit of 2% is not large enough. While an increase in the high v_{\parallel} limit may not significantly change $B_{s,out}$, it significantly affects the spatial structure

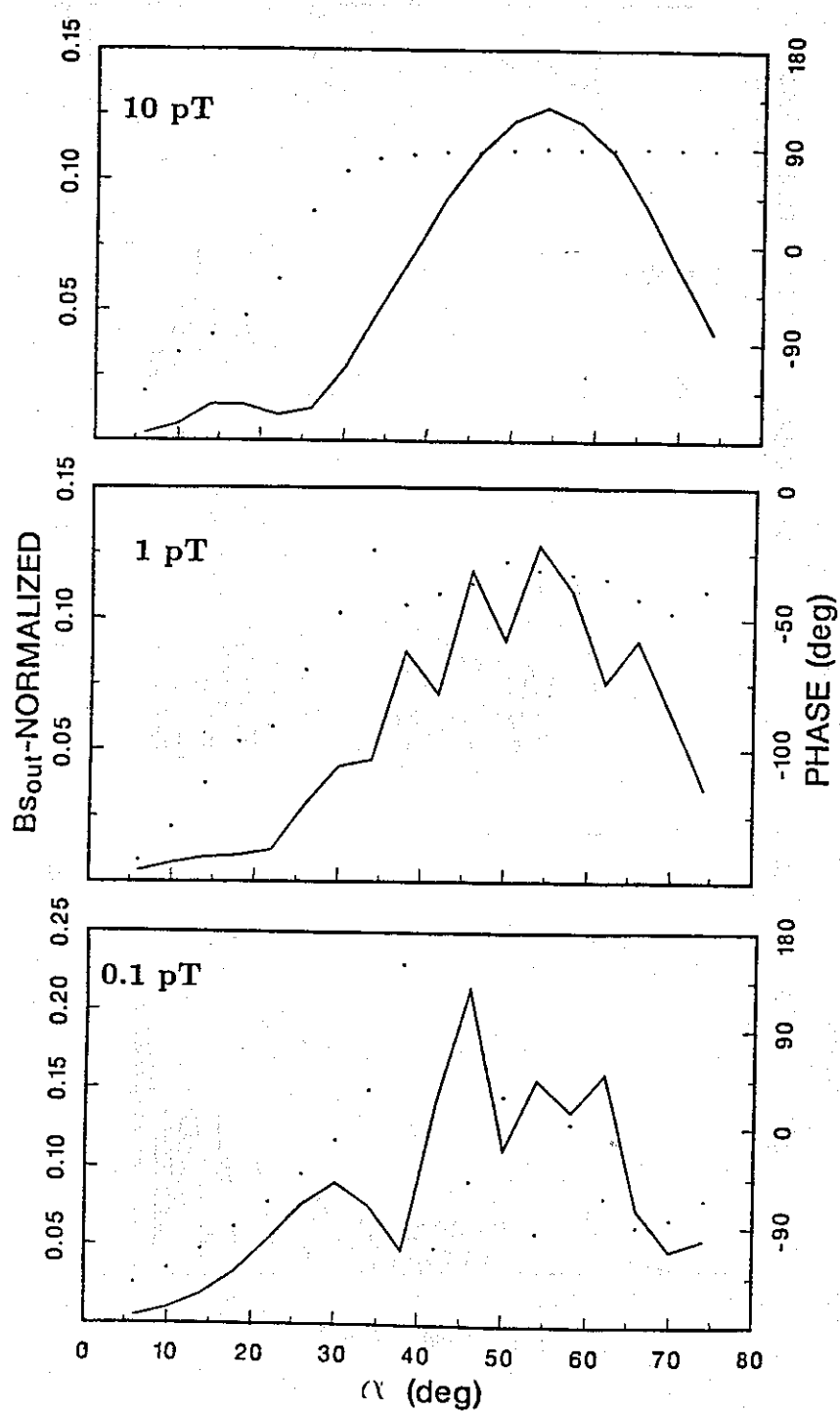


Figure 3.7. Magnitude (solid) and phase (dotted) of $B_s(\alpha_{eq})$ for the same cases in Figure 3.5 with applied wave intensities of 10.0, 1.0, and 0.1 pT in the top, middle, and bottom panels respectively.

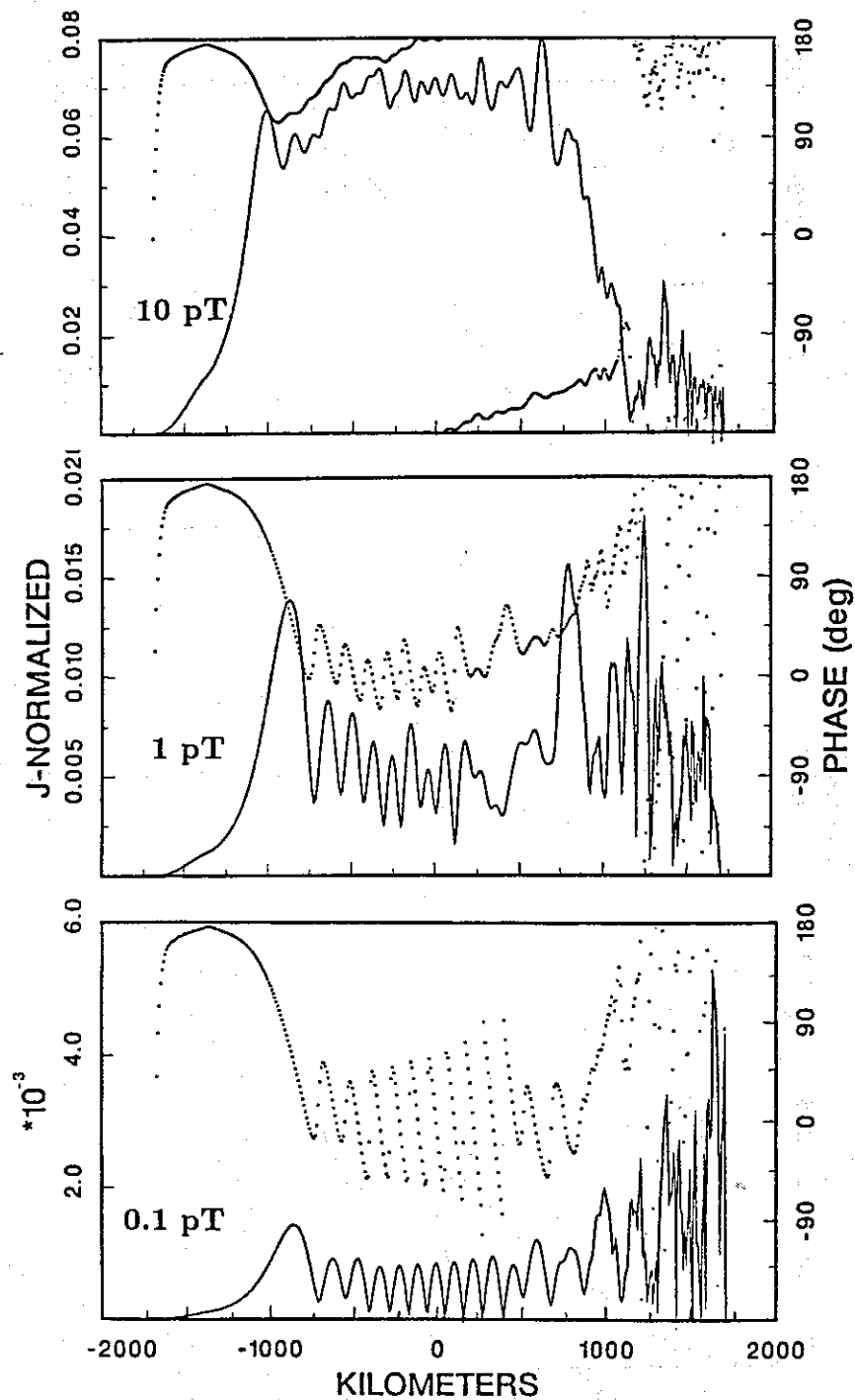


Figure 3.8. Magnitude (solid) and phase (dotted) of $J(z)$ for the same cases in Figure 3.5 with applied wave intensities of 10.0, 1.0, and 0.1 pT in the top, middle, and bottom panels respectively. The abrupt transitions around ± 1000 km result from the limited range of v_{\parallel} 's.

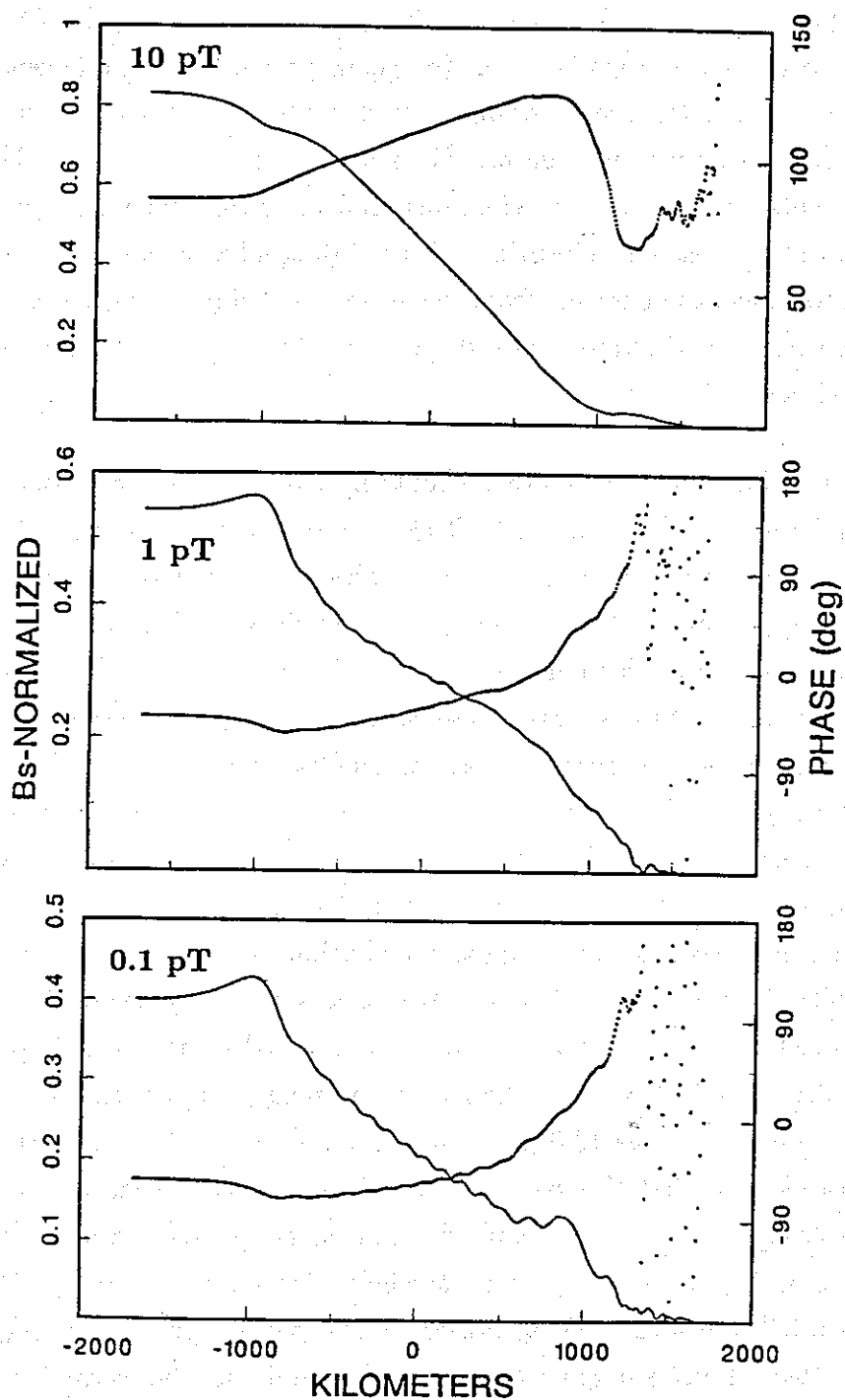


Figure 3.9. Magnitude (solid) and phase (dotted) of $B_s(z)$ for the same cases in Figure 3.5 with applied wave intensities of 10.0, 1.0, and 0.1 pT in the top, middle, and bottom panels respectively. The abrupt transitions around ± 1000 km result from the limited range of v_{\parallel} 's.

and confinement of the current and hence stimulated radiation sources. Tests indicate that an increased v_{\parallel} range tends to decrease B_{sout} magnitude and only slightly shift its phase. One reason that the high v_{\parallel} 's are significant is that while the stimulated radiation from these electrons is small, the geomagnetic field inhomogeneity makes the interaction regions for a range of high v_{\parallel} 's closer together than for a similar range of electrons resonant near the equator. The frustrating aspect of this 'edge effect' is that the currents from the high v_{\parallel} electrons tend to cancel, when integrated over v_{\parallel} and α , except at the resonance locations of the high v_{\parallel} edge where there are no higher v_{\parallel} electrons to cancel the currents from this edge. This effect can be seen as peaks in current (Figure 3.8) and stimulated radiation growth (Figure 3.9) around ± 800 km for the 1.0 pT and 0.1 pT cases.

The phase information in Figure 3.8 contains some very fundamental physics. In the equatorial region of the 0.1 and 1.0 pT cases, the current phase is oscillating about 0° with the current magnitude peaking at 0° crossings of the phase, consistent with resonant or trapped current in a homogeneous medium. This puts the stimulated radiation associated with this current at -90° . Since this radiation is in quadrature to B_{in} , it tends to retard the wave phase rather than grow the wave. However, the edge effect currents have phases in the growth quadrants, 0° to 180° . Thus the growth is coming from the edges rather than the bulk of the distribution. This is consistent with linear theory which predicts that an isotropic distribution is stable and cannot grow the wave. Linear theory requires an anisotropic source of free energy such as the loss cone, an anisotropic pitch angle distribution ($dg(\alpha)/d\alpha \neq 0$), or some other anisotropy like these v_{\parallel} edges. The fact that the edges are growing the wave while these same electrons damp the wave overall, as implied by the $\sim 180^\circ$ phase of the high v_{\parallel} portion of $B_s(v_{\parallel})$, implies significant damping over the equatorial region by these high v_{\parallel} electrons. The 10.0 pT case has a different behavior. In this case, the current phase is such that the wave is being grown on the downstream side of the equator and damped on the upstream side. This same behavior is noted in transient simulations of untrapped electrons in a wave field of comparable strength [Omura and Matsumoto, 1982]. However, the asymmetry of this current phase around the equator implies that there is neither growth nor damping and that the wave is advanced in phase. Figure 3.9 is consistent with phase advance in the 10.0 pT case and phase retardation in the 1.0 and 0.1 pT cases. It is possible that if the edge effects were absent, then the phase of B_{sout} might be exactly $+90^\circ$ or -90° for these cases, respectively.

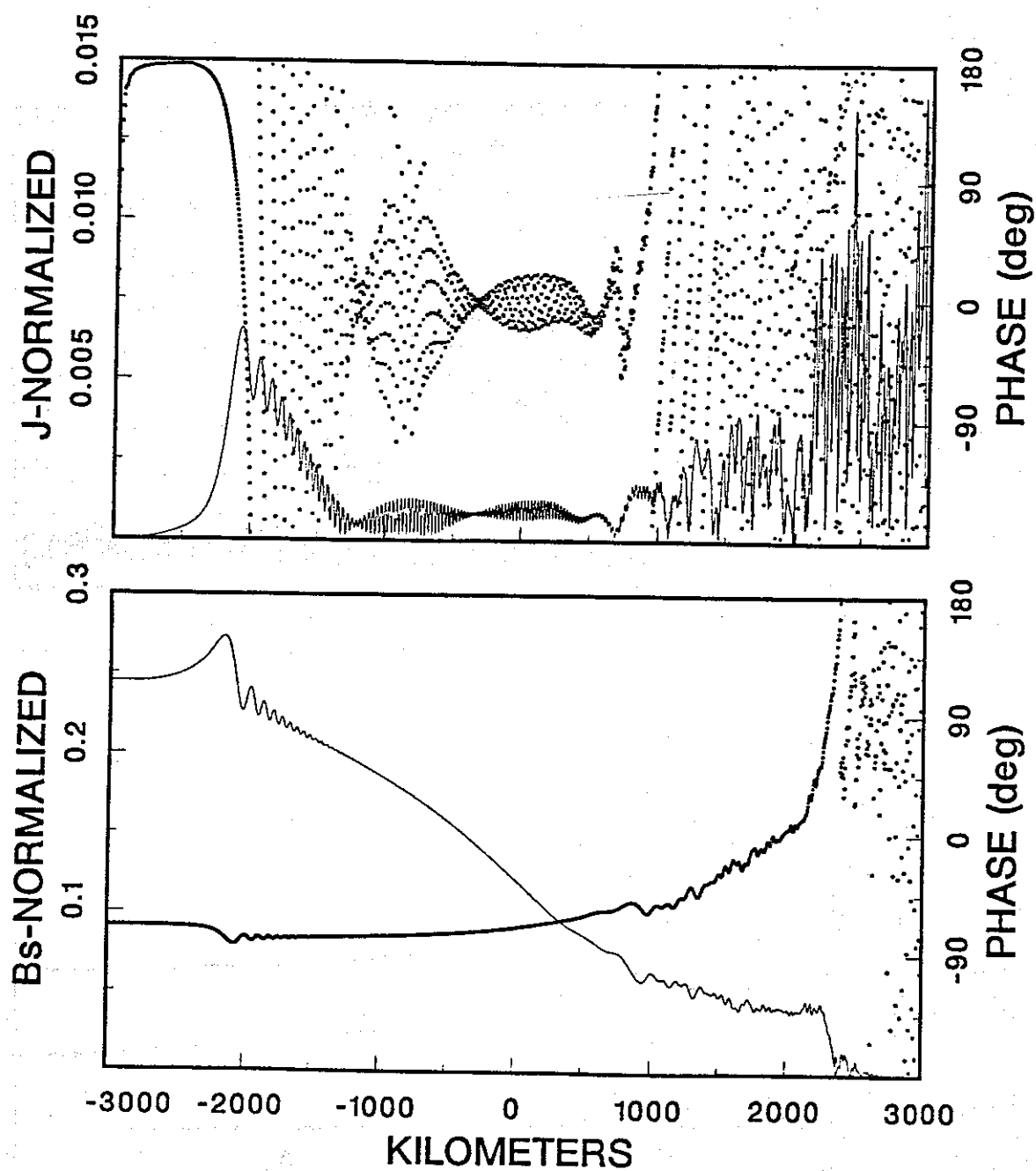


Figure 3.10. $J(z)$ and $B_s(z)$ for v_{\parallel} 's ranging from 2% below to 10% above v_{Req} with $\alpha = 45^\circ$. The edge effects associated with the upper v_{\parallel} limit are identifiable around 1000 to 2000 km off of the equator.

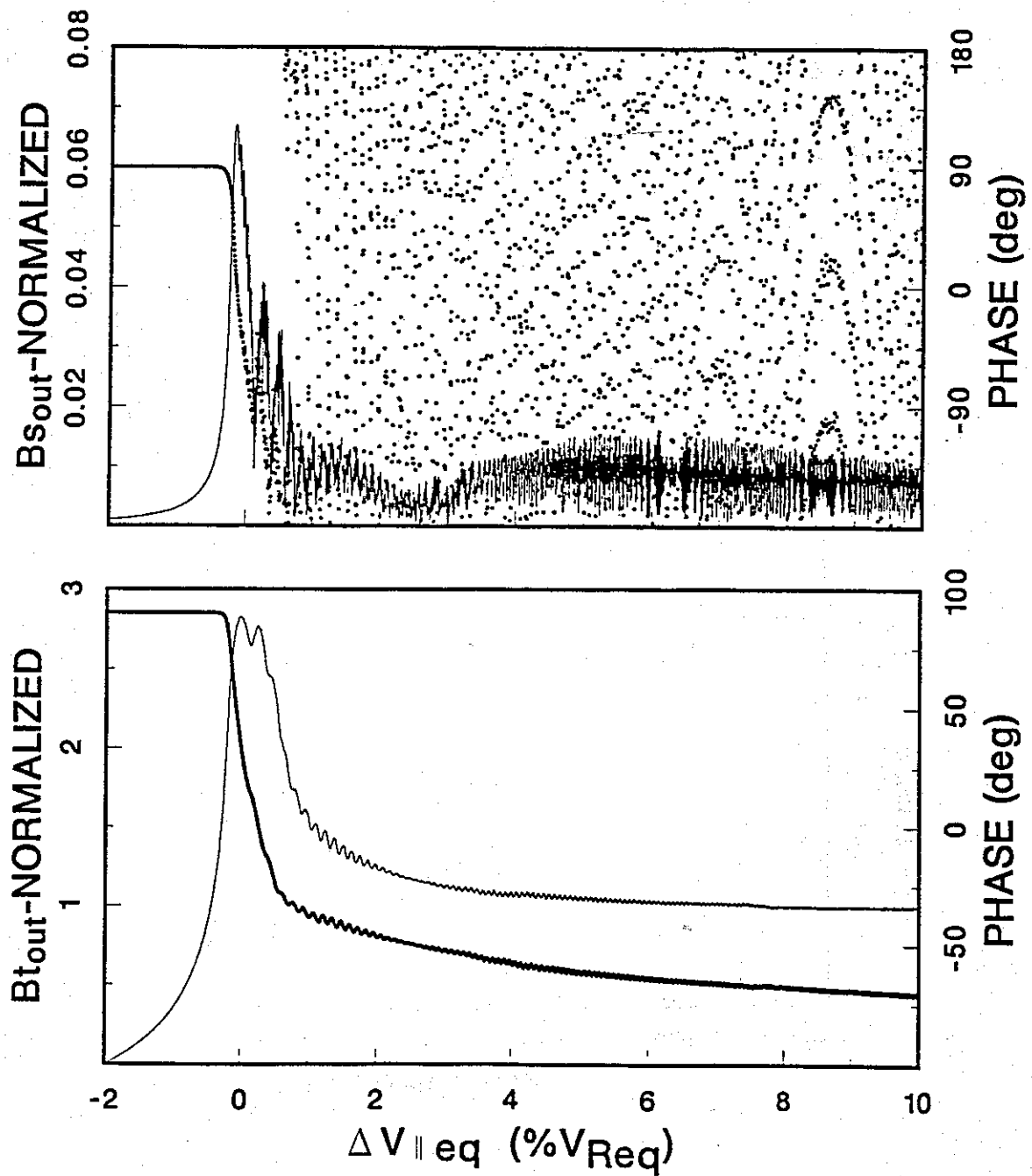


Figure 3.11. $B_s(v_{||})$ and $B_t(v_{||})$ for the same case as Figure 3.10. $B_t(v_{||})$ is the running integration of $B_s(v_{||})$ over $v_{||}$.

The $\mathbf{J}(z)$ and $\mathbf{B}_s(z)$ plots in Figure 3.10 have been specifically produced to better demonstrate 'edge' effects and represent 2401 v_{\parallel} 's ranging from 2% below to 10% above v_{Req} , spaced 0.005% apart with $\alpha_{eq} = 45^\circ$. By integrating over a higher range of v_{\parallel} 's, the edge effect positions have been moved further away from the equator. The magnitude of $\mathbf{J}(z)$ in the equatorial region is only 0.15% of the total current possible from the 2401 injected electrons. This corresponds to the maximum current which could have been generated by less than just 4 of the 2401 injected v_{\parallel} 's, demonstrating the large degree of cancellation which results from the integration over v_{\parallel} . The increase in B_s over the equatorial interaction region (-450 to 450 km) has increased to 26% of the total output B_s compared to 23% in Figure 3.9. In Figure 3.10 and in Figure 3.9, there is an inflection point in the smoothed B_s near the equator. However, $d^3 B_s/dz^3$ at the equator is positive in Figure 3.10 and negative in Figure 3.9. In other words, $|dB_s/dz|$ is a local maximum near the equator instead of a minimum as it is in the smoothed B_s curves in Figure 3.9. This is significant since the equatorial $d^3 B_s/dz^3$ for the equatorial resonant electrons is also positive and, in this case, free of edge effects. However, these results don't give any indication that the total wave growth is going to be completely confined to the equatorial region or if there would be any radiation at all if a full range of v_{\parallel} 's and α 's were included. Figure 3.11 give plots of $\mathbf{B}_s(v_{\parallel})$ and $\mathbf{B}_t(v_{\parallel})$, where $\mathbf{B}_t(v_{\parallel})$ is a running integration over v_{\parallel} given by

$$\mathbf{B}_t(v_{\parallel}) = \sum_{v_{\parallel min}}^{v_{\parallel}} \mathbf{B}_{sout}(v_{\parallel}) \quad (3.10)$$

and equals \mathbf{B}_{sout} normalized by B_{sout} at $v_{\parallel} = v_{\parallel max}$. Figure 3.11 shows several periodicities in the fine structure of $\mathbf{B}_s(v_{\parallel})$ which are resolved by the 0.005% v_{\parallel} spacing. There is evidence in the high v_{\parallel} portion of $\mathbf{B}_s(v_{\parallel})$ of undersampling v_{\parallel} however, $\mathbf{B}_t(v_{\parallel})$ indicates that the sampling is sufficient. This undersampling could be responsible for some of the oscillations in Figure 3.10 though. The contribution of the high v_{\parallel} 's can be deduced from $\mathbf{B}_t(v_{\parallel})$. Subtracting $\mathbf{B}_t(v_{\parallel} = 1.02v_{Req})$ from $\mathbf{B}_t(v_{\parallel} = 1.10v_{Req})$ gives $0.28\angle -172$ which is a small contribution and consistent with the $\sim 180^\circ$ degree phase of the high v_{\parallel} 's discussed earlier.

This study of the stimulated radiation from the equatorial region could be repeated for the upstream or downstream regions separately by starting the current integration at the equator or injecting electrons at the equator, respectively. However, the radiation characteristics are, in general, the same for the upstream and downstream regions separately as they are for the region as a whole. The only signifi-

cant differences can be attributed to the lack of conjugate interaction region coupling, or to the injection at the equator of locally resonant or nearly resonant electrons. The magnitude and phase surfaces of $\mathbf{B}_s(\alpha_{eq}, v_{||eq})$ tend to be smoother and better defined and the magnitude at high $v_{||}$'s is greatly reduced relative to the peak radiation due to the lack of conjugate region coupling.

While this section dealt with the characteristics of radiation in the steady state, its purpose is tutorial since the feedback of the stimulated radiation upon other electrons is excluded. Throughout the rest of this thesis the feedback process is included. Accordingly, $f = f_{Heq}$ is used in all of the following results in order to satisfy the negligible phase delay assumption described in Chapter 2. The rest of this chapter examines the applicability of the steady state field equations (3.2 and 3.4) to the study of wave growth.

3.2. Self consistent steady state simulation

If the energetic electron flux is large enough, then the stimulated radiation significantly alters the total wave field and feedback processes become important. The last section assumed an energetic electron flux so small, that electrons injected into the wave field with identical initial conditions but at different times, traced out identical trajectories. However, the only requirement for having an electron trajectory be independent of the time of injection is for the wave field to be in steady state. The goal of this section is to demonstrate how a signal with substantial wave growth can be in steady state.

In reality, steady state saturated signals with substantial wave growth (> 15 dB) are rarely if ever seen. Examination of wave growth on Siple signals shows that a signal which grows up to a saturated level generally triggers a rising emission or generates sidebands associated with frequency and amplitude fluctuations.

To simulate a steady state saturated field requires self consistency between the stimulated radiation and the wave field. The steady state radiation $\mathbf{B}_s(z)$, from a given distribution of energetic electrons, when added to the input wave field \mathbf{B}_{in} , must produce the same total wave field $\mathbf{B}_w(z)$. This not only outlines a self consistency check but also an iterative method for finding the steady state wave field. Starting with an initial guess for the stimulated radiation $\tilde{\mathbf{B}}_{s_0}(z)$, calculate an initial total field

$$\tilde{\mathbf{B}}_{w_0}(z) = \tilde{\mathbf{B}}_{s_0}(z) + D(z)\mathbf{B}_{in}. \quad (3.11)$$

Inject a distribution of energetic electrons into this wave field and determine the actual stimulated field $\mathbf{B}_{s0}(z)$. Use this stimulated field and the estimated stimulated field to calculate a new estimate for the stimulated field

$$\tilde{\mathbf{B}}_{s1}(z) = \delta \mathbf{B}_{s0}(z) + (1 - \delta) \tilde{\mathbf{B}}_{s0}(z), \quad (3.12)$$

where $\delta \leq 1$ determines the rate of convergence and also the stability. Thus the equation for the i th iteration is

$$\tilde{\mathbf{B}}_{wi}(z) = \tilde{\mathbf{B}}_{si}(z) + D(z) \mathbf{B}_{in}, \quad (3.13)$$

where

$$\tilde{\mathbf{B}}_{si}(z) = \delta \mathbf{B}_{si-1}(z) + (1 - \delta) \tilde{\mathbf{B}}_{si-1}(z). \quad (3.14)$$

One problem with equation (3.13) is that for a given energetic electron distribution, input wave field \mathbf{B}_{in} , and initial guess $\tilde{\mathbf{B}}_{s0}(z)$, there is no guarantee of convergence. Also, It could be the case that equation (3.13) converges to some $\mathbf{B}_w(z)$ for some set of $\tilde{\mathbf{B}}_{s0}(z)$'s, converges to a different $\mathbf{B}_w(z)$ for another set $\tilde{\mathbf{B}}_{s0}(z)$'s, and possibly does not converge at all for yet another set of $\tilde{\mathbf{B}}_{s0}(z)$'s. In other words, whether equation (3.13) converges at all, or which $\mathbf{B}_w(z)$ it converges to, could depend upon $\tilde{\mathbf{B}}_{s0}(z)$ for a given \mathbf{B}_{in} and energetic electron distribution. Given the fact that steady state saturated signals with substantial wave growth are rarely if ever seen, it is appropriate to consider the possibility of convergent solutions to equation (3.13) which would be precluded by the realistic growth history of the wave. While the theoretical aspects of uniqueness, convergence, and existence regarding self consistent steady state fields are of mathematical and physical significance, their details are beyond the scope of this thesis.

An example of self consistent steady state is given in Figure 3.12. The top panel in Figure 3.12 shows $\tilde{\mathbf{B}}_{wi}(z)$ while the bottom panel shows the next iteration $\tilde{\mathbf{B}}_{wi+1}(z)$. As a full test of self consistency, the energetic electron distribution and \mathbf{B}_{in} are held constant for the last iteration and δ is set to unity. Comparison of the top and bottom panels of Figure 3.12 show a slight increase in the magnitude and phase of the output \mathbf{B}_w which probably results from having too few iterations and a δ larger than it should be prior to this last iteration. The energetic electron distribution used is shown in Figure 3.13 and includes a full range of pitch angles and a narrow range of parallel velocities.

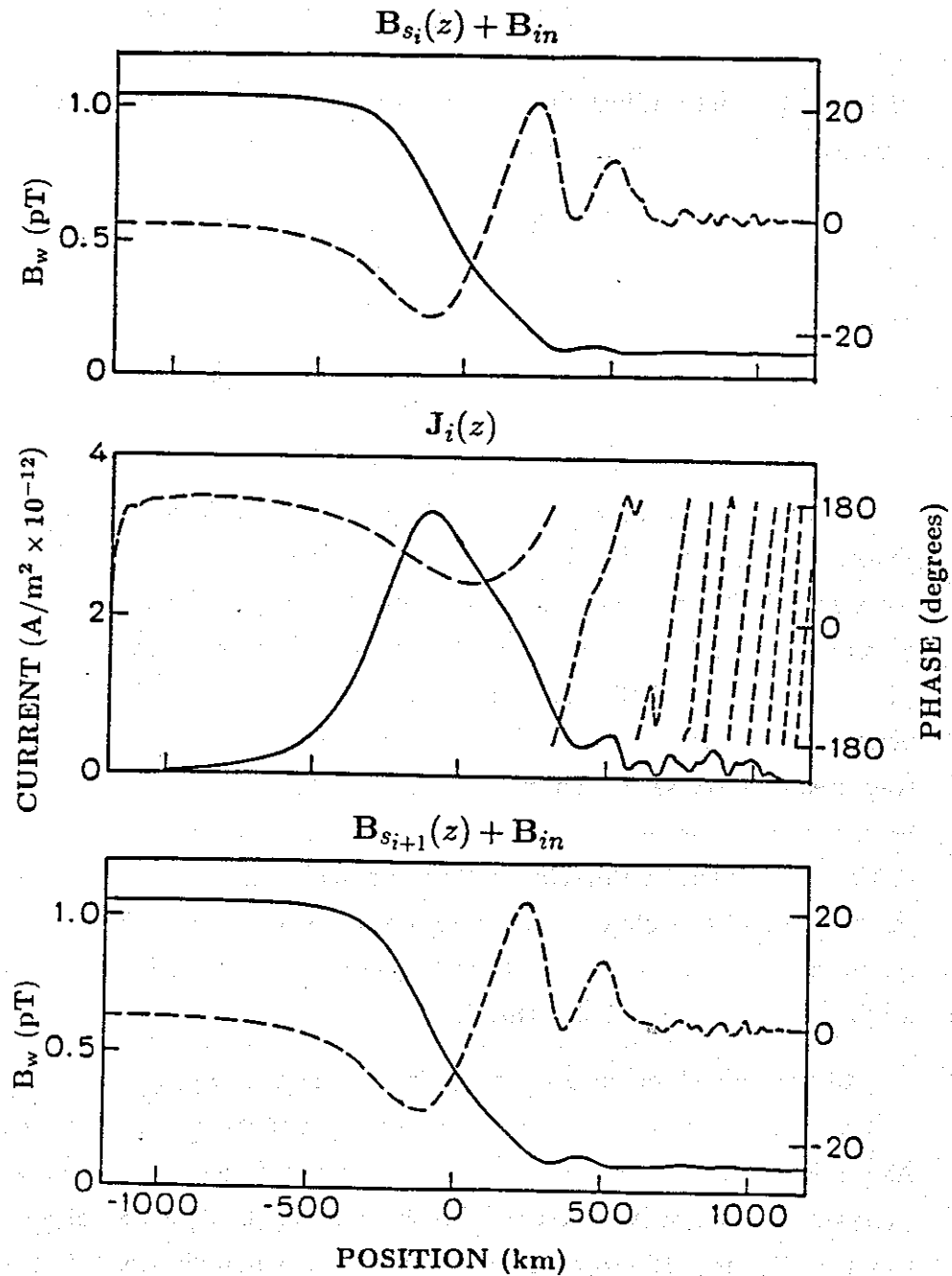


Figure 3.12. Self consistent steady state for the energetic electron distribution in Figure 3.13 and an applied wave intensity of 0.1 pT. Constraints were applied so that the total growth would be ~ 20 dB and B_s at the output would be in phase with B_{in} .

In obtaining this solution, the procedure outlined above is not strictly followed. An additional constraint is applied requiring that the total wave phase and the input wave phase both be 0° at the output. A second constraint requires a total growth of 20 dB. In order to have a steady state solution with these constraints, the center velocity of the energetic electron distribution and flux are allowed to change between iterations prior to the last iteration shown in Figure 3.12. These constraints are arbitrarily selected and, in general, the output phase and magnitude of B_w can be anything. The constraint on the output phase required that the center velocity be shifted to the low v_{\parallel} side of the equatorial resonant velocity. A more centered velocity distribution would presumably converge to a B_w with an output phase lagging B_{in} .

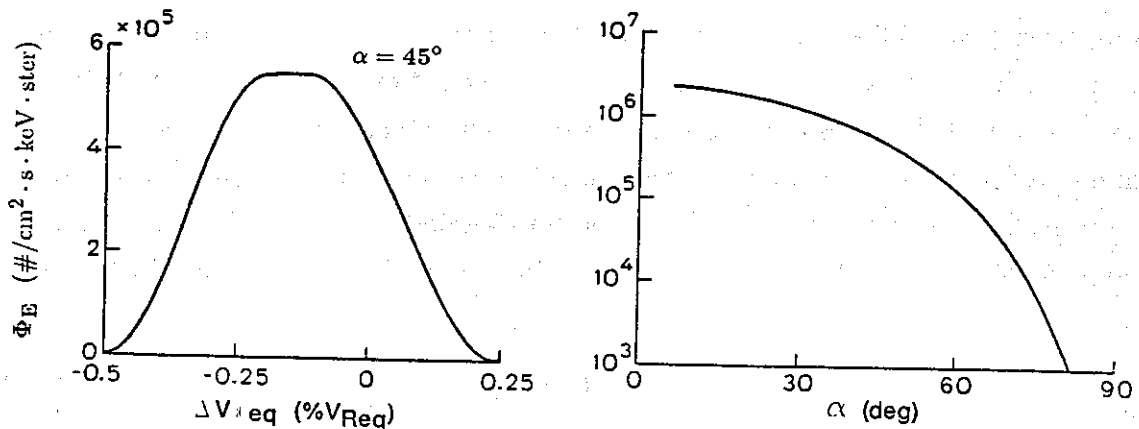


Figure 3.13. Distribution function for Figure 3.12 given in terms of the differential energy spectrum. The center v_{\parallel} is shifted with respect to v_{Req} in order to satisfy the constraint that B_s at the output should be in phase with B_{in} .

One aspect of searching for steady state solutions is that the greater the saturation level, the more unstable the iteration process tends to be, and the more difficult it is to find solutions. This is expected since as the stimulated signal gets larger, the controlling influence of the input signal gets relatively smaller.

3.3. The two port model

A model also based on the steady state radiation equation (3.5), but capable of simulating the transient aspects of wave growth was developed by *Helliwell and Inan* [1982]. Their model, known as the two-port feedback model, treats the interaction

region like an unstable feedback amplifier with a delay line. *Helliwell and Inan* [1982] applied the two-port feedback model using a single α and v_{\parallel} energetic electron distribution. In this section, the two-port feedback model is applied using a full range of α 's and v_{\parallel} 's.

In a full transient simulation of the wave growth process, electrons would continuously flow through the interaction region while launching radiation which would contribute to the total wave field and feed back on later arriving electrons. This approach is a continuous, distributed, and holistic process requiring the simultaneous calculation of electron trajectories and stimulated radiation. In the two-port model, the temporal evolution of the wave field is determined in a discrete updating of the wave field. In the general two-port feedback model, the steady state radiation from a distribution of energetic electrons is calculated in response to an applied steady state wave field. This stimulated radiation is then added to the input field to generate a new steady state wave field. The transformation of the old wave field into the new wave field is assumed to occur over a time interval T , based upon the total time it takes for electrons to cross the interaction region and the radiation from these electrons to propagate back. This process can therefore be repeated to give the time evolution of the wave field. Thus, at the i th time interval, the total wave field is given by

$$\mathbf{B}_w(z, iT) = \mathbf{B}_s(z, iT) + D(z)\mathbf{B}_{in} \quad (3.15)$$

where the stimulated radiation $\mathbf{B}_s(z, iT)$ is found by solving equation (3.4) for the energetic electrons interacting with $\mathbf{B}_w(z, (i-1)T)$. *Helliwell and Inan* [1982] made a further simplification by making \mathbf{B}_w constant over the interaction region. The total wave field at every point in space then becomes

$$\mathbf{B}_w(z, iT) = \mathbf{B}_s(z_{up}, iT) + \mathbf{B}_{in}, \quad (3.16)$$

which is just \mathbf{B}_{in} added to the stimulated radiation at the output $z = z_{up}$.

This discrete feedback model is also described by the block diagram in Figure 3.14 where

$$G = \frac{\mathbf{B}_s}{\mathbf{B}_w} \quad (3.17)$$

is the open loop gain, A represents the amplification or attenuation due to propagation effects, and T_e and T_g are the travel times across the interaction region of the electrons and wave, respectively. Since A is an unknown quantity, it is set to unity.

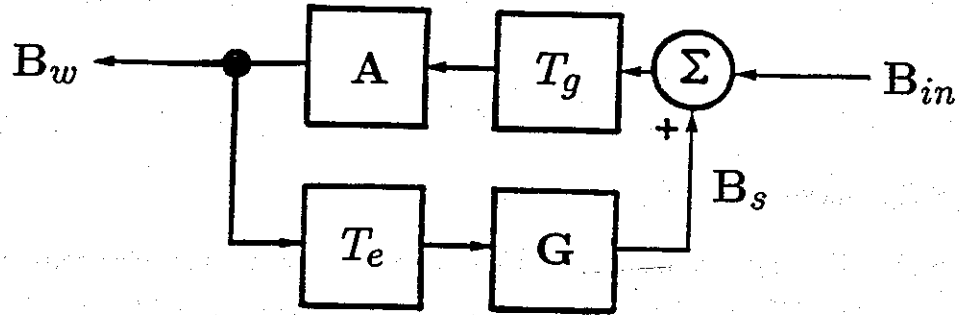


Figure 3.14. Two-port feedback model based upon the open loop gain G , propagation factor A , and electron and wave travel times T_e and T_g , respectively (from Helliwell and Inan, [1982]).

Since the bunching and radiation processes are distributed over the interaction region, T_e and T_g are taken as the travel times over one-half the interaction region or $L_p/2$. Thus

$$T_e = \int_{-L_p/4}^{L_p/4} \frac{1}{v_{\parallel}} dz, \quad (3.18)$$

and

$$T_g = \int_{-L_p/4}^{L_p/4} \frac{1}{v_g} dz, \quad (3.19)$$

and the time interval between discrete updates of B_w is

$$T = T_e + T_g. \quad (3.20)$$

The main advantage of having B_w constant over z is that G becomes a simple function of B_w , allowing G to be generated first and the feedback model applied second. After each iteration, the next value of G is just read off of a curve of $G(B_w)$ and the time evolution of B_w is calculated using the following iteration equation

$$B_{wi} = B_{si} + B_{in}, \quad (3.21)$$

where

$$B_{si} = G(B_{wi-1})A_{i-1}B_{wi-1}(\cos(\Delta\omega_{i-1}T)\hat{x} - \sin(\Delta\omega_{i-1}T)\hat{y}), \quad (3.22)$$

where \hat{x} and \hat{y} are the transverse orthogonal unit vectors in phase with \mathbf{B}_{in} and \mathbf{E}_{in} , respectively, and $\Delta\omega$ is the frequency offset of \mathbf{B}_w from \mathbf{B}_{in} . This frequency offset is given by

$$\Delta\omega_i = \frac{2(\psi_i - \psi_{i-1})}{T} - \Delta\omega_{i-1} \quad (3.23)$$

where ψ is the phase of \mathbf{B}_w relative to \mathbf{B}_{in} .

Examples of G are given in Figure 3.15 for equatorially-resonant electrons and for pitch angles of 20° , 45° , and 70° . Each of these curves is normalized by the 45° pitch angle gain magnitude at low applied fields. A v^{-6} distribution is used, which explains why the gain magnitude is greatest for the 45° case. All of the gain magnitude curves are proportional to the energetic electron flux. The gain curves can be broken into 5 distinct regions. The first region is the low B_w linear region, where doubling B_w simply doubles B_s , resulting in a constant G . The gain phase in this linear region is $\sim 0^\circ$ which is advanced ahead of the -90° phase, corresponding to the bunching of \mathbf{v}_\perp 's about $-\mathbf{B}_w$, by the inhomogeneity of the geomagnetic field. G begins to vary with B_w at the start of the nonlinear region which, within a 10 fold increase in B_w , becomes a saturation region with $\partial G / \partial B_w \simeq -1$. The gain phase shifts negatively in this transition region as T_b approaches T_r . The high B_w region is the strongly nonlinear region with a 90° gain phase and $\partial G / \partial B_w \simeq -1$, and is preceded by a transition region distinguished by a dip in gain magnitude and a transitory swing in gain phase. Saturation actually occurs when $G \simeq 1$. A gain curve like one of these, only for $\alpha = 30^\circ$, is the basis for the analysis done by *Helliwell and Inan* [1982].

The ultimate goal of any simulation is to reproduce the experimental results. From the introduction, the three key features of single frequency wave growth are exponential wave growth up to a saturated level coincident with a parabolic advance in the wave phase. The only way to get exponential growth out of the two-port model is for G to be constant and greater than 1. G is constant over the low B_w range of the gain curves. However, to get advancing phase, the gain phase must be greater than 0° which is only the case for the strongly nonlinear, high B_w region of the gain curves. Since these regions of the gain curves don't overlap, a two-port model based on the gain curves of Figure 3.15 would apparently be unable to reproduce the experimental results. The gain curve used by *Helliwell and Inan* [1982] actually had a gain phase greater than 0° . This discrepancy is possibly due to the different electron injection schemes employed. As discussed in Chapter 2, this model injects electrons having adiabatic trajectories into a tapered wave field. However, *Helliwell and Inan* began

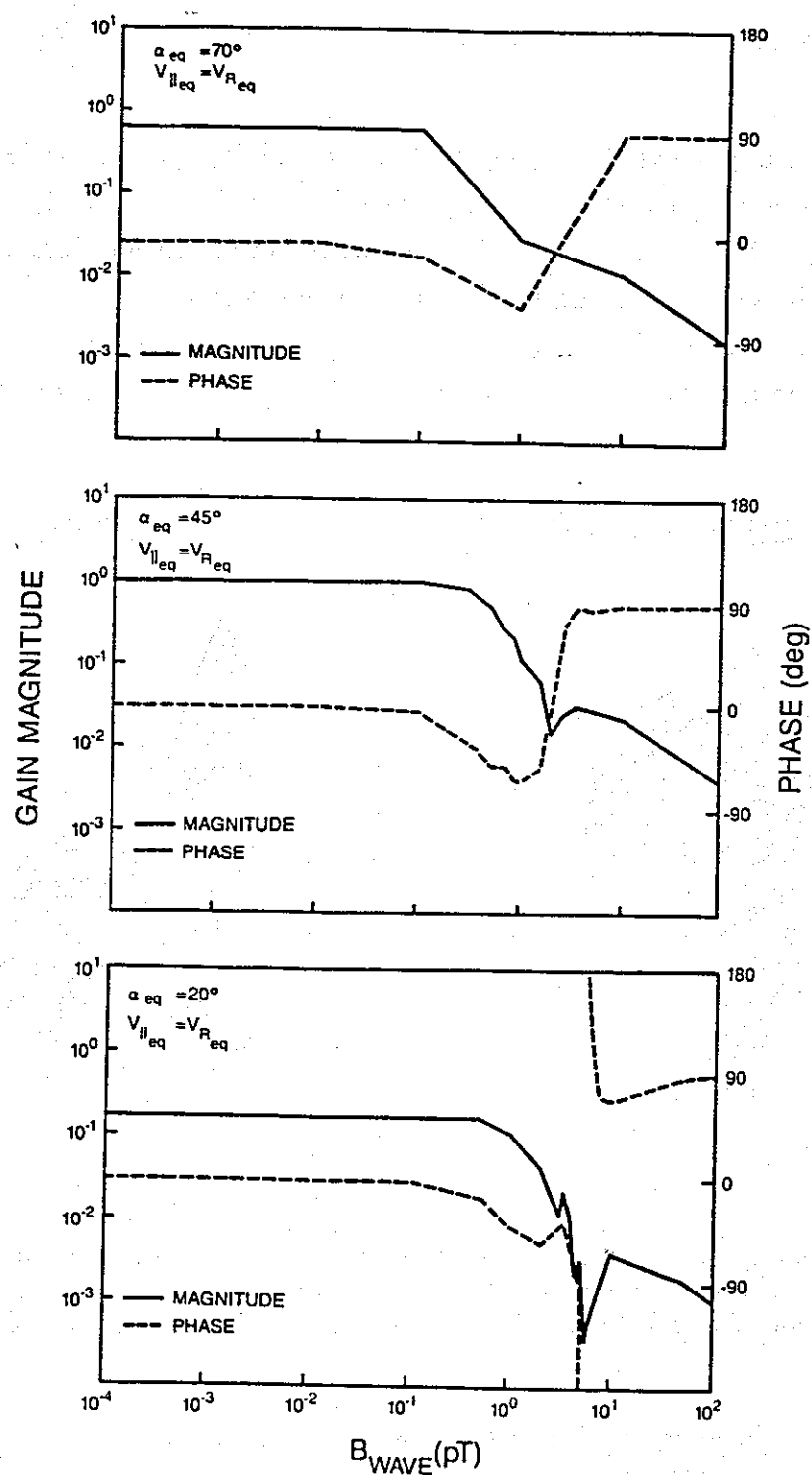


Figure 3.15. Gain magnitude (solid) and phase (dotted) curves for constant applied fields and $v_{\parallel} = v_{R_{\text{eq}}}$ at pitch angles of 70° , 45° , and 20° in the top, middle, and bottom panels, respectively. These curves show the transition from linear to nonlinear response as the applied field is increased. The gain magnitudes are normalized by the low applied field gain magnitude for 45° pitch angles (middle panel).

with the electrons in the full strength of the wave field which results in a noisy 'step response'.

Of course the plots of $B_s(\alpha_{eq}, v_{||eq})$, $B_s(\alpha_{eq})$, and $B_s(v_{||eq})$ in the first section of this chapter are also plots of $G(\alpha_{eq}, v_{||eq})$, $G(\alpha_{eq})$, and $G(v_{||eq})$. Therefore, the plots of B_s can be used to investigate the distribution requirements for obtaining a G with flat magnitude and a phase greater than 0. These figures suggest that advancing phase is associated with high B_{in} 's or low $v_{||}$'s. Figure 3.8 and Figure 3.9 also show that integration over full ranges of $v_{||}$ and α put B_s in quadrature with B_{in} .

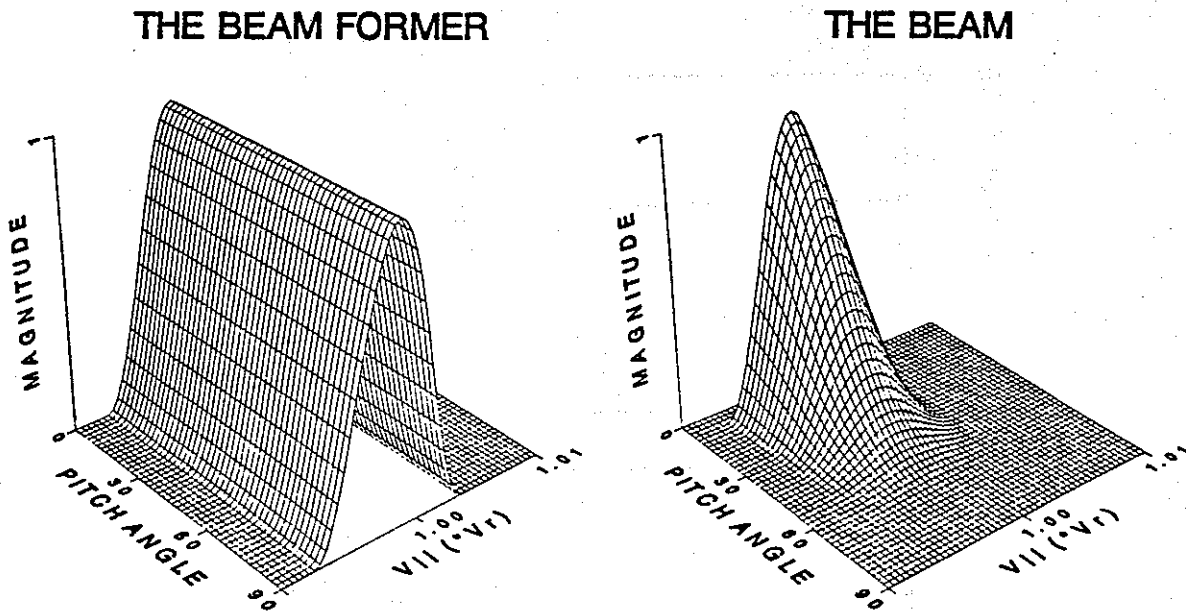


Figure 3.16. The beam (right) which results from multiplying the distribution function v^{-6} , by the beamformer (left). This beam is the distribution used for the two-port model applications. The offset in $v_{||}$ gives the desired gain phase.

In order to investigate G as a function of the energetic electron distribution, a sampling function of the form

$$h(v_{||}) = \begin{cases} 0 & \text{for } v_{||} \leq v_{||c} - \Delta v_{||}; \\ \cos^2 \left(\frac{\pi (v_{||} - v_{||c})}{2 \Delta v_{||}} \right) & \text{for } v_{||c} - \Delta v_{||} < v_{||} < v_{||c} + \Delta v_{||}; \\ 0 & \text{for } v_{||} \geq v_{||c} + \Delta v_{||}. \end{cases} \quad (3.24)$$

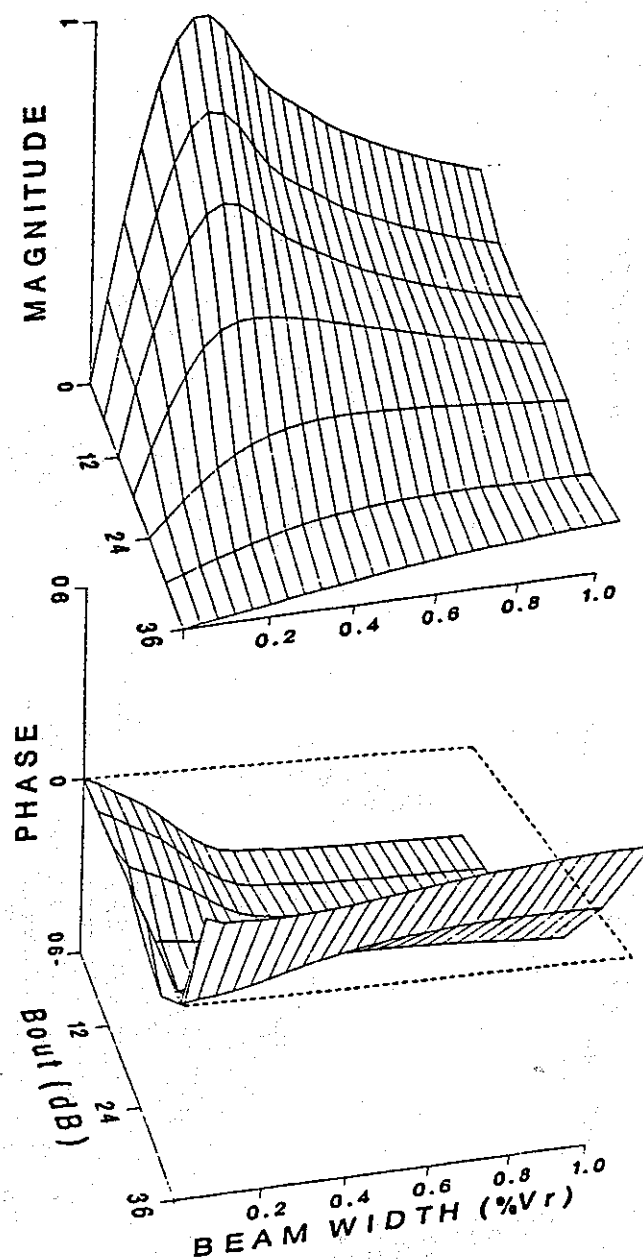


Figure 3.17. Gain versus beamwidth and applied wave intensity field for an an applied field which is tapered across the equatorial region. Since the beam was centered at v_{Req} , advancing phase only occurs at high applied fields.

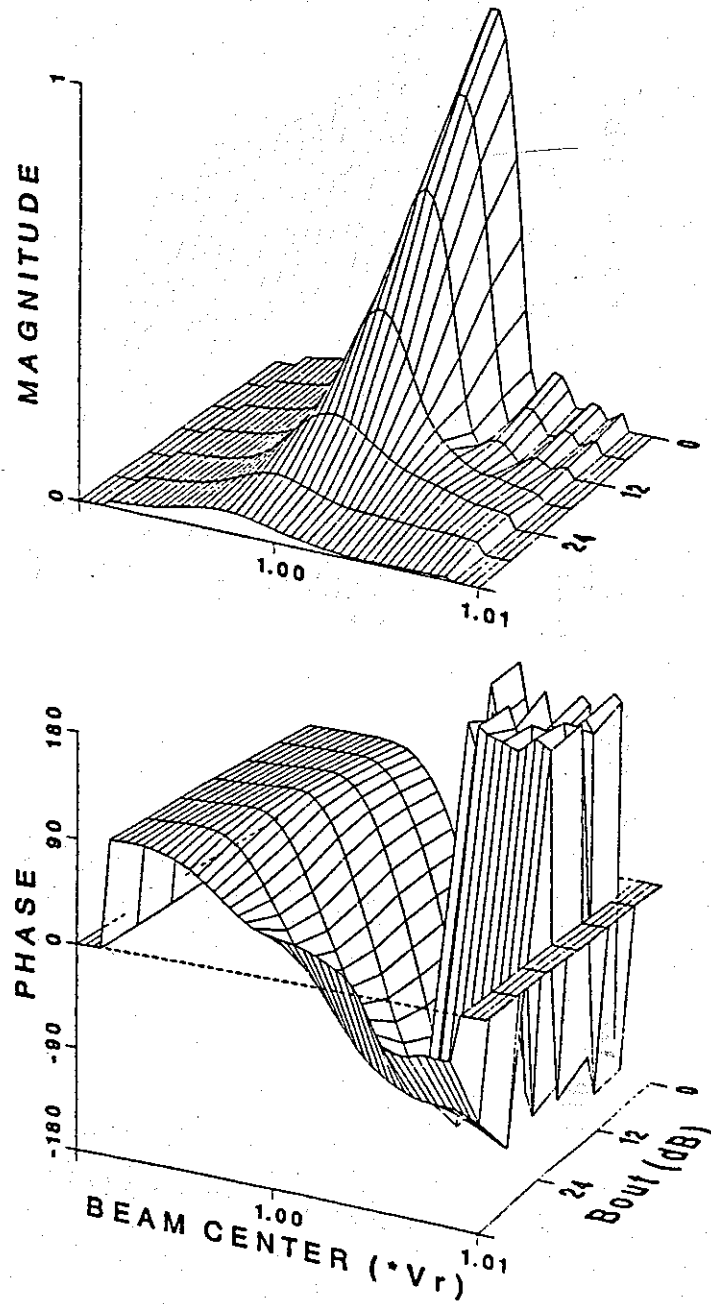


Figure 3.18. Gain versus beamcenter and applied wave intensity for an equatorially tapered applied field and a 0.2% beamwidth. Advancing phase is seen for low $v_{||}$ beamcenters.

is employed. This equation is essentially a beam former with a beam center at $v_{\parallel c}$, and a full width at half maximum beam width of Δv_{\parallel} . An example is plotted in Figure 3.16 versus $v_{\parallel eq}$ and α_{eq} for a 0.56% beam width centered 0.2% below v_{Req} . As Figure 3.16 implies, integration is performed over the full range of pitch angles. Rather than holding B_w constant over position as is done for Figure 3.15 and by *Helliwell and Inan* [1982], a more realistic B_w is used which is tapered over the equatorial interaction region using

$$B_w(z) = \begin{cases} B_s + B_{in} & \text{for } z \leq -L_p/2; \\ B_s \sin^2\left(\pi \frac{z}{L_p}\right) + B_{in} & \text{for } -L_p/2 < z < L_p/2; \\ B_{in} & \text{for } z \geq L_p/2. \end{cases} \quad (3.25)$$

As this equation implies, the wave phase is still constant and aligned with B_{in} . Figure 3.17 plots the gain versus B_w and Δv_{\parallel} , with B_w ranging from 0.05 pT to 3.2 pT, and $v_{\parallel c} = v_{Req}$. As expected, Figure 3.17 shows that an equatorially centered beam does not produce the required phase advance. Figure 3.18 plots the gain versus B_w and $v_{\parallel c}$ for $\Delta v_{\parallel} = 0.2\%$. Aside from the noisy phase structure of the high v_{\parallel} 's, the advancing phase region is restricted to the high B_w portion of the gain surfaces or to beams centered below v_{Req} . However, comparison of Figure 3.15 with Figure 3.17 or Figure 3.18 shows that by tapering B_s over the equatorial interaction region, the gain magnitude versus B_w is no longer constant even for low B_w . Thus, a purely exponential growth is not possible from these gain curves.

Beam parameters which come close to satisfying the criteria for reproduction of the experimental results are $\Delta v_{\parallel} = 0.56\%$ and $v_{\parallel c} = -0.2\%$. These are the same beamformer parameters used in Figure 3.16, and produce the $G(B_w)$ given in Figure 3.19. The energetic electron flux is set so that the initial gain magnitude is 1.25 for $B_{in} = 0.05$ pT. Figure 3.20 shows the wave growth properties for this case. B_w magnitude grows to a saturation level of ~ 13 dB at a rate of ~ 50 dB/sec. Even though initially $G > 1$, this is a case of quasistable growth since the initial phase and frequency variations die down and a steady state is reached. For an initial $G < 1$, stable amplification results [*Helliwell and Inan*, 1982]. Increasing the initial flux to $G = 2$, results in the unstable growth shown in Figure 3.21. In this case B_w grows to a saturated level of ~ 20 dB at an average growth rate of ~ 70 dB/sec. Also, in this unstable case, the wave phase advances continuously resulting in a near linear increase in the wave frequency with time.

While the unstable wave growth generated by the two port feedback model crudely

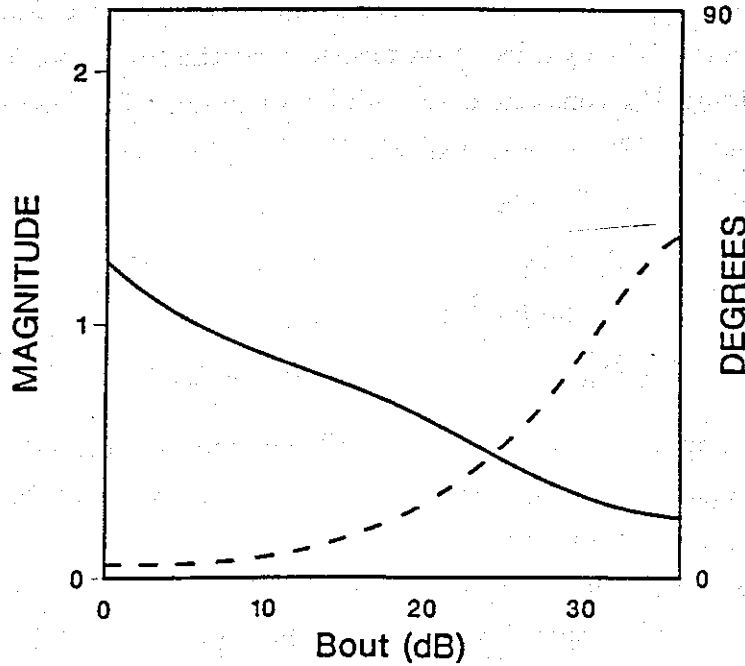


Figure 3.19. Gain magnitude (solid) and phase (dotted) curves for the beam-former in Figure 3.16. This gain curve was used for the stable growth case in Figure 3.20. Increasing the energetic electron flux so that the initial gain magnitude is $G = 2$, gives the gain curve used for the unstable case in Figure 3.21.

reproduced the experimental observations, these results are only possible using a specially selected 'beam' of energetic electrons. Results similar to those of Figure 3.21 could be obtained for a 'step' beam former which would include all electrons with $v_{\parallel \text{eq}} < 1.002v_{R\text{eq}}$ while excluding all electrons above this $v_{\parallel \text{eq}}$. Also, the constant spatial phase approximation, equivalent to setting $d\psi/dt = 0$, restricts the ability of the geomagnetic inhomogeneity to establish an advancing phase in the feedback process.

Repeating the two-port calculations with a highly anisotropic pitch angle distribution $g(\alpha) = 0.2\sin^{0.2}\alpha + 0.8\sin^{12}\alpha$, produced similar results. It could be that growth resulting from pitch angle anisotropies, might be dwarfed by the growth from the v_{\parallel} edges. In other words, a broader range of v_{\parallel} 's might have to be included in order to achieve the degree of cancellation necessary for the pitch angle anisotropies to dominate.

In the next chapter, a transient model is developed and applied to the wave growth

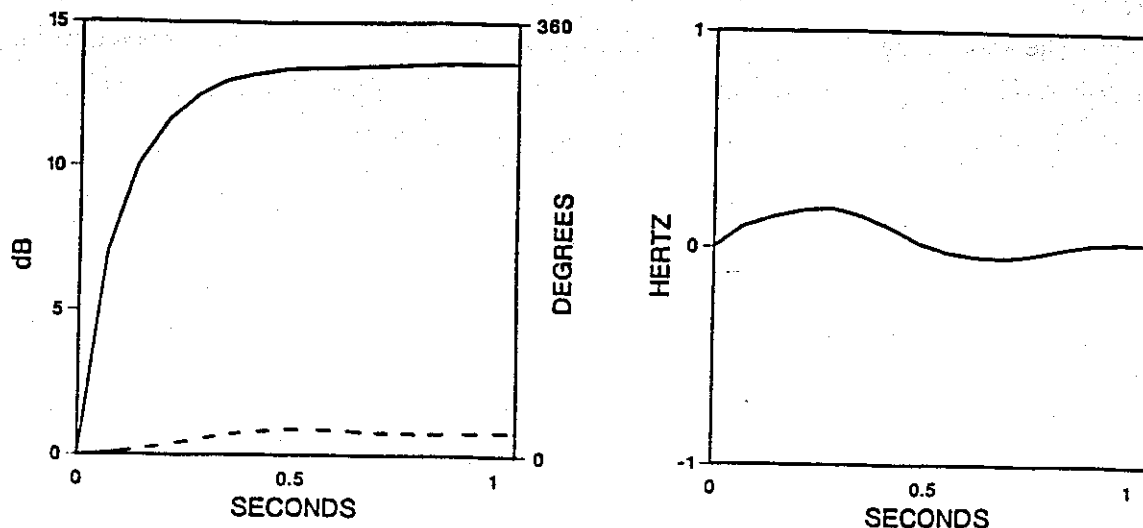


Figure 3.20. Low gain application of the two-port model using the gain curve in Figure 3.19. Output shows ~ 12 dB of growth, ~ 50 dB/s growth rate, a phase offset, and damped frequency oscillations.

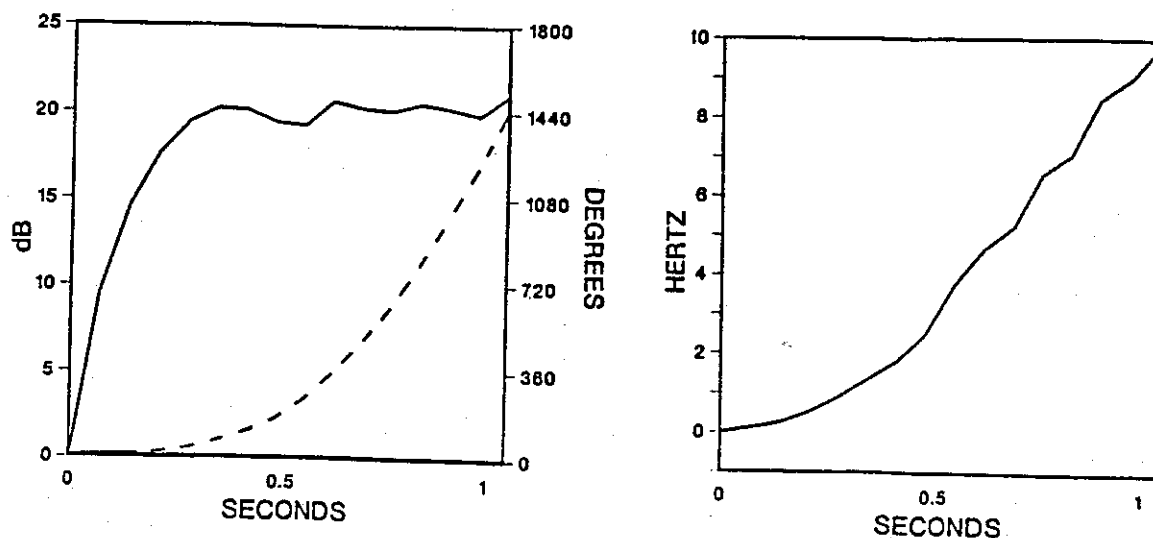


Figure 3.21. High gain application of the two-port model using the gain curve in Figure 3.19 scaled to an initial gain magnitude of $G = 2$. Output shows ~ 20 dB of growth, ~ 70 dB/s growth rate, continuously advancing phase, and a linearly increasing frequency.

problem. It is shown that the transient aspects of the wave front propagating across the equatorial interaction region establish a spatial wave structure which essentially selects the advancing phase portion of the v_{\parallel} distribution. The original motivation for the transient model development was to try to answer some of the questions raised by the apparent inadequacies of the two-port model results.

Chapter 4. Transient model and simulations

In contrast to the steady state models developed in the last chapter, this chapter deals with the development and application of a transient wave-particle interaction model. In a transient model, the complete space-time evolution of the waves and electrons are simulated with a temporal resolution much finer than the $T_e + T_g$ resolution limit of the steady state models. The specific goal of this transient model is to simulate the first half second or less of a single frequency whistler mode wave pulse as it propagates across and out of the equatorial region. The model is able to reproduce exponential wave growth, saturation, and linearly increasing frequency with time.

4.1. The transient model

In a transient model, an attempt is made to make the feedback process more nearly a continuous process. Where the steady state model is described as a two-port process, a transient model can be described as an n -port process with the output of one amplifier connected to the input of the next. This idea of a continuous feedback process is demonstrated in Figure 4.1 which shows how the radiation from the currents in each small slab of space adds to the local wave field and propagates into the previous slab while the electrons move forward to the next slab.

The transient model developed here incorporates ideas from both steady state and particle-in-cell models. The space-time relationships of the basic model are summarized in Figure 4.2. Wave-particle interactions are confined to a region in space between the upstream and downstream boundaries z_{up} and z_{down} , respectively. The wave enters the region at the downstream boundary and exits at the upstream boundary. As the leading edge of the wave propagates across the region, electrons are injected into the leading edge. However, after the leading edge crosses the upstream boundary, electrons are injected at the upstream boundary. In order to avoid 'step responses' caused by injecting electrons at the boundary, an upstream boundary taper is applied to the wave field, essentially the same as the front end taper used in the steady state cases. A similar spatial taper is applied to the phase bunched currents near the downstream boundary in order to reduce the phase noise in the stimulated radiation near this boundary. This phase noise, without the downstream current ta-

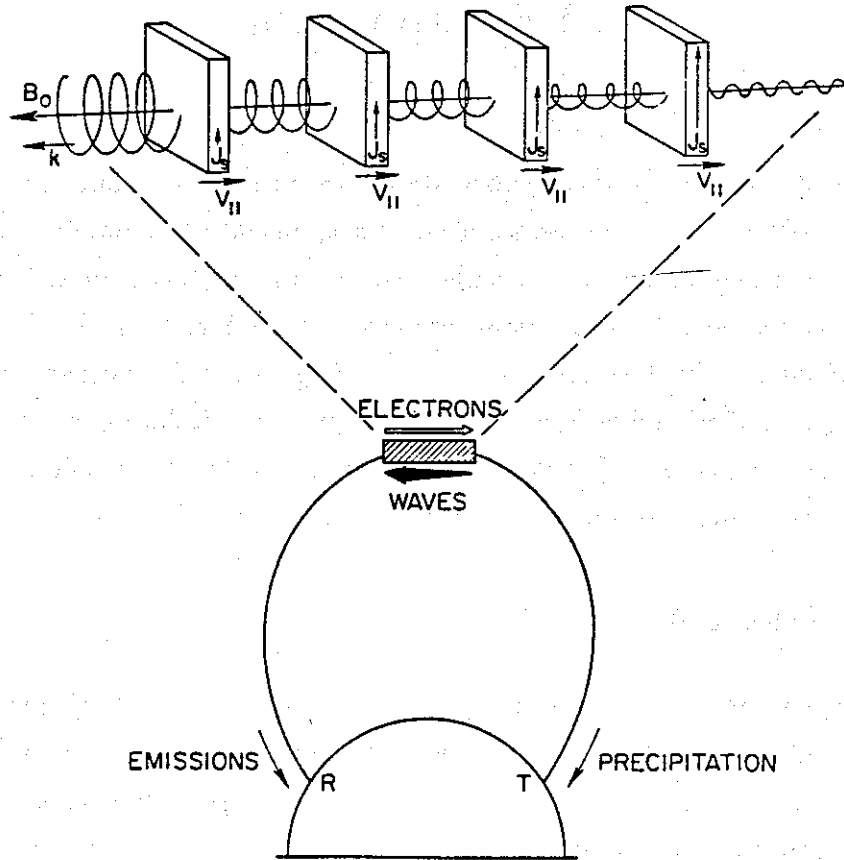


Figure 4.1. Sketch showing the wave growth model as a continuous feedback process (from *Helliwell and Crystal*, [1973]). The radiation from the currents in each small slab of space adds to the local wave field and propagates into the previous slab while the electrons move forward to the next slab.

per, can excite numerical instabilities which propagate through the region, destroying the coherent wave growth. These tapers are depicted as weighting factors at the top of Figure 4.2.

Before explaining how the wave is updated, some general relations need to be developed. First, this model assumes that the relative phase delay of stimulated components is negligible $d\xi_{ref}/d\omega \simeq 0$, and that all energy propagates at the group velocity of the reference wave $v_g(\omega, z) \simeq v_g(\omega_{ref}, z)$. With these approximations, stimulated radiation can simply be added to the applied wave and then propagated without incurring a phase shift. For the idealized wave pulse in the absence of wave growth, if a fixed duration wave pulse is transmitted then an observer at any point

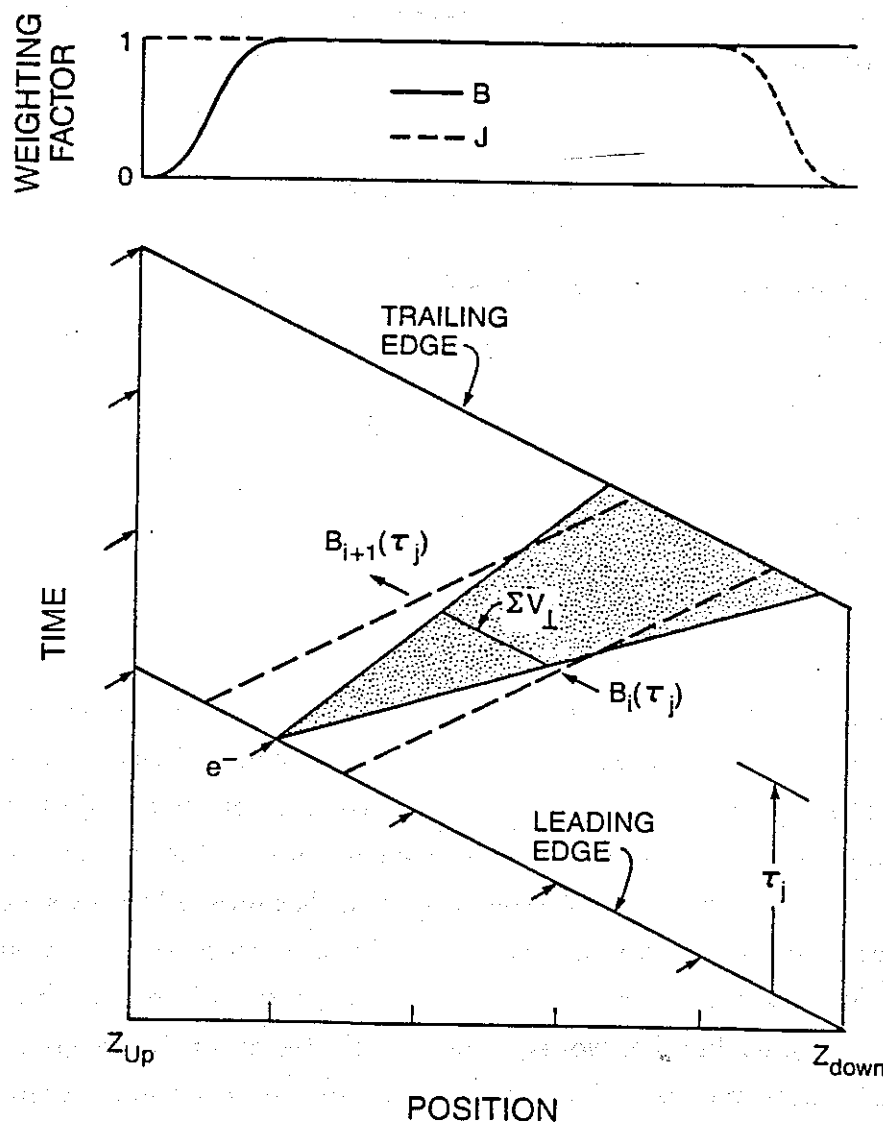


Figure 4.2. Summary sketch of the space-time relationships of the transient model. The wave enters at the downstream boundary z_{down} , and exits at the upstream boundary z_{up} . Electrons are injected into the wave at the leading edge and at the upstream boundary. An upstream boundary taper is applied to the wave field and a downstream taper is applied to the phase bunched currents as indicated by the weighting factors (top). The current is calculated by summing the v_\perp 's at equally spaced τ 's even though these electrons are at different points in space and time. The radiation from these currents propagates forward and is seen by the next set of injected electrons.

along the field line would measure a pulse of the same duration. Thus wave energy τ -seconds into the pulse relative to the leading edge is always τ -seconds into the pulse. Similarly, radiation added to the wave τ -seconds into the pulse remains at τ -seconds into the pulse as the wave propagates. Thus for electrons injected into the leading edge of the wave at position z_0 , and presently at position z , the instantaneous τ measured from the leading edge is

$$\tau(z) = \int_{z_0}^z \left(\frac{1}{v_{\parallel}} + \frac{1}{v_g} \right) dz. \quad (4.1)$$

The time at which the leading edge of the wave is at z is

$$t_{le}(z) = \int_{z_{\text{down}}}^z \frac{dz}{v_g}. \quad (4.2)$$

Therefore, the time at which the electron is at position z is simply

$$t(z) = \tau(z) + t_{le}(z). \quad (4.3)$$

With these approximations, and certain simplifications regarding current and feedback calculations, a first order transient model can be implemented. When dealing with the feedback, it is assumed that all radiation from electrons injected into the wave at earlier times feeds back on all subsequently injected electrons. Conversely, electrons will not see any of the radiation from electrons injected at the same time or at later times. This is not a trivial assumption since, for electrons with a wide range of v_{\parallel} 's and α 's, some trajectories will cross the trajectories of electrons injected at a slightly different time. In other words, electrons injected at a point in space and time fan out in the space-time plane due to their initial spread in v_{\parallel} and α . Even electrons injected with the same v_{\parallel} and α fan out due to the cyclotron phase dependent wave forces.

Calculating the current and stimulated radiation requires the integration over \mathbf{v}_{\perp} within each spatial cell at each instant. However, in this transient model, as is the case in the steady state calculations, electrons are advanced in space rather than time. Due to the fan out, electrons injected at the same point in space and time arrive at some downstream point in space with a range of times. One way to get the electron distribution at a point in space and time is to look at the trajectories of two set of

electrons with the same unperturbed distributions, but with two different injection points, and interpolate. This technique was actually employed but only to verify the accuracy of a simpler approach. This other simpler approach determines the electron velocities at equally spaced τ 's, for all electrons injected at the same point in space and time, by interpolating along each electrons' trajectory. The current is then calculated by summing the \mathbf{v}_\perp 's at each τ even though these electrons are at different points in space and time. Electrons entering the wave at some injection point are taken to represent all of the electrons which would have entered the wave since the previous injection. Determining the stimulated radiation requires that the current from electrons with identical $v_{\parallel \text{eq}}$'s and α_{eq} 's be scaled by the spatial separation from its previously injected counterpart. Thus, the stimulated radiation versus τ from the electrons entering the wave at the i th injection point is

$$\mathbf{B}_{si}(\tau) = \frac{q\mu_0}{2} \int_{\phi} \int_{\alpha} \int_v [\mathbf{v}_{\perp i}(\tau) \times \mathbf{n}] v_{\parallel i}(\tau) \Delta t_i f(v, \alpha) v^2 \sin \alpha dv d\alpha d\phi \quad (\text{T}) \quad (4.4)$$

where $v_{\parallel i}(\tau) \Delta t_i$ and Δt_i are the spatial and temporal separations, respectively, of an injected electron from its previously injected counterpart. When the electrons are injected into the leading edge

$$\Delta t_i = n \Delta z_i \left(\frac{1}{v_{\parallel}(z_i)} + \frac{1}{v_g(z_i)} \right) \quad (4.5)$$

where, at the i th injection point, z_i is the position, Δz_i is the distance per macro-step, and n is the number of macro-steps per injection point. However, when the electrons are injected at the upstream boundary

$$\Delta t = 2n \Delta z \frac{1}{v_g} \quad (4.6)$$

since the leading edge is advanced twice as many macro-steps per injection point in order to keep the Δt about the same in both cases.

Rather than calculating all of the trajectories at the same time, a single electron is injected into the wave at the i th injection point. Once the trajectory is calculated over the desired range (usually up to the trailing edge), the unmodified wave is 'backed up' and the next electron trajectory is calculated. Then, when all of the electron trajectories are calculated, $\mathbf{B}_{si}(\tau)$ is computed and added to the applied wave, giving the applied wave to be used at $(i+1)$ th injection point

$$\mathbf{B}_{wi+1}(\tau) = \mathbf{B}_{wi}(\tau) + \mathbf{B}_{si}(\tau). \quad (4.7)$$

The electron injection and wave field calculation schemes are schematically included in Figure 4.2.

A major detail of the model which has not yet been discussed is the energetic electron distribution function. In the previous chapter, the problems associated with the edges of the v_{\parallel} distribution were analyzed. Care must be taken to keep these edge effects from adversely affecting the transient simulations. If there are significant wave-particle interactions occurring with these 'edge' electrons, then the radiation from these electrons will dominate the wave growth process. One option is to make the v_{\parallel} range so broad that the edge contributions become insignificant. To understand the implications of this option, consider the simulation of a 0.25 s wave pulse propagating across a 3000 km region, using a full range of pitch angles and assuming that a 10% range of v_{\parallel} 's to be adequate. Estimates predict that this simulation would consume on the order of 100 days of VAX/780 CPU time. The same problem, vectorized, would take on the order of 1 CRAY-1 CPU day. While more powerful computers exist than these, and less ambitious problems could be attacked, this approach is not recommended, especially during the trial and error phase of developing and exploring this transient model. Using a single injection v_{\parallel} and a full range of pitch angles with a 0.5 s wave pulse propagating through a 3400 km region requires on the order of 10 VAX/780 CPU hours. This latter approach is taken for all but one of the cases in this chapter. In fact, an agreement between the experimental results and the simulation results help justify the use of a relatively narrow v_{\parallel} range.

The generalized form of the distribution function used throughout this chapter is

$$f(v, \alpha_{eq}) = Av^{-8} \delta(v_{\parallel eq} - v_{\parallel i}) \quad (4.8)$$

where $v_{\parallel i}$ selects the parallel velocity depending on the pitch angle and the injection position and time, z_i and t_i respectively. With this selection function, the resonance location relative to the wave front, can be controlled. An example of $v_{\parallel i}$, for a single injected pitch angle, is given as the solid line in Figure 4.3. This figure shows the range of parallel velocities (shaded) resonant with the wave at any given instant of time. The injection v_{\parallel} is selected, in this case, to be resonant with the wave after moving through the wave field for some fixed distance as the leading edge propagates toward the equator. After the leading edge crosses the point z_{drift} , the electrons are injected so as to supply a fixed interaction region within which the wave frequency is changing at a constant rate. More specifically, the parallel velocity at the i th injection

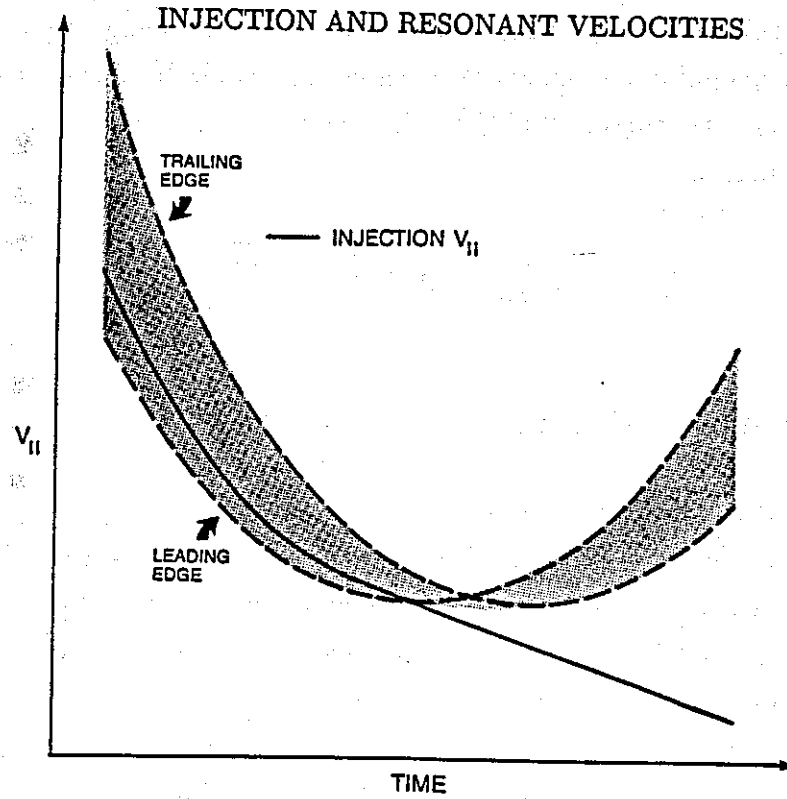


Figure 4.3. Range of parallel velocities (shaded) resonant with the wave at any give instant of time. The injection $v_{||}$ is selected, in this case, to be resonant with the wave after moving through the wave field for some fixed distance as the leading edge propagates toward the equator. After the leading edge has crossed some position, the injection $v_{||eq}$ shifts linearly with time in order to stay in resonance with a fixed interaction region within which the wave frequency is changing at a constant rate.

point is

$$v_{||i} = \begin{cases} v_R(z_i + z_{shift}) \frac{\cos(\alpha(z_i))}{\cos(\alpha(z_i + z_{shift}))} & \text{for } z_i \geq z_{drift}; \\ (v_R(z_{drift} + z_{shift}) - (i - i_{drift})\Delta v_{||}) \frac{\cos(\alpha(z_i))}{\cos(\alpha(z_{drift} + z_{shift}))} & \text{for } z_i < z_{drift}; \end{cases} \quad (4.9)$$

where z_{shift} specifies the resonance location relative to the injection point, the cosine ratio adiabatically translates the resonant velocity to the injection parallel velocity, and $\Delta v_{||}$ is the shift in equatorial $v_{||}$ per injection point approximated by

$$\Delta v_{||} = n\Delta z_{eq} \left(\frac{1}{v_{geq}} + \frac{1}{v_{Req}} \right) \frac{2\pi}{k_{eq}} \left(1 + \frac{f_{Heq}}{2f} \right) \frac{df}{dt}. \quad (4.10)$$

Δv_{\parallel} is the shift in parallel velocity required for the injected electrons to stay in resonance with a wave whose frequency changes at the rate df/dt . Equation (4.10) is calculated by setting $v_{\parallel} = v_{Req}$, using equatorial values, and using the applied wave frequency and wave number. In an exact solution, Δv_{\parallel} would be slowly changing. To help assure a smooth $v_{\parallel i}$ curve, all of the following results determine z_{drift} using the following approximation

$$\left(\frac{1}{z_{drift} + z_{shift}} \right) \frac{df}{dt} \simeq 1 \left(\frac{\text{Hz/s}}{\text{km}} \right). \quad (4.11)$$

4.2. Transient simulations

The transient model is now tested using input parameters consistent with experimental observations. The energetic electron flux is set to give a total growth of ~ 38 dB and growth rate ~ 150 dB/sec. These values of growth and growth rate are slightly larger than what is usually observed; however, since saturation occurs within a shorter period of time, shorter wave pulses can be used resulting in reduced CPU time. Also, the growth tends to be more exponential and the amplitude fluctuations reduced, as the growth rate is increased. The actual input parameters used are given in Table 4.1.

As a check, the model was tested by reproducing some of the results published by *Helliwell and Crystal* [1973] for a homogeneous static magnetic field. However, all of the results presented here include the inhomogeneity of the dipole magnetic field. Also, it is interesting to note that the results of *Helliwell and Crystal* were obtained using a 16-port model. Their concept of a port, although not exactly equivalent, is analogous to the number of macrosteps used in this model which, for most of the results presented here, is 200-300 steps. This larger number of spatial steps is required to faithfully reproduce the wave evolution when the inhomogeneity is included.

One graphical technique for presenting the results is to plot a quantity as a surface in space and time. An example is given in Figure 4.4 for the magnitude and phase of the wave pulse whose parameters are given in Table 4.1 except for the absence of energetic electrons. The plot shows the leading and trailing edges propagating through space with increasing time. The leading edge is slightly shaped in order to approximate an actual pulse and to reduce the step response of injected electrons. In contrast, the trailing edge is abrupt since it represents the point at which electron

Table 4.1. Transient simulation parameters

f	1/2	f_{Heq}
B_{ineq}	0.01	pT
n	8	
α	6°-72°	by 3°
z_{up}	-1350	km
z_{down}	2150	km
z_{drift}	-170	km
z_{shift}	200	km
Current taper	200	km
Field taper	300	km
Front end duration	50	msec
Pulse duration	500	msec
Front end taper	50	msec

trajectory calculations are terminated rather than the physical pulse trailing edge. The phase surface in Figure 4.4 is featureless since there is no shift of the total wave phase from the applied wave phase, an obvious result of turning off the energetic electron flux.

Using the parameters given in Table 4.1, transient simulations are performed. The magnitude and phase surfaces of the total wave field, including wave growth, are shown in Figure 4.5 and in the linear magnitude surface of Figure 4.6. The associated magnitude and phase of the phase bunched current, are shown in Figure 4.7. These surfaces show that the current, and hence stimulated radiation, is generally confined to the equatorial region, between -500 km and 500 km. Examination of $B_w(t)$ at the upstream boundary shows that the output wave field grows exponentially up to a saturated level while the phase advances at an ever increasing rate. Furthermore, examination of the phase surface clearly shows the upstream temporal phase advance evolving from the downstream spatial phase advance due to the geomagnetic inhomogeneity. Thus, the model not only reproduces some of the general features of the experimental results, but also gives insight into the sources and causes of the observed features.

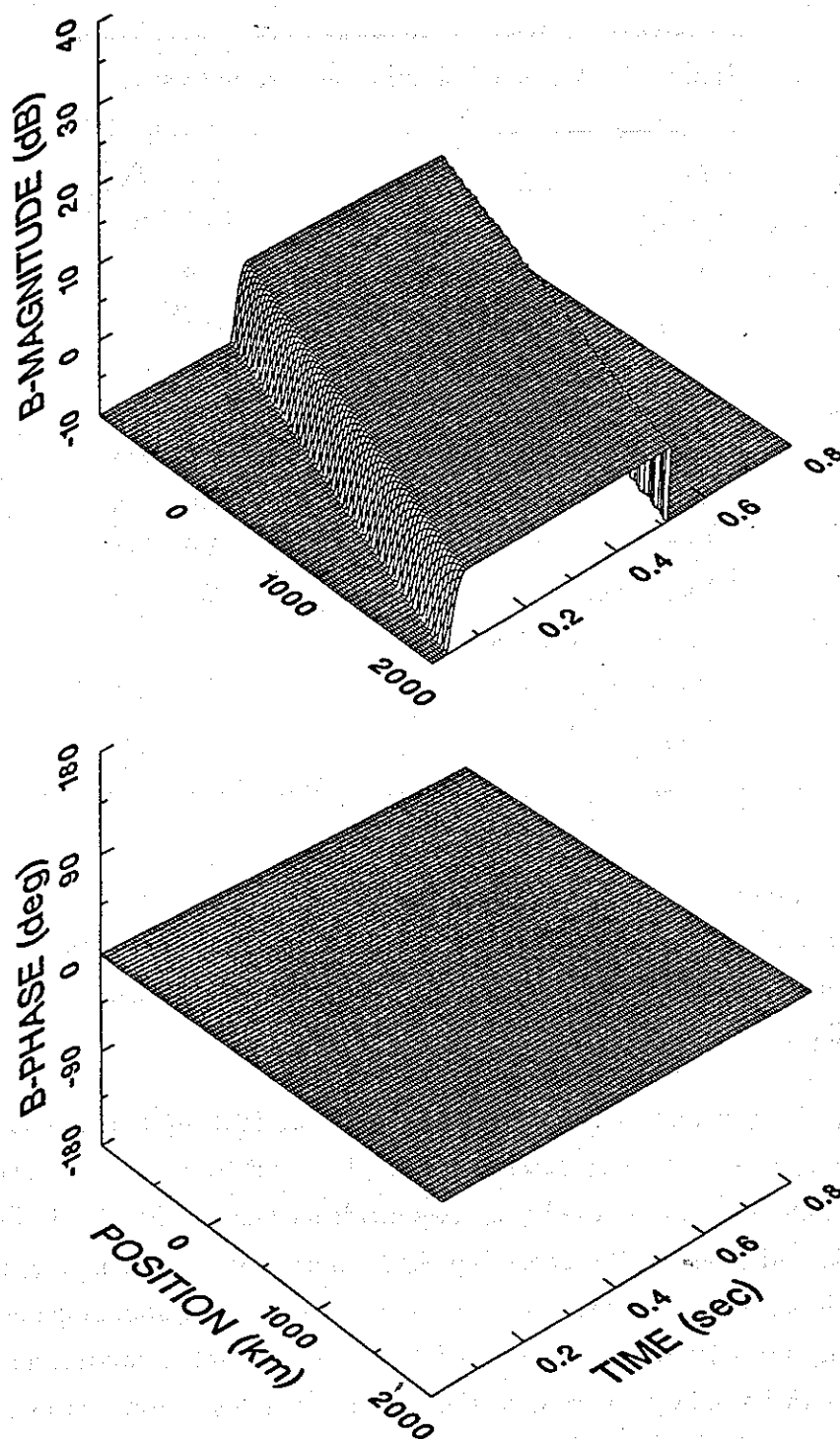


Figure 4.4. Space-time surfaces of the magnitude and phase of the applied wave pulse whose parameters are given in Table 4.1. The plot shows the leading and trailing edges propagating through space with increasing time. The leading edge is slightly shaped in order to approximate an actual pulse and to reduce the step response of injected electrons. The trailing edge is abrupt since it represents the point at which electron trajectory calculations are terminated. The phase surface is featureless since phase is measured with respect to the applied wave.

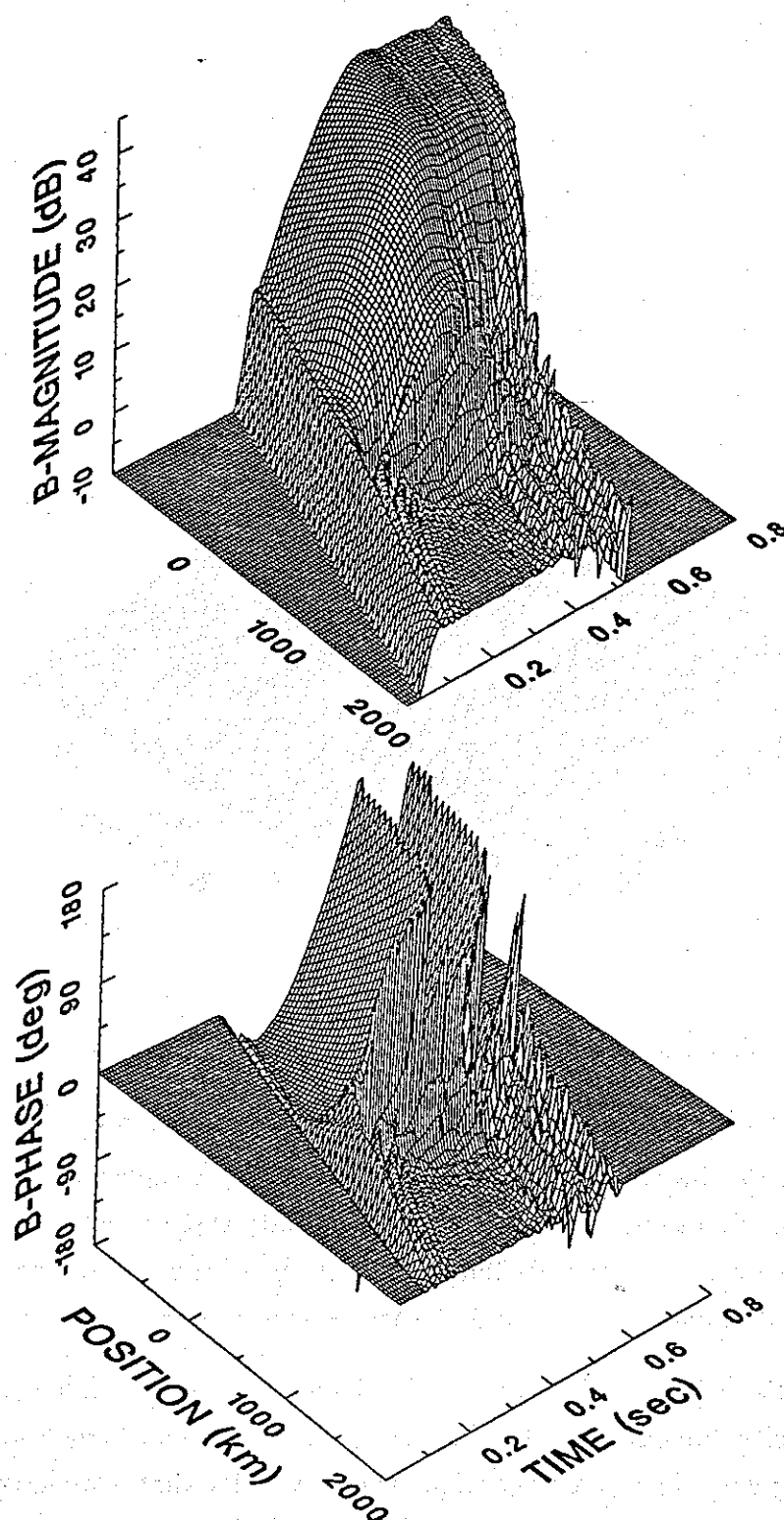


Figure 4.5. Magnitude and phase surfaces for the simulation of wave growth using the parameters in Table 4.1. Exponential growth, saturation, and parabolic phase advance is seen at the upstream boundary while the applied wave is seen at the downstream boundary. The wave growth is confined to the equatorial region. The output phase advance is seen to originate from the effect of the downstream inhomogeneity.

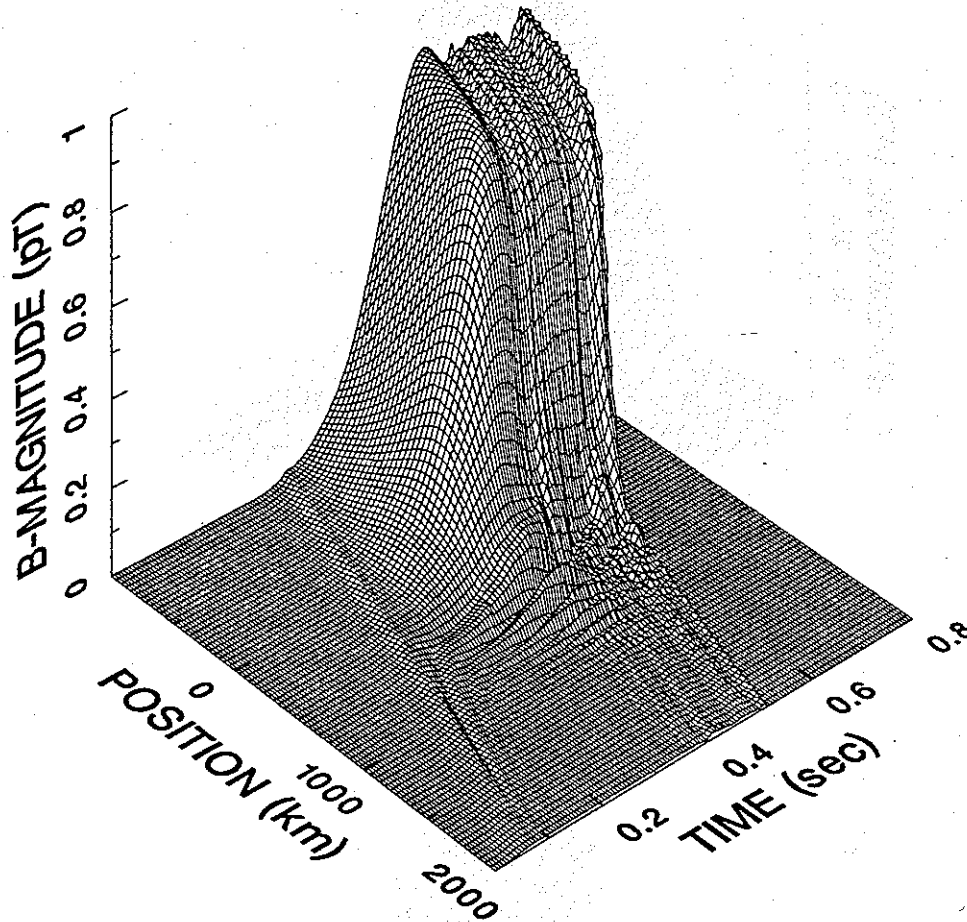


Figure 4.6. Linear magnitude surface for the same case shown in Figure 4.5.

The lack of wave growth in the downstream region results from the efficiency of phase mixing in this inhomogeneous region. This effect is demonstrated in Chapter 2 where equatorially and offequatorially resonant, steady state currents are compared. However, the steady state analysis indicates that the offequatorial currents become relatively more significant as the applied wave intensity increases.

The enhanced levels of downstream stimulated radiation at high τ 's, appears to be associated with the currents near the downstream boundary since these features are not growing with decreasing position. The possibility that a buildup of noise in the downstream region is related to some of the physical phenomena (e.g. saturation, triggering, sidebands) needs to be kept in mind.

A ridge of wave growth along the leading edge of the wave shows the effect of introducing the electrons into the wave. This ridge grows by ~ 8 dB and is due to the fact that, as electrons are introduced into the wave, they all experience the same

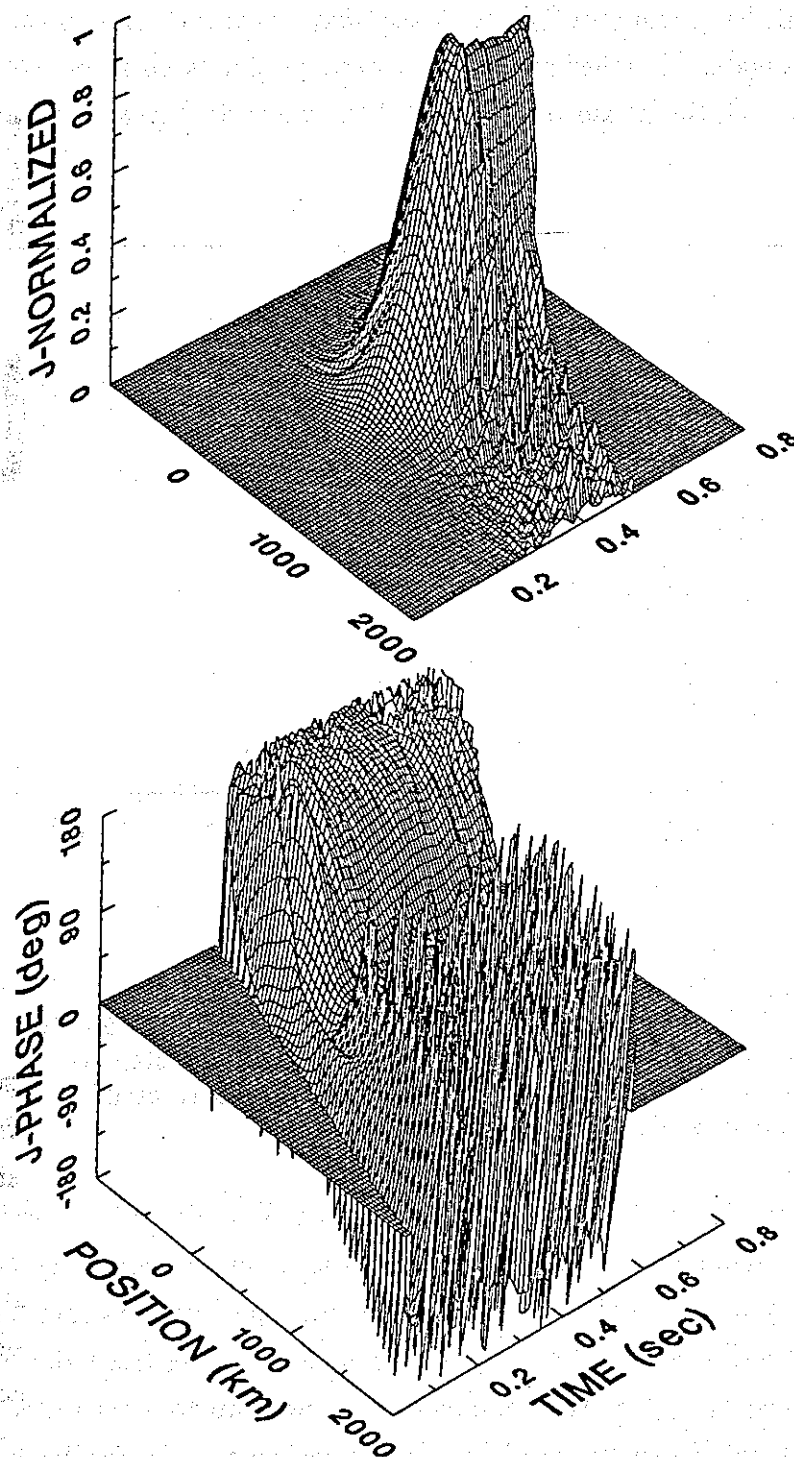


Figure 4.7. The phased bunched current magnitude and phase responsible for the wave growth seen in Figure 4.5. The confinement of the current to the equatorial region is a result of phase mixing effects of the inhomogeneity.

'kick' regardless of the leading edge position. Hence, \mathbf{J} starts out aligned with \mathbf{B}_w and then rotates, depending upon v_{\parallel} and the inhomogeneity. Therefore, at small τ 's (*i.e.* before this 'step response' phase mixes away), this radiation grows coherently as the wave propagates. Further discussion regarding this 'step response' is given later in association with the phase retardation of the wave field near the leading edge.

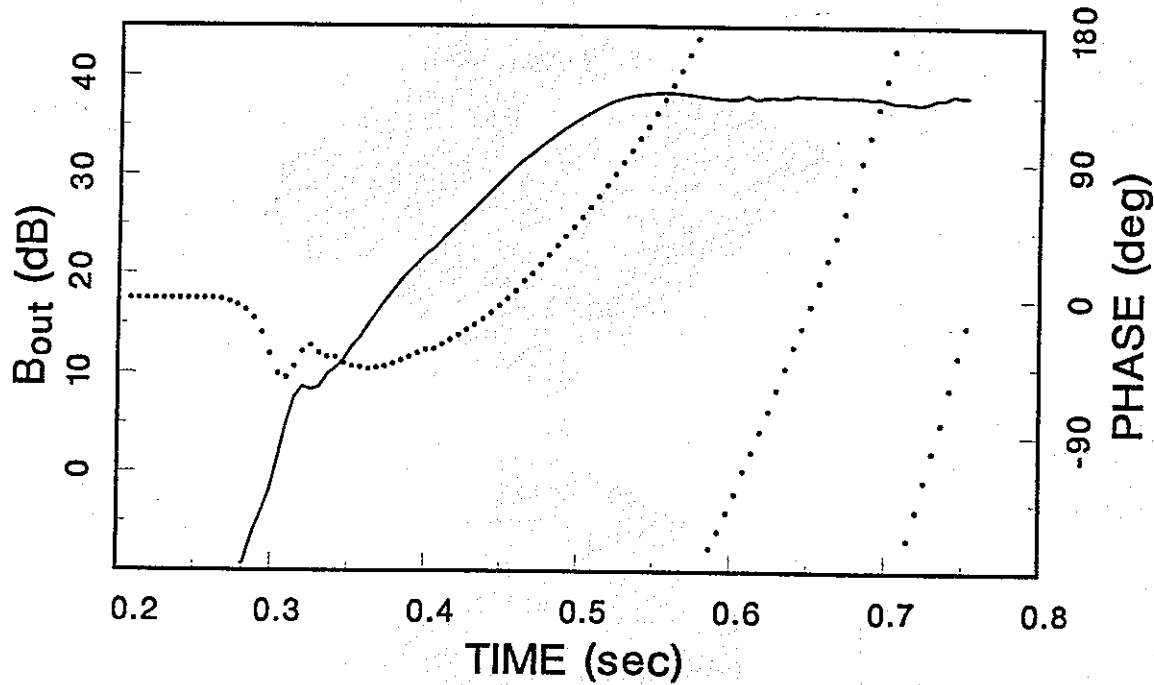


Figure 4.8. Output wave magnitude (solid) and phase (dotted) versus time corresponding to \mathbf{B}_w at the upstream boundary of Figure 4.5. The magnitude plot shows ~ 8 dB of spatial growth resulting from the 'step response' current, followed by ~ 150 dB/s exponential growth up to a saturated level of ~ 38 db. The phase is advancing at a nearly parabolic rate.

Comparison of the wave growth predicted by this model with experimental observations can be made by looking at the field at the upstream boundary $\mathbf{B}_w(z = z_{up}, t)$. Figure 4.8 gives plots of the wave magnitude and phase versus time. The magnitude plot clearly shows the ~ 8 dB of spatial growth resulting from the 'step response' current, followed by ~ 150 dB/s exponential growth up to a saturated level of ~ 38 db. The exponential growth results from the self sustaining feedback process. The saturation results from having both a fixed, narrow v_{\parallel} range and from fully bunching most of the electrons within the equatorial interaction region. Whether or not this saturation mechanism is responsible for the observed saturation phenomenon, is not

clear. It might be supposed that as the wave intensity increases, more v_{\parallel} 's would be significantly perturbed, which would seemingly allow the wave to grow without bound. However, if the range of significant v_{\parallel} 's increases at a slower rate than the range of v_{\parallel} 's within which the stimulated radiation has saturated, then this fully bunched saturation mechanism could still hold. Or saturation could be tied to some other phenomenon such as riser or sideband triggering, or even to the buildup of noise as suggested above.

The wave phase in Figure 4.8 is oscillatory, but generally retarding prior to the onset of parabolically advancing phase. This retarding phase results directly from the step response current being initially aligned to \mathbf{B}_w , generating a lagging \mathbf{B}_s which retards the wave phase and is reinforced by the feedback to subsequent electrons. However, in a more realistic simulation, a wider range of v_{\parallel} 's would be included. This would promote the phase mixing of this step response current which is expected to reduce the time over which the wave phase is retarding. In the limit as the v_{\parallel} range is increased to a full distribution, the phase could start advancing instantaneously from some new offset reference. In other words, the initial phase retardation could actually be the hot plasma contribution to the refractive index. This would explain why phase retardation like that shown in Figure 4.8 is not commonly seen in the actual measurements. Also, if an actual phase retardation existed over a time less than that shown in Figure 4.8, then it would become difficult to detect using the present methods (*Ev Paschal*, private communication).

Taking the derivative with respect to time of the wave magnitude and phase in Figure 4.8 gives the instantaneous growth rate and frequency, shown in Figure 4.9. These curves have been smoothed slightly by convolving with the 3 point sequence $\{0.25, 0.5, 0.25\}$. Examining the frequency versus time plot after the advancing phase is established, shows a nearly linear increase in frequency at ~ 30 Hz/s.

The 30 Hz/s frequency drift rate is chosen not only because it compares to measured drift rates, but also because a maximum likelihood test reveals that this is the rate that the model should produce. This maximum likelihood test is an answer to the following question: At what frequency drift rate do the energetic electrons give up their energy at a maximum rate? To answer this question, simulations were performed at several different df/dt 's and plotted superimposed in Figure 4.10, which clearly shows a df/dt dependent growth. To better see which df/dt gives the fastest growth, amplitude versus df/dt , parametric in τ , is plotted in Figure 4.11. This figure shows a well defined peak in the amplitude versus df/dt curves at a df/dt of ~ 30

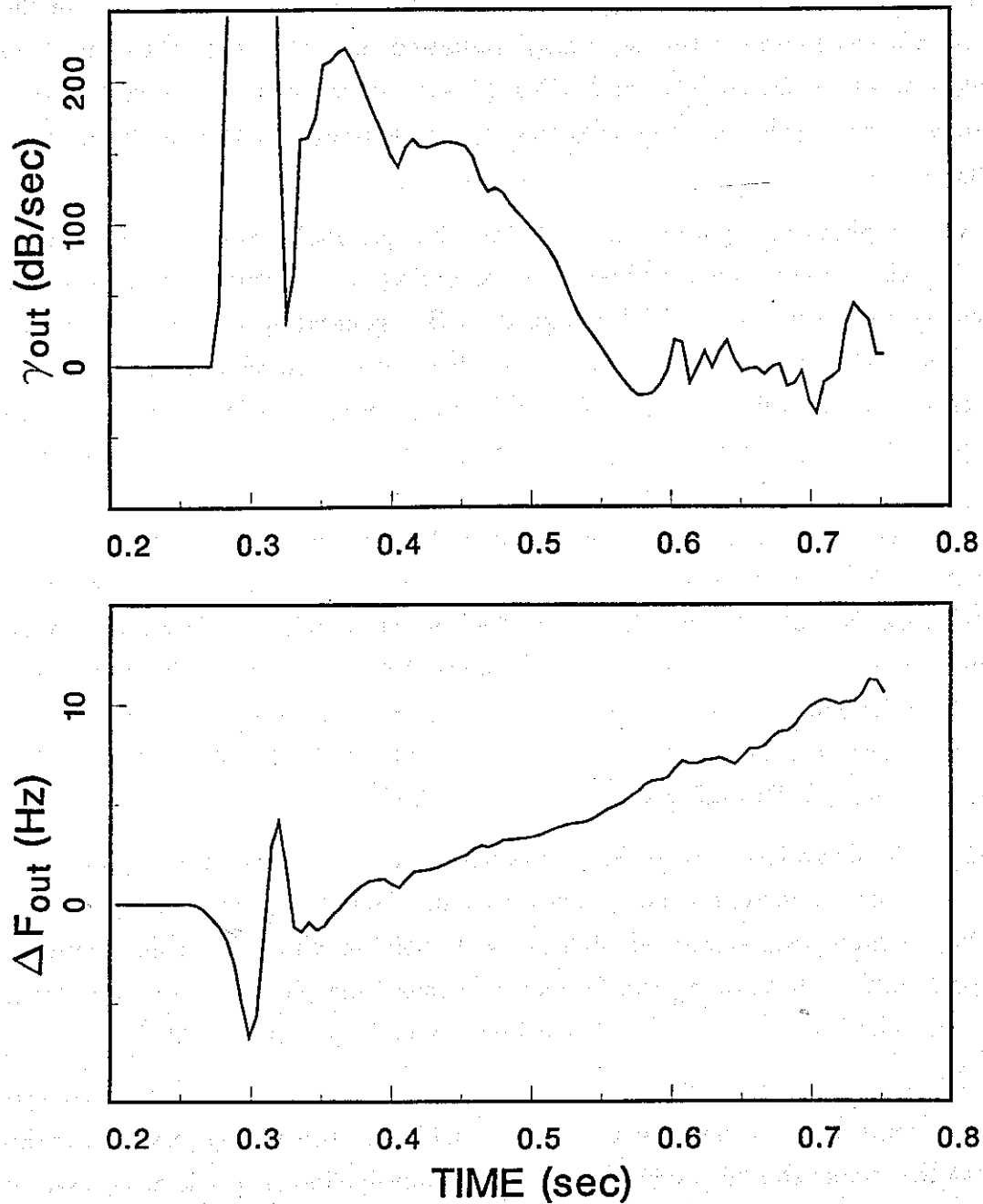


Figure 4.9. Instantaneous growth rate (top panel) and frequency (bottom panel) calculated by taking the derivative with respect to time of the wave magnitude and phase in Figure 4.8. These curves have been smoothed slightly by convolving with the 3 point sequence $\{0.25, 0.5, 0.25\}$. The frequency versus time plot shows a nearly linear increase in frequency at ~ 30 Hz/s.

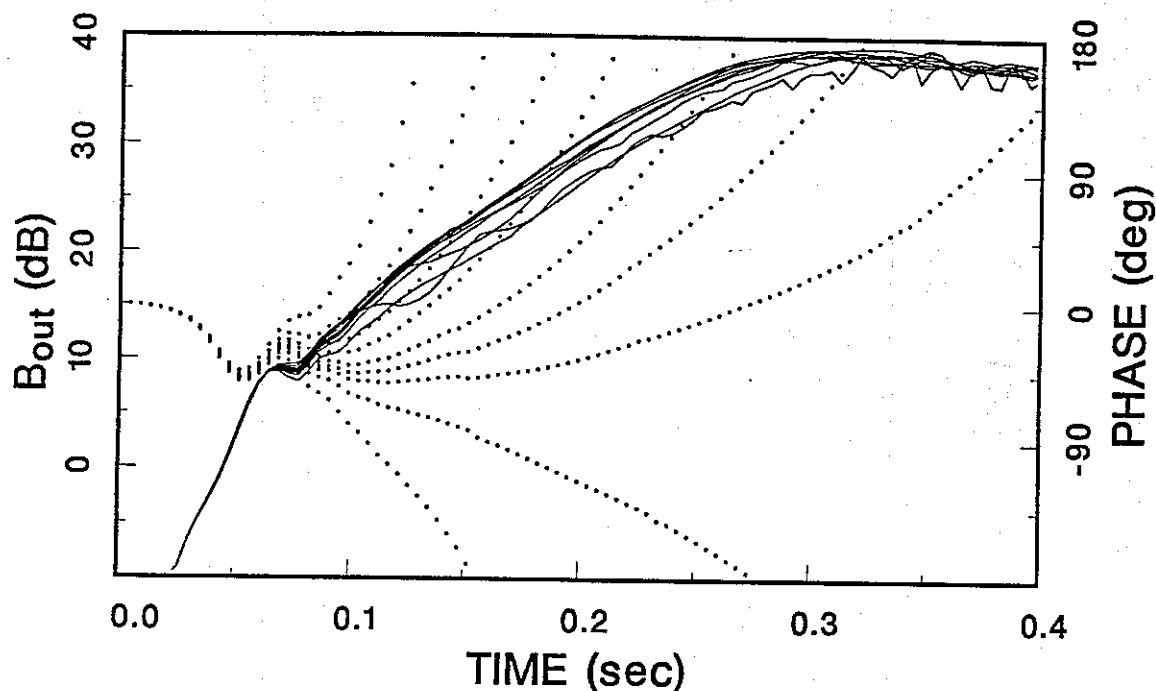


Figure 4.10. Output magnitude (solid) and phase (dotted) from several simulations, each having a different injection v_{\parallel} selection function designed to support a specific df/dt . From these curves it is apparent that one selection function yields a higher average growth rate than the others. This is the basis for a maximum likelihood test which suggests that the selection function resulting in the fastest growth, represents the dominant mode of growth. The results are better displayed in Figure 4.11 in which amplitude versus df/dt are plotted parametric in time.

Hz/s. Thus, Figure 4.11 indicates that ~ 30 Hz/s is the maximum likelihood rate of frequency increase and should be the dominant mode of growth. So not only does this model reproduce the proper frequency advance but, when it does, it maximizes the rate at which energy is extracted from the energetic electrons.

Self excited emissions

This same maximum likelihood test can be applied to self excited emissions triggered by short pulses. Termination of the applied signal can result in a triggered rising or falling emission but most likely a faller especially if the pulse terminates before saturation. Rising emissions can also be triggered prior to termination but generally after saturation or coincident with the end of growth. Observed falling emissions have been triggered by the termination of monochromatic waves or by the beating of two monochromatic waves at closely spaced frequencies [Helliwell *et al.*, 1986a]. In

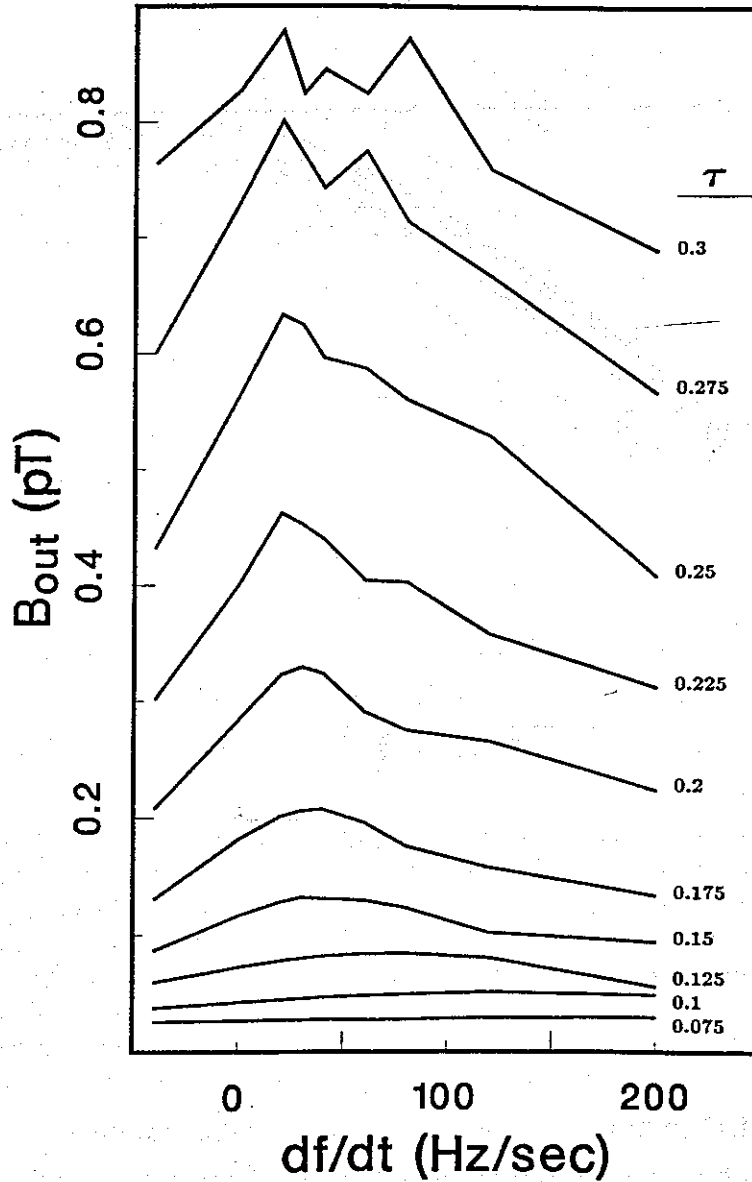


Figure 4.11. The output amplitude of the simulations of Figure 4.10 are plotted here versus df/dt and parametric in τ (the time from the leading edge). df/dt is the rate of frequency increase in the injection velocity selection function. The peak in the curves at a df/dt of ~ 30 Hz/s indicates the fastest growing case and should therefore be the dominant mode of growth. This outlines the maximum likelihood test for determining the injection $v_{||}$ selection function and the mode of growth.

Figure 4.13, an example of termination triggering shows that coincident with pulse termination is a band limited impulse and a falling emission originating from the upper frequency portion of the impulse. The falling emission, or 'faller', is established after a rapid increase in frequency associated with a band limited impulse coincident with the pulse termination. If this model predicts these falling emissions then, for

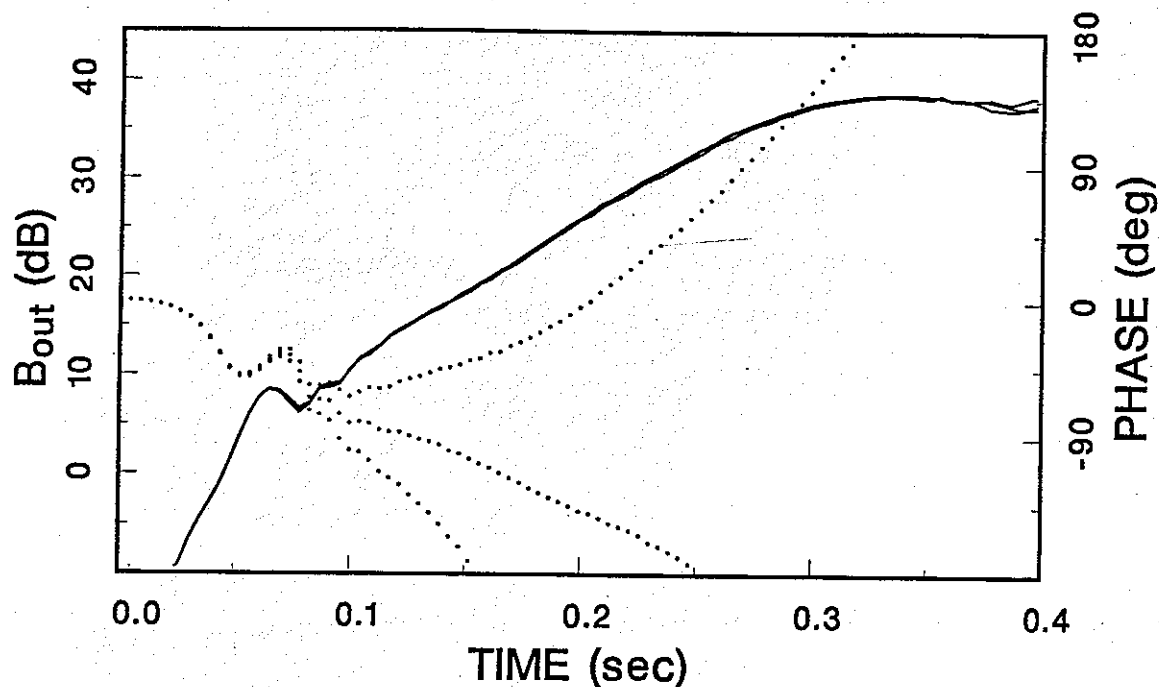


Figure 4.12. Application of the maximum likelihood test for self excited emissions using sinusoidal, 100 msec pulses. However, there are no significant differences in the amplitude versus time curves even though experiments commonly show falling frequency, self excited emissions. This suggests that a broader range of v_{\parallel} 's and a more general center velocity selection function are required to simulate self excited emissions.

short applied wave pulses, the amplitude versus df/dt curves should peak at negative df/dt 's. The pulse to be used in this test is a 100 msec pulse with a half amplitude duration of 50 msec created using a sinusoidal shaping function. The amplitude and phase versus time curves for drift rates of -30 , 0 , and 30 Hz/s, shown in Figure 4.12, indicate no significant differences in the amplitude versus time curves. While this test does not show any evidence that a falling self excited emission is the dominant mode, it also shows no evidence for a rising frequency mode. This is actually a significant and encouraging result. What it suggests is that the frequency advance is a byproduct of the presence of the applied signal. Also, the observed rapid phase swings associated with the pulse termination indicate that a single v_{\parallel} is inadequate for trying to simulate pulse termination effects, which are closely linked to the triggering of falling emissions. Rapid phase rotation at pulse termination seems to require a large degree of phase mixing or cancellation among the phase bunched currents (*Helliwell*, private communication) which, as is demonstrated in the last chapter, occurs when a larger

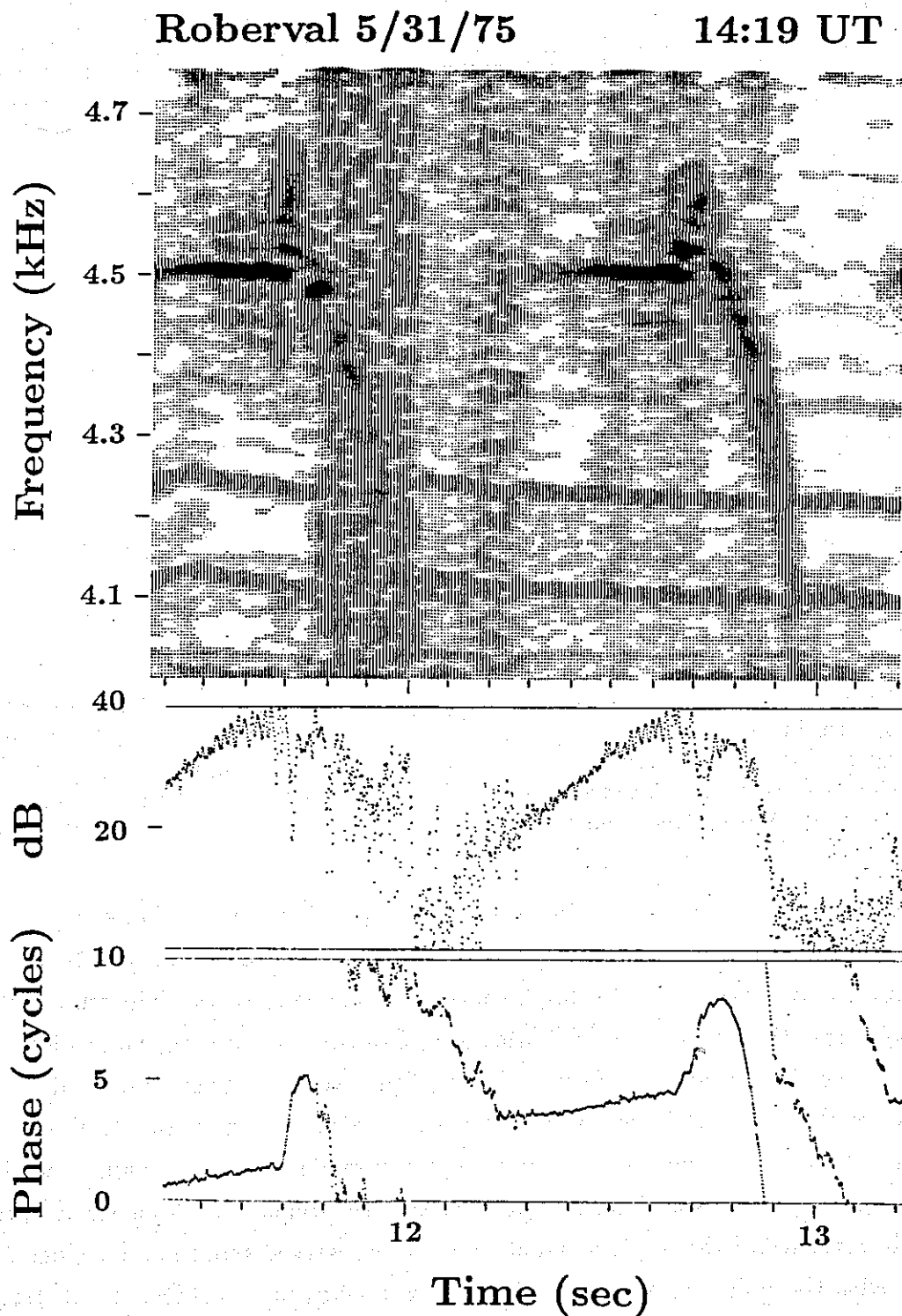


Figure 4.13. Fallers triggered by the termination of 0.5 second pulse. The termination causes a band limited impulse (BLI) extending ~ 150 Hz above and below the applied frequency. The faller seems to originate from the upper frequency portion of the BLI.

range of v_{\parallel} 's is employed.

Besides a broader range of v_{\parallel} 's, a more generalized center velocity selection function is required to simulate a self excited falling emission. By second order resonance theory, a falling emission is generated by an interaction region that drifts upstream of the equator. The possibility of this drift is not included in the center velocity selection function as given in equation (4.9). If the interaction region is drifting at a nearly constant rate, then the wave frequency should be changing at nearly a parabolic rate, from second order resonance theory. Thus, the parallel velocity shift term in (4.9) should be rewritten

$$\left(v_R(z_{drift} + z_{shift}) - (i - i_{drift})\Delta v_{\parallel} + (i - i_{drift})^2 \Delta^2 v_{\parallel} \right). \quad (4.12)$$

where a nonzero $\Delta^2 v_{\parallel}$ should drive an interaction region drift. This self excited interaction region drift is not simulated here but is left as a suggestion for future work.

With the model established and justified, the dependence of wave growth upon other parameters can now be investigated. While the assumed df/dt should be based upon the maximum likelihood test outlined above, for all of the following simulations a 30 Hz/s df/dt is assumed. The parameters which are going to be varied include the applied wave intensity, energetic electron flux, pitch angle distribution, and parallel velocity range. Amplitude and phase versus time are plotted parametric in the varied parameter. All of these plots include the 30 Hz/s case shown in Figure 4.10 so that differences can be quantitatively compared. A summary of the dependence of growth rate and saturation level upon the varied parameter is given in Table 4.2. This table also includes the results from Figure 4.12 (100 msec pulse) and the 30 Hz/s case in Figure 4.10 (Reference) for comparison.

Parametric in applied wave intensity

Amplitude and phase versus time, parametric in applied wave intensity B_{in} , are given in Figure 4.14. Again, these represent the wave magnetic field at the output, or upstream side of the interaction region. Besides the reference case with a B_{in} of 0.01 pT, applied wave intensities of 0.001 and 0.1 pT are included in Figure 4.14. Similar to the results of *Helliwell and Crystal* [1973] for a homogeneous medium, Figure 4.14 indicates that growth rate and saturation level are not significantly dependent upon applied wave intensity. While Table 4.2 does indicate a variation in growth rate with applied wave intensity, this trend is related to the growth curves not being exactly

Table 4.2. Growth rate and saturation levels.

Case	Growth Rate (dB/s)	Saturation Level (dB)
Reference	156	38
100 msec pulse	143	38
$B_{in} = 0.001$ pT	151	38
$B_{in} = 0.1$ pT	163	38
Flux Doubled	268	43
Flux Halved	58	24
$g(\alpha, a = 0.2, x = 0.2, y = 12)$	186	39
$g(, , , y = 2)$	214	40
$h(v_{ })$	79	36
$h(v_{ })g(, , , y = 2)$	98	47

exponential due to an average decrease in growth rate with increasing τ . Thus, since the higher applied wave intensity saturates sooner, it also has a higher overall average growth rate. This nonexponential behavior is due to the presence of the applied wave in the downstream region. When self excited wave growth is stimulated by a short pulse, as is the case in Figure 4.12 and also in *Helliwell and Crystal* [1973], the wave growth tends to be more exponential. The phase curves in Figure 4.14 show that the phase tends to advance more slowly for higher B_{in} 's. This same trend is associated with increasing growth rate in the figures to follow.

Parametric in energetic electron flux

Figure 4.15 shows the results of varying the energetic electron flux. In addition to the reference case, two other cases are shown having half and twice the energetic electron flux as the reference case. In the self excited, homogeneous case (*Helliwell and Crystal*, 1973) the rate of increase in the saturation level with respect to flux is positive but decreasing with increasing flux while the growth rate increased linearly with increasing flux. From Table 4.2, the saturation level shows the same decreasing

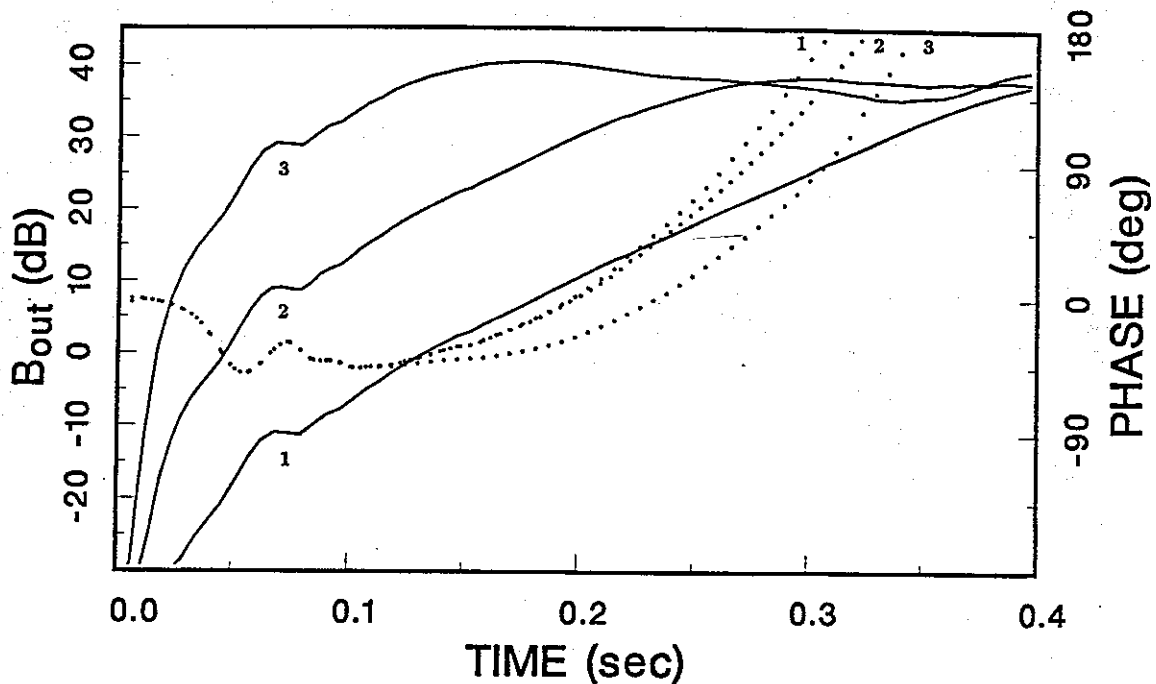


Figure 4.14. Output amplitude (solid) and phase (dotted) versus time, parametric in applied wave intensity. The applied wave intensities of 0.001, 0.01 (Reference), and 0.1 pT are included and labeled 1, 2, and 3 respectively. These curves indicate that growth rate and saturation level are not significantly dependent upon applied wave intensity. The phase curves show that the phase tends to advance more slowly for higher B_{in} 's. This same trend will be associated with increasing growth rate in the figures to follow.

rate of increase with respect to increasing flux; however, the rate of increase in the growth rate with respect to flux is also found to be decreasing with increasing flux. This difference could be due to either the presence of the applied wave or to the inhomogeneity. Also, as mentioned before, the phase tends to advance more slowly with increasing growth rate.

Parametric in $g(\alpha)$

In all of the simulations or results shown so far, a unity pitch angle distribution has been used. Figure 4.16 compares this unity pitch angle distribution with two anisotropic $g(\alpha)$'s of the form

$$g(\alpha) = a \sin^x \alpha + (1 - a) \sin^y \alpha . \quad (4.13)$$

Both have $a = x = 0.2$ but y is 2 in one case and 12 in the other. The effect of these

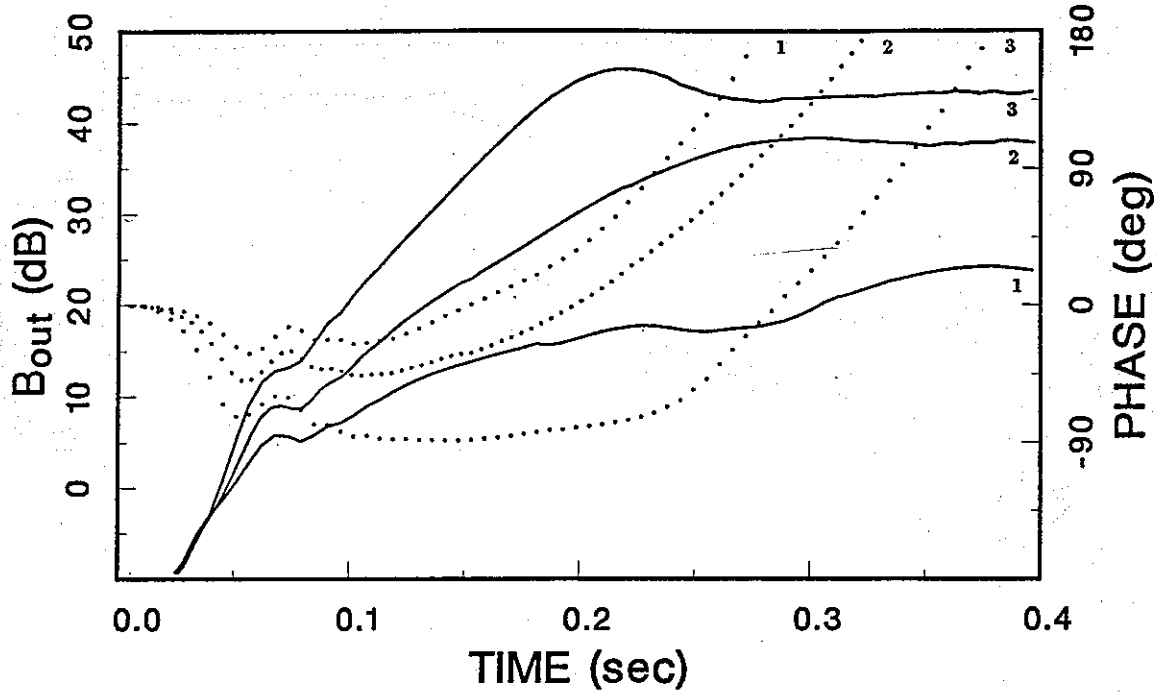


Figure 4.15. Output magnitude (solid) and phase (dotted) parametric in energetic electron flux. In addition to the reference case (2), two other cases are shown having half (1) and twice (3) the energetic electron flux as the reference case. The growth rate and saturation level both increase with increasing flux while the phase tends to advance more slowly with increasing growth rate.

functions is to concentrate more of the electrons at higher pitch angles. Because changing $g(\alpha)$ alters the number density, the distribution function must be rescaled for each $g(\alpha)$ so that the number densities are the same. The number density is given by

$$N(z) = 2\pi \int_{\alpha} \int_v f(v, \alpha) v^2 \sin \alpha \, dv d\alpha \quad (\#/m^3) \quad (4.14)$$

Since the form of the distribution function used is separable

$$f(v, \alpha) = A v^{-n} g(\alpha), \quad (4.15)$$

the number density equation can be rewritten

$$N(z) = 2\pi \int_{\alpha} g(\alpha) \cos^{n-3} \alpha \sin \alpha \, d\alpha \int_{v_{\parallel}} h(v_{\parallel}) v_{\parallel}^{-n+2} \, dv_{\parallel} \quad (4.16)$$

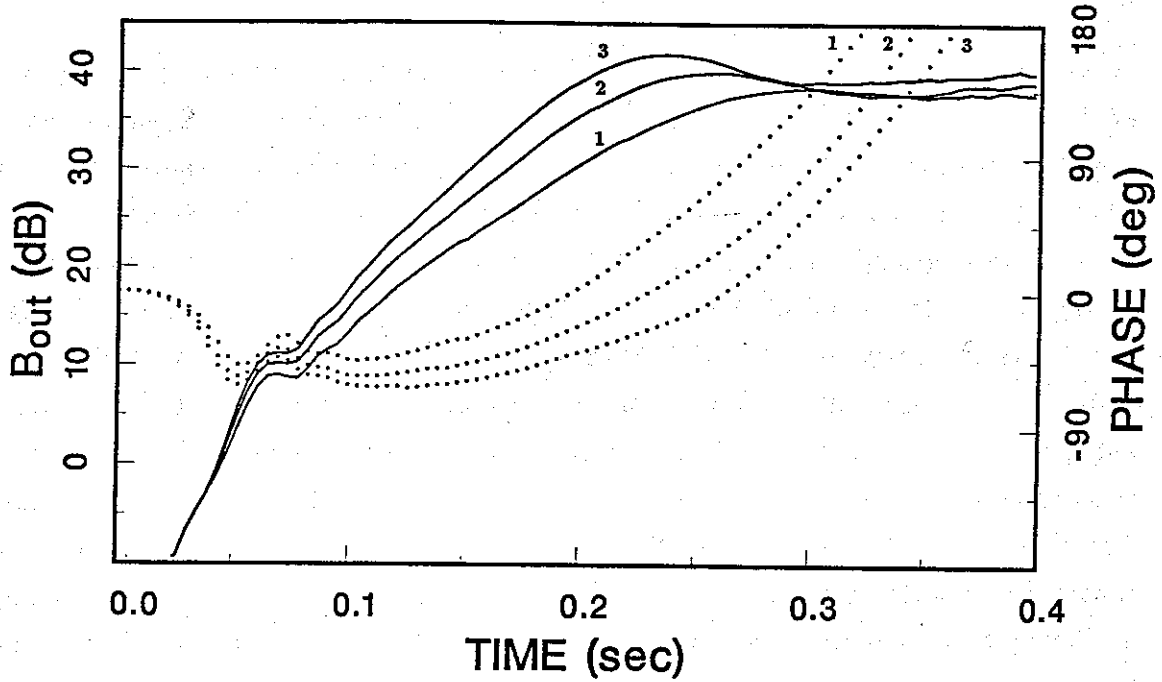


Figure 4.16. Output magnitude (solid) and phase (dotted) parametric in pitch angle anisotropy $g(\alpha)$. The $g(\alpha)$'s are 1 (Reference), $0.2 \sin^{0.2} \alpha + 0.8 \sin^{12} \alpha$, and $0.2 \sin^{0.2} \alpha + 0.8 \sin^2 \alpha$ and are labeled 1, 2, and 3 respectively. The distribution function has been rescaled for each $g(\alpha)$ so that the number densities are the same, resulting in nearly equal saturation levels. $g(\alpha) = 0.2 \sin^{0.2} \alpha + 0.8 \sin^2 \alpha$ resulted in the largest growth rate presumably due to a maximum in $dg(\alpha)/d\alpha$ occurring at $\alpha \simeq 45^\circ$, the pitch angle of maximum radiation.

where $h(v_{\parallel})$ is the v_{\parallel} sampling function. A general expression for $g(\alpha)$ which can be integrated in the above equation is

$$g(\alpha) = \sum_i (a_i \sin^{x_i} \alpha + b_i \cos^{y_i} \alpha) \quad (4.17)$$

performing the pitch angle integration

$$\int_{\alpha_{lc}}^{\pi/2} g(\alpha) \cos^{n-3} \alpha \sin \alpha d\alpha \simeq \sum_i \left(a_i \left[\frac{\Gamma(\frac{n}{2}-1) \Gamma(\frac{x_i}{2}+1)}{2\Gamma(\frac{n+x_i}{2})} - \frac{\alpha_{lc}^{x_i+2}}{x_i+2} \right] + b_i \left[\frac{2}{y_i+n-2} - \frac{\alpha_{lc}^2}{2} \right] \right) \quad (4.18)$$

where α_{lc} is the loss cone pitch angle and is assumed to be small enough to justify the small angle approximation to the value of the integrand at this angle, and where

the following conditions must also hold:

$$n > 2, \quad x_i > -2, \quad y_i > 2 - n. \quad (4.19)$$

Thus, the distribution function must be scaled by factors of 2.7 and 5.6 for $g(\alpha)$'s of $0.2 \sin^{0.2} \alpha + 0.8 \sin^2 \alpha$ and $0.2 \sin^{0.2} \alpha + 0.8 \sin^{12} \alpha$, respectively. Examination of Figure 4.16 shows that this rescaling results in approximately the same saturation levels. The most interesting new feature is the fact that $0.2 \sin^{0.2} \alpha + 0.8 \sin^2 \alpha$ resulted in the largest growth rate. This can be explained in terms of the anisotropy factor $dg(\alpha)/d\alpha$ and the falloff of the number of electrons with increasing energy through the v^{-8} term. Large values of $dg(\alpha)/d\alpha$ are known, by linear theories, to drive the whistler-mode instability. But, in the last chapter it is shown that $\sim 45^\circ$ pitch angle electrons are the largest contributors to the steady state radiation through the balancing of the $\mathbf{v} \times \mathbf{B}$ forces with the v^{-n} falloff in the electron distribution. Therefore, since $d(0.2 \sin^{0.2} \alpha + 0.8 \sin^2 \alpha)/d\alpha$ has a maximum at $\sim 45^\circ$, it is not surprising that this $g(\alpha)$ results in the largest growth rate. The other $g(\alpha)$ actually has a larger maximum slope, but it occurs at higher α 's where the contribution to growth is less significant. Again, the phase tends to advance more slowly with increasing growth rate.

Parametric in $h(v_{\parallel})g(\alpha)$

The next factor to be investigated is the role of the v_{\parallel} integration. In Figure 4.17, triangular distributions in v_{\parallel} are compared to the reference case. In the reference case, a single v_{\parallel} is considered which drifts in accordance with the drift equation given earlier. The triangular sampling function $h(v_{\parallel})$, is centered at the same v_{\parallel} as the reference case and falls off linearly to zero at v_{\parallel} 's 0.5% above and below the center velocity. One of the triangular $h(v_{\parallel})$ cases has a $g(\alpha) = 1$ while the other has a $g(\alpha) = 0.2 \sin^{0.2} \alpha + 0.8 \sin^2 \alpha$. The reason for choosing a triangular shape is that $|dh(v_{\parallel})/dv_{\parallel}|$ is constant over the range of the function. Thus, in terms of the magnitude of this anisotropy factor, there are no edges. If $h(v_{\parallel})$ were a rectangular function, then extreme edge effects would be expected as were demonstrated in the last chapter. In fact, examining the edge effects associated with a rectangular, sinusoidal 'bell', and triangular shaping function revealed that the triangular function resulted in a stimulated current most confined to the equatorial region. Even though the sinusoidal bell function smoothly goes to zero at the high and low v_{\parallel} edges, it has peaks in the magnitude of the derivative with respect to v_{\parallel} midway between the center and edges. To emphasize the effect of cancellation associated with the integration over

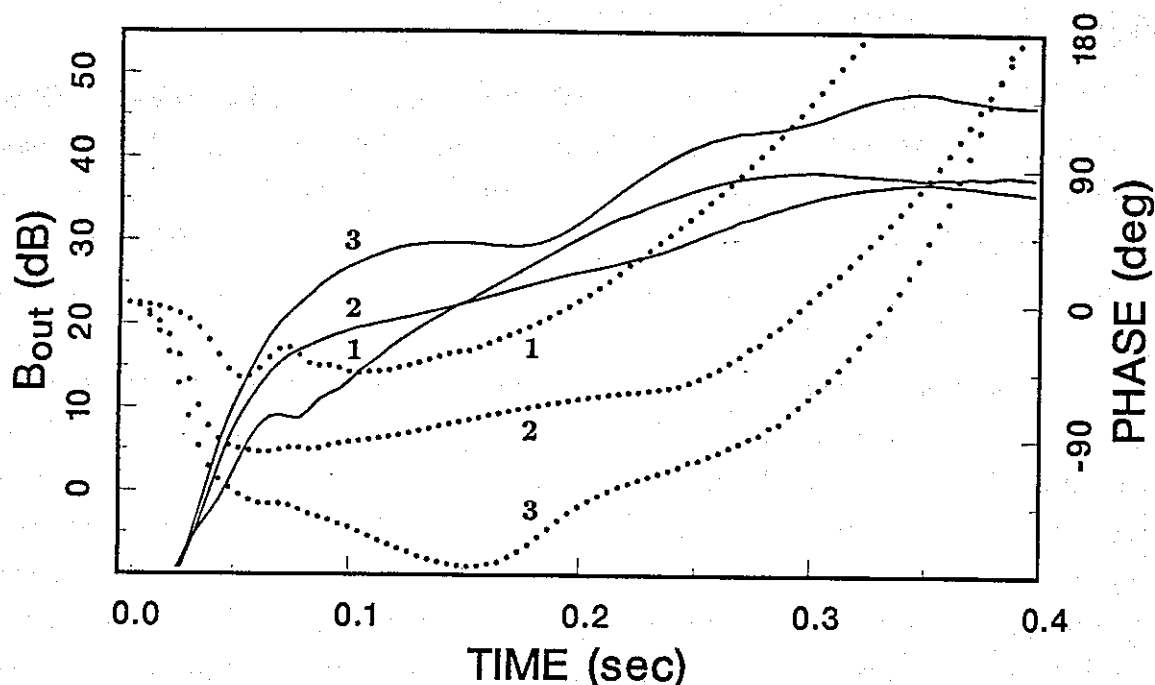


Figure 4.17. Output magnitude (solid) and phase (dotted) parametric in $h(v_{\parallel})$. Compared are the single v_{\parallel} reference case (1) as well as triangular sampling functions $h(v_{\parallel})$ which fall off linearly to zero at v_{\parallel} 's 0.5% above and below the center velocity. One of the triangular $h(v_{\parallel})$ cases has a $g(\alpha) = 1$ (2) while the other has a $g(\alpha) = 0.2 \sin^{0.2} \alpha + 0.8 \sin^2 \alpha$ (3). Even though the number densities are several times greater in the triangular cases compared to the reference case, the saturation levels are comparable, a result of the cancellation associated with the integration over v_{\parallel} . These curves show that the v_{\parallel} integration reduces the growth rate by nearly a factor of 2. Of particular interest is the onset of a stable phase advance at an earlier time in the $g(\alpha) = 1$ case.

v_{\parallel} , the distribution function is not rescaled to compensate for the increase in number density. Even though the number density is about 9 times greater in the triangular cases compared to the reference case, the saturation levels are comparable. This is a direct result of the cancellation associated with the integration over v_{\parallel} . Figure 4.17 also shows that the v_{\parallel} integration reduces the growth rate by nearly a factor of 2. The phase curves indicate one possible difference resulting from the v_{\parallel} integration which could improve the fit of the simulation output with the experimental measurements. This difference is the onset of a stable phase advance at an earlier time in the $g(\alpha) = 1$ triangular case compared to the reference case. While the linear phase advance and abrupt changes in the rate of phase advance, visible in Figure 4.17, are not the nearly parabolic phase advances seen in many of the experimental records, similar phase

behavior is seen in the experimental data.

4.3. Comparison with experiment

To compare the simulations with actual data, a pulse received at Roberval, Quebec, on March 16, 1977 at 14:26:00 UT is selected. This pulse has a higher than average growth rate of ~ 82 dB/s and is a fairly typical 'clean' pulse with smooth amplitude and phase curves. The input parameters for the simulation differ from the parameters used in the previous reference case as follows: $B_{in} = 0.025$ pT, the flux is reduced by a factor of 0.7, and a 50 Hz/s frequency drift rate is selected. These were the only parameters which needed to be adjusted in order to fit the total growth, growth rate, and the frequency drift rate. The comparison is made in Figure 4.18. The top panel in Figure 4.18 shows the simulated amplitude and phase along with the experimental amplitude versus time (open circles). The bottom panel shows the comparison of the simulated and measured frequency versus time. Because the experimental frequency points are computed by taking the derivative of the measured phase, the plotted frequency is convolved by the smoothing sequence $\{0.25, 0.5, 0.25\}$ in order to counter the 'error amplifying' effects of the derivative operation. To first order, the fits are quite good. Even some of the second order features like oscillation periods compare. These oscillations have a period near the characteristic feedback loop delay time for the 45° pitch angle electrons.

The features in Figure 4.18 which don't compare include the growth of the measured frequency oscillations, the details within the first 100 msec, and a general offset in the frequency at any point in time. The sources of these discrepancies possibly lie in the narrowness of the $v_{||}$ range, as discussed before. The frequency oscillations in the simulations are held in check by the narrow $v_{||}$ width and the fixed drift rate of the center velocity. In other words, the wave is not allowed to select the electrons, so the oscillations are not allowed to develop freely. The simulations already performed suggest that an increased $v_{||}$ range could reduce the duration of the leading edge transient phase. To minimize the effects of the 'step' response, a 50 msec leading edge taper is used on the wave field, much longer than natural taper duration which results from dispersion and transmitting system bandwidth. However, a previous study showed that these effects (growing and rotating currents) phase mix away rapidly if a broad enough $v_{||}$ range is included, even if the leading edge is a perfect step. Also, the present form of the experimental data make it difficult to measure the phase and amplitude features to the resolution required to properly compare the first tens of

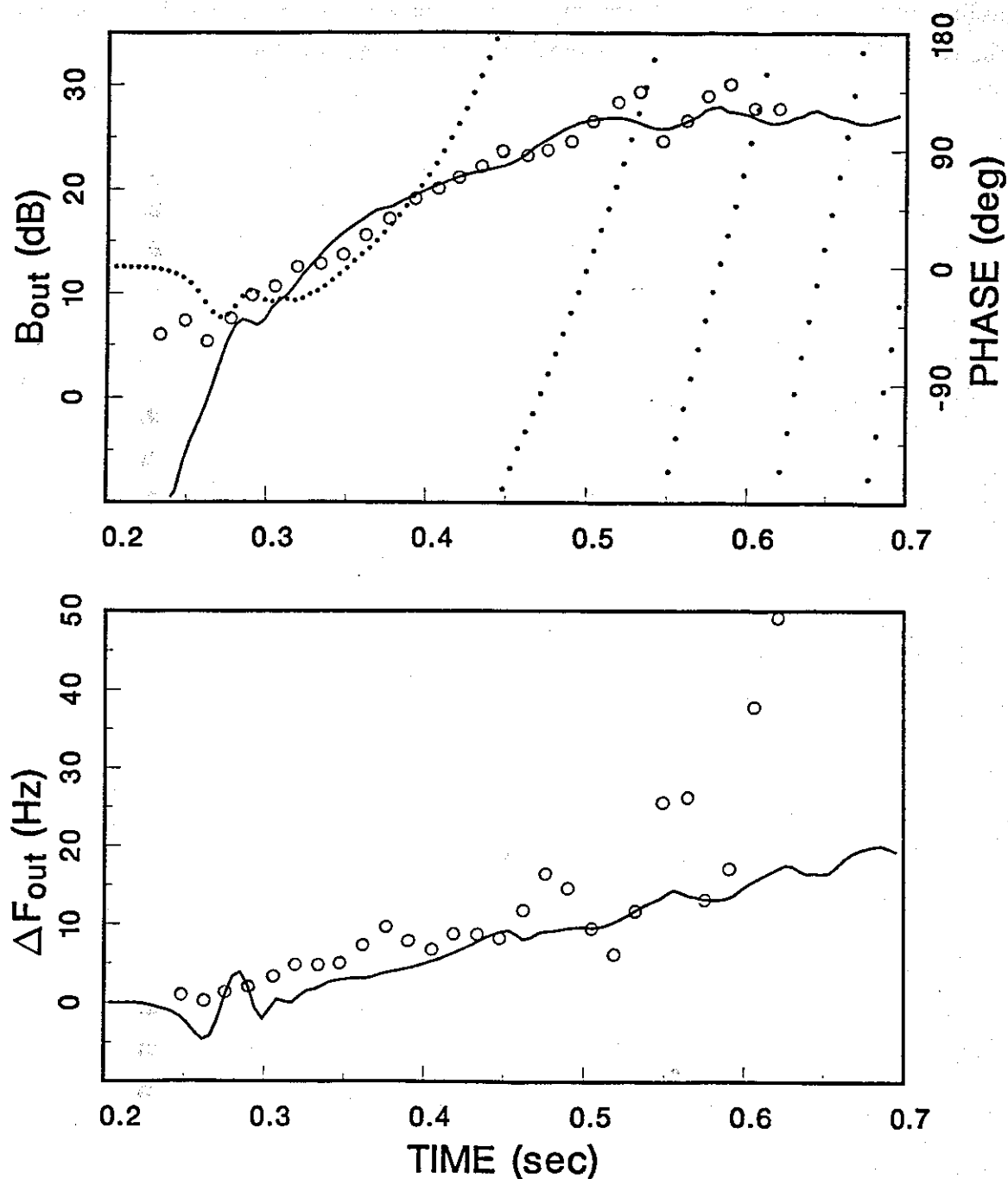
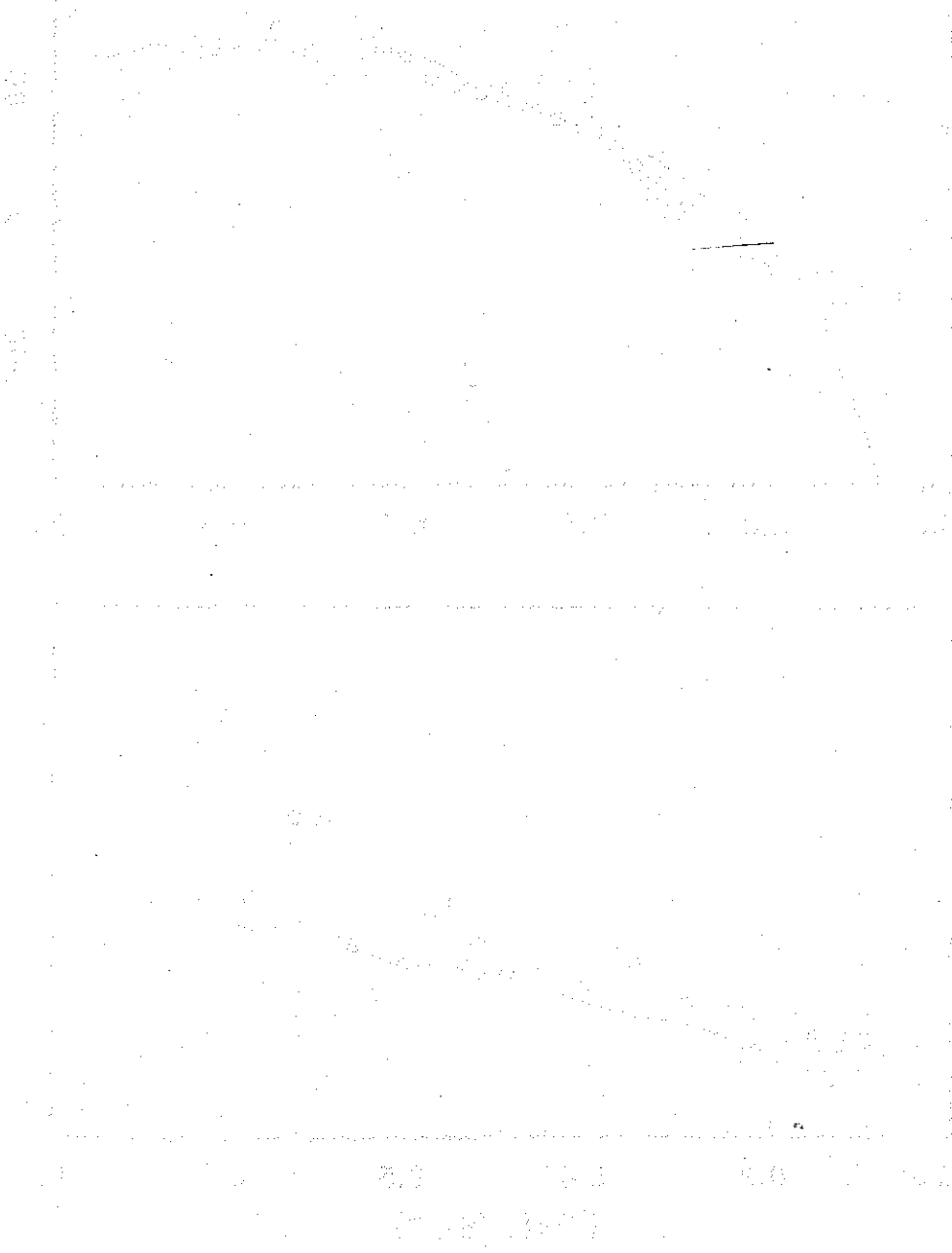


Figure 4.18. Comparison of simulations with a pulse received at Roberval, Quebec, on March 16, 1977 at 14:26:00 UT. The input parameters for the simulation differ from the parameters used in the previous reference case as follows: $B_{in} = 0.025$ pT, the flux was reduced by a factor of 0.7, and a 50 Hz/s frequency drift rate was selected. The top panel shows the simulated amplitude (solid) and phase (dotted) along with the experimental amplitude versus time (open circles). The bottom panel shows the comparison of the simulated and measured frequency versus time. The experimental frequency points have been smoothed by the sequence $\{0.25, 0.5, 0.25\}$. Growth rate, saturation level, and even oscillation periods are comparable.

milliseconds. Proposed directions for future work aim at improving the model and the comparisons with data and are outlined in the next chapter.



as shown in Figure 1. The curve is a smooth, continuous line that starts at a high value on the left and decreases as it moves to the right. The x-axis is labeled with values 0.0, 0.5, 1.0, and 1.5. The y-axis is labeled with values 0.0, 0.5, 1.0, and 1.5. The curve is roughly parabolic, starting near (0, 1.5) and ending near (1.5, 0.5).

Chapter 5. Summary and recommendations

This chapter presents a summary of the previous chapters as well as a list of recommendations for future work. The areas within which future efforts are suggested include data analysis, improved models of the medium, reduction of free parameters, simulations, and optimization of the computer code.

5.1. Summary

Models are developed, based upon test particle trajectory calculations, to simulate and understand the whistler-mode wave growth process. The simulations reproduce, for the first time, exponential wave growth and saturation coincident with a linearly increasing frequency versus time. No other simulation or modeling efforts have simultaneously predicted these features, particularly the linear frequency increase. This breakthrough is made possible by the development of a new transient model for performing wave growth simulations. Besides including the geomagnetic inhomogeneity and electrons ranging in all three dimensions of velocity space, the transient model includes unique methods for calculating the phased bunched currents, stimulated radiation, and the propagation of the radiated fields.

With the transient model, the space-time evolution of a wave pulse can be simulated, with high spatial and temporal resolution, as the pulse propagates across the inhomogeneous equatorial region. Generalized equations of motion are developed so that the frequency and wave number can evolve in space and time. Since only a narrow range of parallel velocities can be included, a scheme is developed to make the center v_{\parallel} be a function of the time and location at which the electrons are introduced into the wave. This relationship is called the selection function. A maximum likelihood test is developed which, for some class of selection functions, determines the selection function that maximizes the average growth rate. This test shows for the first time that, when an applied signal is present, the total wave phase at the output of the interaction region advances with time. Thus, the transient model not only predicts exponential wave growth up to a saturated level, but also predicts the generally observed linearly increasing frequency with time. The frequency increase is found to result from the feedback of radiation from the phased bunched currents

which are rotated by the geomagnetic inhomogeneity. The relationship between the selection function and the rate of frequency increase is consistent with second-order resonance theory [Helliwell, 1967, 1970; Carlson *et al.*, 1985]. In other words, the maximum-likelihood selection function suggests that the most significant electrons are those which satisfy the second-order resonance condition for the observed frequency increase. The transient simulations also show that features like growth rate and total growth are simply related to the various parameters like applied wave intensity, energetic electron flux, pitch angle anisotropy, and the width of the v_{\parallel} range.

While self excited emissions generated at the termination of pulses are generally falling in frequency with time, the transient model and the implemented class of selection functions, did not predict this. However, in the self excited case, it is suggested that the selection function may need to include a term which varies parabolically with time in addition to just a linear term. In other words, it may be that the interaction region needs to be allowed to drift in space with time. Similarly, the triggering of rapidly rising emissions is also not predicted by the transient simulations. However, the inclusion of a broader range of parallel velocities seems necessary before riser triggering can emerge from the simulations.

The comparison of the transient simulations with actual experimental measurements show good agreement in growth rates, total growth, the rate of frequency increase, and even the period of amplitude and frequency oscillations. However, phase oscillations near the leading edge in the simulations, pulse termination triggered transients seen in the experiments, and the triggering of rising or falling emissions all suggest that future simulations should concentrate on increasing the range of v_{\parallel} 's.

Steady state wave field concepts are also used to study the currents and stimulated radiation from the energetic electrons. One aspect of this study is the systematic analysis of the phased bunched currents and total radiation versus electron pitch angle and parallel velocity, and the collective response of the energetic electrons revealed by integrating over velocity space. Single sheet current versus position, obtained by integrating over electron gyrophase, reveal the most basic aspects of resonance and phase bunching. The cancellation of the currents, or 'phase mixing', which results from the integration over pitch angle and parallel velocity, as well as 'edge effects' associated with the finite v_{\parallel} integration limits are investigated. Integration over pitch angle significantly reduces the magnitude of offequatorial currents because of the phase mixing action of the inhomogeneity. The result is that the total phased bunched current tends to be confined to the equatorial region. Integration over v_{\parallel} added two

more significant aspects, extensive cancellation and edge effects. The peak current tends to increase when integrating over a small range of v_{\parallel} 's but then decreases as the v_{\parallel} range continues to broaden. Edge effects are associated with this cancellation process in that current peaks, resulting from the offequatorial resonance of the high v_{\parallel} edge, do not cancel because higher v_{\parallel} electrons are not included. Consequently, there are large current peaks located at the offequatorial resonance locations of the high v_{\parallel} edge of the v_{\parallel} range. Edge effects can be reduced by using a v_{\parallel} weighting function which smoothly goes to zero at the v_{\parallel} edges (*e.g.* a triangle or sinusoidal bell), eliminating the current from these edges.

Steady state stimulated radiation is calculated by simply integrating the phase bunched current over position. A model for calculating self consistent steady state fields with significant wave growth is given and tested. Temporal wave growth, including the advance in wave phase with time, is simulated using a two-port feedback model. However, it is difficult to gain insight into the transient aspects of the wave growth process with this model. Also, the experimental data show many features which can not be simulated using a steady state model including, growth and frequency shifts within the first 50 msec, and also rapid frequency shifts associated with pulse termination. Also, it is not possible to physically justify the sensitivity of the steady state wave growth models to the distribution sampling function. These deficiencies motivated the development of the transient model.

5.2. Recommendations for future work

Data analysis

With the development of the transient model comes the ability to simulate the continuous evolution of the wave amplitude and phase. However, it is presently difficult to compare some of the simulated amplitude and phase features with experimental results because existing data analyses have generally focused on grosser features. For example, the simulation outputs are plotted on scales of approximately 10 dB/inch, 90°/inch, and 50 msec/inch. A typical analysis, on the other hand, might be plotted on scales of approximately 20 dB/inch, 900°/inch, and 500 msec/inch. A particular example of fundamental importance is the evolution of the wave amplitude and phase within the first 100 msec. A proper analysis should give the amplitude and phase of a pulse to better than 1 dB and 5°, respectively, at 5 msec increments. This analysis would show how the electron distribution as a whole responds to the

leading edge of the wave as compared to the expected response from some subset of the electron distribution. In other words, it needs to be determined how much phase mixing and cancellation there is in the phase bunched currents and how broad the v_{\parallel} and α ranges must be in the model to properly simulate the first 100 msec.

Besides the need for higher resolution analyses of the amplitude and phase, overall statistics and correlations are needed which can characterize wave growth. Hundreds of experimental pulses could be measured to develop a data base which could become a standard reference. Measurements to be made should include growth rate, total growth, rate of frequency increase before triggering, initial frequency offset of growth, df/dt of the triggered emissions, rate and magnitude of the phase swing associated with the applied pulse termination, the positive frequency offset of any termination triggered emissions, and the period and growth of frequency and amplitude oscillations. These measurements and their statistics would then be the specifications for any model and simulation of wave growth. Once these measurements are made, correlations can be established such as between growth rate and the rate of frequency advance as mentioned in the Introduction. For any correlation, the parameters within the model that could account for the effect can be isolated.

Improve the medium model

A more complete model of the medium could be incorporated. Since the interaction length is so sensitive to $d\omega_H/dz$, deviations from a dipole model can be significant. The transient code as given in Appendix C includes the option to input a non-dipole geomagnetic field although, in its present form, a dipole field diffusive equilibrium model would be superimposed. Parameters which could be incorporated include ring current, solar wind pressure, universal time, and dynamic effects [Gail, 1987].

Reduce free parameters

One problem with simulating actual pulses is that there are too many free parameters to really be able to use the simulations as a diagnostic tool. Ideally, for a diagnostic, there should be only as many unknown parameters as there are features to be fitted. Presently, the free parameters include applied wave intensity, energetic electron flux, center velocity drift rate, pitch angle anisotropy, parallel velocity range, equatorial electron density, L-shell, and the geomagnetic field structure (*i.e.* perturbations due to ring current, and solar wind pressure). A dispersion analysis can give the equatorial electron density and L-shell, and the center velocity drift rate is given

by the frequency increase rate. Of course, it is desirable to have as wide a v_{\parallel} range as can be included, given the CPU time limitations. This leaves 4 free parameters to fit the measured growth rate, total growth, and also the maximum likelihood test for the center velocity drift rate.

Ways to reduce the number of free parameters include satellite measurements, 3-dimensional raytracing, and ground based experiments. With the aid of satellite measurements, ring current and solar wind pressure can be deduced. However, direct measurement of the geomagnetic field utilizing field aligned orbits would be the most desirable. High resolution satellite measurements of the energetic electron distribution in the 1 to 10 keV range are essential. While the pitch angle anisotropy is listed as a single free parameter, a crude representation for $g(\alpha)$ requires at least 2 variables in the form

$$g(\alpha) = a + (1 - a) \sin^x \alpha. \quad (5.1)$$

One of the most elusive parameters to measure has been the ducted wave intensity. The most ideal situation would be to have a satellite in a field aligned orbit, continuously measuring the wave intensity as the satellite traverses the interaction region within a duct. However, attempts to make this measurement have become analogous to 'looking for a needle in a haystack.' While attempts to make this measurement should be continued, other methods could be used to try to deduce its value. Nonducted satellite measurements, in conjunction with 3-dimensional raytracing, could be used to model the ducted wave intensity. Another approach could come from the analysis of data itself. There is a substantial agreement between data and theory suggesting that sideband triggering in two-wave experiments [Helliwell *et al.*, 1986] is related to the relationships amongst the trapping regions in phase space [Luis Sa, personal communication]. The v_{\parallel} widths of these regions are proportional to the square root of the wave intensity. An experiment from Siple Station during the 1986-87 season (acronymed CBEX) is specifically intended to help determine the applied wave intensity. This experiment varied the frequency spacing and intensity of two constant frequency signals. If the trapping region relationships govern sideband triggering, then the square root of the threshold power for sideband triggering could be proportional to the frequency separation.

Simulations

The main emphasis for future simulations should be to increase the v_{\parallel} range. Simulations using a single v_{\parallel} are able to fit some of the main features of the data,

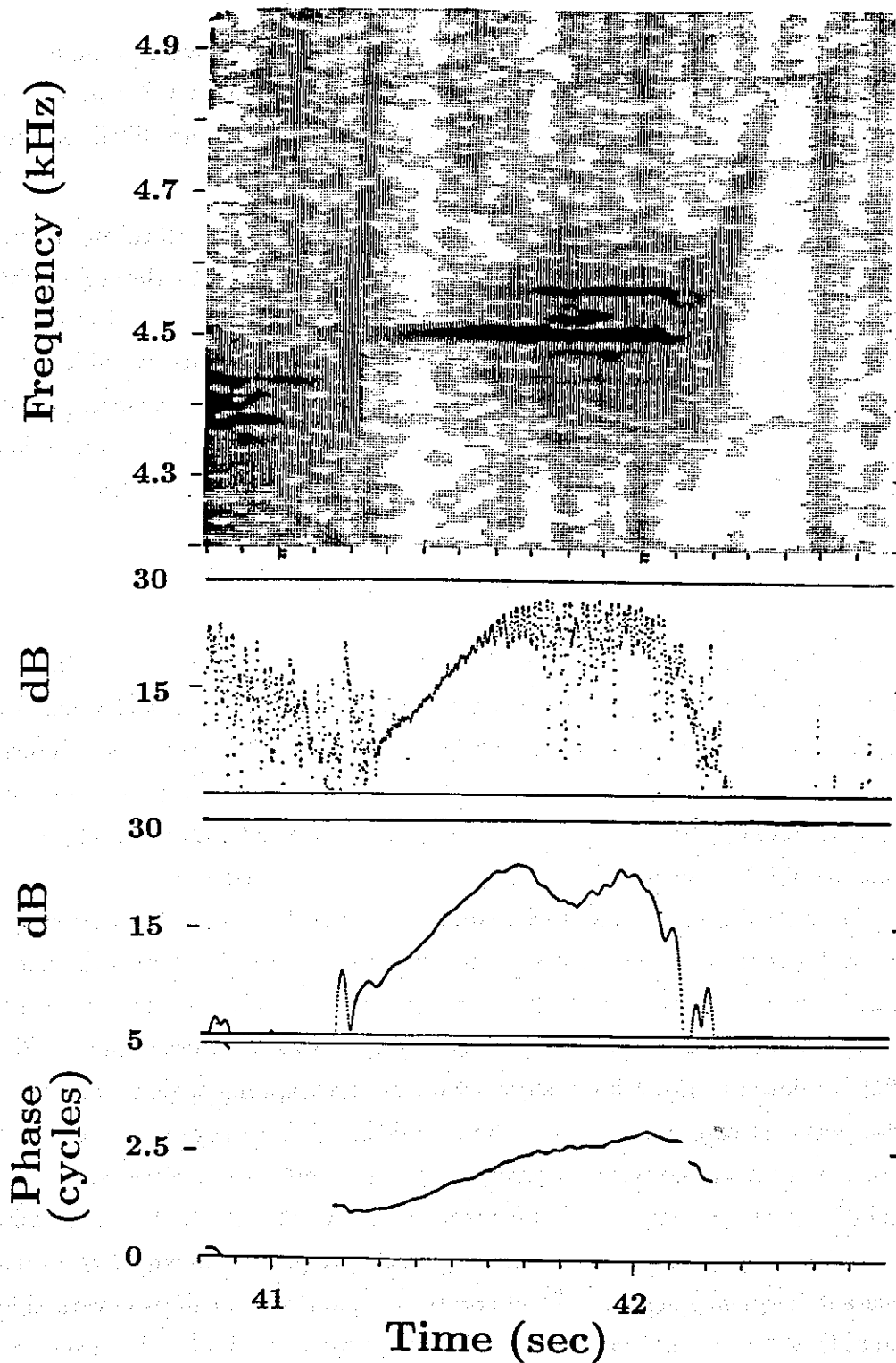


Figure 5.1. A 0.5 second pulse with sideband activity visible in the spectrogram (top panel). The amplitude profile made with a 160 Hz filter bandwidth (upper middle) shows exponential growth up to saturated level. However, a 20 Hz filter bandwidth (lower middle) reveals that energy is 'sloshing' to, from, and between the sidebands. The phase advance (bottom) is nearly linear indicating a constant frequency offset of ~ 2.5 Hz.

like growth rate, total growth, and rate of frequency increase. However, to simulate many features it is expected that a broad range of v_{\parallel} 's will be required. These features include band limited impulses [Helliwell, 1979], positive frequency offsets at pulse termination [Stiles, 1974], enhanced frequency and amplitude oscillations or sidebands, entrainment of free running emissions by other signals [Helliwell and Katsufakis, 1978], and emission triggering. An example of a pulse with intricate spectral detail is shown in Figure 5.1. Two amplitude versus time profiles are shown in Figure 5.1 for two different filter bandwidths. The top amplitude versus time panel was made using a 160 Hz wide filter and shows well defined amplitude modulation of the saturated signal with the peak saturated level remaining nearly constant with time. However, the narrower band filter used in the bottom amplitude versus time profile shows a very deep and slow oscillation in the saturated level at the center frequency. This comparison suggests that while the peak saturated level remains constant in the broadband sense, wave energy is 'sloshing' to, from, and between the sidebands. The phase advance in Figure 5.1 is nearly linear. A survey indicates that this linear phase advance rate tends to be common at times when there is strong sideband excitation. Simulations capable of reproducing the features seen in Figure 5.1 are likely to require a broad range of v_{\parallel} 's.

Many simulation output parameters, including growth rate and total growth, are shown to be dependent upon the v_{\parallel} range. Immediate benefits resulting from an increased v_{\parallel} range include a more rapid convergence of the leading edge phase and amplitude oscillations, and a reduced growth rate which can be offset by increases in the flux. An increased flux will increase both the growth rate and the total growth. The total growth can be reduced to the desired number of dB's by increasing the applied wave intensity. This is desirable because some satellite measurements indicate that at times, the applied wave intensity could be an order of magnitude higher than what is used in the last chapter. However, as mentioned before, it is not known how these measurements relate to ducted wave intensities. An increased v_{\parallel} width will also allow the leading edge taper to be reduced. A 50 msec taper is used in all of the simulations in the last chapter in order to reduce the oscillatory growth of rotating currents caused by the electrons being introduced into the wave. However, a previous study indicates that the same reduction can be achieved by integrating over α and v_{\parallel} , thus allowing the leading edge taper duration to be reduced to a more realistic value.

It is also not clear whether the saturation mechanism in the simulations is the

same as the actual saturation mechanism. For a narrow v_{\parallel} range, the field will saturate when $T_b/T_r < 1$ for all but the small pitch angles. However, even at large pitch angles, there will always be v_{\parallel} 's for which this condition is not met. These other v_{\parallel} 's are either nonresonant or are resonant off the equator. Therefore it is possible that the inhomogeneity reduces the ability of these offequatorially resonant electron to contribute significantly to the growth. It could also be that emission triggering or a loss of coherence, like a buildup of sideband energy, causes saturation. Plotting the saturation level versus energetic electron flux and the width of the v_{\parallel} range would provide a means for investigating the causes of saturation. Also, the steady state, small flux calculations, show that once $T_b/T_r < 1$ is reached for the equatorially resonant, middle pitch angle electrons, then the relative contributions from the offequatorial electrons becomes greater. This could lead to a loss of coherence if the interaction region gets sufficiently elongated so that feedback processes on one side of the equator begin to show independence from the other side.

The expected df/dt versus the other parameters needs to be explored. In the last chapter, the maximum likelihood df/dt is determined for only one set of parameters in the driven (30 Hz/s) and self excited (none) cases. However, the maximum likelihood df/dt should be calculated versus the other parameters as are the growth rate and total growth. Of special interest is the self excited case which, for the case in the previous chapter, shows no expected df/dt when applying the maximum-likelihood test. Experimentally, the termination of a pulse can trigger self excited falling emissions that are preceded by a positive frequency offset. It is expected that a range of v_{\parallel} 's would be required to simulate the positive frequency offset. The falling emission itself is thought to imply a drifting of the interaction region upstream across the equator. If this is the case, then, as is outlined in the last chapter, higher order terms should be added to the injection v_{\parallel} selection function.

Simulations including noise and multiple waves should be performed. The capability for adding noise is already included in the transient model but has not yet been explored. The noise model is given in Appendix A. These capabilities will allow phenomena like suppression and the power threshold for growth to be simulated. Also, the importance of coherence can be studied. One theory for the power threshold is simply related to the signal to noise ratio within the interaction region. Preliminary transient simulations suggest that, in order to make the phase advance coincide with the onset of exponential growth in the threshold experiments, the threshold must first be exceeded in the downstream region. Thus, the growth in the threshold case

evolves very much like the growth in the standard transient cases. The effect of weak noise or power line harmonic radiation should also be studied. Weak line radiation could have a significant effect on sideband growth and structure (*Luis Sa*, personal communications) and both line radiation and noise could partially control the wave phase or establish the frequency offset near the leading edge.

Other parameters remain to be explored and should be varied in future simulations. These include the equatorial electron density, non-dipole field geometries, and interaction regions at other L-shells both within and outside the plasmopause.

Optimize computer code

As computer speed and memory size continue to increase, as new computer architectures emerge including parallel processors, and as the price of powerful computer systems continues to drop, the way in which simulations should be carried out will continue to change. To increase the v_{\parallel} width will require more computing power locally (more power than a VAX/780) and access to supercomputers. Unmodified, the transient code runs 40 times faster on a CRAY-1 than on a VAX/780 and vectorization gave another factor of 2 speedup, and neither of these systems is presently state of the art. Besides porting the code to more powerful computer systems, there are other steps which can be taken to optimize the execution of the computer code. After vectorization, tests show that on a CRAY-1, 50% of the execution time is spent calculating sines and cosines, particularly the trigonometric functions within the equations of motion. A possible improvement could be to use a different coordinate system in which trigonometric functions are not required within the equations of motion. An example of such a system and set of equations is given in Appendix B. Another obvious method for speedup would be the coding of the electron trajectory solver in assembly language.

The sampling schemes used in the present code are also not optimal. These schemes create a uniform velocity space mesh in pitch angle and parallel velocity and a constant spatial step size. The required velocity space sample spacing and spatial step size, all depend upon the parallel velocity and pitch angle. Thus the worst case determines the maximum step sizes. A possible improvement would be to have nonuniform meshes or even adaptively determine the mesh spacing as the calculations proceed.

Appendix A. Noise generation

This appendix outlines the procedure for generating the whistler-mode noise which is included in the transient program ZT.FOR listed in Appendix C. Gaussian noise of unity variance can be generated using a random number generator and the following procedure

$$\lim_{N \rightarrow \infty} \sqrt{\frac{12}{N}} \left[\left(\sum_{i=1}^N x_i \right) - \frac{N}{2} \right], \quad (\text{A.1})$$

where x_i is a random number uniformly distributed between 0 and 1. Approximating Gaussian noise by taking $N = 4$ gives

$$n_x = \sqrt{\frac{3}{2}} \left[\left(\sum_{i=1}^4 x_i \right) - 2 \right], \quad (\text{A.2})$$

where a factor of $1/\sqrt{2}$ has been included so that the variance of the total noise

$$n = n_x \hat{x} + n_y \hat{y}, \quad (\text{A.3})$$

will have unity variance with n_x and n_y being the magnitude of the noise in phase and in quadrature with the reference wave field.

To include this noise in the transient model requires the noise to be in the form of 2-dimensional arrays over position and time

$$n_x(i, j), \text{ and } n_y(i, j), \quad (\text{A.4})$$

where i and j are the array indices for z and τ respectively. However, the noise should be bandlimited in order to assure numerical stability. Since \hat{x} and \hat{y} are with respect to the reference wave, bandlimiting the noise is equivalent to lowpass filtering these components. The lowpass filter scheme shown here will limit the highest noise frequency to be one-quarter cycle per increment in both z and τ . In this way, no matter what the electron trajectory is, the noise will be smoothly varying. The corresponding 1-dimensional impulse response is

$$h(i) = \begin{cases} 1/2, & \text{for } i = 0; \\ \sin(i\pi/2)/i\pi, & \text{otherwise.} \end{cases} \quad (\text{A.5})$$

which is equivalent to the following sequence:

$$\dots, 0, -\frac{1}{7\pi}, 0, \frac{1}{5\pi}, 0, -\frac{1}{3\pi}, 0, \frac{1}{\pi}, \frac{1}{2}, \frac{1}{\pi}, 0, -\frac{1}{3\pi}, 0, \frac{1}{5\pi}, 0, -\frac{1}{7\pi}, 0, \dots$$

The 2-dimensional impulse response, by which the noise arrays should be convolved, is simply

$$h(i, j) = h(i)h(j). \quad (\text{A.6})$$

However, it is not practical to convolve with an infinite sequence, so the impulse response must be limited. Simply truncating the sequence results in significant side-lobes above the cutoff frequency. Therefore, the impulse response should be limited by a weighting function which smoothly goes to zero. An excellent weighting function for this purpose is the binomial distribution

$$w(i) = w(k - n/2) = \begin{cases} \binom{n}{k} \frac{1}{2^n}, & \text{for } |i| \leq n/2; \\ 0, & \text{otherwise} \end{cases} \quad (\text{A.7})$$

where n must be even. The weighted, 2-dimensional impulse response becomes

$$s(i, j) = A_n w(i, j) h(i, j) = A_n w(i) h(i) w(j) h(j), \quad (\text{A.8})$$

In order to maintain unity variance after convolving the unity variance noise by this finite impulse response filter, equation (A.8) must be normalized by

$$A_n = \left(\sum_{i=-n/2}^{n/2} (w(i)h(i))^2 \right)^{-1}. \quad (\text{A.9})$$

In the transient simulation code, $n = 12$ which eliminates all terms beyond and including $-1/(7\pi)$ in $h(i)$ and results in the following sequence for $w(i)h(i)$:

$$\frac{3}{5120\pi}, 0, -\frac{55}{3072\pi}, 0, \frac{99}{512\pi}, \frac{231}{2048}, \frac{99}{512\pi}, 0, -\frac{55}{3072\pi}, 0, \frac{3}{5120\pi}$$

The corresponding normalizing constant for equation (A.8) is

$$A_{n=12} \simeq 49. \quad (\text{A.10})$$

When convolving, additional random numbers are supplied when $s(i, j)$ overhangs an edge of the noise array. This turned out to be easier than implementing a 2-dimensional circular convolution.

Appendix B. Equations of motion

The equations of motion given in Chapter 2 were derived using v_{\parallel} , v_{\perp} , and ϕ as the velocity space basis. One drawback associated with using these equations is the required calculation of sines and cosines of ϕ , which can be CPU intensive. The purpose of this appendix is to derive a new set of equations of motion which will not require the computation of trigonometric functions. A rectangular velocity space coordinate system v_x , v_y , and v_{\parallel} will be used, where v_x and v_y are the velocity components in the \hat{x} and \hat{y} directions. A sketch of this coordinate system is given in Figure 2.3 except here, \hat{x} remains aligned with the reference wave magnetic field. To account for the rotation of an electron with respect to this coordinate system, an equivalent magnetic field is created

$$\mathbf{B}_R = -\frac{m}{e}k(v_R - v_{\parallel})\hat{z}. \quad (\text{B.1})$$

The Lorentz force equation

$$\mathbf{F} = -e[\mathbf{E}_w + \mathbf{v} \times \mathbf{B}_w]. \quad (\text{B.2})$$

can be expanded to

$$\mathbf{F} = -e[E_x\hat{x} + E_y\hat{y}] - e \begin{vmatrix} \hat{x} & \hat{y} & \hat{z} \\ v_x & v_y & v_{\parallel} \\ B_x & B_y & B_R \end{vmatrix}. \quad (\text{B.3})$$

Taking advantage of the plane wave relationships,

$$E_x = -v_p B_y \quad \text{and} \quad E_y = v_p B_x, \quad (\text{B.4})$$

and including the inhomogeneity through the adiabatic equations of motion gives

$$\frac{dv_x}{dt} = -\frac{e}{m}(v_y B_R - (v_p + v_{\parallel})B_y) + \frac{v_x v_{\parallel}}{2f_H} \frac{\partial f_H}{\partial z}, \quad (\text{B.5a})$$

$$\frac{dv_y}{dt} = -\frac{e}{m}((v_p + v_{\parallel})B_x - v_x B_R) + \frac{v_y v_{\parallel}}{2f_H} \frac{\partial f_H}{\partial z}, \quad (\text{B.5b})$$

$$\frac{dv_{\parallel}}{dt} = -\frac{e}{m}(v_x B_y - v_y B_x) - \frac{v_x^2 + v_y^2}{2f_H} \frac{\partial f_H}{\partial z}, \quad (\text{B.5c})$$

$$\frac{dz}{dt} = v_{\parallel}. \quad (\text{B.5d})$$

Appendix C. Program Documentation

This appendix contains the documentation and listing for the VAX/780 version of the transient program ZT.FOR. Although several other programs were written and used in the course of this research, they will not be documented here except for the following partial listing:

ZT.FOR	Transient simulation program which outputs wave intensity versus position and time.
ZTPLOT.FOR	Plotting program for ZT.FOR.
SIMU.FOR	Steady state simulation program which outputs current versus $v_{ }$, α , and z .
SIMP.FOR	Integrates the currents from SIMU.FOR to give steady state current and radiation versus various parameters.
ETRA.FOR	Calculates and plots many aspects of the trajectories of a group of electrons versus z . Also calculates and plots interaction length information.

All parameters, variables, and arrays in ZT.FOR, associated include files and subroutines obey the following rules for precision in this VAX version of the transient simulation program.

1. Names beginning with a-h or o-z are double precision real numbers (real*8) except arrays with names beginning with the letter s, which are single precision (real*4), and the character string `filen` (character*13).
2. Names beginning with i-n are single precision integers (int*4).

All input variables are indicated by **Input** as the first word in their descriptions.

Parameters

The following is a list of all parameter names (always written with capital letters in the program), values, and definitions.

ACCURACY = 1	Iteration error for the root finder algorithm in subroutine <code>latitude</code> .
--------------	---

ADJ = 1.e-15	Adjustment factor used for keeping the stimulated radiation calculation from underflowing.
C = 2.997925e8	Speed of light (m/s).
CC = C*C	Speed of light squared.
C2M = 511.0041176	Electron rest mass energy (keV).
CF = 3.077827553e-3	$\frac{\Omega^2 R_1^5}{2g_0 R_0^3}$. A coefficient in the geopotential height term of the diffusive equilibrium equation.
DISC = U002*QPOA*0.5	The product of all constants required to convert Σv_1 to B_s .
EOM = 1.7588028e11	Electron charge to mass ratio e/m . Used to scale the wave magnetic field in the equations of motion.
H1 = 00T/70.93906493	The reciprocal of the O+ scale height at 1000 km altitude. $H_i = \frac{kT}{m_i g_0} \left(\frac{R_1}{R_0} \right)^2$. H1, H2, H3, S1, S2, and S3 are terms in a DE-1 diffusive equilibrium model.
H2 = 00T/1126.582431	The reciprocal of the H+ scale height at 1000 km altitude.
H3 = 00T/283.5903962	The reciprocal of the He+ scale height at 1000 km altitude.
IPTS = 301	Dimensioning parameter for all spatial and wave field arrays. Establishes the maximum allowable number of spatial steps between upstream and downstream boundaries. Also the maximum number of τ steps between the leading and trailing edges of the wave field.
JTOPT = U002*1.e12	Coefficient for converting a current sheet into magnetic field radiation.
MITR = 6	The maximum number of iterations that will be performed by the Predictor-Corrector algorithm before declaring 'no convergence'.
0024 = 1./24.	Not used in the present version.
00T = -1./1.6e3	-1/T where T is the electron temperature at 1000 km altitude.
P1 = 4./3.	A parameter used in the Predictor.
P2 = 112./121.	A parameter used in the Predictor.
PHIE0 = 1.6261264e-17	The multiplying constant A in the distribution function of the form $f(E, \alpha_{eq}) = Ag(\alpha_{eq})E^{-n/2}$. The differential energy spectrum and reference energy were taken to be 10^{12} and 1 keV, respectively.
PI = 3.141592653589793238	π

PI2 = PI*2.	2π
PI02 = PI*.5	$\pi/2$
PSIO = PI2	Phase offset added to initial electron gyrophases.
Q = 56.41460098	$\sqrt{\frac{e^2}{m\epsilon_0}}$. Part of the plasma frequency term in the wave number calculation.
QE = 1.6021917e-19	Electron charge (C).
QP = C/Q	Not used in this version.
QP0A = PI2*(QE/ADJ)*PHIE0	Product of constants used to calculate the distribution function.
R0 = 6.3712e6	Earth radii (m).
R1 = R0+1.e6	Radii at 1000 km altitude (m).
RIP = PI/180.	Degree to radian conversion factor.
S1 = 0.9	Fractional abundance of O+ at 1000 km altitude.
S2 = 0.08	Fractional abundance of H+ at 1000 km altitude.
S3 = 0.02	Fractional abundance of He+ at 1000 km altitude.
S03 = 7./3.	Not used in this version.
SQR3 = 1.732050807568877	$\sqrt{3}$
U002 = PI2*1.e-7	$\mu_0/2$
WHO = PI2*8.736e5	Coefficient for the dipole model of the gyrofrequency.
YMSF = 236374.	A scaling factor used to determine if the spatial step size needs to be reduced in order for the Predictor-Corrector algorithm to perform properly.

Real variables

bin	Input. Peak applied wave magnetic field (pT).
bmax	Maximum value of $B(r)$. Continuously output to aid monitoring programs progress. Also used to determine the spatial step size for the Predictor-Corrector algorithm.
bw, bwp	Instantaneous magnitude and phase of the wave magnetic field. Phase is with respect to a plane wave at the applied wave frequency ω .
bw0, bwp0	Magnitude and phase of the wave magnetic field at the injection point of the electron into the wave. Phase is with respect to a plane wave at the applied wave frequency.
c1-c7	Temporary variables.
cdbph	Change in wave phase per microstep.

cdwhdz	Change in dw_H/dz per microstep.
cdz	Change in z per microstep.
cwave	Change of the wave magnetic field magnitude per microstep.
cwhz	Change in w_H per microstep.
cykz	Change in $-k$ per microstep.
dd	Predictor-Corrector estimate of the next change in velocity.
ddbph	Change in wave phase per macrostep.
dfdt	Input. df/dt of the applied wave.
dpa	Input. Change in pitch angle between test electrons.
dpha0	Change in cyclotron phase per microstep prior to injection and calculated adiabatically.
dphi	Change in latitude per macrostep.
dpsi	Gyrophase separation between electrons with equal initial pitch angles and velocities.
dpsij	Gyrophase offset added to reference initial cyclotron phase to get actual initial cyclotron phase for each electron.
dt	Time required for an electron to travel to the next microstep.
dtao	Time increment $\Delta\tau$ with which the wave field is divided.
dtle2	Time step per injection at upstream boundry.
dtrtn	Allowable relative difference in cyclotron phase between Corrector iterations.
dvol	Velocity space volume element and other terms.
dvpar	Input. Change in $v_{ }$ between test electrons.
dwdz	dw_H/dz .
dwh0	Change in w_H per microstep at injection.
dwhdz0	Change in dw_H/dz per microstep at injection.
dyb	Part of the cyclotron phase differential equation.
dyk0	Change of $-k$ per microstep at injection.
dz0	Change of z per microstep at injection.
f1, f2, f3	Distance from desired position along field line. Used in the implementation of the Pegasus root finding technique in the subroutine latitude.
fni	Number of macro steps per injection point.

ftao	Floating point value of ntao.
fval	Proportional to the distribution function. Converts Σv_{\perp} to stimulated radiation.
gofaa	Input. The variable a in the pitch angle anisotropy formula $a \sin^n + (1 - a) \sin^m$.
gofam	Input. The variable m in the pitch angle anisotropy formula. See gofaa.
gofan	Input. The variable n in the pitch angle anisotropy formula. See gofaa.
gy	Cyclotron phase.
pa	Initial pitch angle α .
pamax	Input. Maximum pitch angle to be injected.
pamin	Input. Minimum pitch angle to be injected.
patop	Input. Maximum injection pitch angle an electron can have.
phi	Geomagnetic latitude.
phits	Geomagnetic latitude of the field line at 1000 km altitude. Used in the z_to_phi and latitude subroutines.
phzrb	Predictor variable regarding cyclotron phase.
phzrb0	Predictor variable regarding initial cyclotron phase.
req	Equatorial radii.
reqscl	$R_{eq}/2\sqrt{3}$
rmstep	Reciprocal of the number of microsteps per macrostep.
ror	R_1/req
scale	Input. Distribution function scaling factor.
shell	Input. R_{eq}/R_0 ; The L shell of the dipole field line.
spaeq	$\sin(\alpha_{eq})/w_{Heq}$.
spamin	spaeq corresponding to pamin.
srms	Input. RMS noise intensity in pT.
t	A working variable related to τ .
tfend	Inputs. Wave pulse shaping parameter for the initial applied wave. Indicates the τ at which the leading edge of the wave field is brought up to full.
tstart, tend	Inputs. Wave pulse shaping parameters for the initial applied wave. tstart and tend are the starting and ending τ 's over which the wave field trailing edge is tapered to zero.
time	Real time.

timeout	τ at the injection point. Only nonzero after the leading edge has propagated past the upstream boundary.
tout	Input. The amount of time for which the wave leading edge is allowed to propagate past the upstream boundary.
tp	The pulse duration and the total τ over which stimulated radiation is calculated.
trtn	Input. Total sum of relative iteration errors allowed for an electron moving from the upstream boundary to the downstream boundary.
tsum	Variable used to determine if an electron is resonant with the trailing edge of the wave.
v	Total electron velocity (m/s).
v1	Predictor-Corrector v_{\parallel} .
v2	Predictor-Corrector v_{\perp} .
vazrb	Predictor variable regarding v_{\parallel} .
vazrb0	Predictor variable regarding initial v_{\parallel} .
vdft	Input. Resonance frequency drift rate at the point vz .
ve2	Initial v_{\perp}^2 at injection.
vezrb	Predictor variable regarding v_{\perp} .
vezrb0	Predictor variable regarding initial v_{\perp} .
vpa0	Initial v_{\parallel} at injection.
vpamin	Minimum $v_{\parallel eq}$ (m/s).
vpamax	Input. Maximum $v_{\parallel eq}$ expressed as a percentage offset from $v_{R_{eq}}$.
vpamin	Input. Minimum $v_{\parallel eq}$ expressed as a percentage offset from $v_{R_{eq}}$.
vpe0	Initial v_{\perp} at injection.
vpow	Input. n in the distribution function $v^{-n}g(\alpha)$.
vv	Velocity squared.
vz	Input. The point z , at which the center v_{\parallel} of the distribution function begins to drift in accordance with a frequency drift rate specified by vdft which is given in (Hz/s).
w	The reference wave frequency.
wheq	Equatorial gyrofrequency.
whmw	$\omega_H - \omega$.
whoreq	A term used in calculating $d\omega_H/dz$.

whowheq	w_H/w_{Heq} .
whz	w_H at each microstep.
wowheq	Input. Frequency divided by the equatorial gyrofrequency.
x1, x2, x3	Latitudes corresponding to f1 , f2 , and f3 . Used in the implementation of the Pegasus root finding technique in the subroutine latitude .
ykz	Scaling factor for calculating the wave number.
yzk	$-k$ at each microstep.
yms	Parameter used to calculate the number of microsteps per macro step.
ynel	Intermediate term used for scaling in the Diffusive equilibrium model.
yneq	Input. Equatorial cold plasma density (el/cm ³).
yns	Reciprocal of the number of electrons in the gyrophase direction.
z	Position at which the corresponding latitude is desired. Used in the subroutine latitude .
zh	Geopotential height.
zle0	Input. Initial position of the wave leading edge (km).
zm	Magnitude of z in the subroutine latitude .
zpinch	Input. The wave is tapered from the upstream boundary to this position to minimize the effect of particle injection.
zshift	Input. The distance an electron will travel before satisfying the resonance condition.
ztap	The length of the region upstream of the downstream boundary over which B_z is tapered from full strength to zero. This is done to minimize the noise which results from the current discontinuity at the downstream boundary
zts	Field line length from the equator to 1000 km altitude. Used in z.to.phi and latitude subroutines.
zdown	Downstream boundary (km).
zwup	Upstream boundary (km).

Character variables

fext	Input. Filename for the ASCII file which contains the gyrofrequency versus position for a nondipole field model. See iext .
filen	Input. Filename for the binary output file to which the B , z and t versus τ arrays are written. This information is then read and transformed into B versus z and t

information by the program ZTPLOT.FOR which then plots this information on various devices.

Integer variables

i,j,k,l,m	Loop counters, array indices, and temporary variables.
idist	Input. Specifies the relationship between the wave and the distribution function. idist = 0; the center velocity of the distribution remains fixed with respect $v_{R_{eq}}$. idist = 1; vparmin and vparmax are with respect to the minimum and maximum resonant velocity of any electrons injected into the wave at each pitch angle. idist = 2; converts the model to a homogeneous magnetic field and keeps the distribution fixed. idist = 3; the center velocity of the distribution remains fixed with respect to the leading edge resonant velocity. If idist is negative then the distribution center velocity will drift at a constant rate in accordance with a specified frequency drift rate vdfdt, once the leading edge has crossed the point vz.
iext	Input. If not set to zero, then the gyrofrequency versus position is read from a file rather than from the dipole model.
ipa	Counter for looping over pitch angle.
iprop	Pointer to the position of the leading edge of the wave. Equal to jprop until leading crosses the upstream boundary at which point iprop goes negative and jprop remains fixed at 1.
ivp	Counter for looping over parallel velocity.
jprop	See jprop1 and iprop.
jprop1	jprop+1. This is the array index pointing to the injection point of the electrons into the wave.
le	The total number of times that the wave is advanced a macrostep and electrons are injected into the wave.
le0	Initially used to point to the starting spatial grid point for the wave. Then used as the counter for the number of times the propagation loop, or 'outer most loop', is executed. The plotting program ztplot.for, uses this number to determine how many arrays were written into filen.
leq	Array index pointing to the geomagnetic equator.
lfe	Number of macrosteps that the electron has advanced into the wave equal to 1 at injection. Index for the arrays storing the time and electron v_{\perp} at each macrostep.
lmax	Array index pointing to the position where the high v_{\parallel} edge of the distribution function is resonant with the trailing edge of the wave pulse.
lmin	Array index pointing to the position where the low v_{\parallel} edge of the distribution function is resonant with the trailing edge of the wave pulse.

lpnch	Array index corresponding to the downstream edge of the wave field taper which smoothly brings the wave intensity to zero at the upstream boundary.
lshift	Number of macro steps corresponding to zshift.
lvz	Array index pointing to the position corresponding to vz.
mstep	The number of microsteps per macrostep.
mz	Input. Number of points from the upstream to the downstream boundary, inclusively.
n	Input. Number of electrons per gyrophase.
nfend	Array index pointing to the τ at which the leading edge applied wave intensity has become full strength. Corresponds to tfend.
ni	Input. Number of macro steps per injection point.
npa	Number of different pitch angles to be injected into the wave.
npah	Median pitch angle. The ipa index at which time and position will be determined.
nstep	Input. Minimum number of microsteps per macrosteps.
ntao	Number of τ steps from the leading edge to the trailing edge of the pulse, inclusive.
ntend	Array index pointing to the τ at which the trailing edge applied wave intensity has become tapered to zero (see tend, tstart).
ntstart	Array index pointing to the τ at which the trailing edge applied wave intensity begins to taper toward zero (see tend, tstart).
nvp	Number of different v_{\parallel} 's to be injected into the wave.
nvph	Median v_{\parallel} . The ivp index at which time and position will be determined.
nvtap	Input. The number of ivp's over which the v_{\parallel} distribution is to be tapered on both the high and low v_{\parallel} edges.

Arrays

There are basically three different categories of arrays. One group of arrays, those with dimension (4), all store velocity vector information at an electron's four previous microstep positions. This information is utilized by the Predictor-Corrector routine. The arrays bwi, bwg, dbi, dbq, sbi, sbq, sbt, sbz, xcr, and ycr are all arrays over τ . All other arrays are spatial arrays extending from the upstream to downstream boundaries. When difference is specified in the following descriptions it implies that

the array is created by taking the difference of adjacent array elements in the specified array.

bwi	(IPTS)	Inphase wave intensity versus τ .
bwq	(IPTS)	Quadrature wave intensity versus τ .
cpa	(IPTS)	Cosine of the local adiabatic pitch angle.
dbi	(IPTS)	Difference of bwi.
dbq	(IPTS)	Difference of bwq.
ddwhdz	(IPTS)	Difference of dwhdz.
dnoi	(IPTS, IPTS)	Difference in τ of snoi.
dnoq	(IPTS, IPTS)	Difference in τ of snoq.
dph	(4)	Cyclotron phase difference between microsteps.
dph0	(4)	Initial adiabatic cyclotron phase difference between microsteps.
dtle	(IPTS)	Difference of tle.
dva	(4)	v_{\parallel} difference between microsteps.
dva0	(4)	Initial adiabatic v_{\parallel} difference between microsteps.
dve	(4)	v_{\perp} difference between microsteps.
dve0	(4)	Initial adiabatic v_{\perp} difference between microsteps.
dwh	(IPTS)	Difference of wh.
dwhdz	(IPTS)	$\frac{dwh}{dz}$.
dyk	(IPTS)	Difference of yk.
dz	(IPTS)	Difference of z.
ph	(4)	Cyclotron phase.
ph0	(4)	Initial adiabatic cyclotron phase.
pnch	(IPTS)	Spatial wave field intensity shaping factor. This term includes the upstream taper and the field line convergence factor.
sbi	(IPTS)	Inphase wave intensity versus τ . Single precision.
sbq	(IPTS)	Inphase wave intensity versus τ . Single precision.
sbt	(IPTS)	Time versus τ . Single precision.
sbz	(IPTS)	Position versus τ . Single precision.
snoi	(IPTS, IPTS)	Inphase noise component versus z and τ .

snoq	(IPTS, IPTS)	Quadrature noise component versus z and τ .
t1e	(IPTS)	Time at which the wave pulse front will be at each point in space.
tz	(IPTS)	Spatial array of τ for an electron whose first element corresponds to the injection τ .
va	(4)	v_{\parallel} .
va0	(4)	Initial adiabatic v_{\parallel} .
ve	(4)	v_{\perp} .
ve0	(4)	Initial adiabatic v_{\perp} .
vres	(IPTS)	Local resonant velocity.
vx	(IPTS)	v_{\perp} in the direction of the negative reference wave field.
vy	(IPTS)	v_{\perp} in quadrature to the direction of the negative reference wave field.
wh	(IPTS)	Gyrofrequency ω_H .
xcr	(IPTS)	Proportional to the perpendicular current component in phase with the reference wave field versus τ .
ydr	(IPTS)	Proportional to the perpendicular current component in quadrature with the reference wave field versus τ .
yk	(IPTS)	Negative wave number $-k$.
z	(IPTS)	Position measured from the geomagnetic equator and is positive in the direction of electron v_{\parallel} . Increasing z is decreasing latitude since electrons go from north to south in this model.
ztt	(IPTS)	An electrons' real time. First element corresponds to the time of injection.

ZT.FOR listing

Transient simulation of whistler-mode wave growth

```

program Transient
implicit real*8 (a-h, o-z)
parameter ( IPTS = 301 )

dimension
+
+ va(4) , ve(4) , ph(4) ,
+ dva(4) , dve(4) , dph(4) ,
+ va0(4) , ve0(4) , ph0(4) ,
+ dva0(4) , dve0(4) , dph0(4) ,
+ bwi(IPTS) , bwq(IPTS) , tle(IPTS) ,
+ wh(IPTS) , dwhdz(IPTS) , yk(IPTS) ,
+ dwh(IPTS) , ddwhdz(IPTS) , dyk(IPTS) ,
+ dz(IPTS) , xcr(IPTS) , ycr(IPTS) ,
+ vres(IPTS) , ztt(IPTS) , tz(IPTS) ,
+ vx(IPTS) , vy(IPTS) , z(IPTS) ,
+ pncch(IPTS) , cpa(IPTS) , dtle(IPTS) ,
+ dbi(IPTS) , dbq(IPTS) ,
+ snoi(IPTS+10, IPTS+10) , snoq(IPTS+10, IPTS+10),
+ dnoi(IPTS+10, IPTS+10) , dnoq(IPTS+10, IPTS+10)

real*4 sbi(IPTS), sbq(IPTS), sbt(IPTS), sbz(IPTS)
character*13 filen

include 'user1:[curr.dir.library]simula (parameter)/list'

open (unit = 15, file = 'zt.dat', status = 'old')
read (15, *) vparmin, vparmax, dvpar, nvtp, idist
read (15, *) pamin, pamax, patop, dpa
read (15, *) wowheq, bin, srms, dfdt
read (15, *) zle0, tp, tout
read (15, *) zwup, zdown, ztap
read (15, *) tfebd, tstart, tend, zpinch
read (15, *) yaeq, shell, mz, ni
read (15, *) trtn, nstep, n
read (15, *) scale, vpow, vz, vdfdt, zshift
read (15, *) gofaa, gofan, gofam
read (15, 1) filen
read (15, *) iext
read (15, 1) fext
close (unit = 15)
format (a)

if (zle0 .gt. zdown) zle0 = zdown
zpinch = zwup+zpinch
ztap = zdown-ztap
zle0 = zle0 *1000.
zwup = zwup *1000.
zdown = zdown*1000.
zpinch = zpinch*1000.
ztap = ztap *1000.
vz = vz *1000.
zshift = zshift*1000.
tout = min(tout, tp)
yaeq = YMSF/shell
yaeq = 1./float(n)
dpsi = pi2*yaeq
trtn = trtn*.01/float(mz)
vparmin = 1.+0.1*vparmin
vparmax = 1.+0.1*vparmax

if (iext .ne. 0) then
open (unit = 15, file = 'fext.dat', status = 'old')
do 5 i = 1, mz
read (15, *) z(i), wh(i)
if (z(i) .le. 0.) leq = i
if (i .gt. 1) dwhdz(i-1) = (wh(i)-wh(i-1))/(z(i)-z(i-1))
5 continue
close (unit = 15)
if ((zwup .ne. z(i)) .or. (zdown .ne. z(mz))) then
write (6, *) z(1), z(mz)
stop
end if
dwhdz(mz) = 2.*dwhdz(mz-1)-dwhdz(mz-2)
whq = wh(leq)
end if

if (iext .eq. 0) whq = WH0/(shell**3)
req = R01*shell
reqscl = -req*0.5/SQR3
ror = R1/req
cl = R1*CF/shell
c7 = -cl/ror**3
c6 = R1*cl
whoreq = -1.5/(SQR3*req)
w = wowheq*whq
zh = c6-R1*ror+c7
ynel = sqrt(S1*exp(zh*R1)+S2*exp(zh*R2)+S3*exp(zh*R3))
yk = -Q*sqrt(w*yaeq*1.e6/ynel)/C
dvpar = 0.1*dvpar*(w-whq)*sqrt((whq-w)/ynel)/ykc
dpa = dpa*RIP
vpow = -vpow*.5
scale = scale*DISC*dpa*dvpar*yne
pamin = pamin*RIP
pamax = pamax*RIP
patop = patop*RIP

```

< Dimension for spatial and tau arrays

< Velocity vector history for predictor corrector (P-C)
 < Velocity vector difference history for P-C
 < Initial adiabatic velocity vector history for P-C
 < Initial adiabatic velocity difference history for P-C
 < Wave components and leading edge time versus z
 < Gyrofrequency, its spatial derivative, and -k versus z
 < Differences of above versus z
 < Spatial difference versus z and J components versus tau
 < Resonant velocity, time, and tau versus z
 < Perpendicular velocity components and z versus z
 < Spatial wave window, adiabatic term, and tle differences
 < Wave differences versus tau
 < Noise versus position and tau
 < Difference of noise versus position and tau

< Wave components, time, and z output arrays versus tau

< Binary output file name

< Parameter statements

< Ascii input file for job parameters
 < Parallel velocity range and position
 < Pitch angle range and clipping
 < Frequency, wave and noise amplitude, and df/dt
 < Initial leading edge position, pulse length, and time out
 < Boundary positions and downstream boundary J taper width
 < Wave pulse windowing parameters
 < Equator el den, L-shell, # of macro steps, steps per injec
 < Iteration error, # of micro/macro steps, and # of e's/gyro
 < Distribution scale, exponent, drift z and rate, shift
 < G of alpha parameters a, b, m
 < Output file name
 < Flag for inputting a nondipole field
 < Filename containing the nondipole field model

< Limit initial leading edge position to downstream boundary
 < Change zpinch range to zpinch boundary position
 < Change ztap range to ztap boundary position
 < Convert all kilometers to meters

< Avoid propagating entire pulse past upstream boundary
 < Micro step size calculation parameter
 < Reciprocal of # of electrons per gyrophase
 < Radians per electron in gyrophase
 < Convert total percent error to error per macro step
 < Converted to parallel divided by resonant velocity

< Calculate medium parameters using dipole and de models

< Ascii file for field model

< Read position and gyrofrequency
 < Find equatorial index
 < Derivative of gyrofrequency wrt position

< Do model endpoints match input values

< If not, STOP

< Approximate last dwhdz value
 < Equatorial gyrofrequency

< Equatorial gyrofrequency rad/sec
 < Equatorial radius
 < Various parameters used in DE and Dipole calculations

< Frequency rad/sec
 < Geopotential height
 < Proportional to equatorial electron density
 < Part of the terms necessary to go from ynel to -k
 < Convert delta parallel velocity from percent to m/s
 < Convert delta pitch angle from degrees to radians
 < Change from v'(-vpow) to energy (vpow)
 < Include distribution and volume element terms
 < Convert pitch angle terms to radians


```

+      snoi(i+5, j+2) + snoi(i+5, j+8) ) +
+      c3*(c3*(snoi(i+4, j+4) + snoi(i+4, j+6) ) +
+      snoi(i+6, j+4) + snoi(i+6, j+6) ) +
+      c4*(snoi(i+4, j+5) + snoi(i+6, j+5) ) +
+      c4*(c4*(snoi(i+5, j+4) + snoi(i+5, j+6) ) )
+      snoq(1, j)
+      c1*(c1*(snoq(1, j+10) + snoq(1, j+10) ) +
+      snoq(1+10, j+2) + snoq(1+10, j+10) ) +
+      c2*(snoq(1, j+2) + snoq(1+2, j+2) ) +
+      snoq(1+8, j+8) + snoq(1+10, j+2) ) +
+      snoq(1, j+8) + snoq(1+2, j+10) +
+      snoq(1+8, j+10) + snoq(1+10, j+8) ) +
+      c3*(snoq(1, j+4) + snoq(1+4, j+4) ) +
+      snoq(1+6, j+6) + snoq(1+10, j+4) ) +
+      snoq(1, j+6) + snoq(1+4, j+10) +
+      c4*(snoq(1, j+5) + snoq(1+10, j+5) ) +
+      snoq(1+5, j+10) + snoq(1+5, j+10) ) +
+      c2*(c2*(snoq(1+2, j+2) + snoq(1+2, j+8) ) +
+      snoq(1+8, j+2) + snoq(1+8, j+2) ) +
+      c3*(snoq(1+2, j+4) + snoq(1+4, j+2) ) +
+      snoq(1+6, j+2) + snoq(1+8, j+4) ) +
+      snoq(1+2, j+6) + snoq(1+4, j+8) ) +
+      c4*(snoq(1+2, j+5) + snoq(1+8, j+5) ) +
+      snoq(1+5, j+2) + snoq(1+5, j+8) ) +
+      c3*(c3*(snoq(1+4, j+4) + snoq(1+4, j+6) ) +
+      snoq(1+6, j+4) + snoq(1+6, j+6) ) +
+      c4*(snoq(1+4, j+5) + snoq(1+6, j+5) ) +
+      snoq(1+5, j+4) + snoq(1+5, j+6) ) )
+      c4*(c4*(snoq(1+5, j+5) ) )
44      continue
43      do 45 i = 1, mz
+      do 46 j = 2, ntao
+      dnol(i, j) = snoi(i, j) - snoi(i, j-1)
+      dnog(i, j) = snoq(i, j) - snoq(i, j-1)
46      continue
45      end if
C
+      le = int((le0-2)/ni)
+      le0 = ni*le+2
+      fnl = float(ni)
+      dtle2 = 2.*fnl*dtle(2)
+      le = le+int(tout/dtle2)
+      open (
+      unit = 13
+      status = 'new'
+      file = 'filen'
+      defaultfile = 'star$drbl:[scratch.curt].out')
C
+      write (13, *) ntao, le, bin
+      close (unit = 13)
C
+      i = 1+(ntao*le)/32
+      k = 16*ntao
C
+      open (
+      unit = 12
+      status = 'new'
+      recl = ntao
+      recordtype = 'fixed'
+      form = 'unformatted'
+      initialsize = 1
+      blocksize = k
+      buffercount = 2
+      file = 'filen'
+      defaultfile = 'star$drbl:[scratch.curt].dat')
C
+      vdfdt = vdfdt*PI2*fnl*(dtle(leq)+dz(leq)/vres(leq))*
+      (1.+5./wowheq)/(yk(leq)*vres(leq))
+      lmin = leq
+      lmax = leq
+      timeout = 0.
+      iprop = le0-1
C
+      do 49 le0 = 1, le
+      iprop = iprop-ni
+      jprop = max(iprop, 1)
+      jprop1 = jprop+1
+      if (iprop .lt. 1) then
+      timeout = timeout+dtle2
+      iprop = iprop-ni
+      end if
C
+      write (6, *) iprop, sqrt(bmax), mstep
C
+      do 60 i = 2, ntao
+      dbi(i) = bwi(i)-bwi(i-1)
+      dbq(i) = bwq(i)-bwq(i-1)
+      xcr(i) = 0.
+      ycr(i) = 0.
+      sbt(i) = 0.
+      sbz(i) = 0.
60      continue
+      sbt(1) = 0.
+      sbz(1) = 0.
+      whmv = wh(jprop)-w
+      whowheq = wh(jprop)/wheq
+      tz(1) = timeout
+      ztt(1) = timeout+tle(jprop1)
+      i = int(timeout/dtao)+1
+      sbi(i) = bwi(i)
+      sbq(i) = bwq(i)
+      sbz(i) = z(jprop1)
+      sbt(i) = ztt(1)
C
+      if (spamin*sqrt(wh(jprop)) .le. sin(patop)) then
+      cl = min(sin(pamax)*sqrt(wh(jprop)/wheq), sin(patop))
+      cl = asin(cl*sqrt(wheq/wh(jprop)))
+      pa = pamin
+      npa = max(int((cl-pa)/dpa)+1, 1)
+      npah = 1+npa/2

```

< Noise differences in tau

< Adjust le0 so iprop-1 will be an injection point
 < Number of macro steps per injection
 < Time step for advancing the wave past upstream boundary
 < Total number of times leading edge will be advanced
 < Open file for filen.out

< Write statistics necessary to read filen.dat

< Allocation for output file
 < Blocksize

< Open unformatted output file filen.dat, on scratch disk

< Convert df/dt to d(parallel velocity)/dt

< Initialize resonance condition reference points

< Time elapsed since leading edge passed upstream boundary
 < Initialize pulse front index

< Loop over advancement of wave for electron injection
 < Update pulse front index
 < Limit actual pulse front to not be past upstream boundary
 < Injection point index. Adiabatic motion prior to jprop1
 < Is leading edge past upstream boundary
 < Time past since pulse front has crossed upstream boundary
 < Leading edge advanced twice once past bountry

< Write to standard output for monitoring progress

< Initialize tau arrays
 < Inphase wave differences
 < Quadrature wave differences
 < Inphase current
 < Quadrature current
 < Time
 < Position

< Clear first time element
 < Clear first position element
 < Gyrofrequency - reference frequency at pulse front
 < Normalized pulse front gyrofrequency
 < Injection tau
 < Injection time
 < Injection tau index
 < Set output elements since J is zero at injection point

< Loops over parallel velocity and pitch angle
 < If any pitch angles are below clipping pitch angle
 < Clip maximum injection pitch angle
 < Map maximum pitch angle back to the equator
 < Initialize pitch angle to minimum pitch angle
 < Determine number of pitch angle steps
 < The ipa index when time and position will be determined


```

C
+ if ((abs(idist).eq. 3) .and.
  ((idist.ne. -3) .or. (iprop.gt. lvz))) then
  lmin = jprop1
  lmax = jprop1
end if
if ((iprop.le. lvz) .and. (idist.lt. 0)) then
  vparmax = vparmax+vdifdt
  vparmin = vparmin+vdifdt
end if

C
do 50 ipa = 1, npa
  cl = sin(pa)
  spaeq = cl/sqrt(whz)
  do 55 i = 1, mz
    cpa(i) = 1./sqrt(1.-spaeq*spaeq*wh(i))
    continue
  dv01 = scale*(gofaa*cl**gofan+(1.-gofaa)*cl**gofam)*
    sin(pa+pa)*cpa(jprop)/whz
  + if ((abs(idist).eq. 1) .and.
    ((idist.ne. -1) .or. (iprop.gt. lvz))) then
    tsum = 0.
    l = jprop1
  C
  54
    l = l+1
    tsum = tsum+dz(l)*cpa(l)
    cl = tsum/(vres(l)*cpa(l))-tle(l)+ztt(l)
    if ((cl.lt. tp) .and. (l.lt. mz)) go to 54
    if (vres(jprop1).gt. vres(l)) then
      lmin = l
      lmax = jprop1
    else
      lmin = jprop1
      lmax = l
    end if
    if ((l.gt. leq) .and. (jprop1.lt. leq)) lmin = leq
  end if
  i = max(lmin+lshft, 1)
  i = min(i, mz)
  l = max(lmax+lshft, 1)
  l = min(l, mz)
  vparmin = vparmin+vres(i)
  vpa0 = vparmin*cpa(i)/cpa(jprop)
  nvp = max(int((vparmax-vres(l)*cpa(l)/cpa(jprop)-
    vpa0)/dvpax)+1, 1)
  + nvp = l+nvp/2
  C
  do 51 ivp = 1, nvp
    v = vpa0*cpa(jprop)
    vv = v*v
    mstep = nstep*(1.+yms*sqrt((wh(lmin)-w)*sqrt(bmax)-
    + vv/(vparmin*vparmin)-1.)))/vparmin
    rstep = 1./float(mstep)
    dwh0 = rstep*dwh(jprop1)
    dwhdz0 = rstep*dwhdz(jprop1)
    dyk0 = rstep*dyk(jprop1)
    dz0 = rstep*dz(jprop1)
    dtrtn = rstep*trtn
    dpha0 = (whw/vpa0+yk(jprop1))*dz0
    ykz = yk(jprop1)
    dwdz = dwhdz(jprop1)
    whz = wh(jprop1)
    cl = v*spaeq
    vpe0 = cl*sqrt(wh(jprop1))
    if (iprop.eq. jprop) then
      c2 = fni*(dtle(jprop1)+dz(jprop1)/vpa0)
    else
      c2 = dtle2
    end if
    fval = dv01*vv*((C2M/sqrt(1.-vv/CC)-C2M)**vpow)*c2
  C
  if (nvtap.lt. 0) then
    if (2*ivp.lt. nvp+1) then
      fval = fval*float(2*ivp)/float(nvp+1)
    else
      fval = fval*2.*(1.-float(ivp)/float(nvp+1))
    end if
  else
    if (ivp.le. nvtap)
      fval = fval*sin(PI02*float(ivp)/float(nvtap+1))**2
    + if (ivp.gt. nvp-nvtap)
      fval = fval*sin(PI02*float(nvp-ivp+1)/
    + float(nvtap+1))**2
  end if
  C
  do 52 j = 4,1,-1
    ve0(j) = cl*sqrt(whz)
    ve2 = ve0(j)+ve0(j)
    ve0(j) = sqrt(vv-ve2)
    dt = dz0/va0(j)
    dva0(j) = -ve2*dwdz*dt
    dve0(j) = ve0(j)*dwdz*dz0
    dph0(j) = (whz-w+ykz*va0(j))*dt
    ykz = ykz-dyk0
    dwdz = dwdz-dwhdz0
    whz = whz-dwh0
  C
  52
  continue
  ph0(1) = (dpha0+dph0(1))*5+PSI0
  do 53 j = 2,4
    ph0(j) = (dph0(j-1)+dph0(j))*5+ph0(j-1)
  C
  53
  continue
  vazrb0 = vpa0*pl*(2.*(dva0(1)+dva0(3))-dva0(2))
  vezrb0 = vpe0*pl*(2.*(dve0(1)+dve0(3))-dve0(2))
  phzrb0 = PSI0*pl*(2.*(dph0(1)+dph0(3))-dph0(2))
  dpsj = 0.
  if (timeout.eq. 0.) then
    c1 = bwi(1)+snoi(jprop1,1)
    c2 = bwq(1)+snoq(jprop1,1)
  else
    t = tz(1)/dtao
    i = int(t)-1
    t = t-float(i)
    c1 = (dbi(i+1)+dnoi(jprop1,i+1))*t+
    + bwi(i+1)+snoi(jprop1,i+1)
    c2 = (dbq(i+1)+dnoq(jprop1,i+1))*t+
    + bwq(i+1)+snoq(jprop1,i+1)
  end if

```

< Is distribution velocity center relative to pulse front
 < but not drifting yet
 < Pulse front index to minimum and maximum resonant velocity

 < Is distribution velocity center drifting
 < Appropriately drift velocity limits

 < Loop over pitch angle

 < Term for adiabatic mapping to and from the equator

 < Volume element and related terms within current integral
 < Check if distribution center velocity is relative to wave
 < but-not-yet drifting
 < Initialize integrand for tau of locally resonant electron
 < Pulse front index

 < Advance position index
 < Increase tsum by amount related to tau
 < Tau for locally resonant electron
 < Continue until resonant electron is at pulse end
 < Is pulse end a minimum resonant point
 < Index to minimum resonant velocity
 < Index to maximum resonant velocity
 < Pulse end a maximum resonant velocity
 < Index to minimum resonant velocity
 < Index to maximum resonant velocity

 < Is equatorial resonant velocity the minimum

 < Shifted minimum resonance velocity index
 < Keep minimum resonant velocity index within array range
 < Shifted maximum resonance velocity index
 < Keep maximum resonant velocity index within array range
 < Actual minimum parallel velocity at resonance (m/s)
 < Minimum parallel velocity at injection
 < # of parallel velocity steps not to be less than 1

 < The ivp index when time and position will be determined

 < Loop over parallel velocity
 < Injection or adiabatic velocity

 < # of micro per macro step based upon the inhomogeneity

 < Initial gyrofrequency difference per micro step
 < Initial gyrofrequency gradient difference per micro step
 < Initial -k difference per micro step
 < Initial spatial difference per micro step
 < Iteration error difference per micro step
 < Initial cyclotron phase difference per micro step

 < -k at injection
 < Gyrofrequency gradient at injection
 < Gyrofrequency at injection

 < Perpendicular velocity at injection
 < Has the leading edge not crossed the upstream boundary yet
 < Time between injections measured at downstream position
 < Leading edge has propagated past upstream boundary
 < Time between injections measured at upstream boundary

 < Include energy and 'injection separation' to distribution

 < Triangular windowing function

 < Linear weight on the low v parallel side
 < Linear weight on the high v parallel side

 < Smoothly taper low velocity edge of distribution
 < Smoothly taper high velocity edge of distribution

 < Loop from injection backward for adiabatic history
 < Adiabatic perpendicular velocity

 < Adiabatic parallel velocity
 < Time difference between micro steps
 < Parallel velocity difference between micro steps
 < Perpendicular velocity difference between micro steps
 < Cyclotron phase difference between micro steps
 < -k
 < Gyrofrequency gradient
 < Gyrofrequency

 < Cyclotron phase
 < Loop to calculate cyclotron phase
 < Integrate cyclotron phase difference

 < Initial parallel velocity related term used by predictor
 < Initial perp. velocity related term used by predictor
 < Initial cyclotron phase related term used by predictor
 < Initialize cyclotron phase offset
 < Get injection wave intensity at pulse front
 < Inphase injection wave intensity
 < Quadrature injection phase intensity
 < Get injection wave intensity at upstream boundary

 < Tau index
 < Interpolation from indexed tau to actual tau
 < Interpolated inphase injection wave intensity
 < Interpolated quadrature injection wave intensity

```

end if
if (c1 .eq. 0.) then
  bwp0 = sign(PI02, c2)
  bw0 = abs(c2)*EOM*pnch(jprop1)
  if (c2 .eq. 0.) bwp0 = 0.
else
  bwp0 = atan(c2/c1)
  if (c1 .lt. 0.) bwp0 = bwp0-sign(PI, bwp0)
  bw0 = abs(c1/cos(bwp0))*EOM*pnch(jprop1)
end if

do 90 j = 1, n
  time = ztt(1)
  bw = bw0
  bwp = bwp0
  ddbph = 0.
  whz = wh(jprop1)-w
  ykz = yk(jprop1)
  dwdz = dwdz(jprop1)
  vazrb = vazrb0
  vezrb = vezrb0
  phzrb = phzrb0+dpsij

do 91 k = 1, 4
  va(k) = va0(k)
  ve(k) = ve0(k)
  ph(k) = ph0(k)+dpsij
  dva(k) = dva0(k)
  dve(k) = dve0(k)
  dph(k) = dph0(k)
continue
c1 = ve(4)*va(4)*wh(jprop1)*cpa(jprop1)
vy(1) = c1*sin(ph(4))
vx(1) = c1*cos(ph(4))

lfe = 1
l = jprop1
l = l+1
lfe = lfe+1
t = (tz(lfe-1)+dtle(1)+dz(1)/va(4))/dtao
i = int(t)+1
t = t-float(i)
c1 = (dbi(i+1)+dnoi(1,i+1))*t+bwi(i+1)+snoi(1,i+1)
c2 = (dbq(i+1)+dnoq(1,i+1))*t+bwq(i+1)+snoq(1,i+1)
if (c1 .eq. 0.) then
  cwave = rstep*(EOM*abs(c2)*pnch(1)-bw)
  if (c2 .ne. 0.) ddbph = sign(PI02, c2)-bwp
else
  c2 = atan(c2/c1)
  if (c1 .lt. 0.) c2 = c2-sign(PI, c2)
  cwave = rstep*(EOM*abs(c1/cos(c2))*pnch(1)-bw)
  ddbph = c2-bwp
end if
if (abs(ddbph) .gt. PI) ddbph = ddbph-sign(PI2, ddbph)
cddbph = rstep*cddbph
cdz = rstep*dz(1)
cdwdz = rstep*dwdz(1)
cwhz = rstep*dwh(1)
cykz = rstep*dyk(1)

do 110 m = 1, nstep
  include 'user1:[curt.dir.library]simula
    (pre_corr)/list'
  bwp = bwp + cddbph
  time = time+dt
  continue

  if (abs(bwp) .gt. PI) bwp = bwp-
    sign(PI2, float((int(abs(bwp/PI))+1)/2), bwp)
  tz(lfe) = time-tle(1)
  c1 = ve(4)*va(4)*wh(1)*cpa(1)
  vy(lfe) = c1*sin(ph(4)+bwp)
  vx(lfe) = c1*cos(ph(4)+bwp)
  if ((ipa .eq. npah).and.(lvp .eq. nvph))
    ztt(lfe) = time
  if ((tz(lfe) .lt. tp).and.(l .lt. mz)) go to 100

  i = int(tz(1)/dtao)+2
  t = float(i-1)*dtao
  l = 1
  l = l+1
  if (l .le. lfe) then
    if (tz(1) .lt. t) go to 80
    t = (t-tz(1-1))/(tz(1)-tz(1-1))
    ycr(1) = ycr(1)+(vy(1-1)-(vy(1)-vy(1-1))*t)*fval
    xcr(1) = xcr(1)+(vx(1-1)-(vx(1)-vx(1-1))*t)*fval
    if ((ipa .eq. npah).and.(lvp .eq. nvph)) then
      m = jprop+1
      sbt(1) = sbt(1)+(ztt(1-1)+(ztt(1)-ztt(1-1))*t)*yys
      sbz(1) = sbz(1)+(z(m-1)+dz(m)*t)*yys
    end if
    t = float(i)*dtao
    i = i+1
    if (i .le. ntao) go to 81
  end if

  dpsij = dpsij+dpsij
  continue

  vpa0 = vpa0+dvpar
  vpamin = vpa0*cpa(jprop)/cpa(lmin)
  continue
  pa = pa+dpa
  continue
end if
bmax = 0.
do 48 i = 2, ntao
  if (sbz(i) .gt. ztap) then
    c1 = sin(PI02*(zdown-sbz(i))/(zdown-ztap))*2
    ycr(i) = ycr(1)*c1
    xcr(i) = xcr(1)*c1
  end if
  bwi(i) = bwi(1)+ycr(i)*ADJ
  bwq(i) = bwq(1)-xcr(i)*ADJ
  bmax = max(bmax, bwi(i)*bwi(i)+bwq(i)*bwq(i))
  sbi(i) = bwi(1)
  sbq(i) = bwq(1)
48 continue

  Determine injection wave magnitude and phase
  Plus or minus pi/2 since purely quadrature
  Scale magnitude by e/m and spatial shaping window
  Zero phase if magnitude is zero

  Put phase in correct quadrant
  Scale magnitude by e/m and spatial shaping window

  Loop over initial cyclotron phase
  Initialize injection time
  Initialize injection wave magnitude
  Initialize injection wave phase
  Initialize injection wave phase difference per macro step
  Initialize injection gyrofrequency - frequency
  Initialize injection -k
  Initialize injection gyrofrequency gradient
  Initialize predictor parallel velocity related term
  Initialize predictor perpendicular velocity related term
  Initialize predictor cyclotron phase related term

  Loop over initial adiabatic histories for initialization
  Initialize injection parallel velocity history
  Initialize injection perpendicular velocity history
  Initialize injection cyclotron phase history
  Initialize injection parallel velocity difference history
  Initialize injection perp' velocity difference history
  Initialize injection cyclotron phase difference history

  Scale injection perp' vel' by distribution related terms
  Quadrature perpendicular velocity from -B
  Inphase perpendicular velocity to -B
  Send each electron through
  Index relative to injection point
  Initialize position index
  Advance position index to future macro step
  Advance relative index to future value
  # of tau steps into wave predicted at next macro step
  Predicted future tau index
  Predicted fractional tau
  Predicted interpolated inphase wave intensity
  Predicted interpolated quadrature wave intensity
  If no predicted inphase wave component
  Predicted change in wave magnitude
  Predicted change in wave phase
  For predicted inphase wave component

  Put predicted phase in correct quadrant
  Predicted change in wave magnitude
  Predicted change in wave phase

  Correct for phase discontinuity at pi
  Wave phase change per micro step
  Position change per micro step
  Change in gyrofrequency gradient per micro step
  Change in gyrofrequency per micro step
  Change in -k per micro step

  Loop over micro steps to advance one macro step
  Include Predictor-Corrector routines

  Advance wave phase
  Advance time

  Summing x,y velocities for each particle at each point.
  Keep wave phase within +- pi bounds

  Tau at new position
  Scale perpendicular velocity by distribution related terms
  Quadrature perpendicular velocity component relative to -B
  Inphase perpendicular velocity component relative to -B
  If median particles record time

  Continue if not past pulse end or downstream boundry

  Injection tau index
  Tau at indexed value
  Initialize relative macro step index
  Increment relative macro step index
  Don't go further than was actually performed
  Increment until actual tau is >= indexed tau
  Interpolation value
  Sum quadrature velocities along constant tau values
  Sum inphase velocities along constant tau values
  Check for median electron for time and space calculation
  Compute absolute spatial index
  Average time over gyrophase
  Average position over gyrophase

  Next indexed tau value
  Update tau index
  Continue if not past last tau index

  Increment initial cyclotron phase
  Continue looping over gyrophase

  Increment initial parallel velocity
  Corresponding equatorial parallel velocity
  Continue looping over parallel velocity
  Increment initial pitch angle
  Continue looping over pitch angle

  Reset the square of the maximum field intensity
  Loop over tau indicies to calculate new wave fields
  Does current need to be tapered near downstream boundry
  Taper parameter
  Taper quadrature component
  Taper inphase component

  Update inphase wave field
  Update quadrature wave field
  Get maximum wave intensity squared
  Put inphase component into single precision for output
  Put quadrature component into single precision for output

```

```
write (12) (sbi(1), i=1,ntao)
write (12) (sbq(1), i=1,ntao)
write (12) (sbt(1), i=1,ntao)
write (12) (sbz(1), i=1,ntao)
C 49 continue
C close(unit=12)
C stop
C end
```

< Output wave intensity versus position and time

< Continue looping over initial wave position

< Good luck! I hope it was a good run.

Parameter include file listing

Parameters to be included in all simulation programs

```

parameter (
+   PI      = 3.141592653589793238 ,
+   PI2     = PI*2. ,
+   RIP     = PI/180. ,
+   PIO2    = PI*.5 ,
+   SQR3    = 1.732050807568877 ,
+   YMSF    = 236374. ,
+   MTR     = 6 ,
+   PSIO    = PI2 ,
+   WB0     = PI2*8.736e5 ,
+   R0      = 6.3712e6 ,
+   R1      = R0+1.e6 ,
+   P1      = 4./3. ,
+   P2      = 112./121. ,
+   S1      = 0.9 ,
+   S2      = 0.08 ,
+   S3      = 0.02 ,
+   OOT     = -1./1.6e3 ,
+   B1      = OOT/70.93906493 ,
+   E2      = OOT/1126.582431 ,
+   H3      = OOT/283.5903962 ,
+   C       = 2.997925e8 ,
+   CC      = C*C ,
+   CF      = 3.077827553e-3 ,
+   Q       = 56.41460098 ,
+   QP      = C/Q ,
+   OO24    = 1./24. ,
+   SO3     = 7./3. ,
+   EOM     = 1.7588028e11 ,
+   UO02    = PI2*1.e-7 ,
+   JTOPT   = UO02*1.e12 ,
+   CEM     = 511.0041175 ,
+   QE      = 1.6021917e-19 ,
+   PRIO    = 1.6261264e-17 ,
+   ADJ     = 1.e-15 ,
+   QPOA    = PI2*(QE/ADJ)*PRIO ,
+   DISC    = UO02*QPOA*0.5 )

```

< PI
 < 2*PI
 < Degree to radian conversion factor
 < PI/2
 < Square root of 3
 < Scaling factor used to determine the spatial step size
 < Maximum number of iterations performed by P-C algorithm
 < Phase offset added to initial electron gyrophases
 < Coefficient for the dipole model of the gyrofrequency
 < Earth radii (m)
 < Radii at 1000 km altitude (m)
 < A parameter used in the Predictor
 < A parameter used in the Predictor
 < Fractional abundance of O+ at 1000 km altitude
 < Fractional abundance of H+ at 1000 km altitude
 < Fractional abundance of He+ at 1000 km altitude
 < -1/(electron temperature at 1000 km altitude)
 < Reciprocal of the O+ scale height at 1000 km altitude
 < Reciprocal of the H+ scale height at 1000 km altitude
 < Reciprocal of the He+ scale height at 1000 km altitude
 < Speed of light (m/s)
 < Speed of light squared
 < Geopotential height term coefficient of the DE equation
 < Part of the plasma frequency equation
 < Not used in this version
 < Not used in the present version
 < Not used in this version
 < Electron charge to mass ratio
 < One half the free space permeability
 < Converts a current sheet into magnetic field radiation
 < Electron rest mass energy (keV)
 < Electron charge (C)
 < Multiplying constant in the distribution function
 < Adjustment keeps radiation calculation from underflowing
 < Product of constants to calculate distribution function
 < Product of constants to convert v_perp to B_s

Predictor-Corrector include file listing

Predictor-Corrector integration of the equations of motion.

For a description of the method used see "A first course in numerical analysis", second edition by Anthony Ralston and Philip Rabinowitz, copyright 1978, pages 191-195.

```

c4 = dva(4)+dva(4)-dva(3)
c1 = va(4)+((va(4)-va(2))+3.*c4)*0.125
v1 = P2*(va(4)-vazrb)
vazrb = va(1)+P1*(dva(2)+dva(2)+c4)
v1 = v1+vazrb

c4 = dve(4)+dve(4)-dve(3)
c2 = ve(4)+((ve(4)-ve(2))+3.*c4)*0.125
v2 = P2*(ve(4)-vezrb)
vezrb = ve(1)+P1*(dve(2)+dve(2)+c4)
v2 = v2+vezrb

c4 = dph(4)+dph(4)-dph(3)
c3 = ph(4)+((ph(4)-ph(2))+3.*c4)*0.125
gy = P2*(ph(4)-phzrb)
phzrb = ph(1)+P1*(dph(2)+dph(2)+c4)
gy = gy+phzrb

do 120 i = 1,3
  va(i) = va(i+1)
  ve(i) = ve(i+1)
  ph(i) = ph(i+1)
  dva(i) = dva(i+1)
  dve(i) = dve(i+1)
  dph(i) = dph(i+1)
continue
120

c4 = w/ykz
i = 1
dyb = cdz*ykz-cdbph

119
dt = cdz/v1
c5 = (c4-v1)*dt
c6 = v2*dwdz
c7 = bw*sin(gy)
dva(4) = (c7-c6)*v2*dt
dve(4) = c5*c7+c6*cdz
dph(4) = whz*dt+dyb+bw*cos(gy)*c5/v2
va(4) = c1+0.375*dva(4)
ve(4) = c2+0.375*dve(4)
ph(4) = c3+0.375*dph(4)

if (abs(ph(4)/gy-1.) .ge. dtrtn) then
  if (i .ne. MITR) then
    i = i+1
    v1 = va(4)
    v2 = ve(4)
    gy = ph(4)
    go to 119
  end if
  write (6,118) i, m, j, ivp, ipa
  format (' no convergence',5(14,2x),/)
end if

118
bw = bw +twave
whz = whz +cwhz
ykz = ykz +cykz
dwdz = dwdz+cdwdz

< Parallel velocity calculations
<
< Part of the Corrector
<
< Milne Predictor
< Modifier
< Perpendicular velocity calculations
<
< Part of the corrector
<
< Milne Predictor
< Modifier
< Cyclotron phase calculations
<
< Part of the Corrector
<
< Milne Predictor
< Modifier
<
< Loop to shift previous values
<
<
<
<
< Phase velocity
< Initialize iteration counter
< Cyclotron phase terms, don't change each iteration
< Beginning of iteration sequence
< Electron travel time per microstep
<
<
<
< Parallel velocity difference
< Perpendicular velocity difference
< Cyclotron phase difference
< Parallel velocity Corrector
< Perpendicular velocity Corrector
< Cyclotron phase Corrector
<
< Check for convergence
< Check if iteration limit exceeded
< Increment iteration
< Update working variables
<
<
< Iterate
<
< Write out all loop counters when convergence failed
<
< Integration complete for present microstep
< Update quantities for the next microstep
< Update wave field magnitude
< Update gyrofrequency
< Update -k
< Update gyrofrequency gradient

```


References

- Al'pert, Y., 40 years of whistlers, *J. Atmos. Terr. Phys.*, **42**, 1, 1980.
- Anderson, R. R., Wave particle interactions in the evening magnetosphere during geomagnetically disturbed periods, Ph.D. thesis, Univ. of Iowa, Iowa City, 1976.
- Anderson, R. R., Plasma waves in planetary magnetospheres, *Rev. Geophys. Space Phys.*, **21**, 474, 1983.
- Angerami, J. J., and J. O. Thomas, Studies of planetary atmospheres, 1, The distribution of electrons and ions in the earth's exosphere, *J. Geophys. Res.*, **69**, 4537, 1964.
- Artsimovich, L. A., and S. Y. Lukyanov, *Motion of charged particles in electric and magnetic fields*, MIR Publishers, Moscow, USSR, 1980.
- Bak, P., The devil's staircase, *Physics Today*, **39**, 38, 1986.
- Bell, T. F., The nonlinear gyroresonance interaction between energetic electrons and coherent VLF waves propagating in an arbitrary angle with respect to the earth's magnetic field, *J. Geophys. Res.*, **89**, 905, 1984.
- Bell, T. F., The wave magnetic field amplitude threshold for nonlinear trapping of energetic gyroresonant and Landau resonant electrons by nonducted VLF waves in the magnetosphere, *J. Geophys. Res.*, **91**, 4365, 1986.
- Bell, T. F., and R. A. Helliwell, Pulsation phenomena observed in long-duration VLF whistler-mode signals, *J. Geophys. Res.*, **76**, 8414, 1971.
- Bell, T. F., and U. S. Inan, Transient nonlinear pitch angle scattering of energetic electrons by coherent VLF wave packets in the magnetosphere, *J. Geophys. Res.*, **86**, 9047, 1981.
- Bell, T. F., U. S. Inan, and R. A. Helliwell, ISEE-1 satellite observations of VLF signals and associated triggered emissions from the Siple Station transmitter, *IMS in Antarctica*, Tokyo: National Institute of Polar Research, 128, 1980.
- Bell, T. F., U. S. Inan, and R. A. Helliwell, Nonducted coherent VLF waves and associated triggered emissions observed on the ISEE-1 satellite, *J. Geophys. Res.*, **86**, 4649, 1981.
- Bell, T. F., U. S. Inan, I. Kimura, H. Matsumoto, T. Mukai, and K. Hashimoto, EXOS-B/Siple VLF wave-particle interaction experiments: 2. Transmitter signals and associated emissions, *J. Geophys. Res.*, **88**, 295, 1983.
- Bell, T. F., J. P. Katsufakis, and H. G. James, A new type of VLF emission triggered at low altitude in the subauroral region by Siple Station VLF transmitter signals, *J. Geophys. Res.*, **90**, 12183, 1985.

- Birdsall, C. K., and A. B. Langdon, *Plasma Physics via Computer Simulation*, McGraw-Hill Book Company, 1985.
- Brice, N. M., An explanation of triggered very-low-frequency emissions, *J. Geophys. Res.*, **68**, 4626, 1963.
- Budden, J. G., *Radio Waves in the Ionosphere*, Cambridge University Press, Cambridge, England, 1961.
- Carlson, C. R., Siple 21- and 42-kilometer antennas: Measurement and performance, *Ant. J. United States*, **18**, 270, 1983.
- Carlson, C. R., R. A. Helliwell, and D. L. Carpenter, Variable frequency VLF signals in the magnetosphere: associated phenomena and plasma diagnostics, *J. Geophys. Res.*, **90**, 1507, 1985.
- Carlson, C. R., R. A. Helliwell, and D. L. Carpenter, Correction to "Variable frequency VLF signals in the magnetosphere: associated phenomena and plasma diagnostics", *J. Geophys. Res.*, **90**, 6689, 1985.
- Carpenter, D. L., Whistler evidence of a "knee" in the magnetospheric ionization density profile, *J. Geophys. Res.*, **68**, 1675, 1963.
- Carpenter, D. L., Whistler studies of the plasmopause in the magnetosphere, *J. Geophys. Res.*, **71**, 693, 1966.
- Carpenter, D. L., Fast fluctuations in the arrival bearing of magnetospherically propagating signals from the Siple, Antarctica, VLF transmitter, *J. Geophys. Res.*, **85**, 4157, 1980.
- Carpenter, D. L., and Z. T. Bao, Occurrence properties of ducted whistler-mode signals from the new VLF transmitter at Siple Station, Antarctica, *J. Geophys. Res.*, **88**, 7051, 1983.
- Carpenter, D. L., and T. R. Miller, Ducted magnetospheric propagation of signals from the Siple, Antarctica VLF transmitter, *J. Geophys. Res.*, **81**, 2692, 1976.
- Carpenter, D. L., and T. R. Miller, Rare ground-based observations of Siple VLF transmitter signals outside the plasmopause, *J. Geophys. Res.*, **A12**, 10227, 1983.
- Carpenter, D. L., U. S. Inan, E. W. Paschal, and A. J. Smith, A new VLF method for studying burst precipitation near the plasmopause, *J. Geophys. Res.*, **90**, 4383, 1985.
- Chang, H. C., Cyclotron resonant scattering of energetic electrons by electromagnetic waves in the magnetosphere, *Tech. Rep. E414-1*, p. 91, STARLAB, Stanford Electron. Lab., Stanford Univ., Stanford, Calif., 1983.
- Chang, H. C., and U. S. Inan, Quasi-relativistic electron precipitation due to interactions with coherent VLF waves in the magnetosphere, *J. Geophys. Res.*, **88**, 318, 1983.

- Das, A. D., and V. H. Kulkarni, Frequency-time structure of VLF emissions, *Planet. Space Sci.*, **23**, 41, 1975.
- Dowden, R. L., Electron energy spectrum and structure deduced from analysis of VLF discrete emissions by using the Helliwell criterion, *J. Geophys. Res.*, **76**, 3034, 1971a.
- Dowden, R. L., VLF discrete emissions deduced from Helliwell's theory, *J. Geophys. Res.*, **76**, 3046, 1971b.
- Dowden, R. L., A. D. McKay, L. E. S. Amon, H. C. Koons, and M. H. Dazey, Linear and nonlinear amplification in the magnetosphere during a 6.6-kHz transmission, *J. Geophys. Res.*, **83**, 169, 1978.
- Dowell, M., and P. Jarratt, The 'Pegasus' method for computing the root of an equation, *BIT*, **12**, 503, 1972.
- Dungey, J. W., Loss of Van Allen electrons due to whistlers, *Planet. Space Sci.*, **11**, 591, 1963.
- Dysthe, K. B., Some studies of triggered whistler emissions, *J. Geophys. Res.*, **76**, 6915, 1971.
- Gail, W. B., Gyroresonant wave-particle interactions in a dynamic magnetosphere, Ph.D. thesis, Stanford University, Stanford, California, 1987.
- Helliwell, R. A., *Whistlers and Related Ionospheric Phenomena*, Stanford University Press, Stanford, Calif., 1965.
- Helliwell, R. A., A theory of discrete VLF emissions from the magnetosphere, *J. Geophys. Res.*, **72**, 4773, 1967.
- Helliwell, R. A., Intensity of discrete VLF emissions, in *Particles and Fields in the Magnetosphere*, edited by B. M. McCormac, p. 292, Dordrecht, D. Reidel, Hingham, Mass., 1970.
- Helliwell, R. A., Controlled VLF wave injection experiments in the magnetosphere, *Space Sci. Rev.*, **15**, 781, 1974.
- Helliwell, R. A., Coherent VLF waves in the magnetosphere, *Phil. Trans. R. Soc. Lond. A.*, **280**, 137, 1975.
- Helliwell, R. A., Siple Station experiments on wave-particle interactions in the magnetosphere, in *Wave Instabilities in Space Plasmas*, edited by P. J. Palmadesso and K. Papadopoulos, p. 191, D. Reidel, Hingham, Mass., 1979.
- Helliwell, R. A., VLF wave injection from the ground, Active experiments in space, symposium at Alpbach 24-28 May 1983, *Eur. Space Agency Spec. Publ. ESA*, **195**, 3, 1983a.

- Helliwell, R. A., Controlled stimulation of VLF emissions from Siple Station, Antarctica, *Radio Sci.*, 18, 801, 1983b.
- Helliwell, R. A., and T. L. Crystal, A feedback model of cyclotron interaction between whistler-mode waves and energetic electrons in the magnetosphere, *J. Geophys. Res.*, 78, 7357, 1973.
- Helliwell, R. A., and J. P. Katsufakis, VLF wave injection into the magnetosphere from Siple Station, Antarctica, *J. Geophys. Res.*, 79, 2511, 1974.
- Helliwell, R. A., and J. P. Katsufakis, Controlled wave-particle interaction experiments, in *Upper Atmosphere Research in Antarctica, Antarctic Res. Ser.*, vol. 29, edited by L. J. Lanzerotti and C. G. Park, AGU, Washington, D.C., 1978.
- Helliwell, R. A., and U. S. Inan, VLF wave growth and discrete emission triggering in the magnetosphere: A feedback model, *J. Geophys. Res.*, 87, 4427, 1982.
- Helliwell, R. A., J. P. Katsufakis, T. F. Bell, and R. Raghuram, VLF line radiation in the earth's magnetosphere and its association with power system radiation, *J. Geophys. Res.*, 80, 4249, 1975.
- Helliwell, R. A., D. L. Carpenter, and T. R. Miller, Power threshold for growth of coherent VLF signals in the magnetosphere, *J. Geophys. Res.*, 85, 3360, 1980.
- Helliwell, R. A., U. S. Inan, J. P. Katsufakis, and D. L. Carpenter, Beat excitation of whistler mode sidebands using the Siple VLF transmitter, *J. Geophys. Res.*, 91, 143, 1986a.
- Helliwell, R. A., D. L. Carpenter, U. S. Inan, and J. P. Katsufakis, Generation of band-limited VLF noise using the Siple transmitter: A model for magnetospheric hiss, *J. Geophys. Res.*, 91, 4381, 1986b.
- Hess, W. N., *The Radiation Belt and the Magnetosphere*, Blaisdell Publishing Co., Mass., 1968.
- Inan, U. S., Nonlinear gyroresonant interactions of energetic particles and coherent VLF waves in the magnetosphere, Tech. Report No. 3414-3, Radioscience Lab., Stanford Electronics Labs, Stanford, CA 1977.
- Inan, U. S., and T. F. Bell, The plasmopause as a VLF wave guide, *J. Geophys. Res.*, 82, 2819, 1977.
- Inan, U. S., and R. A. Helliwell, DE-1 observations of VLF transmitter signals and wave-particle interactions in the magnetosphere, *Geophys. Res. Lett.*, 9, 917, 1982.
- Inan, U. S., T. F. Bell, D. L. Carpenter, and R. R. Anderson, Explorer 45 and Imp 6 observations in the magnetosphere of injected waves from the Siple Station VLF transmitter,

- J. Geophys. Res.*, **82**, 1177, 1977.
- Inan, U. S., T. F. Bell and R. A. Helliwell, Nonlinear pitch angle scattering of energetic electrons by coherent VLF waves in the magnetosphere, *J. Geophys. Res.*, **83**, 3235, 1978.
- Inan, U. S., T. F. Bell, and H. C. Chang, Particle precipitation induced by short-duration VLF waves in the magnetosphere, *J. Geophys. Res.*, **87**, 6243, 1982.
- Jensen, R. V., Classical chaos, *American Scientist*, **75**, 168, 1987.
- Karpman, V. I., Ja. N. Istomin, and D. R. Shklyar, Effects of nonlinear interaction of monochromatic waves with resonant particles in the inhomogeneous plasma, *Physica Scripta*, **11**, 278, 1975.
- Karpman, V. I., Ja. N. Istomin, and D. R. Shklyar, Nonlinear frequency shift and self-modulation of the quasi-monochromatic whistlers in the inhomogeneous plasma (magnetosphere), *Planet. Space Sci.*, **22**, 859, 1974a.
- Karpman, V. I., Ja. N. Istomin, and D. R. Shklyar, Nonlinear theory of a quasi-monochromatic whistler mode wave packet in inhomogeneous plasma, *Plasma Phys.*, **16**, 685, 1974b.
- Kennel, C. F. and Petschek, H. E., Limit on stably trapped particle fluxes, *J. Geophys. Res.*, **71**, 1, 1966.
- Kimura, I., H. Matsumoto, T. Mukai, K. Hashimoto, R. A. Helliwell, T. F. Bell, U. S. Inan, and J. P. Katsufakis, Jikiken (EXOS-B) observation of Siple transmissions, *Adv. Space Res.*, **1**, 197, 1981.
- Kimura, I., H. Matsumoto, T. Mukai, K. Hashimoto, T. F. Bell, U. S. Inan, R. A. Helliwell, and J. P. Katsufakis, EXOS-B/Siple Station VLF wave-particle interaction experiments: 1. General description and wave-particle correlations, *J. Geophys. Res.*, **88**, 282, 1983.
- Kintner, P. M., R. Brittain, M. C. Kelley, D. L. Carpenter and M. J. Rycroft, In situ measurements of transionospheric VLF wave injection, *J. Geophys. Res.*, **88**, 7065, 1983.
- Lichtenberg, A. J., and M. A. Lieberman, *Regular and stochastic motion*, Applied Mathematical Sciences, **38**, Springer-Verlag, 1983.
- Liemohn, H. B., Stimulation of VLF amplification in the magnetosphere, *Space Sci. Rev.*, **15**, 861, 1974.
- Likhter, Ya. I., O. A. Molchanov, and V. M. Chmyrev, Modulation of spectrum and amplitudes of low-frequency signal in the magnetosphere plasma, *Sov. Phys. JETP Lett.*, **14**, 325, 1971.
- Lyons, L. R., and D. J. Williams, The quiet time structure of energetic (35-560 keV) radiation belt electrons, *J. Geophys. Res.*, **80**, 943, 1975.
- Lyons, L. R., and D. J. Williams, *Quantitative Aspects of Magnetospheric Physics*, Geo-

- physics and Astrophysics Monographs, D. Reidel Publishing Company, 1984.
- Matsumoto, H., Nonlinear whistler-mode interaction and triggered emissions in the magnetosphere: A review, in *Wave Instabilities in Space Plasmas*, edited by P. J. Palmadesso and K. Papadopoulos, p. 163, D. Reidel, Hingham, Mass., 1979.
- Matsumoto, H., Coherent nonlinear effects on electromagnetic wave-particle interactions, *Space Science Reviews*, 42, 429, 1985.
- Matsumoto, H., and Y. Omura, Cluster- and channel-effect phase bunching by whistler waves in a nonuniform geomagnetic field, *J. Geophys. Res.*, 86, 779, 1981.
- Matsumoto, H., and Y. Omura, Computer simulation studies of VLF triggered emissions: Deformation of distribution function by trapping and detrapping, *Geophys. Res. Letter*, 10, 607, 1983.
- Matthews, J. P., Y. Omura, and H. Matsumoto, A study of particle trapping by whistler mode waves in the geomagnetic field: The early development of the VLF quiet band, *J. Geophys. Res.*, 89, 2275, 1984.
- Melrose, D. B., *Instabilities in Space and Laboratory Plasmas*, Cambridge University Press, 1986.
- Molvig, K., G. Hilfer, and J. Myczkowski, Self-consistent theory of triggered whistler emissions, *EOS, Trans., Amer. Geophys. Union*, 67, 44, 1166, 1986.
- Murdoch, N., Theory of weakly nonlinear VLF interactions, *J. Plasma Phys.*, 30, 495, 1983.
- Neubert, T., T. F. Bell, and L. R. O. Storey, Resonance between coherent whistler mode waves and electrons in the topside ionosphere, *J. Geophys. Res.*, 92, 255, 1987.
- Nunn, D., A theory of VLF emissions, *Planet. Space Sci.*, 19, 1141, 1971.
- Nunn, D., A self-consistent theory of triggered VLF emissions, *Planet. Space Sci.*, 22, 349, 1974.
- Nunn, D., The quasistatic theory of triggered VLF emissions, *Planet. Space Sci.*, 32, 325, 1984.
- Omura, Y., Study on nonlinear wave-particle interactions in space plasmas via computer simulations, Ph.D. thesis, Kyoto University, Kyoto, Japan.
- Omura, Y., and H. Matsumoto, Computer simulation of basic processes of coherent whistler wave-particle interactions in the magnetosphere, *J. Geophys. Res.*, 87, 4435, 1982.
- Park, C. G., Methods of determining electron concentrations in the magnetosphere from nose whistlers, *Tech. Rep. 3454-1*, Radioscience Lab., Stanford Electron. Lab., Stanford Univ., Stanford Calif., 1972.
- Park, C. G., Island earth in a solar sea, *MOSAIC*, 47, Sep./Oct., 1978.

- Park, C. G., Generation of whistler-mode side-bands in the magnetosphere, *J. Geophys. Res.*, **82**, 2286, 1981.
- Park, C. G., and D. L. Carpenter, Very low frequency radio waves in the magnetosphere, Paper 4 in *Upper Atmosphere Research in Antarctica, Antarctic Research Series*, **29**, edited by L. J. Lanzerotti and C. G. Park, American Geophysical Union, 1978.
- Park, C. G., and D. C. D. Chang, Transmitter simulation of power line radiation effects in the magnetosphere, *Geo. Res. Lett.*, **5**, 861, 1978.
- Paschal, E. W., and R. A. Helliwell, Phase measurements of whistler mode signals from the Siple VLF transmitter, *J. Geophys. Res.*, **89**, 1667, 1984.
- Raghuram, R., T. F. Bell, R. A. Helliwell, and J. P. Katsufakis, Quiet band produced by VLF transmitter signals in the magnetosphere, *Geo. Res. Lett.*, **4**, 199, 1977a.
- Raghuram, R., T. F. Bell, R. A. Helliwell, and J. P. Katsufakis, Echo-induced suppressions of coherent VLF transmitter signals in the magnetosphere, *J. Geophys. Res.*, **82**, 2787, 1977b.
- Ralston, A., and P. Rabinowitz, *A First Course in Numerical Analysis*, 191, 1978.
- Rastani, K., U. S. Inan, and R. A. Helliwell, DE 1 observations of Siple transmitter signals and associated sidebands, *J. Geophys. Res.*, **90**, 4128, 1985.
- Rathmann, C. E., J. L. Vomvoridis, and J. Denavit, Long-time-scale simulation of resonant particle effects in Langmuir and whistler waves, *J. Comp. Phys.*, **26**, 408, 1978.
- Rietveld, M. T., Monochromatic precursor starts, *J. Geophys. Res.*, **85**, 2027, 1980.
- Rietveld, M. T., R. L. Dowden, and L. E. S. Amon, Micropulsations observed by whistler mode transmissions, *Nature*, **276**, 165, 1978.
- Roederer, J. G., *Dynamics of Geomagnetically Trapped Particles*, Springer, New York, 1970.
- Roux, A., and R. Pellat, A theory of triggered emissions, *J. Geophys. Res.*, **83**, 1433, 1978.
- Scarabucci, R. R., and R. L. Smith, Study of magnetospheric field oriented irregularities: The mode theory of bell-shaped ducts, *Radio Sci.*, **6**, 65, 1971.
- Schild, M. A., and L. A. Frank, Electron observations between the inner edge of the plasma sheet and the plasmasphere, *J. Geophys. Res.*, **75**, 5401, 1970.
- Schultz, M., and L. J. Lanzerotti, *Particle Diffusion in the Radiation Belts*, Physics and Chemistry in Space, Springer-Verlag, 7, 1974.
- Shawhan, S. D., Magnetospheric plasma wave research 1975-1978, *Rev. Geophys. Space Phys.*, **17**, 705, 1979a.
- Shawhan, S. D., Magnetospheric plasma waves, *Solar System Plasma Physics. Volume III*, edited by L. J. Lanzerotti, C. F. Kennel and E. H. Parker, North-Holland Publishing

- Company, 1979b.
- Smith, A. J., D. L. Carpenter, and U. S. Inan, Whistler-triggered VLF noise bursts observed on the DE-1 satellite and simultaneously at Antarctic ground stations, *Annales Geophysicae*, **3**, 1, 81, 1985.
- Smith, R. L., Guiding of whistlers in a homogeneous medium, *J. Res. NBS-D, Radio Propagation*, **64D**, 505, 1960.
- Smith, R. L., Propagation characteristics of whistler trapped in field-aligned columns of enhanced ionization, *J. Geophys. Res.*, **66**, 3699, 1961.
- Smith, R. L., R. A. Helliwell, and I. W. Yabroff, A theory of trapping of whistlers in field-aligned columns of enhanced ionization, *J. Geophys. Res.*, **65**, 815, 1960.
- Sonwalkar, V. S., and U. S. Inan, Measurements of Siple transmitter signals on the DE 1 satellite: Wave normal direction and antenna effective length, *J. Geophys. Res.*, **91**, 154, 1986.
- Sonwalkar, V. S., T. F. Bell, R. A. Helliwell, and U. S. Inan, Direct multiple path magnetospheric propagation: A fundamental property of nonducted VLF waves, *J. Geophys. Res.*, **89**, 2823, 1984.
- Stiles, G. S., Controlled VLF experiments, *ELF-VLF Radio Wave Propagation*, D. Reidel Publ. Co. Dordrecht, Holland, 1974.
- Stiles, G. S., and R. A. Helliwell, Frequency-time behavior of artificially stimulated VLF emissions, *J. Geophys. Res.*, **80**, 608, 1975.
- Stiles, G. S., and R. A. Helliwell, Stimulated growth of coherent VLF waves in the magnetosphere, *J. Geophys. Res.*, **82**, 523, 1977.
- Storey, L. R. O., An investigation of whistling atmospherics, Ph.D. thesis, Cambridge University, Cambridge, England, 1953.
- Strangeways H. J., Determination by ray-tracing of the regions where mid-latitude whistlers exit from the lower ionosphere, *J. Atmos. Terr. Phys.*, **43**, 231, 1981a.
- Strangeways H. J., Trapping of whistler-mode waves in ducts with tapered ends, *J. Atmos. Terr. Phys.*, **43**, 1071, 1981b.
- Sudan, R. N., and E. Ott, Theory of triggered VLF emissions, *J. Geophys. Res.*, **76**, 4463, 1971.
- Tkalcevic, S., Very-low-frequency signals (2-10 kHz) received at Palmer Station, Antarctica, from the 21.4 km dipole antenna at Siple Station, 1400 km distant, *J. Atmos. Terr. Phys.*, **45**, 353, 1983.
- Vomvoridis, J. L., Nonuniform whistler mode propagation, Ph.D. thesis, Northwestern Uni-

- versity, Evanston, Illinois, 1978.
- Vomvoridis, J. L., and J. Denavit, Nonlinear evolution of a monochromatic whistler wave in a nonuniform magnetic field, *Phys. Fluids*, 23, 174, 1980.
- Vomvoridis, J. L., and J. Denavit, Test particle correlation by a whistler wave in a nonuniform magnetic field, *Phys. Fluids*, 22, 367, 1979.
- Vomvoridis, J. L., T. L. Crystal, and J. Denavit, Theory and computer simulations of magnetospheric very low frequency emissions, *J. Geophys. Res.*, 87, 1473, 1982.
- Walker, A. D. M., The theory of whistler propagation, *Rev. Geophys. Space Phys.*, 14, 629, 1976.
- Winglee, R. M., Enhanced growth of whistlers due to bunching of untrapped electrons, *J. Geophys. Res.*, 90, 5141, 1985.

